

LA-7587-PR
Progress Report

CIC-14 REPORT COLLECTION
REPRODUCTION
COPY

Inertial fusion program



LOS ALAMOS NATIONAL LABORATORY
3 9338 00316 7698

January 1 - June 30, 1978

University of California
LLNL
LOS ALAMOS
SCIENTIFIC LABORATORY

The four most recent reports in this series, unclassified, are LA-6616-PR, LA-6834-PR, LA-6982-PR, and LA-7328-PR.

This work was supported by the US Department of Energy, Office of Laser Fusion.

This report was prepared as an account of work sponsored by the United States Government. Neither the United States nor the United States Department of Energy, nor any of their employees, makes any warranty, express or implied, or assumes any legal liability or responsibility for the accuracy, completeness, or usefulness of any information, apparatus, product, or process disclosed, or represents that its use would not infringe privately owned rights. Reference herein to any specific commercial product, process, or service by trade name, mark, manufacturer, or otherwise, does not necessarily constitute or imply its endorsement, recommendation, or favoring by the United States Government or any agency thereof. The views and opinions of authors expressed herein do not necessarily state or reflect those of the United States Government or any agency thereof.

LA-7587-PR
Progress Report

UC-21
Issued: May 1980

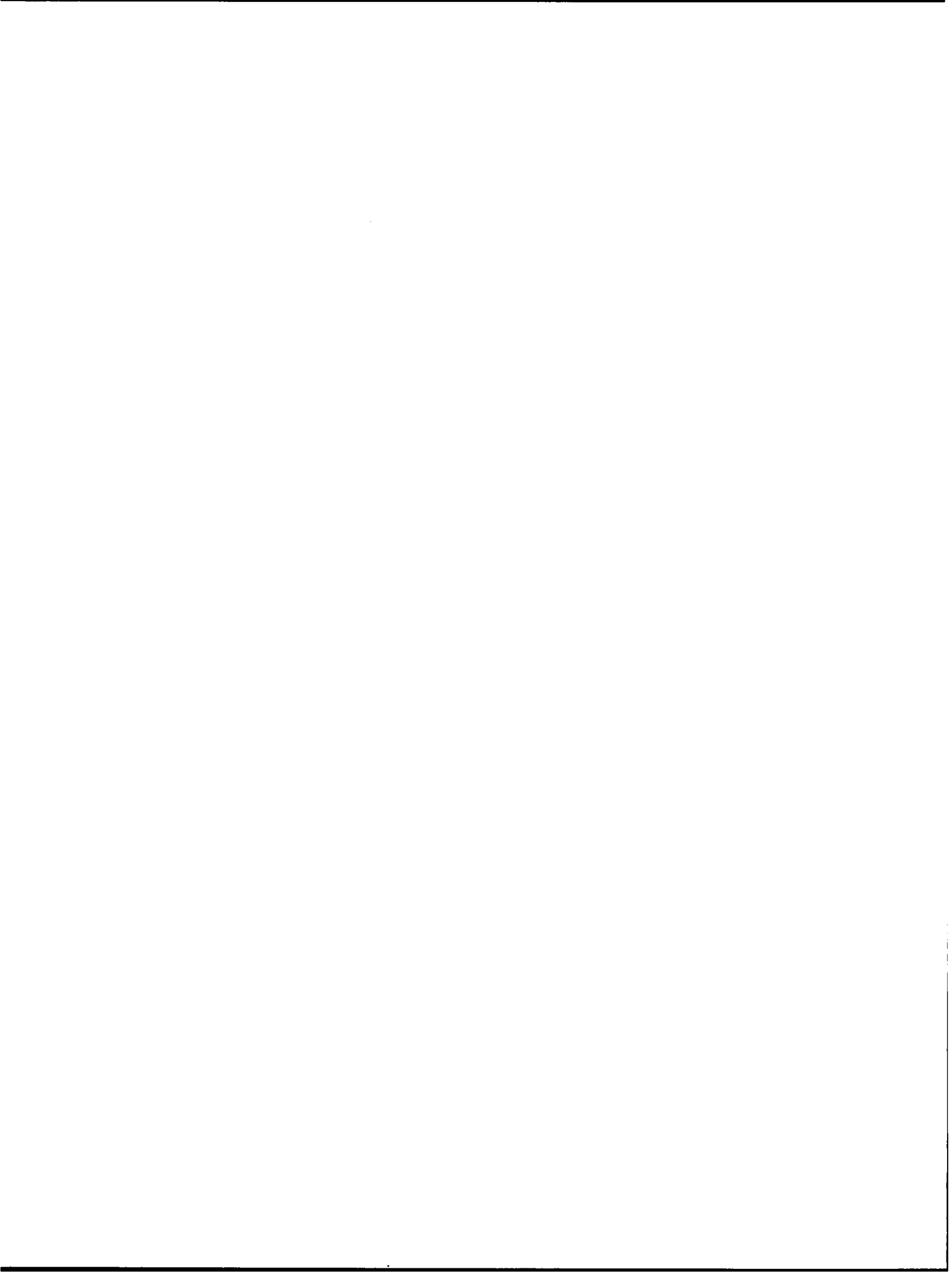
Inertial Fusion Program

January 1—June 30, 1978

Compiled by
Frederick Skoberne

L-1 James Carpenter - 6900
L-4 Ross Godwin - 6684
L-7 Jay Trice - 6461
L-9 Joe Figueroa - 5271
L-10 Hansjörg Jansen - 5827





CONTENTS

ABSTRACT	1
SUMMARY	2
Introduction	2
CO ₂ Laser Program	2
CO ₂ Laser Technology	3
Experiments and Military Applications	3
Theory and Target Design	4
Laser Fusion Target Fabrication	4
Target Diagnostics	4
Applications of Laser Fusion Systems Studies	4
I. CO ₂ LASER PROGRAM	6
Two-Beam System	6
Helios Laser Systems	7
II. ANTARES—HIGH-ENERGY GAS LASER FACILITY	17
Introduction	17
Optical System	17
Front-End System	22
Power Amplifier System	23
Energy Storage System	32
Target System	34
Controls System	34
HEGLF Site and Structures	36
III. CO ₂ LASER TECHNOLOGY	38
CO ₂ Laser Physics	38
Solid State Physics	50
Gas Isolator Development	56
References	65
IV. TARGET EXPERIMENTS AND MILITARY APPLICATIONS	68
Laser Fusion Experiments	68
Military Applications of Lasers and Related Studies	84
References	91
V. LASER FUSION THEORY AND TARGET DESIGN	93
Theoretical Support and Direction	93
Target Design	108
References	119

VI.	LASER FUSION TARGET FABRICATION	123
	Introduction	123
	Target Fabrication	124
	Inorganic Coatings Development	130
	Organic Coatings Development	135
	Polymer Shell Fabrication	140
	Polymer Foam Development	142
	Development of New Materials	143
	Cryogenic Target Development	145
	References	147
VII.	TARGET DIAGNOSTICS	148
	Introduction	148
	Neutron Diagnostics	148
	X-Ray Diagnostics	150
	Pockels Cell Development and Implications	161
	Technology Development	162
	Computer Technology	167
	References	167
VIII.	APPLICATIONS OF LASER FUSION—FEASIBILITY AND SYSTEMS STUDIES	169
	Laser Fusion Reactor and Generating Station Studies	169
	Fusion-Fission Hybrid Reactor Studies	181
	References	184
IX.	RESOURCES, FACILITIES, AND OPERATIONAL SAFETY	187
	Manpower Distribution	187
	Facilities	187
	Operational Safety	187
X.	PATENTS, PRESENTATIONS, AND PUBLICATIONS	188
	Application Filed in US Patent Office	188
	Presentations	188
	Publications	190

**INERTIAL FUSION PROGRAM
JANUARY 1—JUNE 30, 1978**

Compiled by

Frederick Skoberne

ABSTRACT

Progress in the development of high-energy short-pulse CO₂ laser systems for fusion research is reported. Improvements to our two-beam system, Gemini, are outlined, and experiments on Helios, the eight-beam system, culminating in a world record of output energy—10.7 kJ in each of three shots, exceeding the design energy of 10 kJ—are described. Work on Antares, our 100- to 200-TW target irradiation system is summarized, indicating that design work and building construction are 60 and 23% complete, respectively; baseline designs for beam sampling, diagnostic techniques, and beam steering are discussed.

Studies and experiments aimed at investigating the possibility of restoring wavefront quality in optical systems through phase conjugation are summarized, and work that could lead to the development of highly damage-resistant isolators is discussed. The effects of various parameters on pulse-energy uniformity and of multipass extraction on laser efficiency are reported. Results of equation-of-state, shock propagation, multiburst simulation, and opacity measurements are discussed. Target designs are described that should provide a smooth transition from the exploding-pusher regime of experiments to that of isentropic compression. Progress in target fabrication techniques toward creating a 20-times-liquid-density target are outlined, and efforts that led to the extension of our neutron detection capability to levels of less than 10^9 n are summarized.

The results of various studies of laser fusion application, e.g., for producing ultrahigh-temperature process heat or hydrogen from water decomposition are presented, as well as investigations of fusion-fission hybrids for the production of ²³³U from ²³²Th.

SUMMARY

R. B. Perkins and Laser Fusion Staff

INTRODUCTION

The Laser Fusion Program at the Los Alamos Scientific Laboratory (LASL) is pursuing the dual goal of developing inertial confinement fusion for commercial and military applications. For both goals it is essential to achieve scientific breakeven, that is, a fusion energy output that equals the laser energy incident on the target. For this purpose, we invented, and are developing, high-power short-pulse carbon-dioxide gas lasers, which offer the advantage of providing adequate efficiency combined with a repetition rate capability that holds promise for their eventual use in commercial power plants. As our gas laser systems become available, they are used intensively for a vigorous experimental program aimed at achieving thermonuclear burn of fuel pellets. This goal requires that we perform both basic physics experiments, to provide insight into and an understanding of the processes involved, and integral pellet burning experiments, which we expect will successfully culminate in breakeven by the mid-1980's. In support of our experimental program, we are expending significant effort in target design, target fabrication, laser facility support, and diagnostics development. In addition, a modest experimental effort directed toward military applications is under way. Also, a systems group is exploring design concepts for future commercial fusion and fusion-fission hybrid reactor systems and subsystems to identify potential problems at an early date.

CO₂ LASER PROGRAM

Two-Beam System (TBS)

The TBS continued to be our main target experiment facility. In addition to providing hundreds of shots for target experiments, modifications were incorporated into the system to improve performance, reliability, and beam characterization.

Helios

Our efforts on Helios, the eight-beam system, culminated in operating the full system at a level exceeding design specifications, thus meeting a major program milestone on schedule. In April, we produced more than 15 TW, a world record at that time. In June, we operated the system in excess of our design energy of 10 kJ on each of three shots, producing a peak energy of 10.7 kJ, again a world record for a short-pulse laser suitable for fusion studies. Work is continuing to complete the full system and to prepare for near-term target experiments.

Antares

Progress toward completion of the 100-kJ Antares laser continued, with the objective of extending present CO₂ laser capabilities to power levels at which fusion experiments can be expected to yield thermonuclear energy release in the range of scientific breakeven.

Construction of the Antares facility buildings was 23% complete at the close of this reporting period. All Antares systems progressed well, with design work 60% complete. Specifications for three major subsystems, i.e., front-end driver amplifiers, the energy storage banks, and the target chamber and vacuum system, were completed, and requests for proposals were issued.

The optical interfaces between the three major Antares optical systems (front end, power amplifiers, and target system) were defined and baseline designs for beam sampling, diagnostic techniques, and beam steering were established. We decided that two power amplifiers should be assembled and tested in parallel: Power Amplifier 1 will be devoted to electrical checkout and gain measurements, whereas Power Amplifier 6 will be used to confirm the optical beam management techniques. Power Amplifier 1 will then be completely assembled for full-power performance tests.

The Antares front end will consist of a multiline oscillator, an electro-optic switchout, preamplifiers, driver amplifiers, and saturable gas absorber cells to control parasitic oscillations and the pulse contrast ratio. We plan to install a prototype one-beam system that will allow us to verify the performance of the front-end components before their installation in Antares.

The design of the power amplifier units was nearly complete. All long-lead-time parts, such as the electron-gun chamber, the gun bushing, the pressure shells, and the vacuum spools, were released for fabrication. The design of the optical train was completed and procurement started.

More detailed analysis of the optical train, including as-manufactured component quality, showed that the peak irradiance at target would be less than desired. The optical layout in the target chamber was, therefore, redesigned to reduce the focal length from 282 to 160 cm. The peak irradiance will increase threefold because of the smaller f-number. Necessary modifications to the target-chamber and beam-tube layout were forwarded to the firms responding to our request for proposal (RFP) for target-chamber fabrication.

A full-size gas pulser of the Marx type was assembled and tested. The design characteristics of 300-kJ stored energy, 1.2×10^6 V open-circuit voltage, and 3- μ H inductance were met. Some 200 full-energy discharges into a matched load were completed. An RFP with specifications based on experience with this pulser was issued for all 24 units.

A comprehensive analysis of the control functions, which recognized the different needs during installation, checkout, and full-system operation, showed that a tiered system would satisfy the requirements best. Consequently, midlevel minicomputers will be made available to certain systems, particularly the front end, the optical system for beam steering and focusing, the power amplifiers, and the energy storage system. These midlevel control computers will be tied together at the top for full-system operation. Communication will be by serial data transmission over fiber-optic links.

CO₂ LASER TECHNOLOGY

A CO₂ laser technology and research effort is continuing in support of our present and future laser systems. A number of efforts, ranging from the

seemingly abstract to the practical, offer promise of improvements in practical CO₂ laser drivers for fusion.

In this reporting period, we took a significant step forward by demonstrating nonlinear phase conjugation in the infrared for the first time. Optical-phase conjugation is a topic of considerable current interest because it offers the possibility of restoring wavefront quality in optical systems containing unavoidable optical flaws.

A second major development occurred in the demonstration of a solid-state bleachable absorber for CO₂ wavelengths in the solid-state physics area. This work can lead to considerably more efficient, highly damage-resistant isolators for CO₂ laser systems.

Work continued to improve the performance of gas-based isolators. In particular, work centered on recovery of the absorption capability of saturable gases after delivery of the laser pulse. This information is required to prevent postlasing and retro-pulse damage.

In the study of CO₂ laser drivers for commercial applications, emphasis has been on improvement of laser efficiency by multipass energy extraction. Effects of gas mixtures, pulse timing, time separation of pulses, and of starting conditions on efficiency and pulse-energy uniformity were investigated numerically. In addition, the feasibility of experimental verification of the calculated results using either TBS or Helios lasers was examined.

EXPERIMENTS AND MILITARY APPLICATIONS

Successful laser fusion demonstration experiments require precise knowledge of, and an ability to, manipulate the spatial distribution of laser energy incident upon targets. Infrared microscope and aperture transmission measurements demonstrated that beam transport and focusing optics of sufficient quality can be obtained to achieve focal-spot energy distributions of high quality. Sophisticated beam steering and focusing apparatus were used to obtain highly reproducible target performance. Correlations among various observables have demonstrated the validity of models for hot-electron production, fast-ion acceleration, compression of spherical targets, and fusion yield. Experiments with neon impurities in the fuel of spherical

targets demonstrated the possibilities of combining atomic physics models and optical diffraction (from straight edges and apertures) to provide redundant determination of peak fuel densities.

The two-beam Nd:glass laser is being operated for both military applications and development of diagnostics with high-speed time response. Measurements of equation of state, shock propagation, multiburst simulation, and opacity were made and are continuing under the auspices of the Office of Military Application. This facility is also being used for calibration and testing of x-ray streak cameras.

THEORY AND TARGET DESIGN

An understanding of basic plasma physics is crucial to target design. Studies in a number of areas are being continued, with emphasis on electron transport and its implementation in computer calculations.

Code development is an important aspect of our theoretical program, because our target designs can be no better than the physics and numerical techniques available within the codes. Our more significant efforts during the current reporting period included correction of an error in the code's treatment of hot-electron transport and improvements to the atomic-physics data set used by LASNEX.

The target design effort was primarily directed towards classified targets for Helios and Antares. Two types of unclassified targets are being actively studied for near-term use on Helios. A comprehensive analysis of exploding pusher designs for Helios is nearing completion, and a series of targets designed for the 20-times-liquid-density experiment was proposed. These latter targets provide a smooth transition from the exploding-pusher regime to that of isentropic compression, and should serve as a very instructive tool to explore and understand the ablative compression regime. As a secondary utility, these transitional designs provide a test bed for design code and diagnostic measurement studies. Because we are breaking new ground as we move into the ablative compression regime, which requires a measurement of internal aspects of the target as well as of those external features we routinely observe from exploding pusher targets, the diagnostic measurement studies are difficult.

LASER FUSION TARGET FABRICATION

Our ability to fabricate targets for laser fusion experiments increased in several areas. Improvements in plastic coatings now permit uniform, 50- μm -thick deposits on glass microballoons, although some improvement in surface finish is still desirable. We also coated small batches of selected microballoons with thin layers of nickel and recovered more than 90% of the balloons. Both of these improvements were necessary for our 20-times-liquid-density milestone target. In addition, we invented a simple array maker that improves the throughput of our x-ray radiographic analysis for metal microballoons by an order of magnitude and demonstrated that radiography can determine the uniformity of plastic coatings regardless of the uniformity of the microballoon substrate. In the cryogenic target area, we successfully formed uniform DT ice layers inside a two-shell glass target using the Fast Isothermal Freezing technique. This result indicates that the thermal insulation of at least one separated concentric shell does not seriously inhibit the required heat transfer.

TARGET DIAGNOSTICS

Important advances were made in the development of sensitive neutron diagnostics, which extended our detection capabilities down to less than 10^9 n while avoiding target noise and background contamination. Because so much of the useful information obtainable from laser fusion targets is contained in the x-ray emissions, extensive x-ray diagnostics were developed to provide spectral, spatial, and time-resolved information. In particular, spatially resolved x-ray data were shown to contain considerable information, which is not immediately apparent from a casual analysis.

APPLICATIONS OF LASER FUSION SYSTEMS STUDIES

A new plasma model was constructed to investigate the feasibility of using a high-atomic-number buffer gas in inertial confinement fusion (ICF) reactor cavities to attenuate x-ray and debris energies and thus to alleviate first-wall design problems.

A preliminary study was completed of the requirements on fuel pellet injection into laser fusion reactor cavities. We assessed the required accuracy, limits on acceleration, and the effects of residual gas motions on pellet trajectories.

A new reactor concept for producing ultrahigh-temperature process heat while simultaneously maintaining an adequate tritium breeding ratio for fuel-cycle self-sufficiency was proposed and is being investigated. Such a reactor, called the lithium boiler, appears to be capable of delivering process heat at temperatures exceeding 1500 K and could be utilized to efficiently produce electric power or as a heat source in electrothermochemical production of hydrogen.

Studies of hydrogen production from water decomposition continued in cooperation with several LASL groups. During this reporting period,

one blanket concept was evaluated in considerable detail and a reference water-splitting cycle based on bismuth oxide sulfates was studied.

The investigation of fusion-fission hybrids for the production of ^{233}U from ^{232}Th was resumed with emphasis on concepts that maximize the ratio of fissile fuel production to thermal power production. Possible reactor configurations were analyzed and blanket compositions that warrant further study were identified.

In conclusion, we are pleased with our progress toward our goals in all areas of the program. Of great significance was the design-point operation of Helios, which augured well for the success of Antares, and places us on the threshold for an exciting laser-target experimental program in the 10-TW regime.

I. CO₂ LASER PROGRAM

The research and development programs on high-energy short-pulse CO₂ lasers were begun at LASL in 1969. The first system, the Single-Beam System, was designed in 1971, began operation in 1973, and was phased out in November 1977. Two large systems are now operating: the Two-Beam System (TBS) and the Eight-Beam System (EBS) called Helios. Target experimentation continued on the TBS, which will ultimately generate pulses of 2 to 4 TW for target-irradiation experiments. Helios became operational in April 1978 and surpassed the design goal on June 21, 1978, with an output exceeding 10 kJ at a power level of ~20 TW. A third system, Antares, is in the design and prototype stage. This system, described separately in Sec. II, will generate laser pulses of 100 to 200 TW, with the objective of demonstrating scientific breakeven.

TWO-BEAM SYSTEM

Introduction (J. P. Carpenter)

The TBS was devoted to target experimentation as well as to a moderate amount of system characterization and modification. During the past six months 203 target shots were fired, 70% of which produced the desired energy on target with no measureable prelasings.

Laser Performance and Diagnostics (J. P. Carpenter, J. McLeod)

Several system additions and measurements pertaining to laser performance were made. In particular, two transmitting ir microscopes were installed on the target chamber. Each microscope system consists of a relay lens, a pyroelectric vidicon-plus-scan converter, and a television monitor. These microscopes allow us to point the focused laser beams with an accuracy of $\pm 20 \mu\text{m}$. Target experiments in which these microscopes were used displayed an increased symmetry in ion production, as evidenced by detectors collecting data at opposite sides of the target.

The microscopes were also used to monitor the improvement in focal-spot size obtained when the

internal mirrors in one of the triple-pass amplifiers (TPA) were remounted on a superior mirror-holding structure. This new mounting method involved observing the mirror's figure with an interferometer while tightening the clamps and adding shims as necessary to preserve the mirror's optical figure before mounting. Remounting improved the observed focal-spot diameter considerably.

Improved parabolic mirrors were tested and installed in the target chamber. These diamond-turned, hand-polished mirrors have surface errors somewhat less than a tenth of a wave, $\lambda/10$, peak to valley.

An internal saturable-absorber gas cell was designed. This cell will be installed at the recollimating mirror location and should allow the delivery of as much as 1400 J (~1 TW) to a target.

An adaptive optics contract with Hughes Research Laboratories entered the hardware phase. This contract calls for the development and construction of a deformable spherical mirror to replace the recollimating mirror presently used in the TPA. This deformable mirror will be 38 cm (15 in.) in diameter and will have 19 piezoelectrically driven actuators. This system should nullify wavefront errors generated in the TPAs and their associated optical components.

The new optical diagnostics facility was occupied. A screen room was erected with a 1.5- by 3-m (5- by

10-ft) optical table inside. A 5-GHz risetime-monitoring channel was installed and has proven to be very stable. Provisions for diagnosing prepulsing and postpulsing are being installed.

Oscillator-Preamplifier System (P. Goldstone, V. Romero)

Several changes that were made resulted in improved operation and reliability. The orientation of the mode-locker crystal was changed so that the beam is more nearly at the Bragg angle of the phase grating, and the matching network at the mode-locker was reset by using a vector impedance meter. This resetting has resulted in greater reliability of mode-locker behavior. The amount of helium in the oscillator gas mix was increased by ~75%, which lowered the gain and increased the gain risetime so that more passes through the mode-locker are required before the cavity provides significant output. Pulses with risetimes of ~500 ps can now be produced more reliably.

A circuit for monitoring the time at which the pulse was switched out of the oscillator was linked to the main computer, thus providing a continuous check of front-end jitter.

Placing a p-doped germanium crystal into the oscillator cavity did not improve operation significantly. Besides, the antireflection-coated surfaces of this crystal suffered considerable damage, and the crystal was therefore removed.

Computer and Control System (S. Hackenberry, P. Castine)

A new program to record data from transient recorders and event timers was written and tested. Should the data-acquisition computer stop during a shot, this program can recover the data that previously would have been lost.

HELIOS LASER SYSTEMS

Introduction (G. T. Schappert)

The major construction phase for the EBS, recently named Helios, was completed. The power am-

plifier modules for the eight beams and the Helios target chamber are shown in Fig. I-1.

In April 1978 we conducted our first full-power integrated system test, FIST I, which consisted of firing all eight beams simultaneously, each into a calorimeter. The total energy delivered by the power amplifiers was ~8.3 kJ in a ~0.5-ns pulse, resulting in a peak power exceeding 15 TW. This made Helios the world's most powerful laser at that time.

After having gained more experience in tuning the system, we repeated the full-power integrated system test (FIST II) in June 1978 and obtained more than 10 kJ on each of three shots, at power levels of ~20 TW. We exceeded our design goal of 10 kJ.

Presently, our major effort on the Helios system is concentrated on finishing the laser-beam diagnostics system, the alignment system, and the computer interfacing of these two tasks. We also began to interface the laser system with the target diagnostics to commence with our experimental laser target interaction program.

Oscillator-Preamplifier System (R. L. Carlson, R. Quicksilver, M. Weber)

The front end has been operational for some time and is used routinely in the support of various TPA experiments, in alignment development and checkout, and in laser-beam diagnostics. Several upgrades and additions in the front-end area were completed.

An electrically switched 50-W quasi-continuous wave (cw) CO₂ laser was constructed, installed, and is now operating as the prime alignment laser. This laser can deliver 5-J pulses of 0.1-s duration at 1 Hz. By using the alignment stations at the spatial filter SF2 of the front end, this laser has been shown to be stable within ± 30 μ rad pointing and ± 250 μ m displacement. These errors are within the limits of acceptable alignment accuracies of ± 100 μ rad pointing and ± 500 μ m displacement of SF2. These measurements of the cw CO₂ laser include the random errors associated with the electronic "processing boxes" at SF2.

The laser was operated at 60 Hz in synchronization with the Hartmann target alignment system. This operation allows continuous feedback to the



Fig. I-1.

Eight-Beam Helios Laser System; arrangement of power-amplifier modules around target chamber.

target alignment operator for steering the target-chamber turning flats and focusing parabolas. The laser will also be used for aligning the optical diagnostics system, Gallery West (GW), and in anticipated beam-quality measurements. Interface controls are being built to control the laser output and repetition rate as part of the automatic alignment system.

An Invar-stabilized support structure is being built for the resonator optics of the TEA/plasma tube oscillator. The present oscillator-switchout-preamplifier chain exhibits pointing and random displacements of ± 150 and ± 750 μm , respectively, at the SF2 alignment station. Much of this motion appears to originate in the oscillator cavity. The present TEA oscillator employs a curved (wavefront-corrected) output coupler of germanium. A more stable cavity consisting of a plano output coupler and curved reflector will be used with improved Invar mirror-support structure. We noted that the present oscillator exhibits less beam jitter in single-line operation than in multiline operation. If a pulse-to-pulse intracavity dispersion existed, the present curved output coupler might

tend to aggravate beam-steering. However, the present setup is satisfactory for initial target studies.

As part of the mechanical upgrading of the front end, the triple-crystal switchout system will be assembled on a single plate housed in a dustproof enclosure. The repulse isolator, beam expander, and associated turning mirrors will be combined into one unit containing a simple zoom-lens system. This will permit us to easily mode-match and align the beam, entering any switchout configuration, to the first preamplifier stage (PA1).

Finally, the front-end room was carpeted to improve its cleanliness and overall appearance.

Table I-I summarizes the Helios front-end feature and Fig. I-2 shows the general layout.

Laser Experiments (G. T. Schappert, M. D. Montgomery, J. Ladish, D. Casperson, R. Haglund)

The most exciting events of the Helios laser system were two full-power integrated systems tests, FIST I and FIST II. The first test began on April 10,

TABLE I-I

HELIOS FRONT-END FEATURES

Multiline Oscillator

TEM₀₀, single longitudinal mode.
10-MW gain-switched pulse ($t_r \approx 20$ ns, FWHM ≈ 80 ns).
Multiline operation on Lines P-12 through P-22.

Three-Stage Electro-Optic Switchout

Duration, 500 ps to several ns.
Energy contrast improvement of 4×10^4 .

Saturable Absorbers

Sulfur hexafluoride is used for prepulse contrast.
Gallium-doped germanium prevents both self-lasing and postlasing, and improves the contrast.

Spatial Filter Assemblies

Spatially filter forward pulse.
Offer protection against retro-pulse.
Used in alignment stations and mode-matching telescopes.

Output Characteristics

Four beams; each with 250-mJ output.
Pulse FWHM ≈ 750 ps, $t_r \approx 350$ ps.
Prepulse energy per beam, < 5 pJ.
Multiline operation on Lines P-12 through P-22.

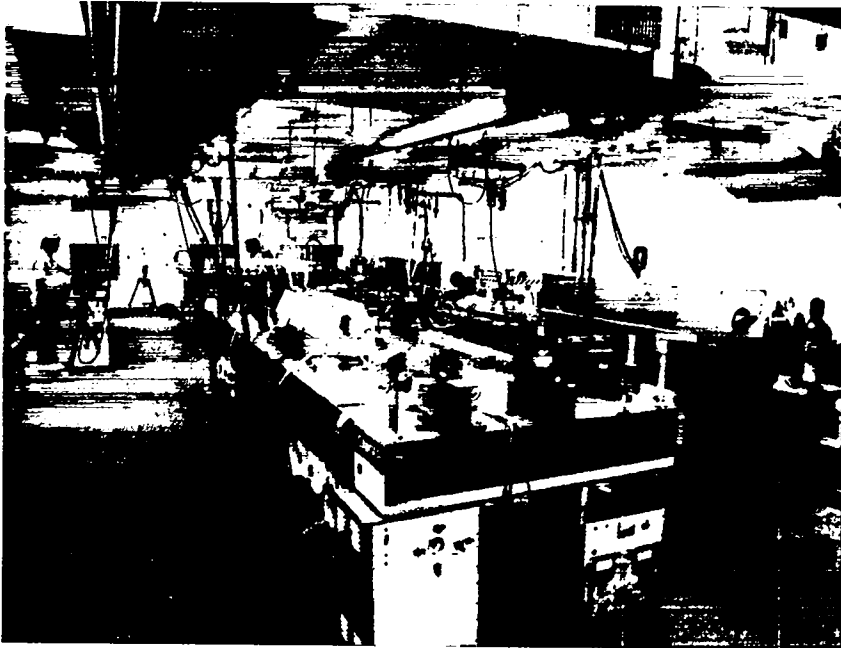


Fig. I-2.
General layout of Helios front end.

1978 with all eight modules firing into eight 40.6-cm (16-in.)-diam calorimeters. Corrections for non-linearity in the calorimeters appear conservatively to be 5% at the 700-J level and 10% at the 950-J level. The average total energy inside the amplifiers on four successful eight-beam shots was 8300 J. These shots represented the first full-power shots of all eight modules without any attempt to tune the system. The electrical operating conditions had previously been determined from experiments on Module 2A at the 1-kJ level.

After this round of measurements the calorimeters were equipped with slit gratings over their apertures, attenuating the incoming beams about 15-fold and eliminating the need for non-linearity corrections. Each slit grating was calibrated by using full-size cw CO₂ beams.

In preparation for the second full-power test, experiments were conducted with Module 4A, the poorest performer, to find a systematic method of increasing the energy output of the TPAs. We know from theory and experience that the laser gas impedance could be varied by changing the electron-beam voltage. This change, in turn, affects the sustainer electric field because of the load impedance seen by the Pulse Forming Network (PFN). In principle, one would expect optimum electrical-energy input into the discharge for a matched load to the PFN. However, the efficiency of CO₂ pumping is a strong function of the electric-field pressure ratio, E/P, so that optimizing laser operation by adjusting E/P can gain more in stored optical energy than optimizing the electrical-energy input into the laser gas.

These considerations led us to experiment with the gas impedance by varying the electron-beam voltage. We found that a change from 60 to 50 kV/stage (five stages) increased the gas impedance, mismatching the PFN to load, and thus presumably increasing the effective sustainer voltage.

In this manner Module 4A stably produced a short-pulse energy in excess of 1500 J, as measured by a calorimeter/slit-grating combination. The other amplifiers were tuned similarly, for four full-power shots on June 21, 1978. Table I-II summarizes the results. The full-power optical pulse width was later measured on one-beam line with GW diagnostics.

The pulse shape of shots as recorded by a fast pyroelectric detector and a 5-GHz oscilloscope is

TABLE I-II

HELIOS FULL-POWER TESTS
June 21, 1978

Module	Energy Output (J)			
	3:30	4:35	5:10	5:15
1A	1408	1465	1422	1399
B	1292	1364	1311	1249
2A	1315	1309	1309	1309
B	1168	1449	prefire	1430
3A	1186	1132	1132	1132
B	1302	1254	1253	1205
4A	1144	1236	1327	1053
B	1446	1471	1521	1371
Total	10261	10680	9275	10148

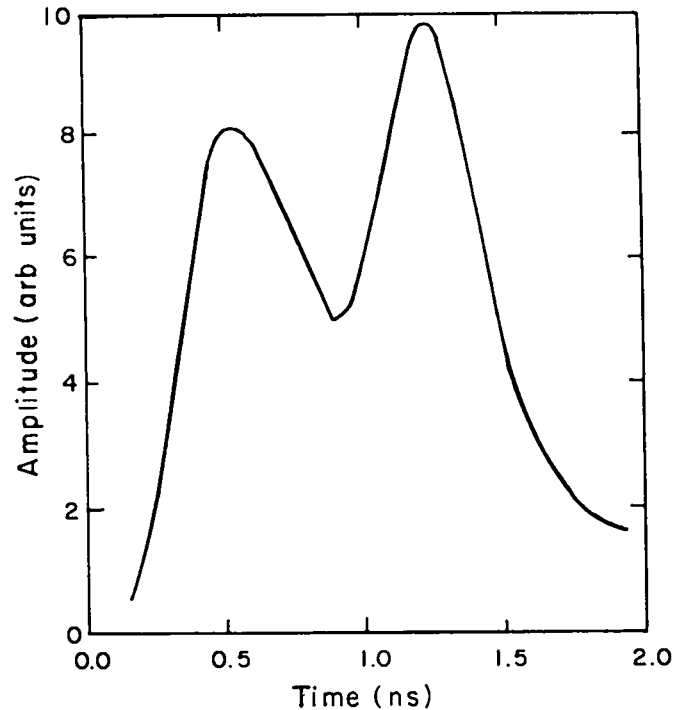


Fig. I-3.
Double-humped Helios pulse recorded by fast pyroelectric detector.

shown in Fig. I-3; the double pulse was caused by the two reflections from a 7.6-cm (3-in.) uncoated salt window.

Deconvolution produced the results shown below.

Front Fit Data

Power	20 ± 2 TW
Pulse Duration, FWHM	525 ± 25 ps

Back Fit Data

Power	18 ± 2 TW
Pulse Duration, FWHM	450 ± 25 ps
Risetime, 10-90%	250 ± 50 ps

These results speak for themselves. The Helios laser has achieved an energy output slightly exceeding our design goal of 10 kJ at a power level of ~20 TW.

Controls Systems (E. L. Jolly, M. D. Thomason, J. Sutton, D. Remington, L. Sanders, D. Wells, W. Hanna)

Installation and testing of the Helios minicomputer-based control system remains on schedule. An operator using the computer can, with two exceptions, control and monitor all essential operations for laser target interaction experiments. The two exceptions are beam alignment within the target chamber and acquisition of beam diagnostic data. Figure I-4 is an overall view of the Helios control room. The keyboard terminal in the center of the room is the operator-machine interface.

Several new features are contained in the Helios control program. The latest program is coded in FORTRAN V, which is faster and more efficient

than the previously used FORTRAN IV. The program also has the capability of charging each high-voltage pulsed power supply to a different voltage. This change is a great aid in amplifier output optimization and system tuning.

The automatic alignment program (ALIGN) became operational. Figure I-5 shows a color display presented to the operator during automatic alignment. The display informs the operator of the alignment status of segments of the beam-transport lines. The displayed color of a line indicates whether alignment of the segment is complete, in process, or waiting to be accomplished.

A second minicomputer, complete with two display terminals, was ordered. It will serve as a spare for the original and provide a means for software development as the original becomes more dedicated to Helios operations.

The target-chamber vacuum control system was completed and documentation of the system has begun. Controls for the target insertion device are operational. The device has the capability of micropositioning the target along any of three axes, thus providing a means for final target positioning within the target chamber.

Optical encoders were being installed on all motorized mirror mounts within the target chamber. These encoders will sense the motion of the stepping motors. This information will be relayed to a microprocessor-based data processing and memory system. This system will be capable of positioning any of the sixteen mirrors with absolute accuracy and will be equipped with a battery back-up power supply to maintain the memory content in case of a primary power failure.

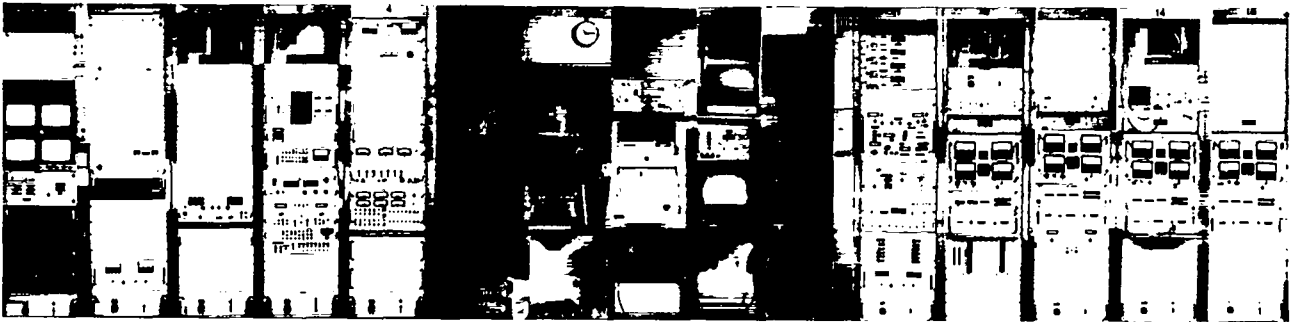


*Fig. I-4.
Helios control room.*

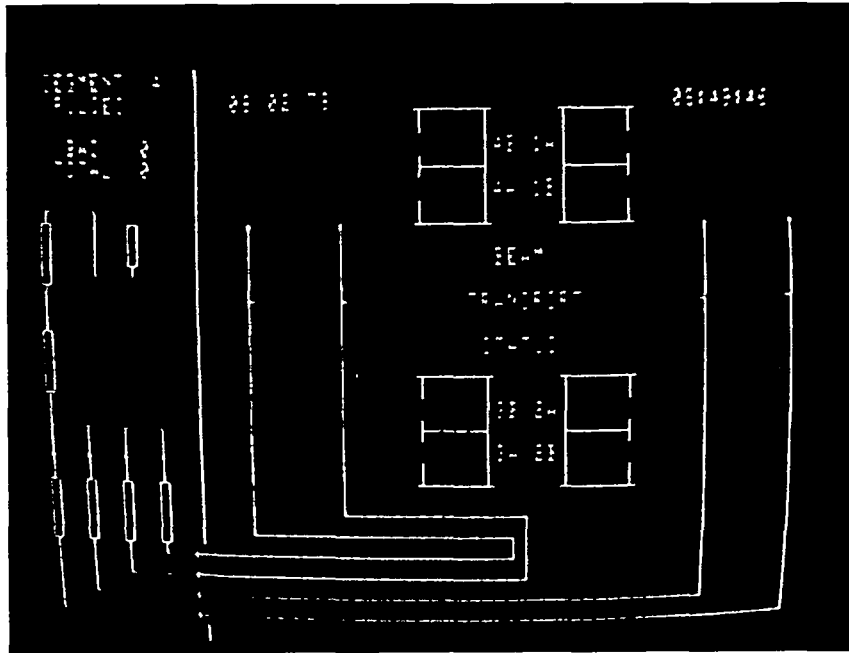


Fig. I-5.
Color display presented to Helios operator during automatic beam alignment.

Mechanical Assembly (E. L. Zimmerman)

Mechanical assembly work on the Helios system was completed and only upgrading of components and maintenance tasks continue.

Electron-beam foil windows are being fabricated by an outside vendor, in the hope that the foil lifetime problem has been solved.

No electrical failure in a pumping chamber occurred after small defects in the chambers were repaired. It is hoped that all weak areas have been eliminated.

A clean room was established whose doors and other wall openings were sealed against dirt contamination.

Initial problems with the target-chamber vacuum system were solved. Vacuum levels were as predicted.

The target-chamber insertion device became operational. Target position reproducibility is very good within 5 to 10 μm .

All mechanical systems were operating well. No problems were anticipated. Maintenance, repair, and upgrading were the main activities.

Laser-Beam Diagnostics (I. Bigio, S. Jackson)

Mechanical Assembly. The structure for the eightfold midair laboratory for output-beam monitoring was installed along the west wall of the building, together with a screen room extending beneath the full length of this setup. This diagnostic facility is referred to as Gallery West (GW). Energy measurements and beam splitting are performed on the eight vertical optics tables, whereas temporal and spectral measurements are derived from beam samples directed into the screen room below. A schematic of the GW is shown in Fig. I-6.

The beam-transport system to Gallery West was completed. This system consists of the mirror mounts on the TPA extensions for the 40.6-cm (16-in.) flat turning mirrors, of the wing plates on GW with the 40.6-cm (16-in.) and 30.4-cm (12-in.) concave mirror mounts to reduce the beams, and of various smaller optical components to guide beam samples into the screen room.

Optical Assembly. All eight 40.6-cm turning flats were mounted. The coatings on the 40.6- and

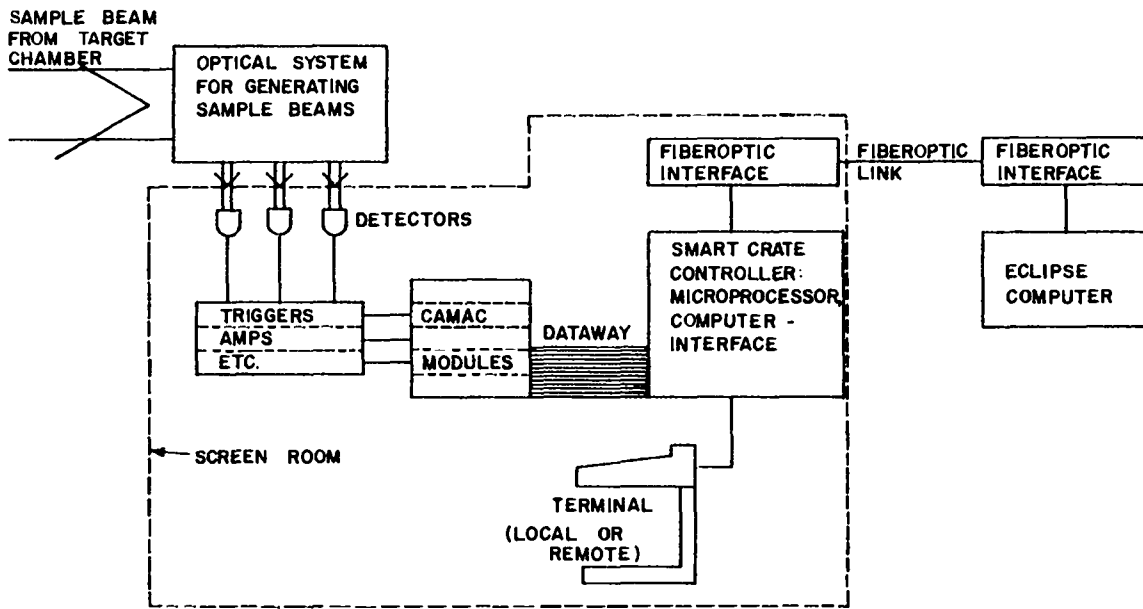


Fig. I-6.
Gallery West, the Helios diagnostic facility.

30.4-cm concave mirrors were unacceptable, and attempts by the vendor to rectify the problem were unsuccessful. A new optical design employing the uncoated 40.6-cm concave substrates was implemented and yielded the additional benefit of eliminating the need for beam dumps because the Pyrex substrate absorbs 82% of the beam intensity. The 30.4-cm mirrors will be recoated by a new vendor. Sufficient optics for four beam lines are available.

All the smaller GW optical components for these four beam lines were located and mounted and all screen-room optical components for these lines were installed.

Electronics Assembly. Detectors for the four established beam lines were installed. All data-acquisition electronics for GW were installed in the GW screen room. Calibration and timing procedures were initiated.

The fiber-optic link from GW to the control room was installed and tested. Communication between the GW microcomputer and the Central Processing Unit (CPU) was established, but required refinement. Bugs in the hardware and software of the microcomputer were identified and corrected.

The computer-interfaced vidicon system for automatic recording of the temporal pulse history from the 5-GHz oscilloscope was ordered.

Alignment. Techniques were established to optically align the myriad of components in GW. In the process, several weak aspects of the main alignment system in Helios were identified. Because of the constantly varying parameters that affect the location and direction of the beams that enter (and are reflected by) the target-chamber windows, alignment was and will continue to be the most difficult aspect of making GW fully operational.

Measurements and System Tests. Calibrations for the total energy measurements have begun. These measurements will determine what fractions of the full beams are reflected towards GW, and what fractions of those reflected are sent to the various detectors.

Noise-immunity tests for the microcomputer were conducted during full-power shots, and no problems were encountered. Preliminary timing procedures were begun.

Pulse temporal history measurements were made in GW for a full-power shot on one beam line. This

was the first such measurement on a whole-beam sample. A fast, modified pyroelectric detector was used in conjunction with a 5-GHz oscilloscope. Results were a risetime (t_r) of 200 ps and a pulse duration FWHM of 500 ps.

Optical Systems (J. Hanlon, V. K. Viswanathan, M. D. Bausman, J. J. Hayden, J. Murphy, M. Calcote, M. Caine, P. Bolin, G. Salazar)

Alignment. Most of the beam transport alignment is now automated, significantly decreasing the alignment task.

We found that a newly installed chopped cw CO₂ laser could be made collinear to the pulsed beam. The shot-to-shot jitter of the 1-ns alignment beam was $\pm 100 \mu\text{rad}$, whereas the cw jitter was $\pm 25 \mu\text{rad}$ (both at the first alignment station). Thus, alignment with the cw beam was superior to that with the pulsed beam. The cw beam is pulsed by varying the duration of the discharge. Thus, at spatial-filter alignment stations, which require more energy for high precision because nearly all the energy passes through the pinhole, the required precision is obtained by increasing the laser pulse duration. This could not be done with the 1-ns beam because sufficient energy is not available, and, if available, would create air breakdown. Therefore, and also because the cw CO₂ laser decreased the use of the front-end 1-ns laser system dramatically, the cw laser became an extremely desirable alignment tool.

A major remaining task is the automation of power-amplifier alignment.

Hartmann alignment of the target-chamber optics was nearly completed. However, because of the qualitative nature of this alignment technique, this task continually requires attention. A procedure for automating the Hartmann test is being tried, but will require much time before it can be implemented in Helios.

The autocollimating microscope for ensuring concentricity of Hartmann sphere and real target was installed. Resolution is better than $10 \mu\text{m}$. All the peripheral apparatus such as light sources, vidicons, and monitors for viewing in the control-room area are operational.

A mockup of the target-chamber optics continued to be useful for various tasks and for the establish-

ment of alignment procedures. For example, encircled energy measurement techniques worked out in the Optics Laboratory before being tried on the TBS show that most of the energy in the mockup system is focused into a $100\text{-}\mu\text{m}$ spot.

The ir microscope to be used in Helios target alignment is being designed.

Computational Support (V. K. Viswanathan). The code we use for end-to-end optical modeling of the Helios laser system, LOTS, was modified to

- allow propagation of the beam in media with varying indexes of refraction,
- handle various types of saturable absorbers,
- graphically plot Twyman-Green or Smartt interferograms at any desired station, and
- improve the statistics of the random wavefronts.

The tradeoffs in terms of (e.g.) Strehl ratio, irradiance distribution, and encircled energy were studied for the cases involving the use and removal of the saturable-absorber cell in the Helios power amplifiers. The results are summarized in Table I-III. The irradiance distribution in the focal plane is shown in Fig. I-7, and the encircled energy distribution in Fig. I-8.

Target Insertion Mechanism (TIM) (C. Cummings, R. D. Day, C. Tucker, R. Teasdale)

The TIM was used in a quasi-operational mode described by the following tasks:

- Prealign the target in the target fabrication laboratory.
- Remove and insert a target when the target chamber is at 10^{-6} torr.
- Move the targets inside the target chamber accurately to the point established by the center of the Hartmann ball.

Results of parasitic tests indicate that the TIM has no effect on the operating point of the laser.

The TIM was tested for repeatability in its working environment. Two orthogonal autocollimators with a resolution of $\sim 5 \mu\text{m}$ were used to establish the reference point. The repeatability was better than $5 \mu\text{m}$.

Hartmann balls with a stem pressed into them were fabricated. One of these, a 1.9-cm (0.7500-in.) ball, is in use in the Helios system.

TABLE I-III

EFFECTS OF SATURABLE ABSORBER ON ENCIRCLED ENERGY AND TOTAL ENERGY IN HELIOS

Diameter of Target (μm)	Encircled Energy (J) and Percentage of Total Energy (%)	
	0.6 kJ without Saturable Absorber	1.2 kJ with Saturable Absorber
100	360 (60)	480 (40)
120 (2 Airy Disks)	444 (74)	600 (50)
200	516 (86)	810 (67.5)
300	540 (90)	960 (80)
Peak Irradiance, J/cm^2	5.6×10^7	4.3×10^7
Strehl Ratio	0.49	0.16

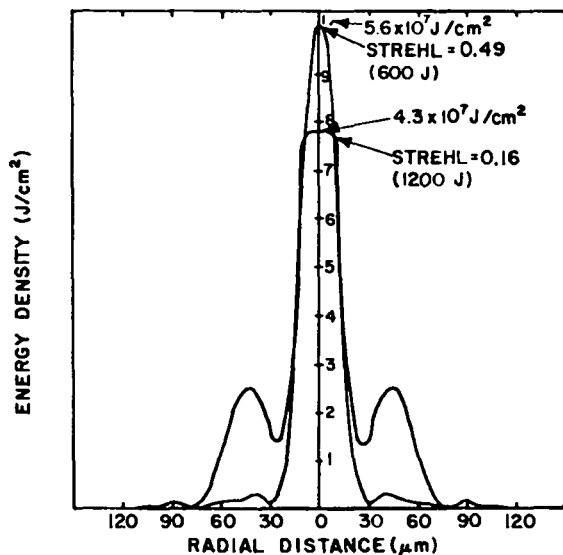


Fig. I-7.

Irradiance distribution in focal plane at Helios target position.

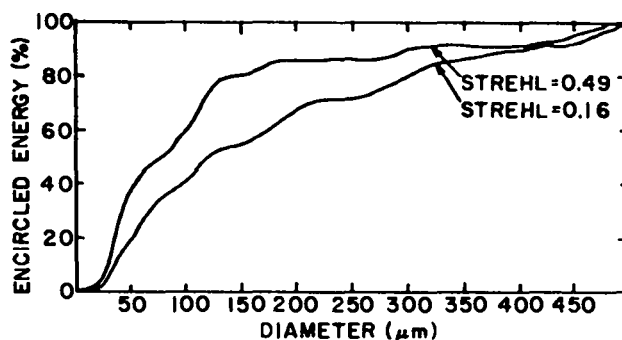


Fig. I-8.

Encircled-energy distribution at Helios target position.

clutches that are connected in parallel. The output shafts of the clutches are connected to universal joints that, in turn, drive friction pads located on a block on the target cart (Fig. I-9). These pads mate to similar friction pads that couple to the target-holder micropositioner through telescoping universal joints. Therefore, when the pads are in contact (Fig. I-10) the target can be moved a particular direction by activating the motor and the appropriate clutch.

The limited present experience has shown that the target insertion mechanism should perform as specified.

The three-axis manipulator (3AM) for positioning targets in the target chamber became operational. Figure I-9 shows the 3AM, with the target holder inserted, on the cart and Fig. I-10 shows it when the target holder is seated in the target chamber. Target translation is accomplished by activating a dc motor, which drives the hub of three magnetic

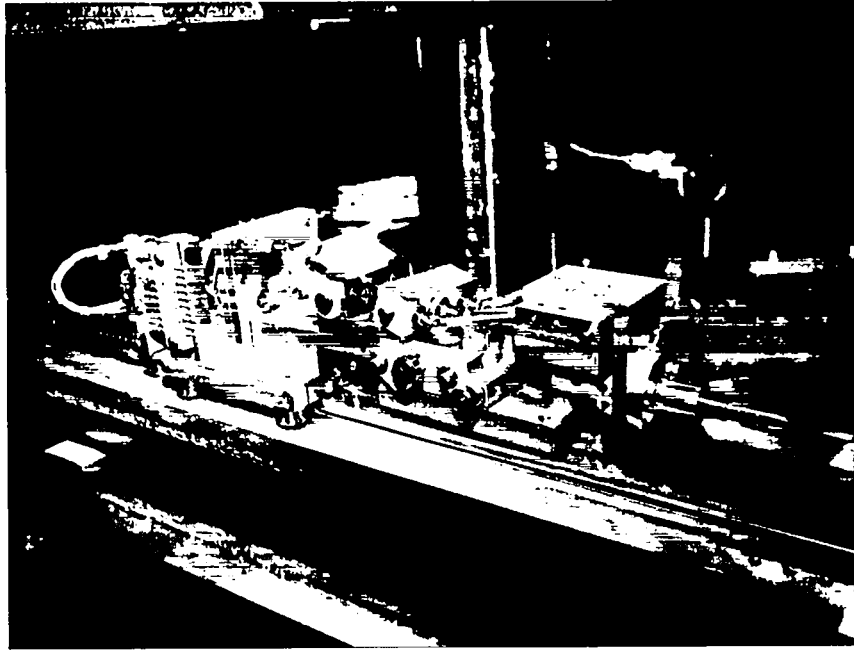


*Fig. I-9.
Three-axis manipulator, with target holder inserted on cart.*

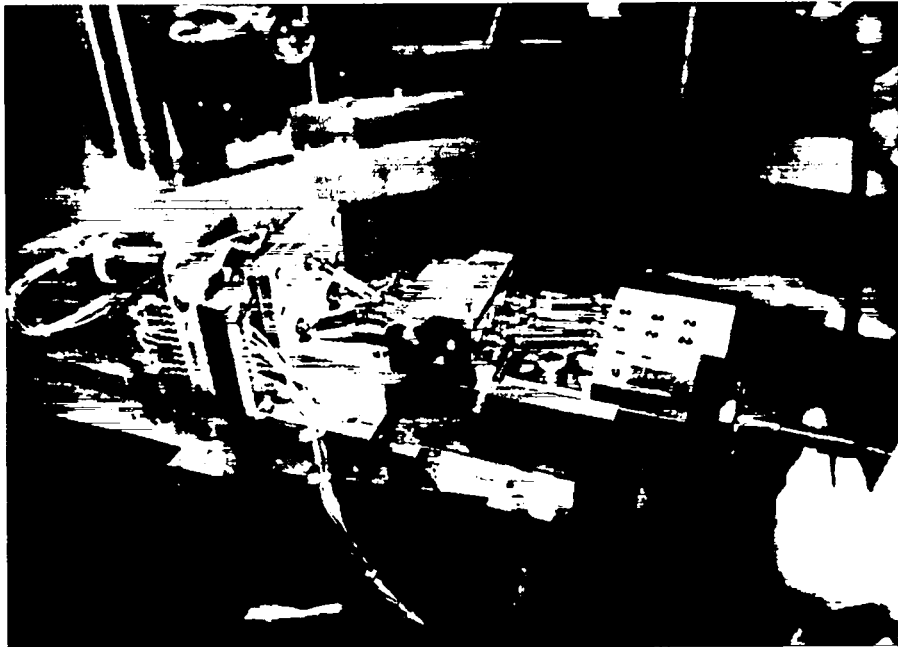


*Fig. I-10.
Three-axis manipulator with target holder seated in Helios target chamber.*

II. ANTARES—HIGH-ENERGY GAS LASER FACILITY

Antares, a CO₂ laser system producing a power level of 100 to 200 TW with a maximum energy of 100 kJ, is being designed to study laser fusion feasibility. Laser building construction and laser-system design work proceeded on schedule toward the 1983 completion date.

INTRODUCTION

The Antares project showed significant progress in building construction and final system design.

A redesign of the target optical geometry reduced the target f-number. Three optical codes were under development and evaluation for interferogram reduction and beam-quality assessment.

Electron-beam pulse voltages were examined to improve the gain distribution in the laser medium. Plans were formulated for beam sampling and diagnostics.

The design of an integrated optical system included plans for an optical-hardware test bed. A beam-alignment study contract was near completion.

Plans and schedules were prepared for the entire front-end system. Vendor proposals were evaluated and procurement was initiated for the six beam-line driver amplifiers.

Long-lead-time procurement items for the power amplifiers were designed and released for fabrication. Tests of the air-bearing support for electron-gun insertion and removal were completed. Analysis of the optical support structures was completed.

A prototype gas pulser was assembled and tested, and results were used in formulating the specifications for procurement of 24 units.

Responses to the RFP for the target vacuum system underwent initial evaluation. Design work started on the space frame to support the redesigned target focusing system.

Controls system design studies concluded that a hierarchical, tree-structured network of control computers would provide optimum flexibility for partial or full Antares operation.

These and other achievements are discussed in detail in this section.

OPTICAL SYSTEM (W. H. Reichelt, A. C. Saxman)

Optical System Analysis (K. Jones, J. L. Munroe)

Error Budget and Component Quality (J. L. Munroe). The f-number of the target focusing optics had been increasing slowly to compensate for a variety of geometry problems encountered within the target chamber. This increase in f-number implied an associated increase in focused spot size, which, according to our analysis, could be reduced by components of improved optical quality. However, the most reasonable way to reduce the spot size was a redesign of the target chamber to minimize the f-number. This redesign was executed successfully, cutting the f-number in half, thus greatly relaxing the requirements on optical-component quality; the required spot size can now be obtained with currently available optics.

Optical Code Development (J. L. Munroe). FRINGE 2, the Optical Sciences Center code for interferogram reduction, was evaluated and modified extensively. The validity of the basic FRINGE-2 calculations was checked by supplying FRINGE 2 with analytically determined fringe coordinates for known cases. For all cases, including scaling the output to a new wavelength, FRINGE 2 performed perfectly. The only known problem involved the calculation of the diffraction encircled energy, which was irrelevant to the planned application of FRINGE 2 to component evaluation. The modifications to FRINGE 2 provided additional output data and improved the print format.

FRINGE 3, an expanded version of the interferogram reduction program FRINGE 2, was

received from the University of Arizona. This version contained many new capabilities and features. For Antares, the most important new feature was the ability to analyze noncircular apertures, required for evaluation of the quasi-trapezoidal large flats and focusing paraboloid. FRINGE 3 will be documented and checked out during the next reporting period.

The University of Arizona LOTS code, in development, will allow an optical designer to determine the beam quality in an optical system composed of mirrors and lenses that have common third-order aberrations and random surface errors. Spatial filters can also be represented by LOTS.

Active Medium Analysis (P. N. Wolfe). For economic reasons, optical-damage design tolerances were set much tighter on Antares than in its smaller predecessors. We, therefore, have continued to reexamine our output-beam uniformity predictions, as new information became available from other systems and as our analytical tools improved. We also concluded that the full optical aperture in the Antares power-amplifier pumping chamber was sufficiently different from that used in the prototype experiments to indicate the need for additional experimental and analytical work. Whereas gain increased somewhat from cathode to anode in the prototype, it was predicted to behave in the opposite fashion in Antares, giving rise to higher gain near the cathode.

We reassessed in detail the energy-extraction design constraints in an effort to restore beam uniformity. We found that by reducing the ionizing electron-beam energy from 500 to ~ 300 keV, enough falloff in gas conductivity from cathode to anode is introduced to offset the geometric decrease in gas current density and thereby produce a nearly uniform deposition of pumping energy. There was concern whether a well-behaved discharge at these low electron energies would be possible, because ionization could not be expected to bridge the cathode-anode gap without the assistance of the discharge field. However, both analytical and experimental investigation confirmed that the technique was indeed practical.

In addition to tailoring gain in the cathode-anode direction by appropriately choosing electron energy, some adjustments in the transverse direction ap-

peared desirable to further improve the margin for optical damage and parasitic oscillations. Two methods were investigated: (1) moving the electron-gun emitters from positions centered on the beam sectors to positions centered between the beam sectors, and (2) physically varying the electron transmissivity of the foil support structure. The first approach was scheduled for evaluation in the Antares prototype laboratory.

Beam Diagnostics (J. E. Sollid)

Power Amplifier. One of the most critical pacing items was the design of the optical diagnostics for the power amplifier. This included small-signal gain (SSG) measurements in start-up, operating, and fault modes, and provision for a diagnostic spool to be installed on the power amplifier. At present, the SSG will be measured only during start-up.

Beam Sampling. The generation of beam samples by Fresnel reflections from transparent elements is impractical in Antares downstream from the power amplifier. Instead, the use of diffraction gratings is anticipated. Either reflecting or transmitting gratings are possible, whose damage thresholds, however, must be established. Preliminary results indicated thresholds near the intrinsic damage limit for the substrate metals. This is adequate for Antares needs.

Questions regarding beam quality in the diffracted wavefront remained. The wavefront quality from a representative wire transmission grating was measured at the University of Arizona. The rms residual error, after removing tilt from the wavefront, was 0.085 waves. This value was too high for precise wavefront measurements, and indicated the necessity for further fabrication studies.

A full-scale experiment on a prototype transmission grating was designed and scheduled to be run on Gemini. These tests will determine experimentally whether the transmission gratings will be adequate for energy and power sampling.

Baseline Diagnostic Design. The most important parameters required for on-line beam diagnostics are total energy, risetime, falltime, peak power, and average power of the optical pulse.

Irradiance distribution is also considered important. A baseline design to accomplish these measurements was completed. The transmission gratings were incorporated as the sampling elements.

This concept is illustrated in Fig. II-1. The beam is illustrated by dotted lines and is shown passing through the final portion of the power amplifier where it encounters the transmission grating. A sample of $\sim 1/900$ th the beam energy from each sector is diffracted in the first order to a large-aperture calorimeter placed in the center of the annular beam at the turning chamber. All 12 samples from the sectors are collected. A small-area pyroelectric detector placed in the center of the calorimeter will furnish the convolved time history of the beam powers.

Detector Program. Because no commercially available pyroelectric detectors meet our requirements exactly, we initiated a program to develop pyroelectric detectors more suited to our needs. Two types were desired: one with a risetime less than 70 ps and an integrating detector whose output is proportional to the input energy. A prototype dual-element detector was produced. Refinements were necessary and the work is continuing.

Optical Systems Engineering (J. L. Munroe)

Front End (J. L. Munroe). The conceptual optical design of the front end was completed. The preamplifier and driver amplifier will be of triple-pass configuration, using Cassegrainian telescopes with gas-cell saturable absorbers separating each pass. The available space and flexibility of the design will allow us to use other geometries, e.g., off-

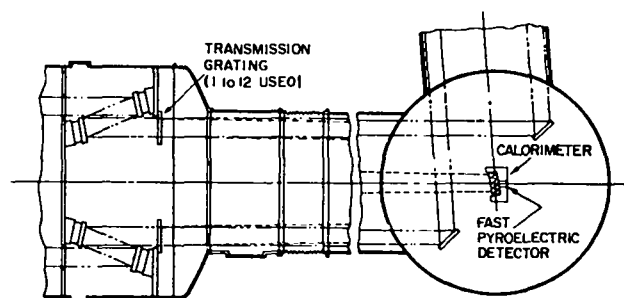


Fig. II-1.

Suggested baseline design for full-beam sampling measurements: total energy, E_t ; power as a function of time, $P(T)$.

axis triple-pass or double-pass, by rearranging the optics.

The optical design provided very high magnification from the effective beam size at the various stages of the front end to the beam size exiting the power amplifier. This high magnification reduced the sensitivity to misalignment in the target chamber resulting from a pointing error in the front end. The beam-pointing requirements in the front end were thus effectively reduced to guiding the beam from element to element without vignetting. In addition, the required optical figure for front-end components was relaxed to a slope-error requirement (e.g., fringes per inch) rather than to an absolute figure. Another important result of this high magnification was a relaxation to the milliradian regime of the collinearity requirement for the multiple lines exiting from the oscillator.

The design incorporated several "dog legs" that act as alignment stations. Here, the angular and spatial alignment errors can be corrected separately, i.e., without cross-talk. These alignment stations simplified the alignment task and enhanced the overall alignment sensitivity.

The spatial filter elements will be fully reflective, except for plano windows enclosing the evacuated region. These spatial filters will be a very convenient place to insert beams for alignment.

Power Amplifier and Target Chamber (K. Jones, W. Sweatt).

Power Amplifier Optical Design. The optical design for the Antares power amplifier was fixed. Emphasis during the past six months has been on minor adjustments of the component locations to facilitate the use of common mounting surfaces, and on documentation. Optical design checks have been performed with the ACCOS, LOTS (University of Arizona), and HEXAGON (Hughes Aircraft Co.) codes. Final checks and tolerancing analyses continued.

Detailed diffraction calculations of the beam propagating through the power amplifier were made with the LOTS code. These calculations will be compared to experimental measurements of diffraction patterns for geometries that are representative of the power-amplifier cavity geometry. The results of these calculations will be used for further analysis of possible internal parasitic modes within the

cavity or of possible optically induced gas breakdown near the dielectric separators.

Target Chamber Optical Design. The target-chamber optical system was redesigned. The focal length was shortened to reduce the spot size and to relax the requirements on optical-component quality. Many optical configurations that would shorten the focal length were examined. The best design had a focal length of 160 cm instead of 282 cm.

The new system retained the rotated cubic illumination symmetry. The numbers and sizes of mirrors also remained the same as in the old system.

The target illumination system consists of three pairs of beams similar to the one shown in Fig. II-2. Three such pairs are equally spaced 120° apart about the center line. One beam in each pair enters the target chamber from the east and the other from the west. Each beam array of 12 segments enters the target chamber, reflects off a turning flat, and bypasses the target on its way to the array of parabolas. The parabolas then focus the light onto the target.

Eight of the twelve segments remain in the annular pattern, but four have been moved inside the array (Fig. II-3). This configuration allows the target to be inserted from the left side of Fig. II-2 without vignetting any of the beams. The array is changed from annular to that shown in Fig. II-3 between the turning chamber mirrors and the folding flats in the target chamber.

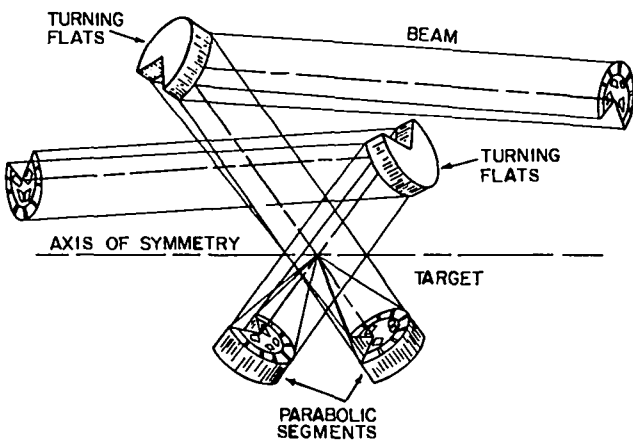


Fig. II-2.

Target illumination system: one of three pairs of beams located about axis of symmetry.

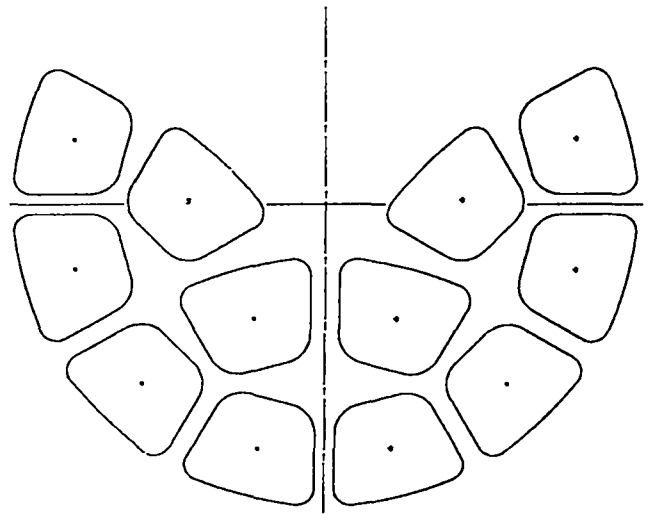


Fig. II-3.

Beam array from fold flats to parabolas.

Parasitics and Retropulse Protection (R. Bjurstrom/W. Sweatt)

The parasitics studies performed at the University of Arizona have thus far been restricted to locating parasitic modes in the power amplifier. Analysis showed that we must reduce the reflection from the anodes, the dielectric dividers (between beams), all structures along the edge of the cavity, and the mounts for mirrors and windows. The parasitic effects of the structure and optical components outside the power amplifier will be examined next.

The retropulse protection system for the Antares power amplifier is a passive system that employs gas breakdown as the primary method of reducing retropulse energy. For CO₂ laser mixes under conditions similar to those in the Antares power amplifier, the breakdown threshold is ~14 J/cm². This energy flux is too high for the various material damage thresholds. However, breakdown is enhanced in the overlap region of the power amplifier, where the apparent intensity is the sum of incident and reflected intensities. This enhanced field reduces, via the induced optical breakdown, the energy flux to the critical optical components.

The breakdown in the overlap region was modeled in a modified version of the gas breakdown code

developed for Gemini, which has been very effective in retropulse suppression. The one-dimensional code was modified to represent the design conditions of the Antares power amplifier as closely as possible. Results indicated that, in the current design, the retropulse will lose enough energy to remain below damage thresholds of the power-amplifier components.

Preliminary analysis with a more refined two-dimensional code (DAMCO) indicated that the current Antares retropulse-suppression design is adequate. Experiments are in progress to verify the codes and the current amplifier design.

Although the power amplifier is apparently adequately protected from retropulses, sufficient retropulse leakage to the front end may damage some front-end components. Methods of limiting the retropulse are under investigation. Passive means, such as modified spatial filters, are being emphasized as well as active means, such as spatial filters, spark gaps, or exploding-wire concepts.

Integrated Optical System (A. C. Saxman)

The optical system and Antares project schedules have been combined. One of the main features of the integrated optical system is the optical-hardware test bed, Beam Line 6. This beam line extends from the front-end output-driver amplifier to the target. Initially, it will be used for optical hardware fit checks, prototyping, and evaluation of the optical subsystems before their installation into the first electrically powered beam line, Line 1.

The final front-end/power-amplifier interface requirements for beam energy, dimensions, temporal profile, and beam quality were reviewed. No major changes were required and none are anticipated.

Mirror Assembly (D. Blevins, W. Turner)

Mirrors. The substrate material for large mirrors, 2124 aluminum alloy, was tested at Southwest Research Institute for dimensional stability and was found to be very stable. Fourteen periscope substrates were procured. Nine were plated by the Y-12 plating vendor. The adhesion of the plating and the masking techniques were excellent. Work continues on some problems with plating-bath composition.

Positioners. Components for the flexure type mirror positioners were being procured. A single-axis flexure type test rig was designed and procured. Initial test results were very promising; hysteresis was very low and repeatability was good.

A focusing attachment for the basic two-axis positioner was designed and parts were being procured.

Cells. A three-post kinematic support system that ties the mirrors to the mirror positioners was designed. A test mirror with prototype support parts was procured. The system, tested at the University of Arizona, induced no distortions in the mirrors.

Optical Component Evaluation (J. L. Munroe, R. Williamson, L. Fuka, E. Yavornik)

The Optical Evaluation Laboratory (OEL) served primarily in support of Helios. The OEL was also preparing for its extensive role in evaluating Antares optics. (1) Formal drawings evolved for most Antares optical components. (2) A vendor development program began. (3) A computerized inventory control system was initiated to track the relevant data and disposition of all Antares optical components. (4) A controlled-environment storage area was found.

A 46-cm (18-in.) salt window-and-cell prototype was tested for pressure worthiness and optical quality under pressure. The window survived a pressure 45% above the Antares operating point, without a measurable change in transmitted wavefront or birefringence relative to the free-standing condition at any pressure.

Dynamic tests were conducted on a 152.5-cm (60-in.) -high, 40-cm (16-in.) -diam circular cylindrical optical support stand, using modal-response-analysis equipment purchased from Zonic Technical Laboratories. The lowest natural frequencies of optical support structures should be as high as possible, preferably above 100 Hz, to minimize vibratory excitations from anticipated floor vibrations in the 10- to 100-Hz range. However, tests performed with the new equipment indicated an unanticipated resonance at frequencies as low as 25 to 30 Hz. This resonance was probably due to a rocking rigid-body motion. Various attempts to modify the stand with additional weight and boundary fixtures

were not successful in raising the lowest frequency. The stand will be shortened and a less massive top plate may be used to alleviate the situation.

Outside Contracts (W. H. Reichelt)

Hughes Research Laboratories Beam Centering Study (A. C. Saxman). The Antares power-amplifier beam-alignment study contract with Hughes Research Laboratories (HRL) neared completion. During the first phase of this study, the Antares power-amplifier optical train was modeled with a geometrical and diffraction optical-system code. The modeling included an optical tolerance analysis of the various mirror motions.

The second phase of the contract provided a baseline design of a power-amplifier beam-alignment system. The alignment system simultaneously collinearized the front-end beam and the center line of the power-amplifier optical train. The design incorporated code-effective beam-detection systems and a beam-alignment scanning periscope subsystem, which sequentially scanned each of the 12 sectors of a power amplifier.

Battelle Optical Blacks Study (W. Sweatt, W. Turner). Optical blacks for 10.6- μm radiation were being studied. We tried to find a noncontaminating material that could be exposed to the high fluxes found in the power amplifier. Thus far, our best choice was flame-sprayed lithium fluoride (LiF). Battelle Columbus Laboratory flame-sprayed samples for us and ran several different mechanical tests on the material.

Air Force Weapons Laboratory Polishing Study (R. Williamson). The continuous polisher, which is being used in developing salt polishing methods, completed its initial shakedown. Mechanical problems were corrected, and a glass test piece showed a figure of 0.0013 λ rms at 10.6 μm , or $\lambda/10$ peak-to-valley visible.

Harshaw Chemical Company NaCl Window Study (W. H. Reichelt). The Kyropoulos/Czocharalski growth-process investigations continued. Large 40-cm-diam boules of NaCl were grown successfully. They were free of haze bands

and other bulk defects. However, bubbles from entrapped gases were still a problem. Controlled contoured growth at the lower solid-liquid interface was investigated. A proper contour will not permit accumulation of gas.

A possible instability in surface figure of the mounted NaCl windows was investigated. Major surface-figure changes were traced to excessive clamping of the mounted window. Changes in temperature of the window assembly were shown not to result in figure changes. This investigation continues.

Optical Coatings Laboratory, Inc. (OCLI) Antireflection Coating Studies of Large NaCl Windows (W. H. Reichelt). OCLI successfully coated 20- and 40-cm-diam NaCl windows with single-layer $1/4\text{-}\lambda$ (at 10 μm) NaF coatings. These coatings showed good sticking ability and a measured damage threshold comparable to that of the substrate material.

Union Carbide Corporation Y-12 Plant's Single-Point Diamond Turning (SPDT) Program (W. H. Reichelt). The technology to turn flat and spherical surfaces to within $1\lambda_{\text{visible}}$, with finishes on the order of $<0.075 \mu\text{m}$, was established. Production technology and reliability were investigated. Parabolic-mirror figuring was demonstrated to $2\lambda_v$ on large $f/1$ systems. Finish remained a problem with parabolic mirrors, and studies in this area continued.

FRONT-END SYSTEM (W. T. Leland, M. Kircher)

System Studies

Plans and schedules were prepared for the entire front-end program. Included in the planning was a prototype one-beam front end, which will be used to verify the performance of front-end components before their incorporation in the Antares system.

Planning, specification of components, and procurement actions dominated the Antares front-end work during the past six months. As part of the specification effort, we studied the performance of major subcomponents of the front-end system. The

calculations used our design codes covering, e.g., energy extraction, discharge kinetics, and electron-gun engineering. The significant results of these studies are referred to in the appropriate paragraphs below.

Oscillator and Switchout (D. Swanson)

We have started evaluation studies on the various oscillator configurations that could be used for Antares. A multiline (four or more) single-band (10- μ m) oscillator with an output pulse adjustable in width from 0.25 to 1 ns and with a contrast ratio of at least 10^7 was required. A misfire rate of less than one per thousand shots was desired. Line content reproducibility and adjustability were also being examined.

Our standard three-section Pockels cell switchouts meet the requirements for pulse length and contrast ratio, and all parts for their construction were ordered.

Performance-testing of a Laser Development Corporation (LDC) multiline, two-band oscillator revealed that the device, in its design configuration, did not have the reliability and line-content adjustability desired.

Driver Amplifiers and Preamplifiers (G. York)

The output pulse amplifiers of the front end were designed to deliver 6 annular beams of 90 J each. Pulse duration was specified as 1 ns or less. The selected design was a dual-beam configuration wherein a single two-sided electron gun served two high-pressure discharge chambers. The discharge chambers were sized to enclose a discharge volume of 18 by 18 by 200 cm. Nominal operation called for 1200 torr (1.6×10^5 Pa) of helium-free mixture, although the capability of operation at up to 1500 torr (2×10^5 Pa) was included in the specifications. The three dual-beam modules will be excited by a single gun energy supply, but there will be individual energy supplies for the six gas discharges. The design permitted gain-length (gL) products of up to 7.5, although the specified output could be obtained with a gL product of 6. A small input-energy requirement (a few millijoules) resulted from the

use of triple-pass Cassegrainian optics with saturable absorbers to provide parasitic stability and contrast-ratio enhancement.

Special attention was given to system reliability and ease of maintenance. Component lifetimes and protection devices were required to guarantee failure-free operation for more than 1000 shots. Misfire rates were specified as less than 1 per 100 shots. Detailed specifications commensurate with the above general specifications were prepared, vendors' proposals evaluated, and procurement initiated.

Energy for the final stages will be provided by a standard, commercially available amplifier (a Lumonics 602). Calculations were made for such a unit equipped with triple-pass optics and (if needed) saturable absorbers. All the prerequisite procurement actions are complete.

Beam Line (C. Knapp)

Specifications for beam-line optics were prepared and orders were placed for those needed in the planned tests of the preamplifier and final-stage driver amplifier.

Saturable absorber cells, along with a gas-handling system, were designed and parts were ordered.

POWER AMPLIFIER SYSTEM (R. D. Stine)

General

The Antares power amplifier is shown in Fig. II-4. The unit is 16 m (53 ft) long, 3.7 m (12 ft) in diameter, and the centerline is 3.2 m (10.5 ft) from the floor. The total weight is over 90 000 kg (200 000 lb). The basic design incorporates a centrally located 12-sided electron gun, which discharges into annular pumping volumes. The light beam from the front-end room is directed to a 12-sided polyhedron, which splits the beam into 12 separate rays that traverse the power amplifier. The first pass is an expanding pass to the back reflector and the second near-collimated pass is directed toward the periscopes, which reduces the diameter of the annular beam. In an annular region outside the central electron gun is the lasing gas, a mixture of CO_2 and

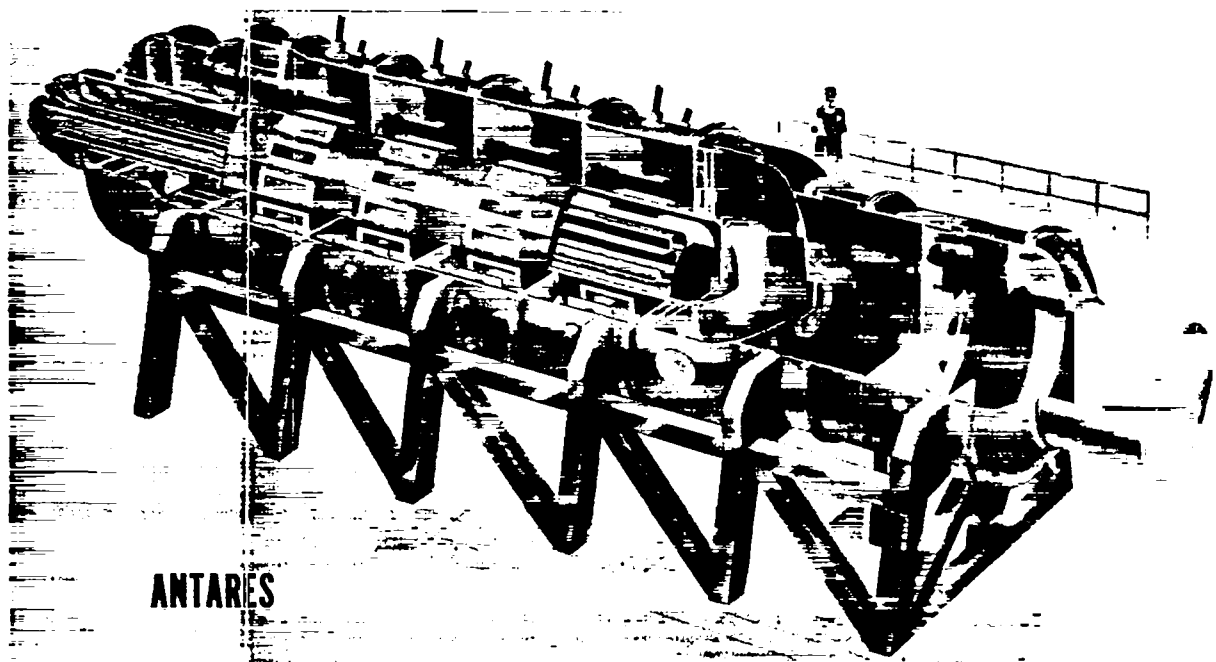


Fig. II-4.
Antares power amplifier.

N₂; salt windows with a diameter of 46 cm (18 in.) separate the pressure vessel from the vacuum of the in/out optical section.

Primary design emphasis was on the long-lead-time items shown in Fig. II-5. All except the end domes were ordered or out on request for quotations (RFQ). The salt-window dome and the back-reflector dome drawings were essentially completed. The longest-lead-time item was the electron-gun vacuum-vessel shell, a 1.5-m (5-ft)-diam, 9.1-m (30-ft)-long chamber made of 5-cm (2-in.)-thick steel. It consisted of four rolled sections, each with its machined hibachi ribs. These four sections were then pulse-arc-welded into one large chamber. Because of this multiple process, the chamber was considered the longest-lead-time item and was therefore procured first. As of June, the rolled sections were in fabrication and the machining order was placed. The coaxial feed bushing—a 1.5-m (5-ft)-diam, three-piece plastic part—was waiting for final approval before contract award.

There will be two parallel activities in the Laser Hall during initial installation of the power amplifiers. The Laser Hall floor plan (Fig. II-6) shows the six power amplifiers. Two, Power Amplifiers 1

and 6, will be installed almost simultaneously. Power Amplifier 6 will consist of the stand, pressure vessel, optical shells, optical support structure, and one beam-line worth of optical components. It will be used as an optical test bed to check out the installation and stability of all optical components. Initially, there will be no electrical power to this amplifier. Power Amplifier 1 will be installed a few weeks after Power Amplifier 6 and will be equipped with a full complement of electrical hardware. This power amplifier will be tested electrically and the small-signal gain measurements will be completed before optical components are installed. The information gained with Power Amplifier 6 will be used in installing the optical components in Power Amplifier 1, which will then deliver energy to the target region.

Pumping Chamber

Electrical (R. Lindstrand). To increase high-voltage cable reliability and decrease cost, we studied the effect of feeding several discharge anodes with a single cable. Previously, we intended

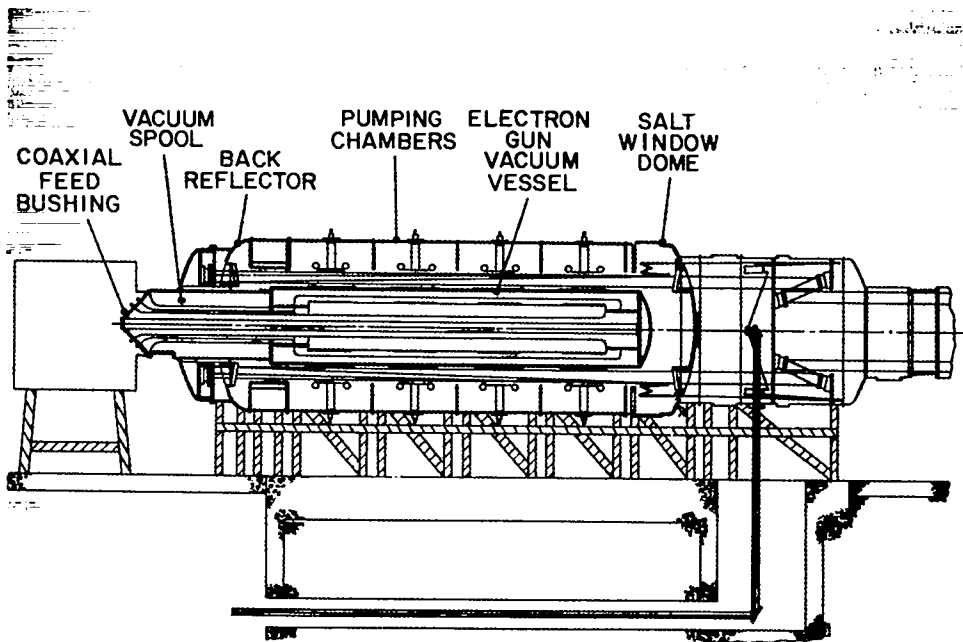


Fig. II-5.
Power amplifier long-lead-time components.

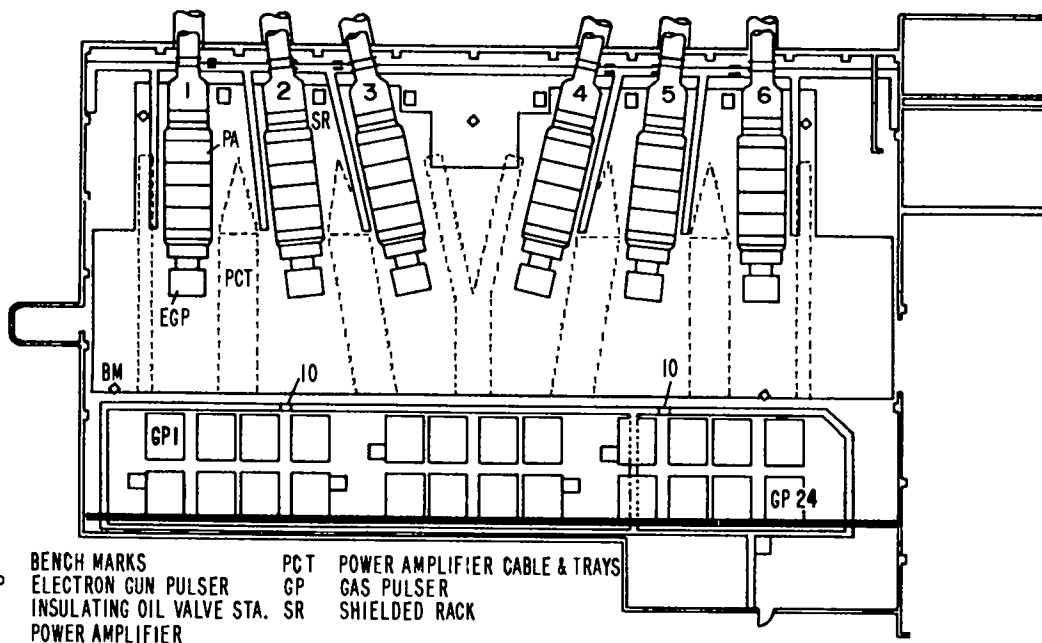


Fig. II-6.
Laser Hall floor plan.

to use one cable per anode. Geometry analysis and experiments with the prototype power amplifier addressed the question of increased magnetic fields in the discharge region due to currents running along interconnected anodes. The information acquired indicated that only one cable is needed for each pair of anodes. This reduced by half the number of high-voltage cables and feed-through bushings required for Antares.

Anode bushing development and evaluation received limited attention. The bushing design was closely related to the specification of the high-voltage cable. Final bushing selection awaited the determination of the proper cable. Tests of cable from General Cable Co. showed that the cable design was incompatible with a laser-gas-filled epoxy bushing. Hardware fabrication was started for several other bushing designs.

Mechanical (G. Ross, W. Turner). The pressure-vessel shell drawings were essentially completed. Eight pumping-chamber section units were ordered for Power Amplifier 1 and Power Amplifier 6. The adjacent spacer spool design was also completed, and two units (for Power Amplifier 1 and Power Amplifier 6) were ordered. The back-reflector shell and dome, and the salt-window dome were 95% completed. The dome design in the vicinity of the large salt windows was based on a steel forging stock, which will be ordered separately and supplied as raw material. A design for the hydrostatic-pressure test equipment needed for these domes was 60% completed. All interfaces to the pressure-vessel shells were finalized, including laser-gas fill ports, optical and electrical ports in the salt-window dome, high-voltage cable and gas circulation ports in the pumping chambers, as well as absorber gas-fill, optical, and electrical ports in the back-reflector shell and dome. In addition, mounting plates, which connect to the support stand, were included on all sections of the pressure vessel.

The in/out section, spacer, dome, and diagnostic section were 90% completed, with all known interfaces included. These units constituted intermediate-range procurement and will be ordered in the fall of 1978.

The air-bearing support concept for electron-gun insertion and removal was tested in a special fixture to duplicate the weight and motion desired. These

tests showed the concept to be adequate, although small modifications to the air bearing were being made to improve the final design and performance. The balance of the electron-gun support system design, e.g., structures and rails, was 30 to 40% completed.

Plasma spraying of LiF coatings onto carbon steel substrates was developed. This coating was 1.5 mm (0.060 in.) thick and was applied to absorb 10.6- μ m light. It will be used on, e.g., anodes, baffles, and covers. Also, a sample of Fe₃O₄, which has similar nonreflecting properties as LiF, was being procured for testing.

Electron Gun

Electrical (R. Lindstrand, G. Allen). Electrical breakdown tests were performed on several insulating materials proposed for the electron-gun support bushings. The materials were polyurethane, polypropylene homopolymer, and methylmethacrylate. The high-voltage pulse testing was designed to compare the surface holdoff properties of the materials relative to the successful epoxy bushings in service on the prototype power amplifier. Test data qualified the material as equivalent electrically under anticipated conditions. Mechanical tests were unnecessary for final selections.

Experiments were conducted on the high-voltage test vehicle to determine the effects of reducing the cold-cathode electron-gun voltage from -500 to -300 kV. Operation of the Antares electron gun at -300 kV was proposed to improve the laser small-signal gain distribution. Our first concern was the possibility of gas breakdown in the discharge region due to the reduced range of the primary electrons. However, tests showed such breakdown will not occur with Antares pulse shapes. Additional tests were performed to determine the level of electron-beam current density necessary to produce a desired gas discharge-current density. Test module results showed a shot-to-shot inconsistency in gas currents for a selected beam current. The results were not confined to gun operation at -300 kV. Further investigation will be performed on the large prototype power amplifier.

The initial evaluation of the electrical contacts between the gun vacuum vessel and the gas pressure

vessel was completed. Using 90 contact fingers per contact assembly resulted in insignificant arcing at 100 000 A peak current, higher by a factor of 5 than the worst-case requirement. The total side loading of these finger contacts on the gun vacuum vessel would be ~72 000 N (16 000 lb), requiring a large force to extract the gun from the pressure vessel. Considering the large electrical safety factor, a tradeoff was made between the side loading of the vacuum vessel and the number of contact fingers. A new contact assembly, with only 30 contact fingers, was constructed and will be tested.

The multiline band joint in the multicoaxial-line gun feed was tested, again at about five times the expected current requirements, with no significant arcing or burning evident. The only problem encountered with this test was the out-of-roundness of the large-diameter tubular sections. This problem will be eliminated by tighter specifications on the procurement drawings.

Mechanical (G. Ross, W. Turner, E. Yavornik, L. Fuka). The electron-gun design was essentially completed. The shell design was completed; one unit was ordered, including weldments, machining, and weld assembly. The vacuum-spool design was completed and an RFQ for three units initiated: one for Power Amplifier 1, one for Power Amplifier 6, and one for electron-gun testing.

The stress analysis of the vacuum-vessel cylindrical sections was completed. The results showed stresses less than critical, design loads less than required to produce overall buckling of the cylinder, and the hibachi ribs would not buckle under the anticipated static and dynamic loads.

The design of the coaxial feed bushing was completed, and seven units were ordered. One unit will be tested before the others are fabricated. The quantity represented the requirements for all six power amplifiers, plus one spare. The cathode support bushings were designed and an RFQ for seven sets was initiated to cover the requirements of all six power amplifiers. The cathode, grid, and coaxial lines were in final check and were not released.

A program was in progress to fabricate and test titanium-brazed foil-grid assemblies. The parts were designed, and orders for material and fabrication were placed. We plan to use 1-mm (0.040-in.)-thick titanium for the grid material to which

titanium foil will be brazed. Arnold Engineering, a division of Allegheny-Ludlum, was cladding 1-mm (0.040-in.)-thick titanium sheet with 0.05-mm (0.002-in.)-thick AMI-389 brazing material (aluminum-silicon alloy). This material will be punched to the grid configuration and then brazed to titanium foil. We expect that this process will place brazing material only at the joints of the assembly without any runout onto the foil.

Previously, brazed grid-foil assemblies were made in the laboratory, wherein strips of brazing material were placed between the grids and the foil. This was a tedious, time-consuming process. Also, it was impossible to prevent some braze-material runout onto the foil. In pressure tests these assemblies performed very well, with only small pinholes developing at rupture pressures. The present program is expected to result in the fabrication of high-quality economical assemblies for use in our lasers.

Fault Protection (K. B. Riepe, R. Lindstrand). A fault protection plan was written and entered into the Antares Project Data Document. The plan detailed the equipment needed to protect the power amplifier and gas pulsers in the event of an electrical malfunction. A typical example was overvoltage protection gaps, which prevent voltage ring-up. The plan also provided for diagnostics to isolate the fault condition, such as cable current sensors, which identify high-voltage cable failure.

An individual power amplifier will have one overvoltage protection gap for each section containing 12 anodes—a total of 4 gaps per amplifier. These gaps were specified to protect the high-voltage cables from voltage-doubling due to an electron-gun misfire. The gaps, though similar to those designed to prevent overvoltage in the gas pulser, must operate in an external environment of laser gas, rather than in transformer oil. Computer-generated electrostatic analyses were applied to arrive at a favorable design. Design drawings were completed and a prototype gap was in fabrication.

Gas and Vacuum Subsystem (N. G. Wilson). The power amplifier includes three primary controlled-environment areas, i.e., the electron-gun high-vacuum zone, the laser-gas pressurized zone, and the absorber-gas zone. The areas are shown in Fig. II-7. The arrangement of the various elements

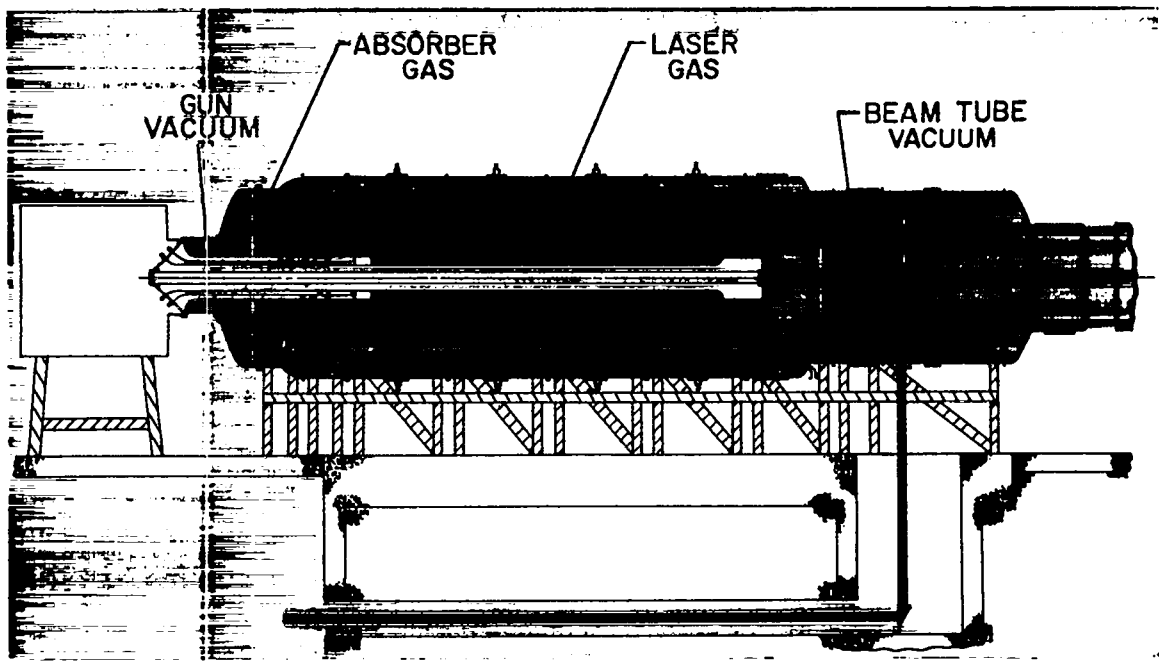


Fig. II-7.
Power amplifier vacuum and gas volumes.

of this system is shown in a schematic block diagram, Fig. II-8. General functional requirements of these elements are: (1) provide an operating environment in the electron gun of less than 10^{-5} torr; (2) provide a controllable laser-gas fill system for the $\text{CO}_2\text{:N}_2$ gas mixture at a nominal pressure of 1800 torr; (3) provide the absorber gas (five-component Mix 804) for the optional absorber cell through a gas mixing system capable of filling the cell in less than 1 min; (4) provide the absorber-cell vacuum system, which offers an independent evacuation capability to $\sim 10^{-1}$ torr; (5) provide a laser-gas recirculation system to permit gas cooling and filtering before complete exchange of a laser gas fill; (6) provide an air circulation system to supply positive filtered air flow through any zone of the power amplifier that can be occupied by personnel during assembly, maintenance, and alignment operations; and (7) provide a manifolding system,

which connects the vacuum roughing system installed in the Laser Hall with each of the six power amplifiers, so that each power amplifier system is independent and provided with its own dedicated local system controller. With this arrangement, all the gas and vacuum systems of a specific power amplifier are individually operable from the power-amplifier location, independently from the main control room.

Detail engineering of each of the elements of the gas and vacuum system was in progress. Where possible, long-lead-time items were identified and procured for assembly into a first system for design checkout.

The turbomolecular pump and the gate valve for the electron-gun high-vacuum system have been ordered. The mechanical backing pumps for the turbomolecular pump have been received. Detailed

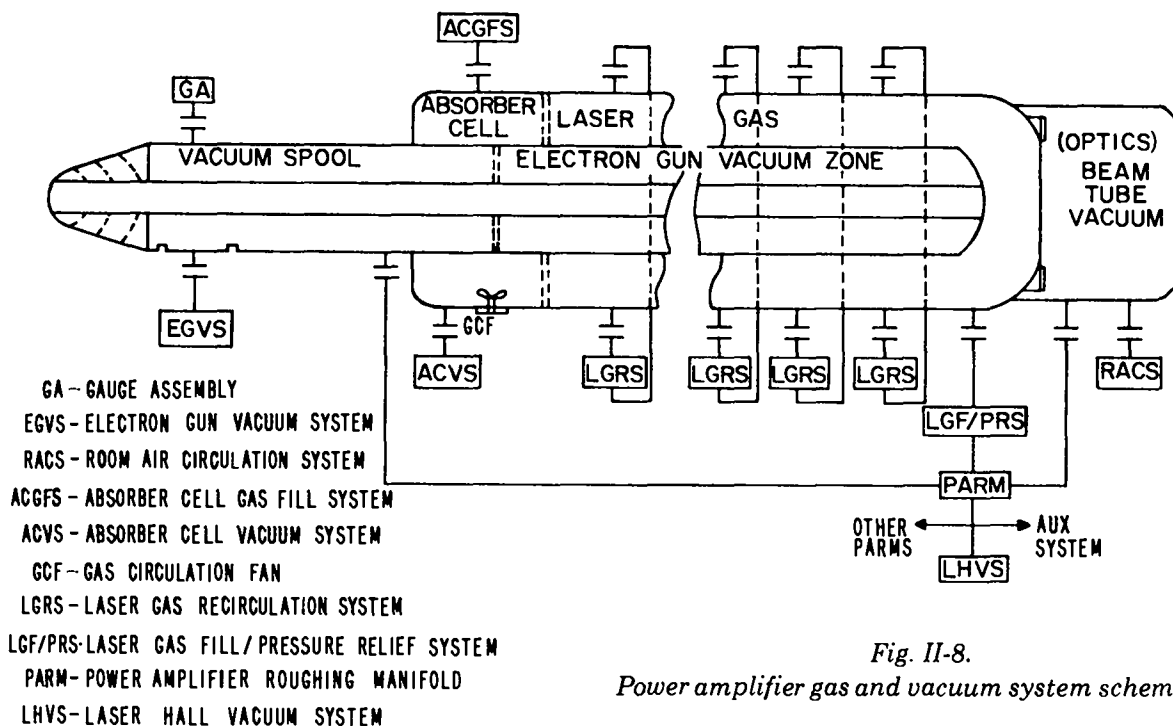


Fig. II-8.
Power amplifier gas and vacuum system schematic.

design of the electron-gun vacuum-system components and of the mounting frame, handling fixture, and tooling is in progress.

Handling Equipment (G. Ross, B. Weinstein). A master list of all auxiliary (handling) equipment was started to keep track of all the requirements for fixturing and need dates. This list will be used to schedule the design and fabrication of these items.

Concepts and preliminary design for an electron-gun dolly and for two pallets were completed. These units were required for the assembly and insertion (or removal) of the electron gun within the power amplifier as well as for electron-gun testing. A final design of the pallets was started and was 10 to 20% completed.

Diagnostics (R. Lindstrand). A list was compiled of the diagnostics needed to characterize the performance of each power amplifier. The list was entered into the Antares Project Data Document and will serve as the reference point as details of individual diagnostics are developed. Diagnostic requirements were specified for checkout, startup, operating, and fault-diagnosis phases.

A study was performed to determine the necessity of small-signal gain measurements as a tool for fault diagnosis. Such measurements on a fully assembled power amplifier introduce considerable mechanical complexity. A fault-diagnosis flow chart was developed to evaluate the importance of the measurement relative to alternative diagnostics. It was decided that sufficient diagnostic data will exist to allow elimination of the fault-condition gain measurement. Small-signal gain will still be measured during the start-up phase of each power amplifier.

Characterizing the behavior of the grid-controlled, cold-cathode electron gun will be an important step in achieving design output from the power amplifiers. One of the critical measurements will be the time-integrated electron-beam distribution. Normally, this measurement is made by using blue cellophane to detect the beam. However, the anticipated levels of electron current density are below the threshold for blue-cellophane detection. Tests made on a nylon-base radiochromic film and on a polychlorostyrene sheet determined that these alternative materials are sensitive enough for a calibrated response on a single-shot basis.

Optical Support Structures (W. O. Miller). The preliminary designs and structural analyses for the three power-amplifier optical support structures (Fig. II-9) were completed. For each optical support structure we established the design configuration, size, and weight, and evaluated its structural behavior. The results of the finite-element structural models were used largely to confirm these designs, which then formed the basis for detail design.

The salient features of the structures and their structural characteristics are summarized in Table II-I. Our main thrust in preparing these design arrangements was to achieve high structural stiffness with a cost-effective approach. Structural stiffness was achieved, as evidenced by the substructure's high natural frequency and by minimum structural distortion from shell-induced loads. The design configuration was cost-effective because the required manufacturing techniques were straightforward. The relatively high static deflection of the relay optics was acceptable. The misalignment sensitivity of this section was low and the error could be indexed out.

Support Stand (W. O. Miller). The power-amplifier support stand is composed of 30- by 30-cm

steel box beams, interconnected in a truss-like arrangement. The combined weight of the power amplifier and support stand is ~100 000 kg, with 75 000 kg of this mass being concentrated in the power amplifier 3.2 m (10.5 ft) above the floor. This is a large mass to be cantilevered off the floor, and thus its structural dynamic behavior is of prime concern to the performance of our optical system.

To establish the predicted dynamic motion of the optical support structures within the power amplifier, we have

- (1) used a finite-element model of the Antares facility to predict the laser hall floor motion due to subseismic and machinery-induced vibrations;
- (2) incorporated the optical support structures (exclusive of the relay optics) in the finite-element model of the power amplifier and power-amplifier support stand; and
- (3) used the base motions from Item (1) as dynamic inputs to the model described in Item (2).

A determination of mode shapes and natural frequencies for the support stand revealed that our lowest two modes were very close, 43.66 and 44.42 Hz. The lowest corresponded to a lateral motion of the stand, i.e., normal to the longitudinal axis.

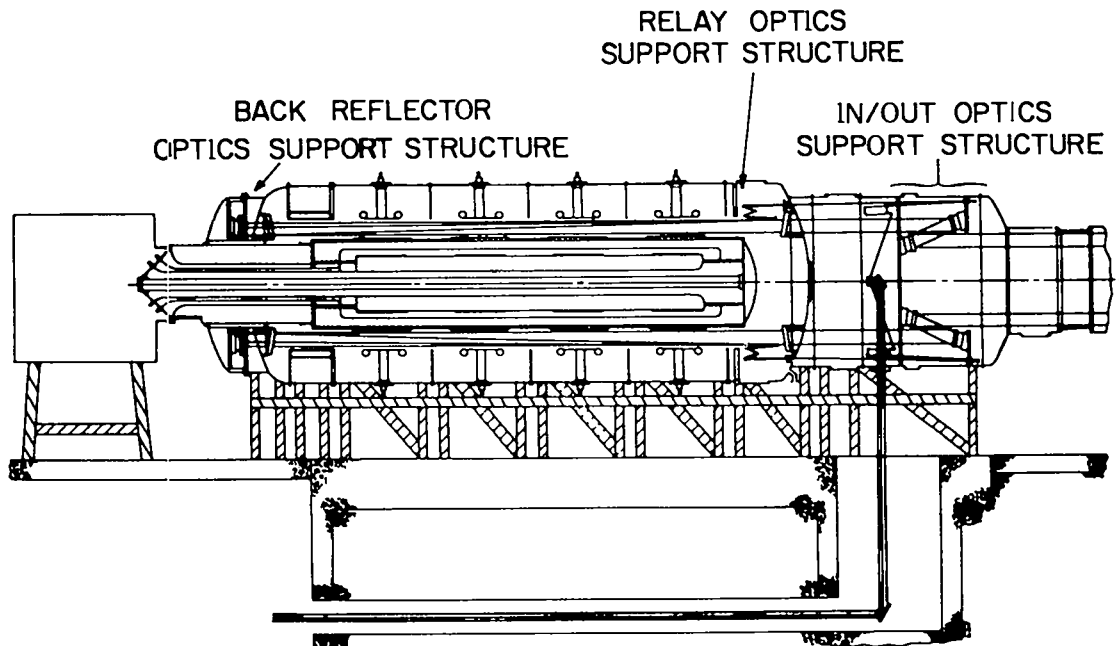


Fig. II-9.
Power amplifier optics support structures.

TABLE II-I
POWER AMPLIFIER OPTICAL SUPPORT STRUCTURES

<u>Optical Section Description</u>	<u>Weight (kg)</u>	<u>First Structural Mode (Hz)</u>	<u>Max Static Deflection from Shell Loads (arc-s)</u>
In/Out			
Aluminum welded structure; 5-cm-thick face plates, 3-m o.d.; interconnected with 12 radial shear plates 1.2 m long.	2273	91.3	4
Relay			
Aluminum ring structure; 7.6-cm-thick face plate, 3.6-m o.d., 1.2-m i.d.	1175	67.1	77
Back Reflector			
Aluminum welded structure; 5-cm-thick face plates, 3-cm o.d.; separated by 12 radial shear plates 36 cm long.	1807	90.9	6.4

Resonance along the axis occurred at 44.42 Hz, the second mode of vibration. Fortunately, there was weak coupling between the two modes, i.e., lateral motion did not contribute significantly to axial motion. Coupling was of concern because it was probable that excitation in both directions would occur simultaneously.

Our predictions to date indicated that the peak dynamic response in the power-amplifier optics occurred in the back-reflector support structure. The maximum amplitude was $0.62 \mu\text{m}$ ($24.4 \mu\text{in.}$) at 44 Hz, in the direction of the longitudinal axis of the power amplifier. The optics support structure did not distort; rather, the deformation occurred in the power-amplifier shell to which the structure connects. As a rigid body, the optical structure underwent a rotation of 0.025 arc-s, an order of magnitude below our design goal. This desirable consequence provided us with greater permissible motion within the articulated back-reflector mirror mount.

The predicted optical-support motion of $0.62 \mu\text{m}$ ($25 \mu\text{in.}$) will be used as the dynamic-vibration input to the articulated mirror mount. Tests on the mount will establish its modal response and damping factor. Based on these results, we will prepare a model prediction of the mirror dynamic response as a final part to our design-confirmation process.

High-Voltage Cable, Terminations, and Testing (G. Allen, R. Lindstrand). The high-voltage cable initially used for the prototype and test vehicle had an unacceptably high failure rate for use in the Antares laser facility at the 550-kV operating voltage. A search for higher quality high-voltage cables identified two possible suppliers: General Cable Co. in Union, New Jersey, and Sieverts Kabelverk in Sweden. Both use a special dry-curing process for treating the polyethylene insulation, which results in fewer and smaller microvoids than conventional steam-curing. The

high-voltage cable made by General Cable Co. has an additional insulation layer of high dielectric constant, called an emission screen, which is placed over the center conductor semiconductor layer. This emission screen reduces any field enhancement that may be caused by protrusions from the inner semiconductor layer. We tested a sample of 230-kVac cable from General Cable Co., which incorporated these special features, and found it to be of excellent electrical quality. Four 7.6-m (25-ft) -long samples were subjected to 10 000 impulses (risetime, 0.5 μ s; decay time, 20 μ s) at 800-kV peak voltage with no failures. The major drawback of this particular cable was that it was experimental and General Cable Co. had only manufactured small quantities for test purposes. The Antares laser facility will require a full production run of \sim 6096 m (20 000 ft). An additional problem with this cable was its poor geometric quality; the sample we received was oval rather than circular and the center conductor was not concentric with the insulation layer. These problems were discussed with General Cable Co., and additional tests were planned.

Sieverts Kabelverk supplied us with a 91-m (300-ft) -long test sample, which we should have on test near the end of August 1978. This particular sample was rated at 145 kVac and has been produced commercially since 1976. Sieverts tested a segment of cable from the same production run our test sample came from, with an impulse (1- μ s risetime, 40- μ s decay time) at 1.0 MV peak voltage and obtained a failure at 200 impulses. This single-point test result was encouraging, but additional tests will have to determine whether this cable is suitable for use in Antares. The gun pulser prototype was modified for testing this cable.

The most economical and convenient method of terminating these high-voltage cables in the gas pulser tanks is to strip back the jacket and outer conductor an appropriate length and allow the outer semiconductor layer to perform the electric-field grading, preventing surface flashover in the mineral oil. Two problems may be associated with this approach. First, the semiconductor layer resistance increased with exposure to mineral oil, which could reduce its effectiveness as a field-grading layer. Second, the polyethylene insulation swelled when soaked in mineral oil, which caused mechanical problems with the termination-end contacts. These possible problems will be thoroughly investigated. If

they prove to be significant, there are two alternative termination techniques that will be evaluated. The first alternative is simply to exclude the mineral oil from contact with the termination by fitting a dielectric tube around the termination and filling the tube with silicone oil, which is compatible with polyethylene. The second approach is to exclude the mineral oil through the use of shrink tubing and a special adhesive. Major activities relating to terminations have been delayed until the final cable is chosen.

ENERGY STORAGE SYSTEM (K. B. Riepe)

General

The energy storage system supplies the high-power, high-voltage pulses to the gas discharges and electron guns in the power amplifiers. It consists of 24 gas pulsers and 6 gun pulsers.

The first gun pulser is needed in June 1979 to begin checkout of the electron gun for the first power amplifier. After this checkout, the pulser will be integrated with the pumping chamber, and electrical checkout of the full-power amplifier is scheduled to begin in January 1980. This checkout will require four gas pulsers.

The schedule for installation of the first gas pulsers allows time for procurement of the gas pulsers from a commercial vendor. Because the gun pulser requirements are not fully defined, and because time is short, the gun pulsers will be designed and fabricated in-house.

Gas Pulser (K. B. Riepe)

The gas pulsers were designed as single-mesh pulse-forming networks based on 1.2-MV, 300-kJ Marx generators with 3- μ H internal inductance. A double-folded current path minimized the inductance. To maximize the reliability of electrical insulation, there were no insulating supports (which collect dirt) from the capacitors to the floor. Thus, the Marx stages were supported from the top by a dielectric structure. Switching was by symmetrical, mid-plane-triggered spark gaps pressurized with dry air. Analysis of laser prepulse energy on target placed a very stringent jitter limit of 10 ns (1 standard deviation) on the gas pulsers.

Development of spark gaps rated for the Marx short-circuit conditions (400 kA, 6 C) and solid resistors able to handle fault energy was completed, and spark gaps and resistors were ordered. In the meantime, a prototype Marx operated for over 300 full-energy shots into a dummy load resistor using smaller spark gaps and liquid resistors. In the initial configuration, the Marx columns, 2725 kg (6000 lb), were supported by six pultruded polyester threaded rods, with a fiber-glass-reinforced core (Permal trade name Superstud). The 1.9-cm (3/4-in.) rods were rated, and tested out, to tensile strength of over 2725 kg (6000 lb). However, after a few weeks in use, the strength decreased considerably. The suspension system was redesigned, and the dielectric rods were replaced with steel rods inside a nylon jacket. Full-energy operation (550 kV on the load, 250 kA) was generally satisfactory. Jitter measurements were not possible because of noise problems, which, however, can be solved with a fiber-optic signal link.

Preparations are under way for procurement of the gas pulser system. Proposals are being prepared by four vendors. The contracts will be fixed price, with bonuses for improved performance (lower inductance, lower jitter). The first Marx will be run through extensive life tests. Although the design does not have to follow our prototype, it is expected that certain aspects of our design will be incorporated. In addition, our experience with our prototype provides a basis for evaluation of proposed designs. Proposals are due in September with a contract award expected by January 1979.

Electron Gun Pulser (G. Allen)

The Antares gun pulser will be a two-section type-A Guillemin-Marx. This circuit was analyzed extensively and a detailed design of a 30-kJ prototype was completed. However, data from the Antares prototype power amplifier subsequently indicated that the energy requirement of the gun pulser should be 50 to 70 kJ rather than the initially estimated 30 kJ. Also, recent energy-extraction calculations suggested it may be advantageous to operate the gun pulser at 300 kV rather than 500 kV. Therefore, additional experiments with the Antares prototype power amplifier are planned to assess more accurately the gun-pulser energy and voltage

requirements. Until these experiments are complete, detailed design of the final gun pulser cannot proceed. However, extensive computer modeling of the basic circuit type will allow rapid completion of a detailed final design, regardless of final energy and voltage requirements.

The 30-kJ prototype pulser was under construction. This pulser will be used to verify the computer modeling and test components to be used regardless of final pulser requirements, such as the gun feed-line bushing and the peaking circuitry. Also, the Marx generator portion of the 30-kJ prototype will be used to test the high-voltage anode cables. In addition, the 30-kJ prototype may be upgraded to 50 kJ without redesign by simply changing components in the existing layout.

Component Development (J. Bickford, W. Turner)

400-kA Prototype Spark-Gap Testing and Development. Development of the 400-kA spark-gap switch for the gas-pulser Marx generator continued. The prototype was life-tested by discharging a 120-kV, 27-kJ capacitor bank for 2000 operations without maintenance. The resulting stresses on the switch exceeded the worst-case fault conditions occurring during firing of the gas pulser. The test operating parameters (per shot) were peak current, 490 kA; charge transfer, 5 C; blocking voltage, 120 kV; and ringing frequency, 185 kHz. The copper tungsten electrode material, Schwarzkopf K25 (sintered tungsten infiltrated with copper), proved superior to other refractory metals.

A copper-sulfate load resistor was fabricated and installed in series with the test circuit to simulate the actual normal operating conditions of the spark-gap switch in the gas pulser, resulting in an underdamped current oscillation with a peak of 240 kA, 25% overshoot, and a period of 8 μ s. Life-testing the spark gap under these normal operating conditions was planned, with self-breakdown tests spaced throughout the life test to statistically predict the prefire rate over the lifetime of the switch. Trigger jitter measurements were under way. At $M = 1.7$ ($M = \text{self-breakdown voltage/operating voltage}$), a standard deviation of 5 ns was easily attainable. A faster risetime, higher-voltage trigger generator was

installed in the test facility and should reduce the jitter significantly below 5 ns, even as M approaches 2.

High-Energy Pulse Resistors. Testing of the pulse-energy dissipation capabilities of high-voltage resistors for stage charge coupling and trigger coupling in the gas pulser was concluded. Carborundum Corp. successfully developed an epoxy-laminar coating process that sealed against saturation by transformer oil. Although the coating reduced the average power rating, a 2.5-cm-diam (1-in.) by 30-cm-long (12-in.) coated resistor was able to dissipate more than 10 kJ in 10 ms, which is acceptable for the gas pulser, and affords a cost and reliability advantage over liquid resistors.

TARGET SYSTEM (V. L. Zeigler)

Target Vacuum System (J. Allen)

Three firms responded to our request for proposals on the target vacuum system. The firms were evaluated with respect to technical capabilities and company resources, demonstrated understanding of the project, quality-control capability, project management, and cost. Two proposers were selected for follow-on negotiation.

Space Frame (V. L. Zeigler)

Preliminary design work started anew on the space frame because the selection of a new target focusing system invalidated the previous space frame (and target chamber). Whereas the target chamber was resized to keep the target vacuum-system contract moving, the redesign of the space frame had to wait for more detailed calculations of location for folding and focusing mirrors.

The new space frame will be higher and wider than before, but shorter along the east-west axis of the target system. It will fit into a target chamber whose diameter was increased from 6.86 m (22.5 ft) to 7.32 m (24 ft) and whose length was decreased from 5.79 m (19 ft) to 5.03 m (16.5 ft).

CONTROLS SYSTEM (M. Thuot, F. McGirt)

Front-End Controls (D. Gutscher)

A detailed Work Breakdown Structure (WBS), complete with cost and manpower estimates, and a tentative schedule were generated for the front-end controls effort. These results were incorporated into the total Controls System effort to obtain a comprehensive plan of action.

A study of the Controls System requirements for the front end was completed and a tentative system design was proposed. The design envisions a minicomputer located in the front-end screen room connected to several microprocessor-based machine interface controllers. The interface controllers will translate control and monitor signals coming from and going to laser equipment, such as power supplies, into computer-compatible digital signals. Fiber optics will isolate all microprocessors and the minicomputer from the high electromagnetic-interference (EMI) environment of the front-end room.

A microprocessor will be used as the machine interface controller. A prototype controller was under construction and will be tested on the front-end prototype. The prototype controller will contain, initially, the microprocessor with its associated control modules, a relay driver card, a binary monitor card, a slow-speed analog monitor capability, and a slow-speed analog control output. The prototype will be connected to a minicomputer by telephone lines and fiber-optic lines.

An investigation was undertaken to determine the best approach for providing the slow analog control and monitor functions. Two approaches were considered: (1) analog-to-digital (A/D) and digital-to-analog (D/A) converters and (2) voltage-to-frequency (V/F) and frequency-to-voltage (F/V) converters. Both will be evaluated in the prototype controller when PC boards become available.

Laser Hall Controls (D. Call)

Project Administration. The controls effort organization was changed. All controls and instrumentation functions in the Laser Hall were grouped together. This change is discussed below.

The planning stage neared completion. Three documents were generated: a WBS listed hardware items, software programs, and support activities; a hardware cost estimate was based on the items in the WBS; and a manpower estimate, which was also based on the WBS. The manpower estimate included the times and activities up to the electrical test of Power Amplifier 1 in April 1980. All aspects were discussed in a presentation at the Controls System Design Review.

System Design and Test. A complete controls-system design study was conducted early in this reporting period. The design includes several minicomputers.

One of the minicomputers will be used exclusively for the electron-gun test area, because it requires a large control and data acquisition effort.

A shielded box for sensitive analog and digital circuits was tested. A microcomputer with support electronics and an isolation transformer were put in the box. Connections to the box were one power cord and fiber-optic cables for signals. With the box sealed, fields about 10 times those expected in Antares were generated outside the box with a high-voltage capacitor. The computer inside operated perfectly throughout the test.

Beam Alignment (B. G. Strait). The Antares controls system will be implemented with a hierarchical, tree-structured network of control computers. A block diagram showing the beam-alignment controls in the computer network is shown in Fig. II-10. The lowest-level control computer is a microcomputer shown as the alignment

controller. The total Antares beam-alignment system will require about 12 alignment controllers, each controlling ~100 stepping motors. The beam-alignment sensors are also connected to the alignment controllers. During automatic alignment, the alignment controllers position the stepping motors on the basis of information collected from the sensors.

Because of the very high electromagnetic fields developed during the firing of large CO₂ lasers, serial communications over fiber-optic cables will be used throughout the Antares controls system. In the beam-alignment control system, fiber optics are used between the control room and the alignment controllers, between the alignment controllers and the motor drivers, and from the sensors to the alignment controllers.

The motor-driver circuits and sensor electronics both use Universal Asynchronous Receivers and Transmitters (UARTs) to handle the serial transmission functions. Each eight-bit byte received by the motor driver contains the stepping-motor sequencing information to control two stepping motors. The motor driver also sends limit-switch information to the alignment controller via the UART.

The sensor electronics contain an A/D converter, which digitizes the sensor output and transmits this information to the alignment controller with a UART. It does this continuously at a high rate. The alignment controller simply reads the receiving UART when it needs the sensor information for alignment.

A fiber-optic bulkhead feed-through was developed, which provides an inexpensive means of passing the fiber cables into both the vacuum and CO₂ gas regions of Antares. The feed-through is required because the motor drivers are located on the mirror positioner assemblies as are the sensor electronics.

Microcomputer System Development (W. Seifert). In the past six months, several events precipitated substantial changes in the Antares controls-system design. A distributed processing approach was recently adopted that lends itself more readily to the use of a microprocessor that is software-compatible with machines located higher in the network architecture.

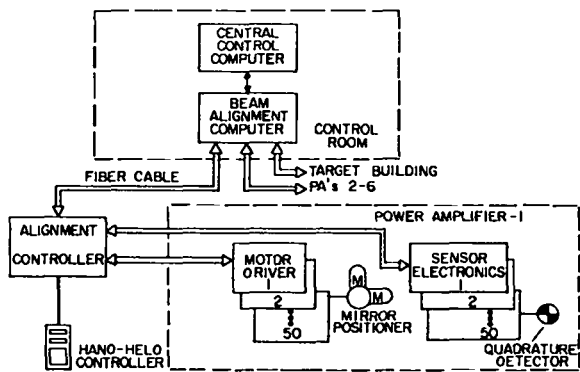
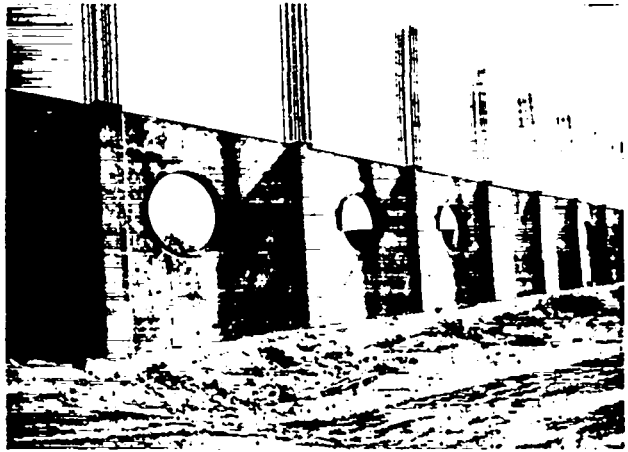


Fig. II-10.
Beam alignment controls.

HEGLF SITE AND STRUCTURES (J. Allen, E. O. Swickard)

Construction Package I (J. Allen)

Package I includes the following. The Laser Building, which contains the large Laser Hall, control rooms, laboratories, shops, laser front-end room, and offices; the Mechanical Building; a warehouse; and the Office Building. Construction is 23% complete, with a scheduled completion date of July 1979. Figure II-11 shows the front-end room after completion of concrete work, whereas Fig. II-12 shows the beam-tube penetrations in the Laser Hall wall.



*Fig. II-12.
Laser hall beam-tube penetration.*

Construction Package II (J. Allen)

Package II includes the Target Building; additions to the site fire-protection system; the site power-transmission system; and the final grading, paving, and landscaping. The contract was awarded to the Allen M. Campbell Co. (also the Package-I contractor) in January 1978. Construction is 21% complete, with a scheduled completion date of May 1979. Figure II-13 shows reinforcing bars in place for the 6-ft-thick walls of the Target Building.

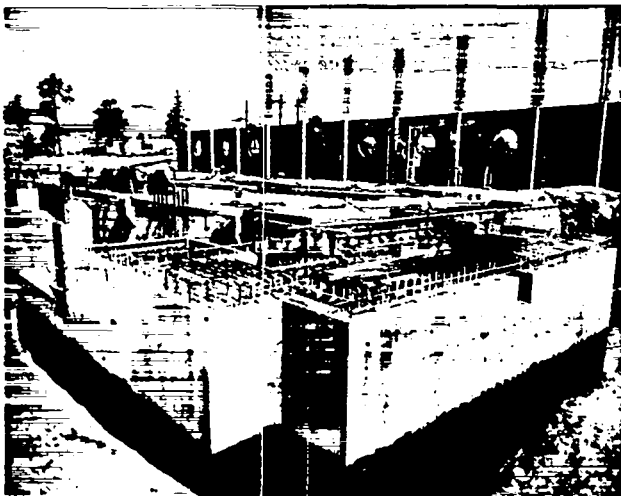


*Fig. II-11.
Front-end room construction.*

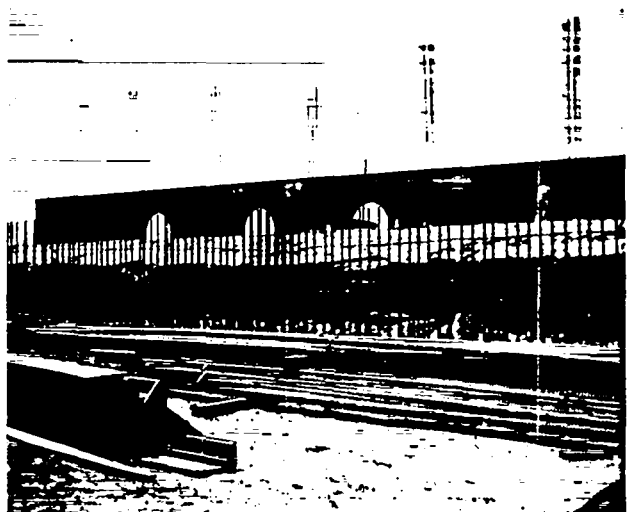


*Fig. II-13.
Target building wall reinforcing bars.*

High-Voltage and New Optical Evaluation Laboratories (J. Allen)

The contract for these structures was awarded in January 1978 to the John R. Lavis Co. Construction is 56% complete, with a scheduled completion date of October 23, 1978. Figures II-14 and -15 show the status of the buildings.

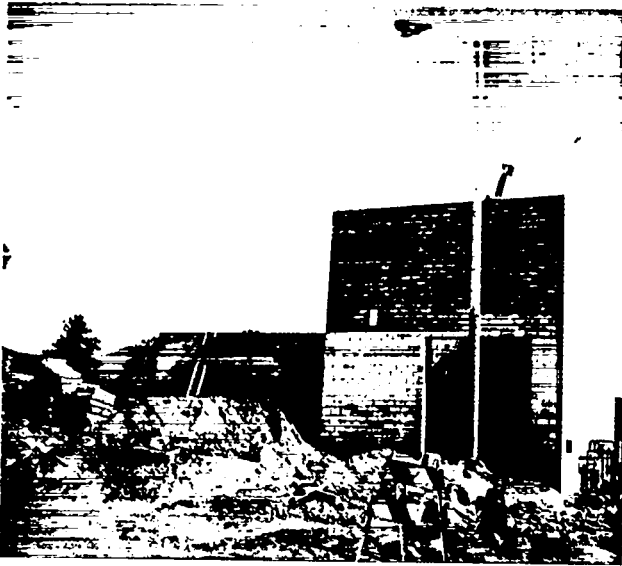


*Fig. II-14.
High-voltage laboratory.*

*Fig. II-15.
Optical evaluation laboratory.*



Modal Response Analysis Equipment (L. Fuka)

The modal response analysis equipment was received from Zonic Technical Laboratories and

checked out. During the checkout phase, a number of equipment performance deficiencies attributable to hardware and software problems were identified for correction.

III. CO₂ LASER TECHNOLOGY

Each of our CO₂ laser systems described earlier represents a significant advance in the state of the art of reliable CO₂ laser subsystems, components, and diagnostics. The design, construction, and improvement of the systems require, therefore, basic support of CO₂ technology. Some important areas are the development of short-pulse multifrequency oscillators, amplifier optimization, development of subsystems for the prevention of system self-oscillation and removal of prepulse energy, improvement of the transverse profile of the amplified laser pulses, and measurements of optical damage thresholds in systems components.

CO₂ LASER PHYSICS

Introduction

We report the first observation of phase-conjugation or degenerate four-wave mixing in the infrared. The conjugate reflection was obtained with germanium, using an intracavity technique that simplifies the experimental procedures required to observe the effect. We measured 2% efficiency in conversion of the 10.6- μm probe wave to its phase conjugate. Wavefront quality of the aberrated probe wave was dramatically recovered after phase-conjugate reflection.

We also report extensive measurements of the SF₆ absorption cross section for CO₂ laser radiation on four different lines in the vicinity of 10.59 μm . Measurements were performed at molecular densities of 1 to $2 \times 10^{19} \text{ cm}^{-3}$ and temperatures of 140 and 300 K. CO₂ laser fluences employed ranged from 10^{-4} to nearly 1 Jcm^{-2} .

Phase-Conjugate Reflection via Degenerate Four-Wave Mixing at 10.6 μm (B. J. Feldman, R. A. Fisher, T. Bigio, E. E. Bergmann*)

The theoretical analysis of phase-conjugate reflection via four-wave mixing has been discussed

by several authors.¹⁻⁴ In the simplified theory, a pair of oppositely propagating (pump) waves at the same frequency ω , in a material exhibiting a nonlinear index of refraction, provide the conditions for which a third (probe) wave, also at frequency ω , causes a fourth wave to be emitted from the sample that precisely retraces the \mathbf{k} -vector of the third wave. The probe wave may be incident on the sample from any direction, because phase-matching is guaranteed in this degenerate case independently of the angle between $\bar{\mathbf{k}}_3$ and the pump waves $\bar{\mathbf{k}}_1$ and $\bar{\mathbf{k}}_2$. Using the formalism of Ref. 1 for $E_3, E_4 \ll E_1, E_2$ and in the absence of absorption,

$$E_4 = E_3^* (\tan \kappa l) . \quad (\text{III-1})$$

In Eq. (III-1), κ is the strength of the nonlinear mixing process [$\kappa = (2\pi/\lambda_0) n_2 E_1 E_2$] and l is the geometric interaction length. Note that the wave E_4 is proportional to the complex conjugate of E_3 ; this is the essential feature of the phase-conjugation effect. It was recognized very early⁵ that an initially undistorted beam passing through a phase-distorting optical system can be reflected by such a phase-conjugating "mirror" to return through the imperfect system and emerge distortion-free.

Degenerate four-wave mixing can occur in any material possessing a nonzero χ^3 . Bespalov and Talanov, and also Chiao, Kelley, and Garnire first

*On leave from Lehigh University.

discussed⁶ the near-forward degenerate four-wave mixing problem (then called elastic light-by-light scattering), and Carman, Chiao, and Kelley⁷ subsequently demonstrated the effect in liquid CS₂.

Our experimental interest in infrared phase conjugation was motivated by the attractive possibility of improving the operation of large CO₂ laser systems for laser fusion experiments and other applications. The optical quality requirements and, hence, the cost of components in a large CO₂ laser fusion system could be reduced significantly by operating in a double-pass phase-conjugation mode. If the laser fusion target were illuminated diffusely, the scattered light could travel backwards through the amplifier chain, be reflected by a conjugating four-wave mixing medium, return through the imperfect optical elements, and impinge directly on the target. Such a procedure would have the double advantages of automatically compensating for small beam-target misalignments and of illuminating the target with a relatively distortion-free beam. Such a phase-conjugation mirror will undoubtedly find other applications, such as providing stable laser operation in a gain medium experiencing time-varying inhomogeneities,⁸ and helping to diagnose laser-plasma interactions.

Numerous demonstrations of extracavity, visible-wavelength phase-conjugate reflection via degenerate four-wave mixing have appeared recently.⁹ These experiments have used beams from frequency-doubled YAG lasers, from dye lasers, from ruby lasers, and from cw argon-ion lasers. Four-wave mixing media have included liquid CS₂, resonant, near-resonant, and two-photon-resonant absorbing sodium vapor, and ruby crystal. In addition, nondegenerate phase conjugation has been observed in the visible using stimulated Brillouin scattering in both liquid CS₂^{5,10} and in gaseous methane,⁵ and using stimulated Raman scattering¹¹ in liquid CS₂.

We generated a phase-conjugate, 10.6- μ m reflection by means of four-wave mixing using counterpropagating waves in a germanium sample located within an oscillating TEA double-discharge CO₂ laser cavity. This was the first demonstration of nonlinear phase conjugation in the infrared.

We used a hybrid low-pressure/high-pressure TEA CO₂ laser¹² operating on the P(20) line with an output intensity of 2 MW/cm² in a temporally smooth pulse of 50-ns FWHM duration. The output beam diameter was 0.4 cm. As depicted in Fig. III-1, the

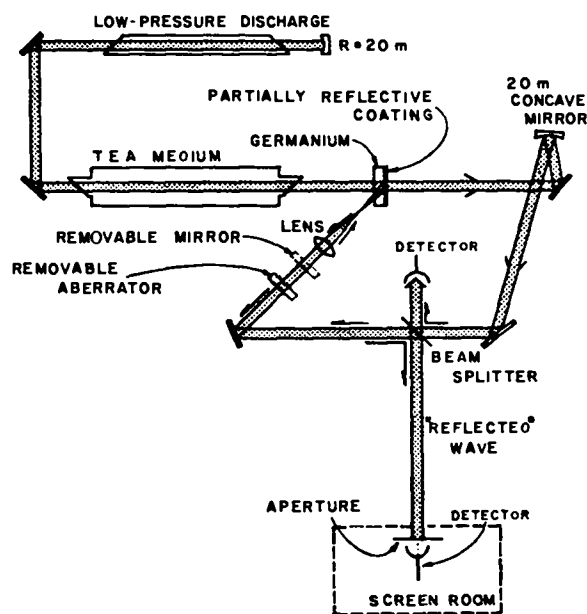


Fig. III-1.

Experimental arrangement. A low-pressure/high-pressure hybrid CO₂ laser is employed in a conventional cavity configuration with the exception that the germanium output coupler is "turned around" so that the germanium is within the optical cavity. The output from the laser is redirected through the inner surface of the germanium overlapping the "active" region in the sample. The internal angle of overlap is $\sim 10^\circ$. It is within this region of overlap in the germanium that phase-conjugate reflection occurs.

slightly wedged, intrinsic, polycrystalline germanium flat output mirror ($R = 95\%$) was reversed so that both the antireflection-coated surface and the 0.5-cm-thick germanium substrate were internal to the optical cavity. The substrate of the germanium output coupler therefore served as the nonlinear medium. This simple intracavity technique eliminated the difficulty of precisely aligning a pair of counterpropagating beams in the nonlinear sample.

Germanium was chosen for our experiment because it was readily available and has¹⁸ an exceptionally large third-order susceptibility of order 1.5×10^{-10} esu. The laser output was then routed by mirrors through a 50% ZnSe beam splitter to impinge upon the "active" region of the germanium

output coupler. A ZnSe lens ($f = 14$ cm) was placed at a distance $3/2 f$ in front of the germanium; this lens improved the overlap by partially concentrating the probe beam on the active region. The phase-conjugate beam was then redirected by the beam splitter along the rest of a 6-m-long path and then through an adjustable aperture into a high-speed HgCdTe detector for diagnostics. A removable, flat, 100% reflective mirror could be placed in front of the lens and accurately aligned* to provide a reference reflection for comparison with the backscattered signals.

The peak power of the phase-conjugated beam passing through the 6-mm-diam aperture corresponded to a reflectivity of 2%, in approximate agreement with theoretical predictions. The simple scattering through the same aperture (measured with only the low-power, low-pressure section of the hybrid laser operating) was less than 2×10^{-6} of the power measured with the reference mirror in place. Appropriate beam-blocking tests were performed to distinguish the signal from other sources of scattering. The usual test for phase conjugation, in which a severely aberrating element is placed in the probe beam line, had little effect on the intensity of the conjugate signal, whereas the same aberrator in front of the reference mirror reduced the reflected signal by more than 99%.

In a second demonstration of the effect, an infrared-sensitive, pyroelectric vidicon replaced the detector and aperture in the screen room. Photographs of the video monitor are shown in Fig. III-2. To obtain sufficient sensitivity, we placed a 2.54-cm-diam (1-in.) collecting lens in front of the vidicon to focus the 10.6- μm radiation on a plane well beyond the vidicon's sensitive surface. As can be seen in Fig. III-2b, the phase-conjugate signal is quite compact and is hardly modified by the presence of the aberrator 6 m away (Fig. III-2a), whereas the aberrator has a very deleterious effect upon the signal returned by the reference mirror (Fig. III-2c). The aberrations in Fig. III-2c are probably more severe than the photograph indicates because of truncation by the finite aperture of the collecting lens.

Finally, the time behavior of the laser and phase-conjugate signals were recorded on a fast oscil-

loscope. Typical traces are shown in Fig. III-3. Both cases depicted have the same vertical and horizontal deflections. To avoid problems associated with possible detector nonlinearities, calibrated CaF_2 attenuators were placed in front of the detector to keep the electrical signals roughly equal. Figure III-3a shows the pulse returned by the reference mirror with a 100-fold attenuator in front of the detector; the FWHM duration is ~ 50 ns. Figure III-3b shows the conjugate-reflected pulse with no attenuation in front of the detector. The observed shortening of the pulse by $\sim 1/\sqrt{3}$ agrees with theoretical predictions as does the 2% reflectivity due to the nonlinear effect.

Occasionally, damage has occurred to the germanium, and therefore we are uncertain how far the conjugate-reflected efficiency could be increased by raising the circulating intensity without a corresponding reduction in pulse duration. However, by varying the voltage applied to the TEA laser, we observed that the conjugate-reflected pulse intensity increased in proportion to the cube of the intensity, with no evidence of saturation at the maximum available intracavity optical intensity of ~ 40 MW/cm². The observed efficiency may increase with longer interaction lengths.

In conclusion, we have demonstrated 2% efficient phase-conjugation via four-wave degenerate intracavity mixing of 10.6- μm light in germanium. This development is directly applicable to other laser systems in which phase distortion is a problem. In addition, because germanium and other nonresonant nonlinear materials have broadband nonlinearities, the method we have described can possibly be used simultaneously for all wavelengths in a multiline phase conjugation feature and can be especially advantageous for large, multiline CO₂ laser fusion systems.

Suppression of Target-Induced Parasitic Oscillations in Antares (J. C. Goldstein and C. J. Elliot)

Spurious laser oscillations (parasitics) often constitute a primary limitation on the output of large, high-gain laser systems. We have studied theoretically the problem of parasitics induced by the optical coupling of the fusion target to the main power amplifiers of the Antares system and have

*The mirror was optimally aligned by maximizing its influence on the low-power lasing with just the low-pressure tube operated.

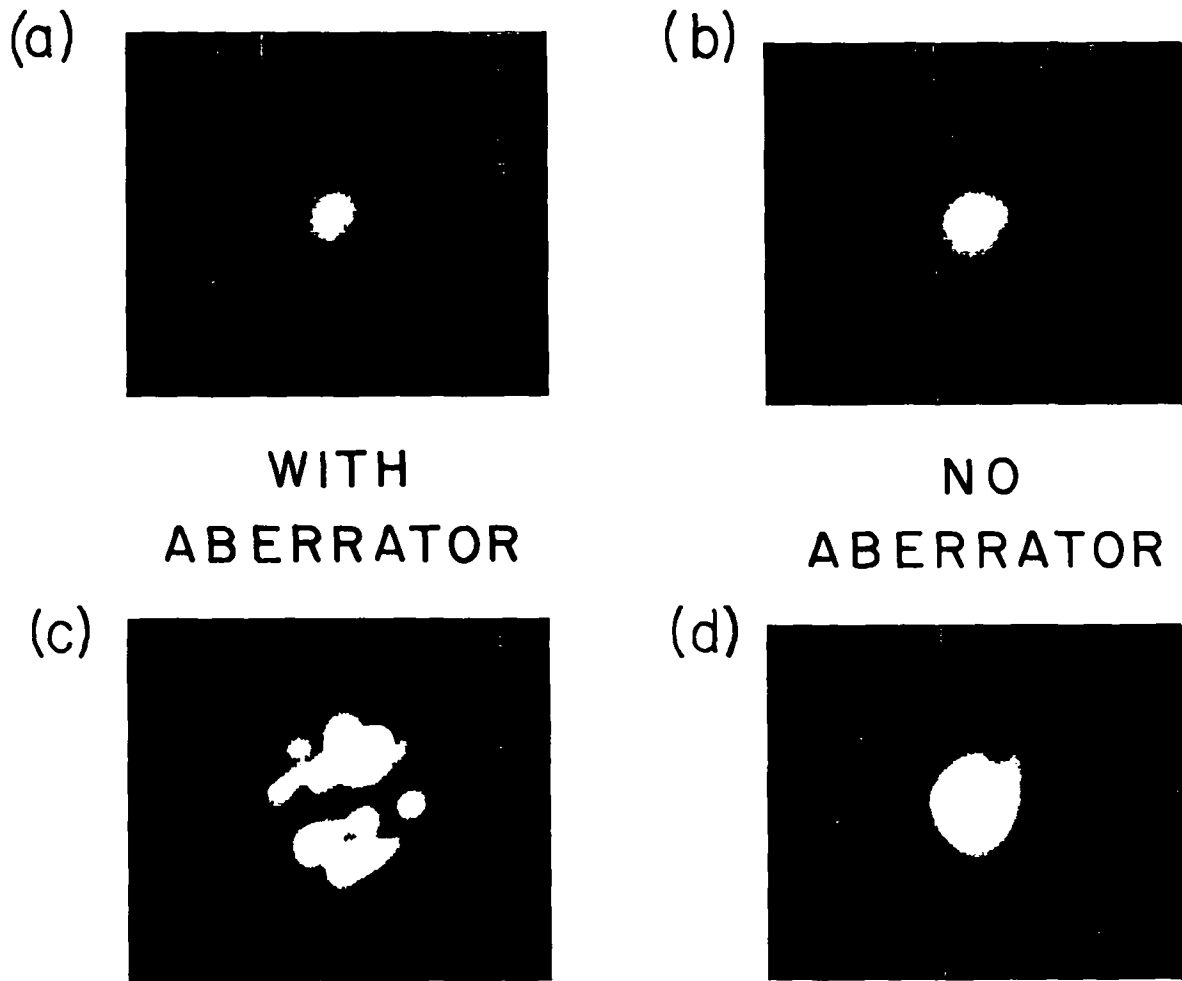


Fig. III-2.

Typical photographs of video signals taken as described in the text. (a) and (b) are the phase-conjugated signals with and without the aberrator in place, respectively. In both cases there is a 10-fold attenuator in front of the vidicon. (c) and (d) are the reference-mirror reflected signals with and without the aberrator in place, respectively. There is no attenuation in picture (c), whereas a 100-fold attenuator was used in obtaining picture (d).

found that these modes will be effectively suppressed by the combined effects of fast pumping of the amplifying media and very long amplifier—target optical pathlengths. Both of these features occur naturally in the Antares design and therefore no redesign is needed to eliminate this problem.

The particular parasitic oscillation studied occurs as a mode of an effective optical cavity formed between the spatial filter at the input end of a power amplifier and the fusion target. A finite fraction of

the spontaneous emission of the inverted medium is emitted into this mode, which has high end losses as the target and spatial filter diffusely scatter a small fraction of the light incident on them back into the mode. The losses can be overcome by the time-dependent gain of the power amplifier particularly because the optical path through this cavity traverses the amplifier twice. When this occurs, the radiation density in the mode will grow and because the light is focused onto the fusion target, the target

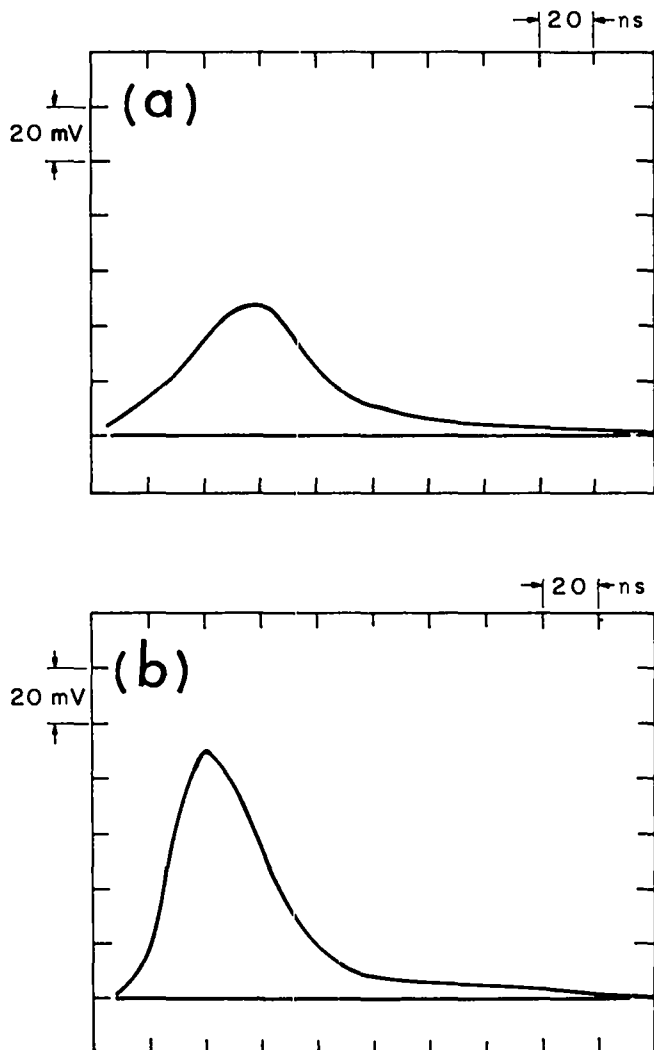


Fig. III-3.

Time history of the laser pulse and phase-conjugated pulse. In both oscillograms the vertical and horizontal deflections are the same. (a) shows the mirror-reflected reference laser pulse with a 100-fold attenuator in front of the high-speed detector. (b) shows the phase-conjugated pulse with no attenuation in front of the detector; the comparison of the two figures gives the 2% reflection efficiency. Note that the phase-conjugated pulse is shorter by approximately $1/\sqrt{3}$, in accordance with the effect having a cubic dependence.

can be damaged before the intended driver pulse reaches it. The damage threshold of glass microballoons (GMB) for nanosecond pulses from a CO_2 laser

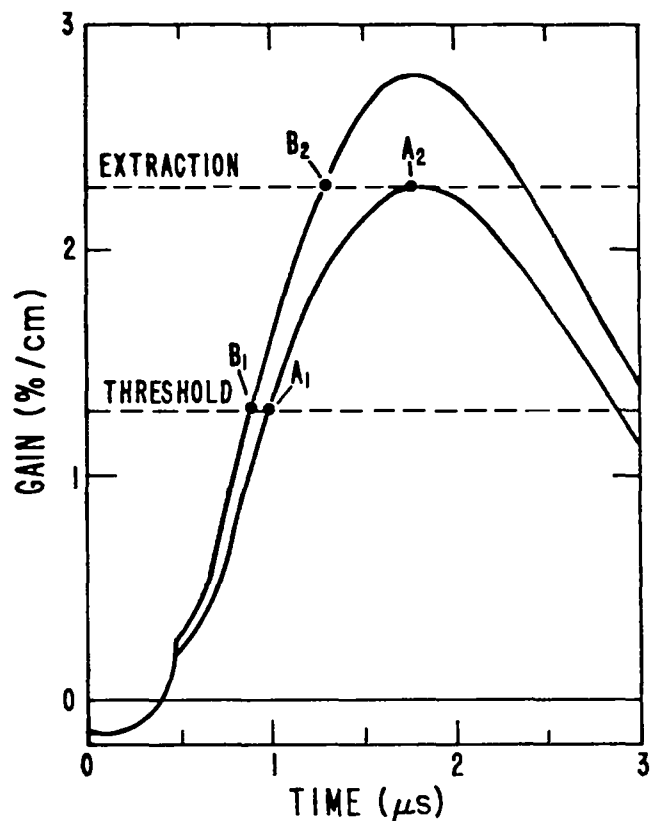


Fig. III-4.

Idealized gain curves for weak and strong pumping.

has recently been determined to be a few tenths of a joule per square centimeter.

The buildup of the radiation density in this parasitic mode was studied by means of propagation equations for forward-going (toward the target) and backward-going intensity waves. The equations were solved by three different analytical and numerical methods and all results agreed to within a factor of 2. A principal conclusion was that the time interval between threshold gain (when the amplification factor for light that makes one round trip in the cavity is unity) and the short-pulse energy extraction (when the gain corresponds to the desired energy storage in the amplifier) should be minimized. One way to accomplish this is to pump the amplifier harder, as in the upper curve of Fig. III-4. The time interval B_1-B_2 is thus made considerably shorter than the interval A_1-A_2 for the minimum pumping curve, which just reaches the desired energy storage at its peak.

Results for the maximum intensity and time-integrated absorbed energy density at the fusion target are shown in Figs. III-5 and -6. Increasingly harder pumping is reflected by increasing values of the Marx bank voltage, the abscissa in these figures. Also shown are the effects of 100-ns short-pulse injection timing errors relative to the nominal energy extraction point. These results were obtained by using gain curves calculated with the relevant amplifier electrical parameters; they include the multiline nature of the laser transitions in CO₂ as well as the finite spectral bandwidths of those transitions. Conservative values of all parameters were assumed so as to overestimate the parasitics' growth.

Small variations in the amplitude of the gain can affect the energy absorbed by the target as much as timing errors. If the short pulse is injected into the amplifier at exactly the correct time but the gain coefficient is 5% higher than expected throughout the pumping process, the target will absorb 10 times

more energy from the parasitics. Thus, jitter in both the pulse injection time and the gain amplitude must be minimized to achieve maximum operational reliability.

These calculations will be updated as more refined performance information on the power amplifiers is determined. The current results, however, indicate that this particular parasitic oscillation mode should not be troublesome in the Antares machine.

Six-Tube Low-Pressure cw CO₂ Oscillator (R. Carman, N. Clabo, F. Wittman, H. Lane)

A six-tube, low-pressure, cw CO₂ oscillator was constructed to demonstrate the feasibility of replacing TEA CO₂ oscillators as the pulse generators for driving our large power amplifier systems.¹⁴ This somewhat complex oscillator can generate an output

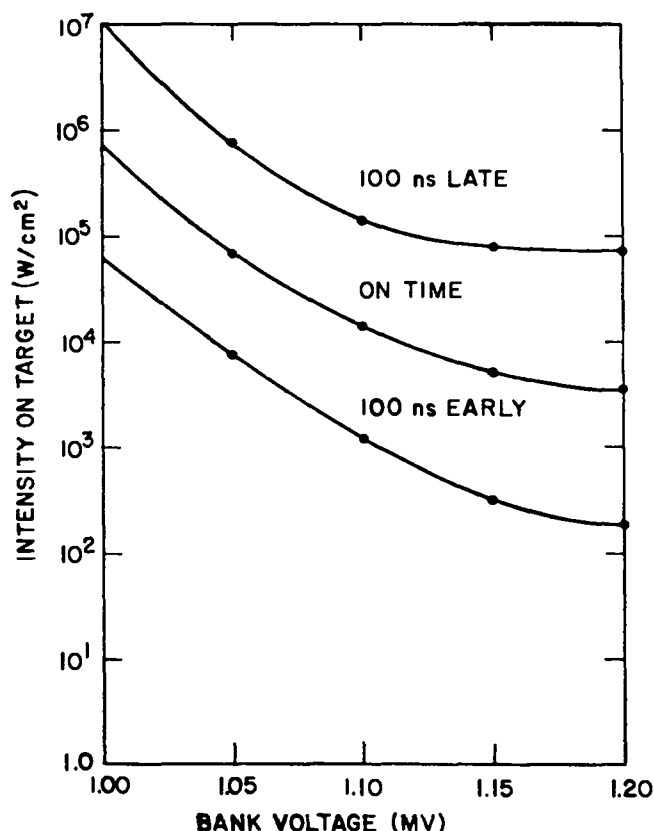


Fig. III-5.

Maximum parasitics intensity on target in Antares vs Marx bank voltage for three different timings.

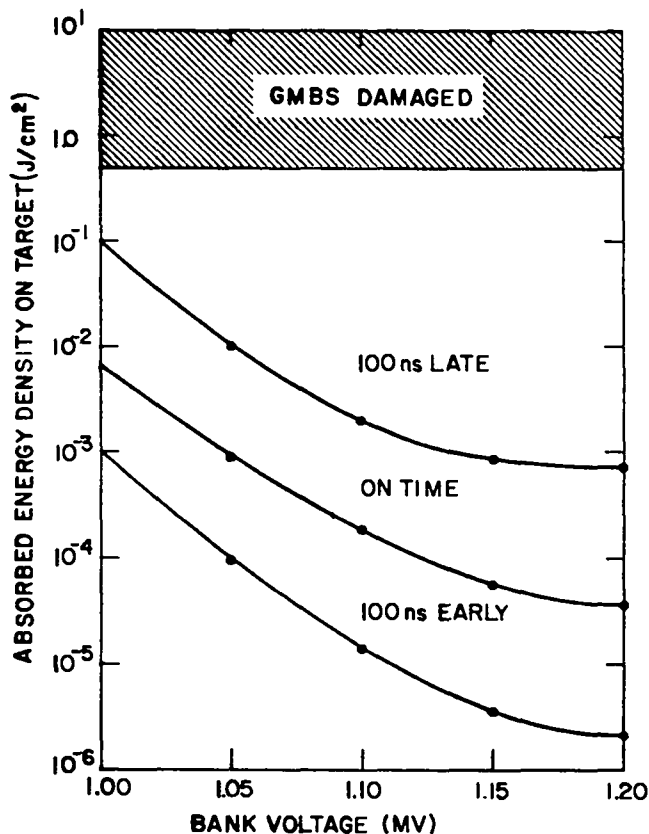


Fig. III-6.

Maximum parasitics energy density on target in Antares vs Marx bank voltage for three different timings.

consisting of six lines of any amplitude ratio for any of 72 lines in the P- and R-branches of the 9- and 10- μ m bands. The oscillator has operated under both pulsed and cw conditions. Pulsed, each tube produced several kilowatts with the optimum mix of 1:1:1::He:N₂:CO₂; risetime, ~60 ns and falltime, ~120 ns; or it produced 4 to 8 W cw in the TEM₀₀ mode for all 72 lines. As a result of temporal spiking in the output, much above pulsed threshold, and because of the requirement for synchronization of the outputs of the six tubes in the pulsed mode, both of which lead to undesirable amplitude uncertainties, we concentrated on cw operation only. By using the 1:1:1 mix without active feedback stabilization, we obtained the cw performance summarized in Table III-I. Changing the mix recently to 4:2:1:0.4::He:N₂:CO₂:Xe, almost doubled these cw results. Long-term (two months) angular alignment stability

provided by the Invar structure, shown in Fig. III-7, was sufficient to hold the oscillator output constant to better than 5%. Manual cavity length adjustments via piezoelectric translators (PZT) coupled to the output mirrors indicated only a short-term stability of 10% over about one hour. We are installing an active feedback system that will not only guarantee long-term stability of the output, but will also allow initial line-amplitude ratios to be selected and maintained automatically. Only the initial setup of the desired six line frequencies will remain manual (grating angular adjustment).

The feedback stabilization will be accomplished by first chopping the six outputs and detecting them with gold-doped germanium detectors. Liquid-nitrogen cooling is supplied by two dewars, each containing four detectors. The logic of the feedback

TABLE III-I

cw POWER OUTPUT OBTAINED WITH A 1:1:1::Ne:N₂:CO₂
USING 22.5-mA CURRENT AND ~400 K BALLAST RESISTORS*

P Branch	cw Power Output (W/torr)		R Branch	cw Power Output (W/torr)	
	9- μ m Band	10- μ m Band		9- μ m Band	10- μ m Band
P6	0.7/5.2 and 3.6	2.8/8.7 and 5.0	R4	---	1.5/8.7 and 5.0
P8	2.3/5.2 and 3.6	3.0/8.7 and 5.0	R6	1.6/6.2 and 3.9	3.3/8.7 and 5.0
P10	3.4/5.2 and 3.6	5.7/8.7 and 5.0	R8	3.2/6.2 and 3.9	4.6/8.7 and 5.0
P12	5.3/5.2 and 3.6	6.1/8.7 and 5.0	R10	4.2/6.2 and 3.9	5.1/8.7 and 5.0
P14	5.4/5.2 and 3.6	6.3/8.7 and 5.0	R12	2.7/6.2 and 3.9	5.5/8.7 and 5.0
P16	6.0/5.2 and 3.6	6.3/8.7 and 5.0	R14	3.5/6.2 and 3.9	5.6/8.7 and 5.0
P18	6.0/5.2 and 3.6	6.1/8.7 and 5.0	R16	2.6/6.2 and 3.9	5.8/8.7 and 5.0
P20	6.2/5.2 and 3.6	6.7/8.7 and 5.0	R18	3.5/6.2 and 3.9	5.9/8.7 and 5.0
P22	5.9/5.2 and 3.6	6.6/8.7 and 5.0	R20	5.0/6.2 and 3.9	6.3/8.7 and 5.0
P24	6.0/7.0 and 4.2	6.4/8.7 and 5.0	R22	5.7/6.2 and 3.9	6.1/8.7 and 5.0
P26	5.4/7.2 and 4.3	6.2/8.7 and 5.0	R24	5.2/6.2 and 3.9	6.2/9.0 and 5.1
P28	4.1/7.2 and 4.3	6.0/8.7 and 5.0	R26	5.2/6.2 and 3.9	6.0/9.0 and 5.1
P30	5.1/7.2 and 4.3	5.6/8.7 and 5.0	R28	4.2/6.2 and 3.9	5.6/9.0 and 5.1
P32	4.0/7.2 and 4.3	5.0/8.7 and 5.0	R30	1.5/6.2 and 3.9	5.1/9.0 and 5.1
P34	2.9/7.2 and 4.3	3.4/8.7 and 5.0	R32	1.6/6.2 and 3.9	4.3/8.0 and 4.5
P36	2.9/7.2 and 4.3	4.2/8.7 and 5.0	R34	1.9/6.2 and 3.9	3.7/8.0 and 4.5
P38	2.0/7.2 and 4.3	3.6/8.7 and 5.0	R36	0.2/4.6 and 3.6	3.0/8.0 and 4.5
P40	1.2/6.2 and 3.9	2.5/8.7 and 5.0	R38	---	1.9/8.0 and 4.5
P41	0.5/6.2 and 3.9	---	R40	---	0.6/6.8 and 4.0

*Much work was done on the 1:1:1 mix because we originally expected to use the system in the pulsed mode; cw operation was anticipated only for alignment purposes. The pressures listed are the input and output gauge readings.

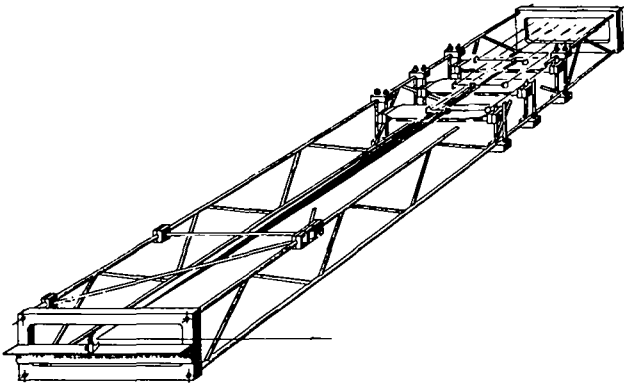


Fig. III-7.

Invar structure providing stability for six-tube oscillator.

system is as follows. One of the six tubes is arbitrarily chosen as the reference. Its output is stabilized by stabilizing its frequency to correspond to line center, by displacing the front mirror with an ac PZT drive signal, and detecting the zero-crossing of the derivative of the laser detector output signal. A calibrated power meter then adjusts the total pressure in the tube to obtain the desired output power. The remaining five tubes are then stabilized in output power by using the PZT signal to adjust their cavity lengths so as to obtain the correct output ratio with respect to that of the reference tube. The chopped detector signals are then properly attenuated, so that all are equalized for the proper output amplitude ratios. To avoid running any oscillator at a cavity length far off optimum, both total pressure and CaF_2 attenuators at the output will be used for coarse adjustment.

The grating beam-combining optics and an Invar-stabilized mounting structure were designed and are in the final fabrication stages. Some details are shown in Fig. III-8. We evaluated the losses in such a beam-combining system, and found that more than 90% of the incident cw power survives the grating beam-combining optics.

The single six-line beam was then directed through a GaAs Pockels cell of 5-mm-square cross section. Transport optics were required and were crudely set up. An electronics package for driving the Pockels cell was assembled, which, in essence, is a 5- to 10-kV square-wave generator of adjustable pulse width from 50 to 200 ns. This generator was constructed with krytrons.

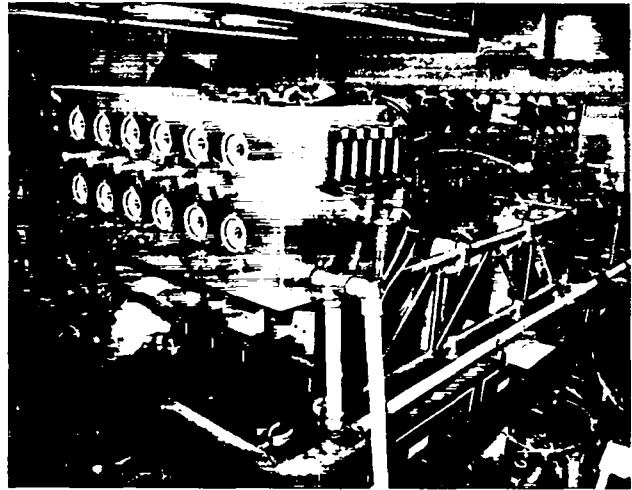


Fig. III-8.

Details of grating beam-combining optics and Invar-stabilized mounting structure.

We plan to amplify the six-line output further, after pulse-clipping, in a 15-torr, 2-m-long amplifier. We set up a double-pass optics system and successfully measured the quality of the transmitted beam and the losses of unamplified transmission. The original TEM_{00} mode of the oscillator output was maintained through the entire front end, and more than 30% of the total six-line output was transmitted. This transmission could be further improved by antireflection-coating four lenses in the transport optics.

Initial tests of the electrical characteristics of the low-pressure 2-m amplifier demonstrated a design flaw. Whereas a wealth of data was obtained on similar 1-m amplifiers consisting of two anodes and one cathode (two 50-cm discharges), the extension to a 2-m system with four anodes and two cathodes in one envelope led to electrical problems in reproducibly igniting the two central 50-cm regions. We are modifying this amplifier by inserting a Brewster-angle NaCl window between the separated 1-m tubes, and hope to obtain the previous performances. Gain coefficients of 2.7 to 3%/cm were obtained previously for the P-20 line at $10\ \mu\text{m}$.

Once fully operational, we will amplify this front-end output with two $> 1\text{-atm}$ TEA amplifiers. This attempt will first involve five passes through an 80-cm-long system with a rectangular cross section of 4.5 by 1.5 cm. A four-stage Pockels cell pulse clipper

operating at ≤ 1 ns, two spatial filters, two germanium saturable absorbers, and a plasma shutter will be incorporated between passes. The final 3.5-cm-square cross-section amplifier of ~ 1.4 -m length will then be double-passed to obtain the final output of nominally 1 J.

Gain-uniformity measurements on both TEA media were made by using amplification of a cw driver and by using them to make an oscillator. Whereas the smaller TEA medium was completely acceptable as supplied, the tighter tolerances on gain uniformity combined with the much larger volume of the larger TEA medium dictated substantial changes. We further desired the ability to operate at total pressures to ≥ 1200 torr. By incorporating a 120-kV Marx-bank into this unit instead of using the standard 45-kV bank supplied, we were able to achieve gain uniformities of better than 5% over $\sim 90\%$ of the pumped area. These conditions are well within our requirement to obtain a 1-J nominal beam that can be focused to a spot size of ≤ 25 μm .

Because the total length of our system from oscillator to final output beam is 47 m (154 ft) and because our pointing accuracy must be much better than that of our larger lasers, successful operation of the total system will allow us to establish the alignment stability of our low-pressure front end and beam-combining optics as it might apply to Helios or Antares.

Multipulse Energy Extraction With CO₂-Laser Amplifiers (H. C. Volkin and E. E. Stark)

General. Multiple-pulse energy extraction in CO₂-laser amplifier systems was studied to determine the laser efficiencies and pulse properties obtainable with this type of operation. In multipulse energy extraction, a sequence of two or more optical pulses is sent through the amplifier during the time interval between the start of successive electrical discharges. The effect of gas mix, starting temperature, and timing of the optical pulses (with respect to the discharge) on efficiency and output pulse energies were determined by calculations with a discharge kinetics computer program. After energy extraction by a pulse, the population inversion of the laser transition is depleted, but very fast collisional equilibration of the resulting energy within the vibrational modes involved occurs. Thereafter,

vibrational energy transfers in the gas are followed by the kinetics code until the arrival of the next optical pulse.

In general, multipulse extraction permits efficiencies significantly higher than the maximum attainable with single-pulse operation. When a short optical pulse ($\lesssim 1$ ns) propagates through the amplifier, energy residing in the vibrational excitation of the nitrogen molecules and in the levels of the CO₂ asymmetric-stretch A-mode above the first excited level is not available for extraction because the time scale for vibrational relaxation (intermode and intermolecular) is much larger than the pulse duration. The optimum amount of this unavailable stored energy can be extracted by the next optical pulse at approximately a vibrational relaxation time (~ 0.3 μs at 1800 torr in a 3:1:1::He:N₂:CO₂ mix) following the previous energy extraction, in which time vibrational energy transfers will have restored the inversion on the lasing transition by repopulating the upper level and depopulating the lower level.

Parameter Studies. The following He:N₂:CO₂ gas mixtures were considered: 0:1:4, 3:0.25:1, 3:1:1, and 3:2:1. For each mix the E/N value in the discharge was chosen to maximize the fraction of total power deposited in the gas that goes into direct excitation of the A-mode and the N₂ vibration. The required vibrational excitation rates are calculated for a given gas mix and value of E/N from the electron velocity distribution $f(\vec{v})$ that occurs under these conditions. The function $f(\vec{v})$ is governed by the electron collision processes in the discharge and is obtained by numerical solution of the Boltzmann transport equation.

A set of calculations was performed to compare multipulse efficiencies for various gas mixes. In all cases the starting pressure and temperature were 1800 torr and 300 K, respectively, and the discharge current was 20 A/cm². After the initial optical pulse, the time interval between successive pulses was the same (usually 0.25 μs), and it was assumed that each optical pulse extracted all the available inversion energy in the gas at the time of the pulse. In general, we found that the relatively high efficiencies for a given mix occurred over a rather broad plateau in the parameter space of discharge duration and pulse timing. This extra freedom can be used to select the timing sequence so as to obtain other desired properties, such as equalized pulse energies. Typical high

TABLE III-II

HIGH MULTIPULSE
EFFICIENCIES FOR THE
VARIOUS MIXES WITH A
DISCHARGE DURATION OF 0.5 μ s

He:N ₂ :CO ₂ Mix	Electrical-to-Optical Efficiency (%)	
	Multipulse	Single Pulse
0:1:4	15	5.7
3:1/4:1	19	6.2
3:1:1	22	5.0
3:2:1	20	3.5

values of multipulse efficiency for each mix in the case of 0.5- μ s discharge duration are given in Table III-II. Also included in Table III-II are the maximum single-pulse efficiencies, which are obtained by energy extraction with a single pulse at the time of peak gain (generally, somewhat after the end of the 0.5- μ s discharge). Because the 3:1:1 mix gave the highest efficiency under the prescribed conditions, this mix was used in the subsequent calculations.

Table III-III shows pulse energies and efficiencies for the 3:1:1 mix with a sequence of nine pulses

timed as indicated. The efficiency shown at each pulse time is the net electrical-to-optical energy-conversion efficiency in terms of total energy deposited in the gas and extracted by all pulses up to that particular time. The duration of the discharge was 0.5 μ s, and the discharge field and current density were 13 000 V/cm and 20 A/cm², respectively, for a total energy deposition of 130 J/l. After lengthening the discharge duration, it became a relatively simple matter to find a timing of the pulses that produced about equal energies for the first N-pulses in the sequence. In general, as N increases the discharge time tends to become longer. As an example, with a 1- to 2- μ s discharge that deposited the same 130 J/l in the 3:1:1 mix, the first four pulses could be made approximately equal. The performance for the entire nine-pulse sequence is summarized in Table III-IV. Starting at 0.71 μ s into the discharge and using an interpulse time of 0.164 μ s, the first four pulses are essentially equalized and by themselves deliver an efficiency of 12.3%. A pulse sequence adapted to a 2- μ s discharge at 130 J/l gave five equal pulses that by themselves had an efficiency of 14.2%, as shown in Table III-V.

Higher efficiency is obtained by lowering the starting temperature of the gas, because the rate coefficients for vibrational energy transfer are more favorable at lower temperatures. Table III-VI gives

TABLE III-III

NINE-PULSE EXTRACTION EFFICIENCIES
FOR THE 3:1:1 MIX WITH THE
INDICATED PULSE TIMING
(0.5- μ s DISCHARGE AT 130 J/l)

Pulse Time (μ s)	Pulse Energy (J/l)	Efficiency (%)
0.4	4.89	4.71
0.65	5.55	8.04
0.9	4.67	11.6
1.15	3.81	14.6
1.4	3.06	16.9
1.65	2.43	18.8
1.9	1.91	20.3
2.15	1.49	21.4
2.4	1.16	22.3

TABLE III-IV

NINE-PULSE EXTRACTION FOR THE
3:1:1 MIX WITH PULSES TIMED TO
EQUALIZE THE FIRST FOUR PULSE
ENERGIES (1.2- μ s DISCHARGE AT 130 J/l)

Pulse Time (μ s)	Pulse Energy (J/l)	Efficiency (%)
0.71	3.96	5.16
0.874	3.91	8.32
1.038	4.00	10.6
1.202	4.11	12.3
1.366	3.58	15.0
1.530	2.97	17.3
1.694	2.43	19.2
1.858	1.97	20.7
2.022	1.59	21.9

TABLE III-V

NINE-PULSE EXTRACTION WITH PULSES TIMED TO EQUALIZE PULSE ENERGIES (2- μ s DISCHARGE AT 130 J/l)

<u>Pulse Time (ns)</u>	<u>Pulse Energy (J/l)</u>	<u>Efficiency (%)</u>
1.1	3.74	5.24
1.325	3.64	8.53
1.55	3.65	11.0
1.775	3.67	12.8
2.00	3.69	14.2
2.225	3.11	16.6
2.45	2.50	18.5
2.675	1.99	20.0
2.5	1.56	21.2

TABLE III-VI

NINE-PULSE EXTRACTION WITH SAME PULSE TIMING AS IN TABLE III-II BUT STARTING AT 200 K INSTEAD OF 300 K (0.5- μ s DISCHARGE AT 130 J/l)

<u>Pulse Time (ns)</u>	<u>Pulse Energy (J/l)</u>	<u>Efficiency (%)</u>
0.4	5.86	5.65
0.65	6.09	9.21
0.9	4.93	13.0
1.16	4.01	16.1
1.4	3.25	18.6
1.65	2.61	20.6
1.9	2.07	22.2
2.15	1.63	23.5
2.4	1.26	24.4

an illustrative example, in which the 3:1:1 mix is initially at 200 K and 1800 torr, the 0.5- μ s discharge (19 500 V/cm and 13.333 A/cm²) deposits 130 J/l, and the pulse timing is the same as in Table III-III. A nine-pulse efficiency of 24.4% is obtained, compared to 22.3% with a starting temperature of 300 K.

Demonstration of Multiple-Pulse Extraction Efficiency.

General. A theoretical study was carried out to evaluate the feasibility of demonstrating multiple-pulse energy extraction efficiency on the TBS or Helios. To make the calculations sufficiently realistic, this procedure was followed.

- Electric-discharge data from Helios were used in the discharge kinetics calculations. Both a medium discharge (peak $g_0 L = 5.3$) and a high discharge (peak $g_0 L = 5.9$) were considered.
- A previously developed model of the TBS was used in the pulse-propagation calculations. The model accurately describes the TBS¹⁶ and therefore approximates Helios closely enough for the purposes of this study.
- In all cases the input pulse was chosen to be Gaussian, with the following characteristics: a pulse width of 0.8 ns FWHM and equal energy on four lines P(20, 18, 16, 22) of the 10.6- μ m band.
- When a pulse enters the amplifier system, the energy extracted is calculated by the pulse-propagation code using the value of gain prevailing at that time as given by the kinetics code. After passage of the pulse, the kinetics code resumes describing the energy-transfer and excitation conditions in the gas starting from the conditions that exist immediately after energy extraction. Hence, when the next pulse arrives, the amplifier gain is known at that time.
- Energy extraction is timed during the discharge so that the gain never exceeds 2.75% cm⁻¹; therefore, amplifier operation does not require saturable absorbers to suppress parasitic oscillations.

Discharge and Energy Extraction Characteristics. With a rectangular pulse of 6315 V/cm and 7.5 A/cm² for 3.8 μ s, maximum gain (in the absence of pulse input) occurs at 3.23 μ s, and has the value of 3.44% cm⁻¹. At the end of the discharge the gain was 3.37. The gain value 2.78 is reached at 1.75 μ s.

The available energy and the percentage of energy extracted in the TBS as a function of gain for pulses whose total energy is 50, 150, and 600 mJ are shown in Fig. III-9. In the region to the right of the dashed

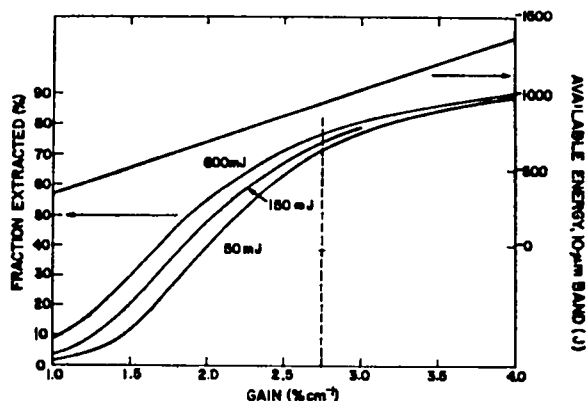


Fig. III-9.

Shown as a function of amplifier gain in the Two-Beam-System model are (1) the available inversion energy and (2) the fraction of available energy extracted by a 0.8-ns, four-line P(20, 18, 16, 22) pulse for input energies 50, 150, and 600 mJ.

vertical line at $g_0 = 2.75\% \text{ cm}^{-1}$, the results are hypothetical because the calculations do not include the effects of the gain isolators required in this region. However, the main features of energy extraction with the triple-pass optics are revealed. At large gain values, the percentage of energy extracted (PEA) increases relatively slowly with gain and the input-pulse energy above 50 mJ is relatively unimportant. For gains below $2.5\% \text{ cm}^{-1}$, the PEA falls off rapidly with decreasing gain and the input pulse energy becomes relatively more important.

The maximum gain of $2.75\% \text{ cm}^{-1}$ is reached on the first pulse, and the gain is less for all subsequent pulses. Clearly, the main goal in any multiple-pulse scheme is to maintain a reasonably high gain value for as many pulses as possible after the first one. Hence, multiple-pulse extraction efficiency requires as high a discharge as the system can produce. All results given here are based on high discharge data.

Single-Pulse Efficiency. Our calculations refer to an average element volume in the gain region and to discharge electric power delivered to the gain region. Losses due to other factors, e.g., geometric use of the gain volume and pulse-forming networks, are not included. To establish the relative improvement in multiple-pulse efficiency, we compared our

multiple-pulse results with the calculated single-pulse efficiency. A single pulse at $3.2 \mu\text{s}$, $g_0 = 3.44$, that extracts 85% of the available energy has an optical-to-electrical energy-conversion efficiency of 3.2%. The result is relatively insensitive to gain value and pulse energy in the high-gain region, as can be seen from Fig. III-9. However, the value of 3.2% is artificially high, because the effects of the required saturable absorbers are not included.

Two-Pulse Efficiency. No impressive improvement in efficiency is obtained with two pulses. Even with two 600-mJ pulses, the first entering at $1.7 \mu\text{s}$, $g_0 = 2.75$ with PEA = 76.5%, and the second occurring $1.89 \mu\text{s}$ later when the gain has peaked to 3.20 and the PEA is 83%, the efficiency is only 5.33%. If the second pulse occurred only 100 to 150 ns later, no improvement in efficiency over a single pulse would be shown, because at that time the gain has only recovered to 2.2.

Multiple-Pulse Efficiency. Two cases of multiple-pulse efficiency were considered.

- A four-pulse series was calculated in the following sequence: the first pulse at $1.75 \mu\text{s}$, $g_0 = 2.78$, PEA = 72%, with subsequent pulses timed to enter when the gain has recovered to the value of 2.7. The results are summarized in Table III-VII, where the efficiency at each time is calculated in terms of total electrical energy deposited and the optical energy extracted up to that time. The final four-pulse efficiency is 8%.
- Series of 12 pulses with equal interpulse intervals ($0.25 \mu\text{s}$) were calculated for 50- and 600-mJ pulses. The first nine pulses occurred during the

TABLE III-VII

FOUR-PULSE ENERGY
EXTRACTION TIMED FOR GAIN
VALUE $2.7\% \text{ cm}^{-1}$ AT EACH PULSE TIME

Time (μs)	Gain ($\% \text{ cm}^{-1}$)	Efficiency (%)
1.75	2.78	4.30
2.25	2.70	6.72
2.91	2.70	7.93
3.91	2.67	8.06

TABLE III-VIII

**TWELVE-PULSE ENERGY EXTRACTION WITH
CONSTANT TIME INTERVAL (0.25 s) BETWEEN PULSES**

<u>Time (μs)</u>	<u>Gain (% cm^{-1})</u>	<u>PEA (%)</u>	<u>Eff (%)</u>	<u>Gain (% cm^{-1})</u>	<u>PEA (%)</u>	<u>Eff (%)</u>
1.75	2.78	72.0	4.3	2.78	77	4.6
2.00	2.43	60.0	6.6	2.39	68.5	7.2
2.25	2.30	55.0	8.0	2.21	63.0	8.8
2.50	2.21	51.0	9.0	2.10	59.0	9.9
2.75	2.14	47.5	9.7	2.02	56.0	10.7
3.00	2.10	45.0	10.2	1.95	53.0	11.2
3.25	2.05	42.5	10.6	1.90	51.0	11.6
3.50	2.02	41.0	10.8	1.85	48.8	11.9
3.75	1.97	39.5	11.0	1.81	46.7	12.1
4.00	1.70	22.0	11.5	1.53	32.0	12.7
4.25	1.50	12.0	11.7	1.31	20.5	13.0
4.50	1.35	7.0	11.8	1.15	13.8	13.2

discharge and the later pulses occurred during the "coasting" period following the discharge. Results are summarized in Table III-VIII. Again, all efficiencies refer to energy deposited up to the time indicated. Efficiencies up to 13% were obtained, corresponding to a fourfold improvement over single-pulse efficiency.

SOLID STATE PHYSICS

Introduction

A specific alkali halide window material (KCl) with a KReO_4 saturable, substitutional dopant was characterized for CO_2 laser isolator applications. Saturation intensity was measured at two temperatures, and the saturation process was found to obey a homogeneously broadened, two-level model over a wide range of CO_2 laser intensities. This behavior was explained by correlating measurements of excited state absorption with a phenomenological model for the anharmonicity of the dopant molecule in its lattice site.

The $\text{KCl}:\text{ReO}_4^-$ saturable absorber was used to provide passive mode-locking of a CO_2 laser, and to provide free-induction-decay (FID) short-pulse generation at the 10- μm P(26) wavelength.

New Saturable Absorber for the CO_2 Laser Using Doped KCl (R. K. Ahrenkiel, J. F. Figueira, C. R. Phipps, D. J. Dunlavy, S. J. Thomas, A. J. Sievers*)

General. A nonlinear saturable absorber for 10.6 μm has a variety of applications in CO_2 laser technology. For high-power short-pulse systems, efficient amplifier isolation devices are a continuing need. Other applications such as pulse compression and passive modelocking also depend upon developing better saturable materials. In CO_2 laser fusion systems, a nonlinear absorber with a subnanosecond recovery time would be useful in suppressing retroreflected pulses from the fusion target if the material could also tolerate high optical intensities (of order 1 GW/cm^2) which are present at the interface between the laser system and the target chamber. P-type germanium has been shown to be a very useful material for many of these applications.¹⁹ Its disadvantage is an optical damage threshold that is inadequate for the laser target interface application.^{17,18} Also because of visible opacity, system

*Laboratory of Atomic and Solid State Physics and Materials Science Center, Cornell University, Ithaca, New York.

alignment with a visible wavelength laser is not possible.

There are a number of advantages to doping alkali halides with a saturable impurity. The damage thresholds of the alkali halides are among the largest known in the ir.¹⁸ The alkali halides are transparent to visible light so that red beam alignment can be used. And finally, the salts are commonly used as CO₂ laser windows so that the isolation element could be easily incorporated into existing systems.

Saturation Spectroscopy. The perrhenate ion ReO₄⁻ substitutes for the halogen anion in many alkali halides. The ν₃ absorption of the vibrational mode of the ReO₄⁻ is ir-active in the 10-μm-wavelength range.¹⁹ Saturation of this internal vibrational mode in KI and KBr containing ReO₄⁻ ions has been observed recently.²⁰

Czochralski-grown crystals* of KCl were doped with KReO₄ producing ReO₄⁻ concentrations of about 10¹⁶ atoms/cm³ as determined by neutron activation analysis. Absorption spectra of these crystals were taken with a CO₂ laser spectrometer at 300 and 105 K, as shown in Fig. III-10. The solid curves are Lorentzian lineshape-fits to the data. Best fits were obtained with a linewidth of 0.33 cm⁻¹ at 105 K. At 300 K, the linewidth increases to 0.93 cm⁻¹ and the peak of the band shifts slightly to the low-energy side of P(28). Near liquid-helium temperatures, the band has moved between P(24) and P(26) and no absorption is observable on either line. At room temperature, the absorption cross section α_p/N is 7.9 × 10⁻¹⁷ cm², where α_p is the peak absorption coefficient and N is the ionic concentration per cm³.

The room temperature saturation of a 5.5-cm-long crystal is shown in Fig. III-11. The pulsed CO₂ intensity was varied by means of calibrated CaF₂ attenuators. The beam had a Gaussian profile in space and time with a FWHM of ~1.8 ns. Curve A in Fig. III-11 evolves from a computer routine that calculates the total transmission of a space-time Gaussian pulse based on a homogeneously broadened two-level model²¹ for the nonlinear material. The steady-state approximation²² implied by the model (T₁ << τ) is justified in our case.

*These crystals were grown at the Cornell University Materials Science Center Crystal Growing Facility.

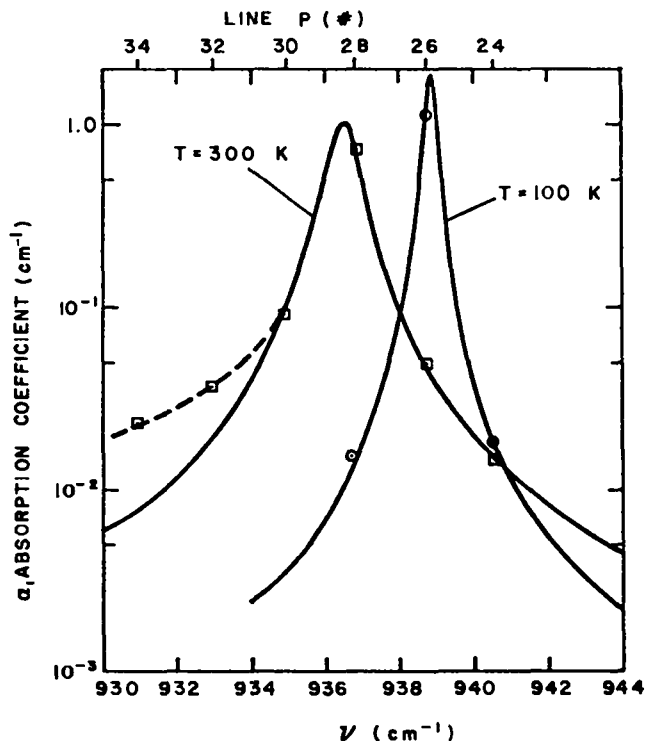


Fig. III-10.

Small-signal absorption of KCl crystal doped with ReO₄⁻ ions.

T₁ is the relaxation time for the upper level as deduced from our measurements of saturation flux I_s and cross section σ. Here T₁ is always much less than the laser pulse duration τ. The relaxation time T₁ is determined from the expression

$$T_1 = h\nu/\sigma(1 + g_0/g_1) I_s, \quad (\text{III-2})$$

where hν is the photon energy in joules and g₀ and g₁ are the degeneracy of the ground and excited states, respectively (here g₀ = 1 and g₁ = 3). The homogeneous two-level model shown in Curve A, Fig. III-11, is an excellent fit to the experimental data over three decades of intensity, and yields a saturation intensity I_s = 1.45 MW/cm² at 300 K. Using this I_s value, Eq. (III-2) gives T₁ = 122 ps at 300 K, which is consistent with the steady-state assumption. The small-signal absorption indicated by the computer fit is α₀ = 0.71 cm⁻¹, which compares well with the measured value of 0.75 cm⁻¹.

On the other hand, the data could not be fit with an inhomogeneous model (Fig. III-11). We conclude

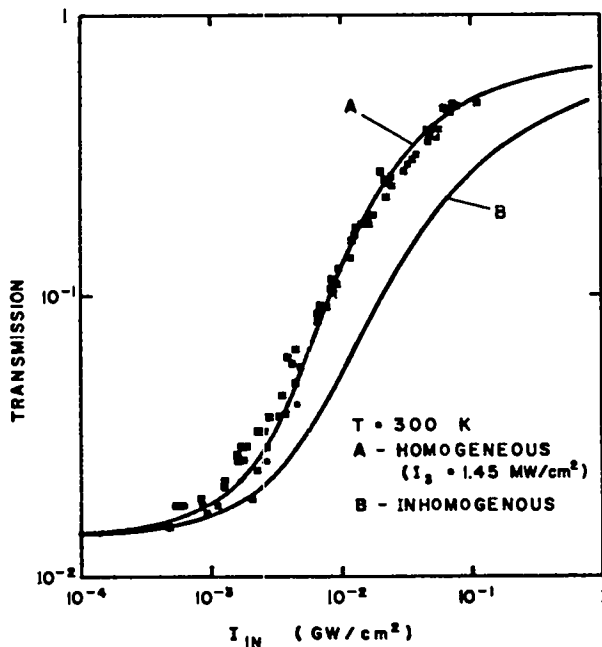


Fig. III-11.

Transmission of a doped crystal at room temperature vs peak laser input power at the 10- μ m P(28) wavelength. Curve A is a fit to the data using homogeneous model. Curve B uses an inhomogeneous model.

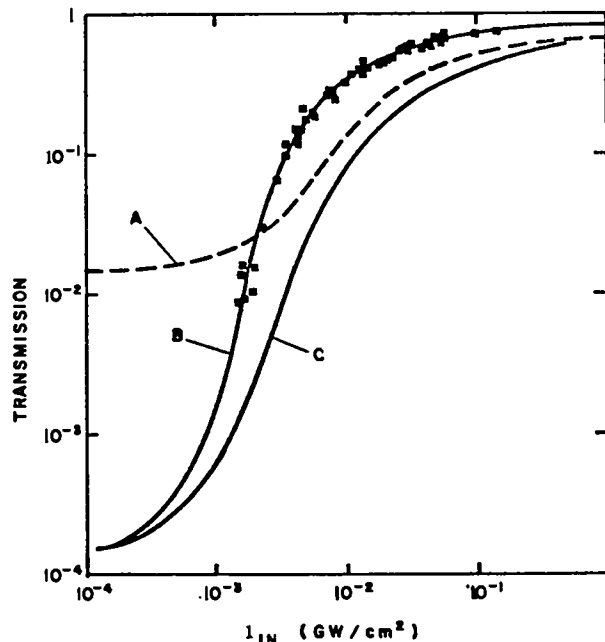


Fig. III-12.

Transmission of a doped crystal at 105 K vs peak laser input power. Curve A is identical to Curve A of Fig. III-11. Curve B uses a homogeneous fit to the data. Curve C uses an inhomogeneous model.

that the broadening is homogeneous at 300 K and is caused by the coupling of the molecular ion to the lattice phonons.

The saturation behavior of the same crystal at 105 K is shown in Fig. III-12. Using the computer routine, we again obtain a good fit to the data using a homogeneous broadening mechanism and a steady-state two-level model as shown in Curve B. The saturation intensity is reduced by a factor of 6.9 and the saturation parameter produced by the fit is $I_s = 0.21$ MW/cm². Using Eq. (III-2), the relaxation time T_1 is found to be 320 ps at 105 K. The steady-state approximation is marginally valid here with $T_1/\tau \approx 0.18$. Curve C is the best attempt at fitting an inhomogeneous model to the data and Curve A is the room-temperature curve of Fig. III-11 for comparison.

As a homogeneous model describes the saturation at both 105 and 300 K, the dominant broadening interaction is related to phonon interactions at both temperatures. The ratio $T_1(300\text{ K})/T_1(105\text{ K})$ is inversely proportional to the ratio of transverse-optical

phonon densities at these temperatures. However, the relaxation process must involve the emission of several lattice phonons and such processes can be very complex.²⁸

Transient Spectroscopy. To measure T_1 directly, a double-resonance or transient spectroscopy configuration was employed. A high-power pulsed CO₂ beam operating at P(26) was propagated coaxially with a low-power cw probe beam. Changes in the sample transmission, when irradiated with the high-power beam, were then determined by monitoring the cw beam with a Santa Barbara Ge:Hg detector. The time resolution of the detection system was about ± 0.5 ns. The resolution was limited by jitter in the mode-locked pulse width and by the time response of the Ge:Hg detector. For pump (pulsed source) isolation, the pump and probe beams were cross-polarized. Here the transient bleaching at P(26) was easily observed.

The decay time of the bleaching was less than could be resolved by our instrumentation. Hence, by

direct measurement, T_1 is less than about 0.5 ns at 300 and 105 K. These results are consistent with the values of T_1 calculated from the fit to the saturation data.

By tuning the probe laser to adjacent CO_2 lines, we find the transient absorption spectrum shown in Fig. III-13. Here the sample temperature is about 100 K. The probe transmission under pulse illumination may be written

$$T = (1 - R)^2 e^{-(\alpha_0 + \Delta\alpha)t}, \quad (\text{III-3})$$

where $(1 - R)^2$ is the reflection loss of the two surfaces, α_0 is the small-signal absorption, and t is the sample thickness. Here $\Delta\alpha$ is the average change in absorption coefficient through the length of the crystal which is produced by the pump beam. At P(26), we see that $\Delta\alpha \cong -\alpha_0$ as the sample is completely

saturated for this power level. At P(30) a new absorption band is observed. This absorption is tentatively identified to be that of the ν_3 ($n = 1$) to ν_3 ($n = 2$) vibrational state, whereas the small-signal absorption arises from ν_3 ($n = 0$) to ν_3 ($n = 1$) vibrational states.

Free molecules display some anharmonicity for higher excitation states as the molecular potential is nonparabolic for large-amplitude vibrations. The anharmonicity produces a frequency shift and if this shift is greater than the absorption bandwidth, there can be efficient bleaching of the fundamental absorption. If the anharmonic shift is less than the power-broadened absorption bandwidth, then excited-state absorption can occur and the observed saturation will deviate from the two-level model of Figs. III-11 and -12. For constant absorption bandwidth $\Delta\nu^0$, we have a criterion for multilevel saturation, namely

$$\Delta\nu^0 \ll \Delta\nu_{\text{ah}}^{n+1,n}. \quad (\text{III-4})$$

In Eq. (III-4), $\Delta\nu_{\text{ah}}^{n+1,n}$ is the anharmonic shift in the resonance between the n and $n + 1$ vibrational levels. With an energy spacing $E_{n+1} - E_n$ between the $n + 1$ and n vibronic levels, this criterion becomes

$$h \Delta\nu_{\text{ah}}^{n+1,n} = (E_{n+1} - E_n) - (E_1 - E_0). \quad (\text{III-5})$$

As seen in Fig. III-13 for the ν_3 band in KCl:ReO_4^- there is a shift of about 4 cm^{-1} between ν_3^0 and ν_3^1 . This shift is greater than the bandwidth $\Delta\nu_3^0$, which is about 0.3 cm^{-1} at 105 K. The inequality in Eq. (III-4) is satisfied for the $n = 0$ to $n = 1$ transition and therefore the ReO_4^- ion behaves like an ideal two-level system in saturation.

The source of this high degree of anharmonicity may be related to the interaction of the ReO_4^- complex with the polar lattice. The molecule in the ground state is compact and interacts very slightly with the host lattice as seen by the narrow linewidth. The free-ion absorption¹⁹ is 918 cm^{-1} and the peak in KCl is only slightly shifted to 937 cm^{-1} . Because the excited molecule has a larger molecular diameter, the excited state interacts strongly with the host ions. Interaction with the host ions could produce the red shift that is observed in Fig. III-13 where ν_3^1 is completely shifted out of coincidence with ν_3^0 .

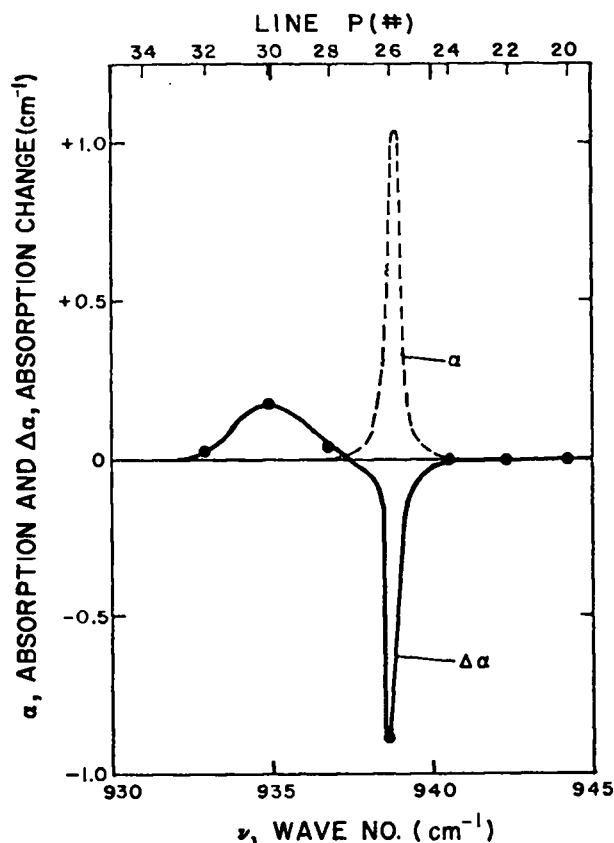


Fig. III-13.

Induced absorption $\Delta\alpha$ in KCl:ReO_4^- at 105 K with P(26) excitation. The small-signal absorption α_0 is also shown for comparison.

Conclusion. We have shown that it is possible to construct a homogeneously broadened solid-state saturable absorber based on a KCl host matrix. For the KCl:ReO_4^- system described in this paper, saturation parameters of 1.45 MW/cm^2 and recovery times of 120 ps were measured at room temperature.

Further work will be concerned with ways to enhance the crystal-induced anharmonic interaction so that absorption bands with broader widths can be considered for saturable absorption schemes in multiline CO_2 lasers. Also, attempts are being made to shift the absorption peak closer to the P(20) CO_2 line by means of other molecular impurities and other alkali halide host materials.

Passive Mode-Locking of a TEA CO_2 Oscillator Using Doped KCl (R. K. Ahrenkiel, J. F. Figueira, D. J. Dunlavy)

The nonlinear or saturable absorption of KCl doped with ReO_4^- has been described. Because this is a homogeneous absorber, the onset of absorption is fairly abrupt compared to an inhomogeneous absorber like p-type germanium.¹⁶ Therefore, this material should be useful for passive mode-locking²⁴⁻²⁶ on CO_2 lines that are absorbed by the material.

Initial attempts to obtain lasing in a stabilized TEA oscillator were unsuccessful, even when the cavity was tuned to P(20). The latter line is near the peak of the gain curve and the P(20) wavelength is not absorbed by the perrhenate (ReO_4^-) ion.

The KCl:ReO_4^- crystals as grown were found to contain extensive strain fields when viewed under crossed polarizers with visible light. A number of annealing experiments were carried out to remove these strains. Ultimately, significant strain reduction was obtained by taking the crystal to 1000 K (40 K below the melting point) and cooling over a period of 4 h. A segment of this crystal was placed in the laser cavity and lasing was achieved at P(20) although the beam profile showed a residual strain pattern and the output intensity was reduced by about a factor of 5.

Upon tuning to P(28) (the peak of the perrhenate ion absorption), several weak pulses were observed in the output detector that had a period of 18 ns, corresponding to the round-trip transit time of the laser cavity. The crystal was successively cleaved to find an optimum thickness. Upon cleaving the crystal to

about 4-mm thickness, corresponding to small-signal transmission of 80%, definite mode-locked behavior was observed.

In Figs. III-14a and -14b, the laser output of two successive shots are shown with the KCl crystal removed from the cavity. These waveforms are characteristic of self-mode-locking in CO_2 lasers. Figure III-14c shows the laser output with the KCl:ReO_4^- crystal in the cavity. These pulses are definitely phase-locked by the saturable absorber in the cavity, and have a period $2 t_0 = 18 \text{ ns}$. The number of pulses in the train varied from about 8 to 10 depending on the energy of the particular shot.

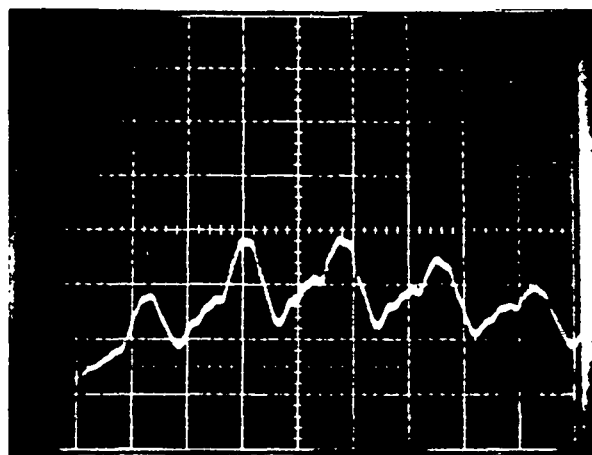
The observed pulse width in Fig. III-14c is about 10 ns. However, because the combined risetime of the Tektronix 7844 oscilloscope and pyroelectric detector employed is about 2 ns, the actual pulse width is somewhat shorter. Further improvements in the quality of the doped KCl should result in higher output and shorter pulses as the cavity gain is increased.

Generation of Ultrashort CO_2 Pulses by Free-Induction Decay in Doped KCl (R. K. Ahrenkiel, D. J. Dunlavy, A. J. Sievers)

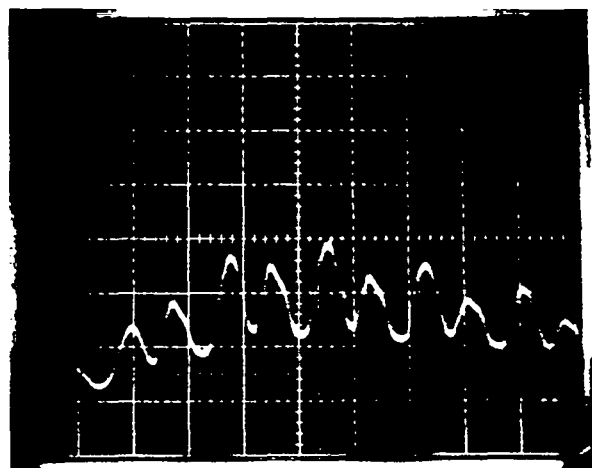
The generation of short CO_2 pulses by optical free-induction decay has been described.²⁷ In previously reported experiments, a laser-induced spark produced an abrupt termination of a longer pulse, and hot CO_2 was used as a resonant absorber in which sidebands produced by the pulse termination are transmitted and produce a short pulse of approximate duration $T_2/\alpha_0 L$. Here T_2 is the homogeneous lifetime, α_0 is the absorption coefficient, and L is the absorber path length.

In gases such as CO_2 , T_2 is dominated by molecular collisions and is adjustable by changing pressure and temperature. For a molecular impurity incorporated in a solid, T_2 is usually related to a lattice phonon collisional process and is, therefore, related to the crystal temperature. These collisional times are commonly much faster than the collision times of comparable molecular concentrations in a gas. Therefore, a pulse of shorter duration will be generated in the solid solution than in the gaseous system of comparable molecular concentration.

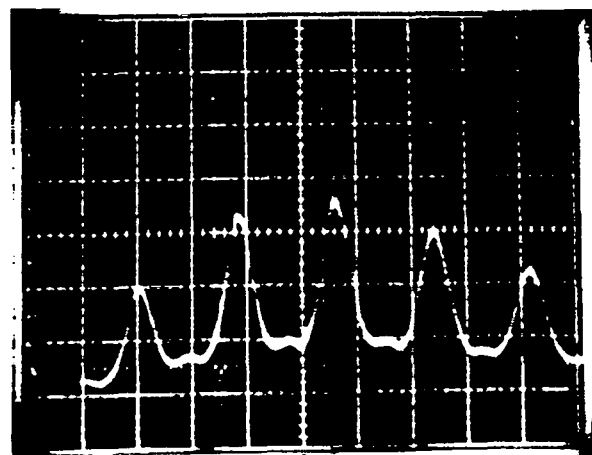
The linear and nonlinear optical properties of the substitutional impurity ReO_4^- in KCl has been



(a)



(b)



(c)

described recently.²⁸ At liquid nitrogen temperatures, the FWHM of the ir-active ν_3 vibrational mode is about 0.33 cm^{-1} and the transition is homogeneously broadened as determined by saturation spectroscopy. Therefore, the homogeneous relaxation time T_2 of the transition is about 32 ps. The absorption coefficient of our sample at P(26) is 1.06 cm^{-1} and the sample length is 4.27 cm. For infinitely rapid termination of the input laser signal, the FID pulse could be as short as 7.1 ps. The material should be an excellent resonant absorber as the peak of the absorption coincides almost exactly with the $10\text{-}\mu\text{m}$ P(26) CO_2 laser line.

The experimental setup for generating FID pulses from this material is similar to that described by Yablonovitch.²⁹ In the latter experiment, the pulse termination time was determined to be about 30 ps by measuring the transient sideband spectrum with a double monochromator. Therefore, the input pulse termination time is apt to be the limiting factor in achieving short FID pulses with this material.

Figure III-15a, upper trace, shows the input pulse after passing through the breakdown cell and spatial filter. This pulse is recorded on a Ge:Cu photoconductive detector with a risetime of about 2 ns. The output is displayed on a Tektronix 7844 oscilloscope with a time scale of 20 ns/per division. Figure III-15a, lower trace, shows the transmitted or FID pulse that is coincident with the laser termination. Figure III-15b shows the FID pulse on a 5-ns-per-division time scale. The displayed width is ~ 2 ns and is identical essentially to the response time of the detector-oscilloscope combination to the pulse termination, so that the actual pulse width is much less than the response time of our detection system. The displayed FID pulse amplitude is therefore reduced relative to the actual amplitude by a factor given approximately by the ratio of the FID pulsewidth to

Fig. III-14.

(a, b) Oscilloscope trace of laser output on two successive shots with KCl crystal removed from the cavity; (c) oscilloscope trace of laser output with KCl crystal installed. The sweep speed for all pictures is 10 ns per division.

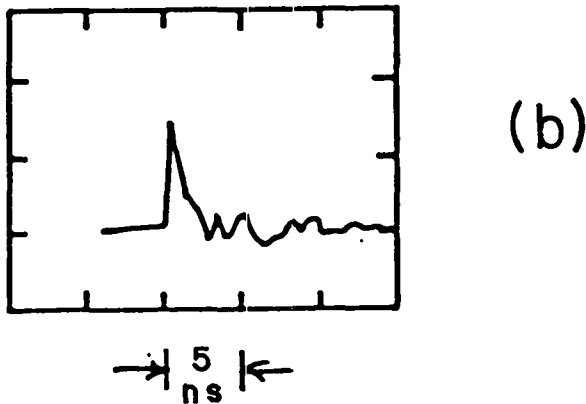
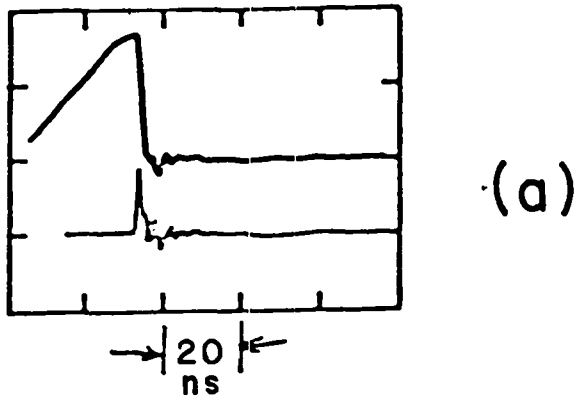


Fig. III-15.

(a) (upper trace) signal produced by breakdown cell, 20 ns per division; (lower trace) FID signal trace at 20 ns per division; (b) lower trace in (a) displayed at 5 ns per division.

the detection system response time, 0.015. A further, physical amplitude reduction is expected due to a finite spark termination time that is larger than the characteristic time $T_2/\alpha_0 L$ of the absorber. The magnitude of this factor is not well known, because the exact functional form of the breakdown spectrum would be required to determine what part of the spectrum is passed and what part is blocked by the KCl:ReO_4^- absorber. However, the observed FID amplitude $P_{\text{FID}} \cong 0.01 P_{\text{IN}}$ is not inconsistent with our expectations, based on the preceding estimates.

The discovery of a faster breakdown system used in combination with a KCl:ReO_4 crystal would efficiently produce CO_2 pulses of several picoseconds duration with crystals of about 10-cm length. This method of short-pulse production has the capability of producing shorter pulses than previously described techniques.

GAS ISOLATOR DEVELOPMENT (S. J. Czuchlewski, A. V. Nowak, E. Foley)

Introduction

Research on gas isolators concentrated on determining the rate at which the gases return to their normal absorbing state after optical saturation by an intense laser pulse. Definition of the gas isolator requirements of the Antares front end was begun, and a series of experiments to study the performance of plasma-breakdown shutters as they pertain to the Antares power amplifiers was outlined.

Studies were continued to gain a comprehensive understanding of the multiphoton absorption characteristics of SF_6 , which is vital to the use of this gas as a saturable absorber to prevent self-lasing in CO_2 laser systems. Our efforts may lead to a device preventing retroreflections from the target and are also important for other DOE programs, e.g., laser isotope separation.

Saturable Absorber Recovery (A. V. Nowak)

Introduction. Gaseous saturable absorbers have become an essential component of the TPAs of our Helios laser system. They will also be an integral part of the Antares CO_2 laser system. Without them, the maximum gain to which the amplifiers can be pumped is severely limited by the onset of parasitic oscillations.

We wish to know the degree and rate of recovery of the absorption capability of these saturable gases after delivery of the 1-ns pulse. The answers to these questions determine the extent to which special precautions must be taken to prevent postlasing and repulse damage. If their recovery is slow (several microseconds), then the danger of postlasing and repulse damage may be significant.

These considerations have motivated the experiments described below, in which we measure the time that the gas remains saturated after the passage of a 1-ns pulse. In these experiments the saturable absorber is SF₆ buffered by other gases.

The data we have taken to date indicate that the rate at which SF₆ relaxes to equilibrium after passage of a saturating 1-ns pulse depends not only on the collision partner but also upon the transition being monitored and the pulse energy. Note that on a 100- μ s time scale, the gas generally does not return precisely to its normal transmission level. This is attributable presumably to bulk heating of the sample, which relaxes to room temperature with a millisecond time constant.

In all the experiments described below, the 1-ns pumping pulse was tuned to the CO₂ 10- μ m P(20) line and had a Gaussian cross section with a 1/e-diameter of 9.5 mm. The gas was irradiated with pulses in the energy range of 1 to 360 mJ. The weak monitor beam that probed the region excited by the 1-ns pulse was about 4 mm in diameter and traveled in the same direction as the pulse, making a 5° angle with it. The saturable absorber was contained in a 10-cm glass cell with NaCl windows, in the center of which the two beams crossed. The power of the monitor beam was sufficiently low⁴⁹ that it did not disturb significantly the level populations in the SF₆. A monochromator was used to reduce the amount of scattered light from the pulse that could enter the detector. The monitor beam was detected with an unbiased, photovoltaic liquid-nitrogen-cooled HgCdTe detector (SAT). The signal was amplified by a Tektronix 1A-1 preamplifier and displayed on a Tektronix 7844 or 7903 oscilloscope. The bandwidth of the detector-oscilloscope combination was 10 MHz. Care was taken to operate in the linear region of the detector.

Relaxation in an SF₆-Ar Mix. We studied the simple gas mix consisting of 0.150 torr of SF₆ in 100 torr of argon. Pure SF₆ relaxes on a millisecond time scale, which is beyond the range of practical interest. Therefore, a noble gas was chosen as a buffer because it simplifies analysis of the relaxation process to one of vibrational-to-translational energy transfer. The following double-resonance results were observed.

10- μ m P(20) Saturator, 10- μ m P(16) Probe. The gas mixture became abruptly more transparent upon passage of the 1-ns pulse (Fig. III-16a). The sample transparency then continued to increase for \sim 500 ns, undoubtedly due to intermolecular and/or intramolecular processes which serve to redistribute the excitation energy. The transient increase in the transmission eventually decayed to the prepulse level as a simple exponential with a decay constant τ of 6.65 μ s. Interestingly, the decay constants were found to be linear functions of the input pulse energy, as shown in Fig. III-17. In this case τ decreased as the pulse energy increased at a rate of -0.12μ s per 100 mJ.

10- μ m P(20) Saturator, 10- μ m P(24) Probe.

Pulse energies > 35 mJ. As above, the gas first became more transparent upon passage of the pulse but then began losing this transparency, and next became more opaque than before transmission of the 1-ns pulse (Fig. III-16b). The time for this reversal was about 0.5 to 1 μ s. The transient opacity finally decayed to the prepulse transmission level via a simple exponential, with a 6.85- μ s decay constant, approximately equal to that observed at P(16). We again observed that higher energy pulses caused a decrease in τ , in this case at the rate of -0.07μ s per 100 mJ (Fig. III-17).

Pulse energies < 35 mJ. In contrast to the above cases, the sample first became more opaque upon passage of the 1-ns pulse, and finally returned to the prepulse transmission level as in the higher energy case (Fig. III-16c).

10- μ m P(20) Saturator, 10- μ m P(20) Probe. The gas became more transparent upon passage of the pulse, followed by a decay to the prepulse transmission level with the following features (Fig. III-16d):

- The decay is not a simple exponential. On a semilogarithmic plot it is "concave down," suggesting that the relaxation speeds up as the gas approaches equilibrium.
- The overall relaxation time increased with increasing pulse energy, just the opposite of the behavior observed when monitoring at P(16) or P(24) (Fig. III-17).

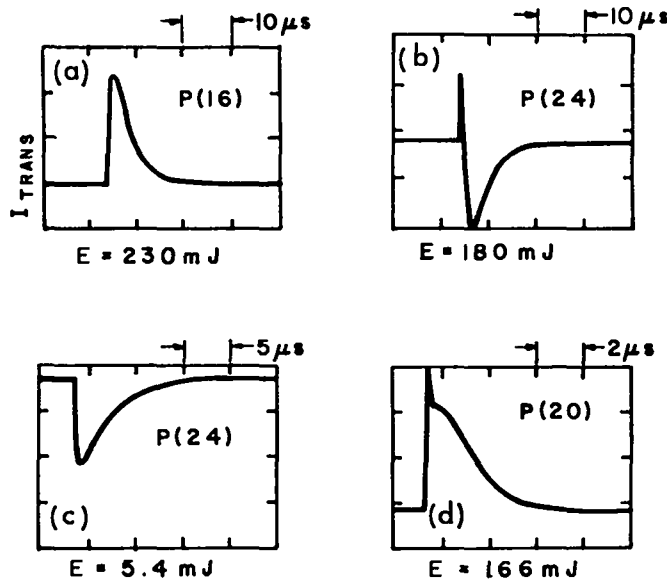


Fig. III-16.

Transmission vs time of cw monitor beam during double resonance experiment in $SF_6:Ar$ mixture with partial pressures of 0.15 and 100 torr, respectively. Pump pulse is at $10\text{-}\mu\text{s}$ P(20). The identity of the monitor line, input-pulse energy, and sweep speed are indicated. The large signal occurring during the first $0.5\ \mu\text{s}$ of (d) results from the detector being temporarily saturated by scattered P(20) pump light.

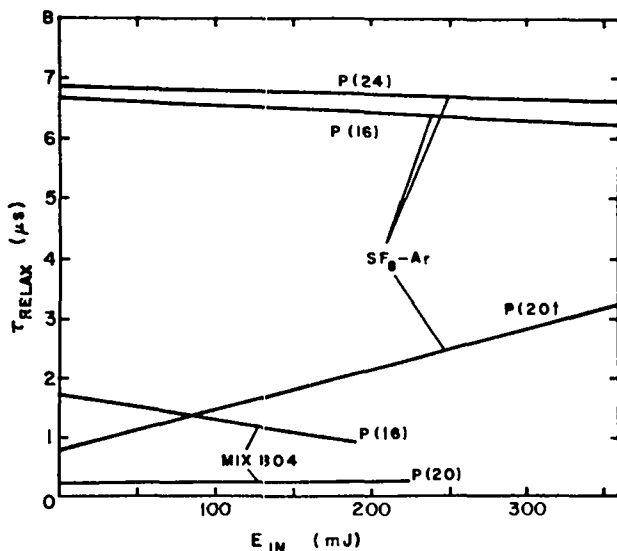


Fig. III-17.

Dependence of the recovery time on incident pulse energy for an $SF_6:Ar$ mix with partial pressures of 0.15 and 100 torr, respectively, and for Mix 804 at 10 torr.

- The decay was significantly faster than that observed at P(16) or P(24). After excitation by a 3-mJ pulse, the "decay constant" was about $1\ \mu\text{s}$ and lengthened to $2.5\ \mu\text{s}$ for a 250-mJ pulse. The ratio of time constants at the 2 wavelengths, extrapolated to zero energy, is

$$\tau [P(16), E = 0] / \tau [P(20), E = 0] \approx 6.5$$

Relaxation in Mix-804.⁸⁰ Results in Mix 804 were similar to those observed in the $SF_6:Ar$ case; however, relaxation times were shorter. Studies were made at 7.5 and 10.0 torr, which correspond to SF_6 partial pressure of 0.11 and 0.15 torr, respectively. The latter is the same SF_6 pressure as used in the $SF_6:Ar$ studies.

$10\text{-}\mu\text{s}$ P(20) Saturator, $10\text{-}\mu\text{s}$ P(16) Probe.

Upon passage of the 1-ns pulse, a sudden increase in the transparency was observed. The risetime of this signal was limited to the risetime of the detector system (35 ns). The transmission decayed to the prepulse level by a simple exponential (Fig. III-18a).

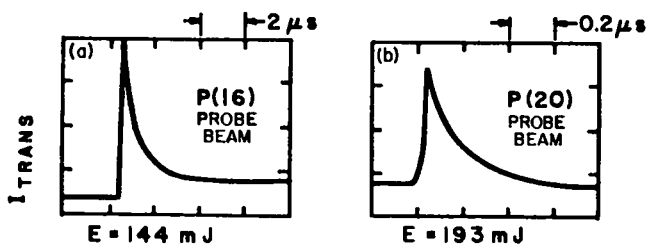


Fig. III-18.

Transmission vs time of cw monitor beam during double-resonance experiment in Mix 804 at 10 torr. Pump pulse is at 10- μm P(20). The identity of the monitor line, input-pulse energy and sweep speed are indicated. In (b) approximately the first 150 ns of the pulse represents the detector recovering from scattered pump light and is not a true transmission signal.

The decay constant (extrapolated to zero pulse energy) was 2.24 μs at 10.0 torr. As with the SF_6 :Ar mix, higher energy pulses were followed by a faster return to equilibrium. At 7.50 torr the decrease in τ is $-0.38 \mu\text{s}$ per 100-mJ increase in incident energy, and at 10 torr it is $-0.41 \mu\text{s}$ per 100 mJ. This is a much more pronounced effect than that observed in the SF_6 :Ar mix (Fig. III-17).

10- μm P(20) Saturator, 10- μm P(20) Probe. An increase in the transmission was observed upon passage of the pulse (Fig. III-18b). The decay of the transient transparency to the prepulse level appears to be a simple exponential, although noise problems made it impossible to establish this conclusively. The relaxation time increased with increasing pulse energy, but not as dramatically as for the SF_6 :Ar mix. In 10 torr of Mix 804, τ was 230 ns for a 10-mJ pulse and 290 ns for a 200-mJ pulse (Fig. III-17). Here, the ratio is

$$\tau [P(16), E = 0] / \tau [P(20), E = 0] \approx 7.6 .$$

This is very close to the value 6.5 observed for the SF_6 :Ar mix.

Conclusion. A catalog of preliminary experimental observations on the recovery of SF_6 after it has been saturated by an intense, short laser pulse has been presented. Clearly, this is a complicated process, and further experimental and theoretical

work will be required before this phenomenon is understood.

The recovery time observed in Mix 805 at 10 torr when both the saturating pulse and the probe beam were tuned to P(20) was 250 ns. This may be fast enough to offer protection against postlasing and repulse damage in a high-power laser, depending on the geometry of the system. However, these experiments also suggest that the relaxation of SF_6 following saturation by a multiline pulse may be quite different in character from that observed after single-line saturation.

Multiple-Photon Absorption Experiments in SF_6 (J. L. Lyman, R. A. Fisher, B. J. Feldman)

Room-Temperature Results. Unimolecular, multiple-photon energy absorption cross-sections were measured in room-temperature SF_6 . Measurements were compared for single- and multiple-longitudinal mode CO_2 laser pulses at three separate frequencies over a four-decade energy fluence range.

Previous workers³¹⁻³⁵ have measured multiple photon absorption cross sections as a function of fluence. Figure III-19 summarizes these measurements. The low-intensity cross sections cited in the figure caption are taken from Nowak and Lyman.³⁶ The multiple photon data of Deutsch³¹ and Black et al.³² were obtained by optoacoustical methods, whereas the remaining data³² were deduced from transmission measurements. Black et al.³⁴ used both a single-mode (smoothed) pulse and an ultrashort pulse generated by optical FID; all others used multimode (unsmoothed) pulses with some degree of self-modelocking. The data of Black et al. are especially noteworthy because they compared cross sections at two pulse durations and found them similar.

Our CO_2 laser was a hybrid high-pressure/low-pressure arrangement in a 2.6-m-long cavity composed of a 75% reflecting output coupler and a 100 line/mm grating in Littrow. When the high-pressure (600-torr) double discharge was operated, the output was a 150-ns-long sequence of ultrashort pulses (multiple longitudinal mode). When the low-pressure longitudinal discharge was pulsed 200 μs before the high-pressure discharge, we obtained a temporally smooth pulse (single longitudinal mode). Pulse durations and energies for both shapes

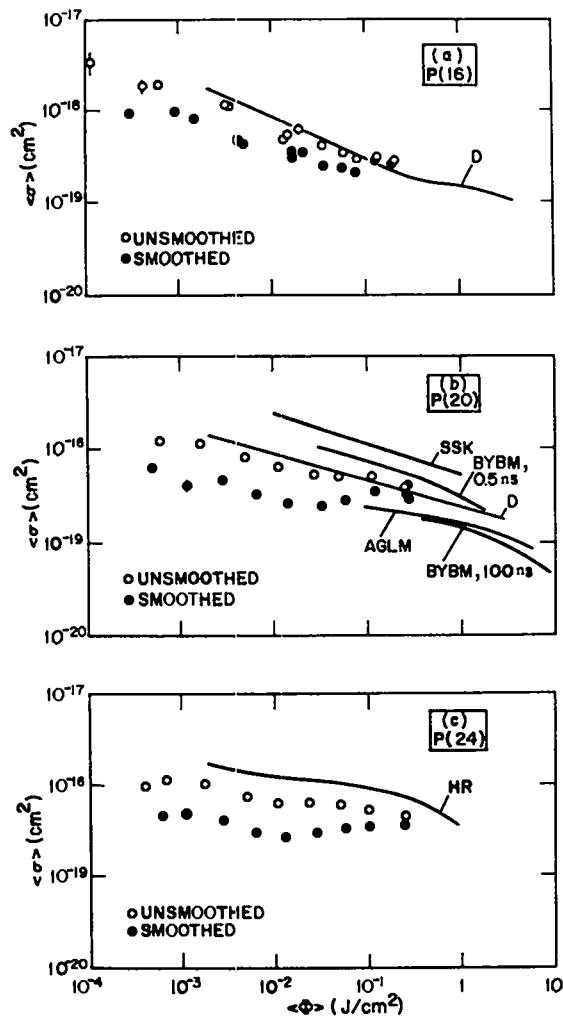


Fig. III-19. Measured absorption cross section vs energy fluence for 0.35 torr SF₆. The symbol "D" refers to Deutsch (Ref. 31), "SSK" to Stafast, Schmid, and Kompa (Ref. 33), "BYBM" to Black, Yablonovitch, Bloembergen, and Mukamel (Ref. 32), "AGIM" to Ambartzumian, Gorokhov, Letokhov, and Markarov (Ref. 34), and "HR" to Ham and Rothschild (Ref. 35). The data of Deutsch were relative and have been adjusted to agree with ours at 0.1 J/cm². (a) P(16) CO₂ laser line; the low-intensity cross section is 3.2×10^{-17} cm² and the slope of the unsmoothed data is -0.37 . (b) P(20) CO₂ laser line; the low-intensity section is 1.7×10^{-17} cm², and the slope of the unsmoothed data is -0.20 . (c) P(24) CO₂ laser line; the low-intensity cross section is 5.0×10^{-18} cm², and the slope of the unsmoothed data is -0.15 .

were comparable. The laser beam was directed through a NaCl beam splitter to generate a reference beam, and the rest was then passed through calibrated CaF₂ or polyethylene attenuators. This pulse was then transmitted through a room-temperature 1.0-m-long stainless steel absorption cell (1.27-cm diam) with AgCl windows. The beam diameter within the cell was 0.9 ± 0.1 cm. The cell was filled with 0.35 torr of SF₆ (99.8% purity) and the ratio of transmitted energy to reference beam energy was measured for each type of pulse (smoothed and unsmoothed), both with and without SF₆ in the cell. From these ratios, an effective energy absorption cross section $\langle \sigma \rangle$ was obtained,

$$\langle \sigma \rangle = -\ln(T)/\rho l, \quad (\text{III-6})$$

where T is the sample transmittance, ρ is the absorber density, and l is the cell length. We assume that there is no radial dependence in the incoming pulse and that it is attenuated by the factor $\exp(-\langle \sigma \rangle \rho l)$. These assumptions permit us to define an effective fluence $\langle \Phi \rangle$ given by

$$\langle \Phi \rangle = \Phi_0 \{ [1 - \exp(-\langle \sigma \rangle \rho l)] / \langle \sigma \rangle \rho l \}, \quad (\text{III-7})$$

where Φ_0 is the incident fluence.

The observed dependence of effective absorption cross section on effective fluence (J cm⁻²) for the two CO₂ laser pulse types are also shown in Fig. III-19. Measurements were made for the CO₂ P(16) line (947.74 cm⁻¹) near the peak of the SF₆ ground-state Q-branch, for the P(20) line (944.19 cm⁻¹), and for

the P(24) line (940.55 cm^{-1}). For the latter two lines, P(20) and P(24), the low-intensity SF_6 absorption is dominated by population in thermally excited vibrational states.

In trying to find physical meaning in the unsmoothed-to-smoothed cross-section ratios, it must be noted that the two exciting pulses vary in their peak intensities, spectral widths, and their temporal autocorrelation widths; our unsmoothed pulse is a "burst" of ultrashort pulses. It is reasonable to assume that at very low fluences, the smoothed and unsmoothed pulses interact with different distributions of states in the SF_6 gas and that the excitation pathways may also be different. The SF_6 absorptions from the vibrational ground state have been assigned in the vicinity of both the CO_2 P(16) line³⁷ and the CO_2 P(20).³⁸ For example, an unsmoothed pulse (with 5 to 10 longitudinal modes) would have a spectral width on the order of 300 MHz, which is sufficient for direct overlap with 1 to 2% of the SF_6 population at 300 K, compared to 0.02 to 0.1% for the smoothed pulses. However, at the fluences used in our measurements, the power broadening by Rabi flopping is sufficient to nearly mask the spectral differences between the two pulse types. At 10^{-3} J/cm^2 , for example, this broadening is $\sim 300 \text{ MHz}$, which corresponds to the approximate bandwidth of the unsmoothed pulse.

Our data reduce the lower limit of fluence for which the cross sections are not strongly intensity dependent by three orders of magnitude. We would suspect that the lack of such a striking difference in absorption of smoothed and unsmoothed pulses reflects broadening effects and the fact that most coherent processes lose much of their special properties when averaged over many nearly degenerate initial states; such a situation has already been shown³⁹ to obscure the observation of self-induced transparency⁴⁰ in SF_6 . Some additional averaging and cancellation of intensity-dependent effects may also arise from the multiple pulse nature of our unsmoothed pulses.

Multiphoton Absorption Measurements in SF_6 at 140 K (J. L. Lyman, R. G. Anderson, R. D. Fisher, B. J. Feldman)

Optimal use of infrared lasers for molecular isotope enrichment schemes and in infrared laser-

induced chemical reactions requires a thorough understanding of absorption of intense infrared laser radiation by polyatomic molecules.⁴¹

In the measurements reported here, we studied the absorption of pulsed CO_2 laser radiation by SF_6 in an experiment designed to eliminate, insofar as possible, contributions to the absorption by processes that are of secondary interest. Examples of such processes are mode-locking or mode-beating^{42,48} common in multimode, pulsed CO_2 lasers; the long "tail" present on CO_2 laser pulses under normal operating conditions;⁴⁴ a high collision rate during the pulse; the thermal population of excited vibrational states, which dominates the absorption at some frequencies. This work was performed at low temperature and pressure yielding results that complement the wealth of SF_6 absorption data that have been obtained at room temperature^{31-33,35,43-46} as well as the low-temperature results from optoacoustic techniques.^{31,49}

In our experiments, the absorption cell was a 1-m-long, 2.54-cm-diam copper tube with CsI windows. The tube was enclosed within a 6.4-cm-diam cooling jacket, which, in turn, was contained within a 1.27-m-long, 20-cm-diam, stainless steel vacuum insulating cylinder with one 2.54-cm-diam KCl window at the center of each flange. The cell was equipped with gas inlet and exit, four thermocouples for monitoring cell temperature, and ports for the liquid-nitrogen vapor-phase coolant. Automatic control of coolant flow rate permitted cooling the cell to any desired temperature above 80 K, and maintaining the set temperature for periods up to 5 h. Temperature differentials within the cell were less than 2 K.

The measurements reported here were performed at $140 \pm 3 \text{ K}$. At this temperature, the SF_6 vapor pressure is $\sim 1 \text{ torr}$,⁵⁰ and 90% of the SF_6 molecules are in the ground vibrational state. Single-longitudinal mode CO_2 laser signals were used to measure SF_6 transmission at several frequencies within the ν_3 absorption band, using the experimental setup described in a previous section.

The average fluence $\langle \Phi \rangle$ for each transmission measurement was defined as in Eq. (III-7), above, with

$$\Phi_0 = E_0/2\pi a^2, \quad (\text{III-8})$$

where E_0 is the incident energy and a is the radial parameter for the Gaussian beam profile. I_0 ranged from 10^{-6} to 1.0 J/cm^2 . The effective cross section $\langle\sigma\rangle$ is defined in Eq. (III-6).

Table III-IX lists the frequencies of the four laser lines used and the corresponding 140 K low-intensity absorption cross sections, which were derived from an SF_6 spectrum simulation routine.^{51,52} Experimental values for the absorption cross sections were obtained from measurements at these frequencies as functions of fluence. The values of T for a given ρ , E_0 , $\langle\sigma\rangle$, and $\langle\Phi\rangle$ were obtained with a cubic spline interpolation of the experimental data. For comparison purposes, the densities used for P(16) and P(20) measurements were chosen near those of earlier experiments.^{51,43}

Discussion. Figures III-20 and -21 compare data obtained at 140 K with those reported in a previous section. The 140 K curves show a monotonic decrease of $\bar{\sigma}$ with increasing fluence, $\langle\sigma\rangle \propto \langle\Phi\rangle^{-1/3}$, up to about 10^{-2} J/cm^2 . At higher levels, the trend of $\langle\sigma\rangle$ with increasing fluence is constant or slightly increasing (Fig. III-21). At 140 K there is very little thermal population of vibrationally excited states, so that absorption begins from the ground state.

Even at room temperature, ground-state molecules still dominate the P(16) absorption; for this reason the data taken at the two temperatures are nearly indistinguishable (Fig. III-20). On the

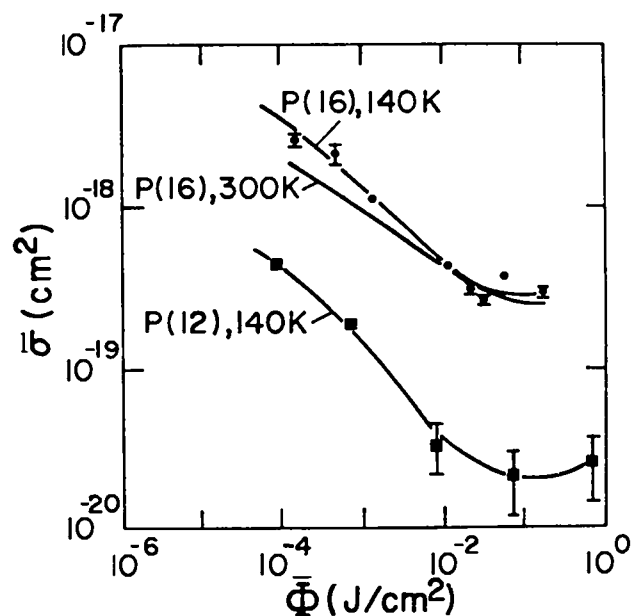


Fig. III-20.

Absorption cross section vs fluence at 140 K at the P(16) and P(12) CO_2 laser lines. Molecular densities were 1.0×10^{16} and $2.0 \times 10^{16} \text{ cm}^{-3}$, respectively. Also shown is the 300 K curve we obtained with the same laser (Ref. 3) for the P(16) line. In this case the molecular density was $1.1 \times 10^{16} \text{ cm}^{-3}$.

TABLE III-IX

LASER LINE FREQUENCIES
AND 140 K LOW-INTENSITY
ABSORPTION CROSS SECTIONS

Line ^a	$\nu(\text{cm}^{-1})^b$	$\sigma(\text{cm}^2)^c$
P(12)	951.19	2.5×10^{-16}
P(16)	947.74	8.3×10^{-17}
P(20)	944.19	4.6×10^{-16}
P(24)	940.55	$\approx 2.0 \times 10^{-16}$

^a10- μm band.

^bRef. 35.

^cSee text.

other hand, as the frequency is decreased to the P(20) and P(24) lines (Fig. III-21), the room-temperature absorption is dominated by molecules that initially have some degree of thermal vibrational excitation. This leads to cross sections for these frequencies that are higher at room temperature and less dependent on fluence. These results are in qualitative agreement with the low-temperature optoacoustic data of both Deutsch⁵¹ and of Akulin et al.⁴⁹ in the fluence range where comparison is possible.

We note that a slope of $-1/3$ has been predicted for curves of the type shown in Figs. III-20 and -21 based on the intensity dependence of the maximum excitation level achieved by a classical anharmonic oscillator driven with a coherent infrared field.⁵³ On the other hand, the reasoning of Cox⁴⁸ for a two-level model would suggest that the observed decrease of $\langle\sigma\rangle$ for intermediate fluence results from a combination of power-broadening and level saturation with a predicted slope of -0.5 , and that the observed

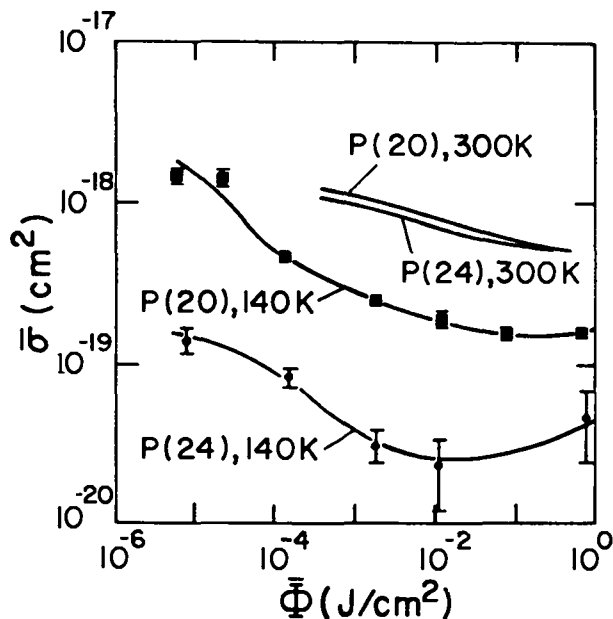


Fig. III-21.

Absorption cross section vs fluence at 140 K at the P(20) and P(24) CO₂ laser lines. The molecular densities were 1.0×10^{16} and $4.5 \times 10^{16} \text{ cm}^{-3}$, respectively. Curves at 300 K for both laser lines obtained with the same laser (Ref. 3) are also shown at a molecular density of $1.1 \times 10^{16} \text{ cm}^{-3}$ for each line.

leveling of the trend at higher fluence is due to the onset of multiple-photon absorption.

Conclusion. Our data clearly show that absorption of CO₂ laser radiation at frequencies slightly lower than band center [P(20) and P(24), for example] is dominated by thermally vibrationally excited species at room temperature. Therefore, room-temperature absorption data at these frequencies should not be interpreted as if the absorbing-molecules were initially unexcited.

Status of GWTF (S. J. Czuchlewski, A. V. Nowak, E. Foley)

The Gigawatt Test Facility (GWTF) was used to support research on gas isolators, doped alkali-halide saturable absorbers, damage studies, and a new laser-triggered spark-gap, designed to provide low-jitter high-voltage pulses suitable for accurately

triggering plasma diagnostics. Toward the end of 1977 the electro-optic switchout system was replaced with a new, more reliable model. The single antireflection-coated p-doped germanium isolator was also replaced with two pieces of uncoated p-doped germanium at Brewster's angle, a configuration less subject to surface damage. Finally, the high-voltage components of the amplifiers were immersed in oil to obtain higher operational reliability.

Prototype for GWTF Upgrade (E. McLellan, E. Foley, S. J. Czuchlewski)

To conduct a wider range of saturable-absorber, damage-study, plasma-physics, and plasma-diagnostic experiments, it has been decided to upgrade the GWTF into a higher power (5 to 10 GW), short-pulse, high-repetition-rate system. This system will consist of three essential components: a four-passed oscillator/amplifier module, an electro-optic pulse slicer, and a three-passed Lumonics-600 amplifier (Fig. III-22). A preliminary evaluation of this system with 0.8-ns pulses was completed.

The oscillator/amplifier and the E-O pulse slicer were described in previous reports.⁵⁴ Briefly, the lowest path through the module is part of an oscillator cavity that produces a multiline 200-mJ, 60-ns gain-switched pulse. The three-stage E-O switch slices a 2-mJ, 0.15- to 1.2-ns duration pulse from the gain-switched pulse. The short pulse is then reinjected into the upper portion of the oscillator gain medium for four stages of amplification—a technique that yields a multiline 300-mJ, 0.65-ns pulse when a 1.15-ns pulse is reinjected.

The output of the four-pass oscillator/amplifier was expanded with a 6:1 Galilean telescope into a slowly diverging beam and then directed into the triple-passed Lumonics-600 amplifier. This is a commercial 1-atm, double-discharge device with a 9-cm electrode separation. Energy and temporal pulse shape were measured on each pass, and the frequency spectrum was monitored after the final pass.

Energy, power, and pulse-shape characteristics are presented in Table III-X. It is seen that this system is capable of producing 9-GW, 0.78-ns pulses. The frequency content consisted primarily of lines in the 10- μm P(12)-to-P(24) range with an occasional contribution from lines in the vicinity of 9- μm R(18). For the particular tests reported here, the

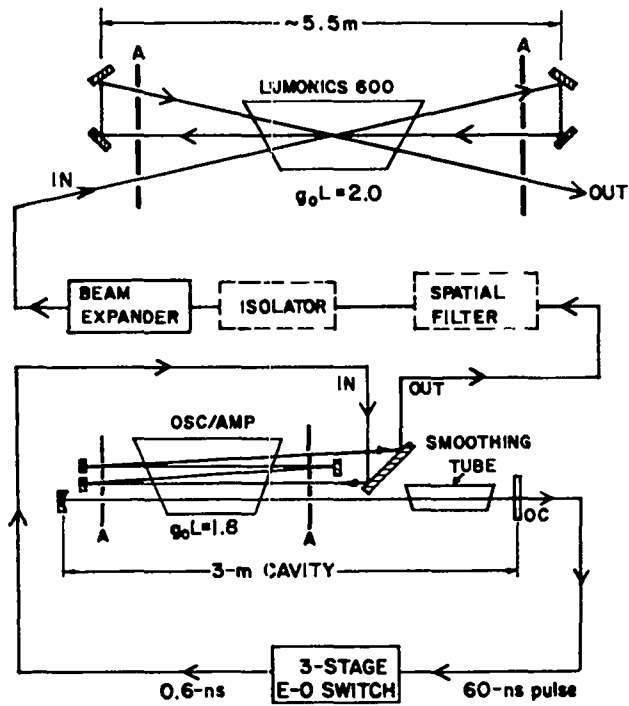


Fig. III-22.
Two-stage multipass oscillator-amplifier system. Components labeled "A" are apertures; "OC" is the output coupler of the oscillator cavity. The isolator and spatial filter shown in the dashed boxes were not used in the present setup but will be installed later.

TABLE III-X

PRELIMINARY PERFORMANCE SPECIFICATIONS FOR
THE MULTIPASSED LUMONICS-600 AMPLIFIER

PARAMETERS

Laser mix: (He:N₂:CO₂) = (7:1:2)
 Pressure = 580 torr
 Beam Area = 25 cm² (first pass)
 56 cm² (second and third passes)
 $g_o L = 2.0$
 $L = 50$ cm

RESULTS

Stage	Energy (J)	Power (GW)	τ_{Rise} (10-90%, ns)	τ_{FWHM} (ns)	τ_{Fall} (90-10%, ns)
Input	0.23	0.21	0.19	1.02	1.43
Pass-1	1.2	1.0	0.26	1.09	1.36
Pass-2	4.3	4.2	0.22	0.87	1.51
Pass-3	8.7	9.2	0.19	0.78	1.30

four-pass oscillator was operating at an abnormally low gain. Consequently, the output pulse (i.e., the input in Table III-X) was significantly wider than usual. Nevertheless, noticeable pulse-shortening occurred within the Lumonics amplifier. The long tail observed in the output pulse generated in the initial phase of this work can be corrected by proper adjustment of the third crystal in the E-O switch unit. The observed data are plotted in Fig. III-23, which presents theoretical Frantz-Nodvik predictions⁵⁴ of the output as a function of input energy for a g_0L of 2.0, with the effective saturation energy E_{sat} as a parameter. In this way, E_{sat} can be determined to fall in the range of 40 to 70 mJ/cm².

We conclude from the present experiments that this setup will provide an efficient, reliable system for the upgraded GWTF. Further measurements for 0.25-ns pulse propagation will be conducted early in 1978.

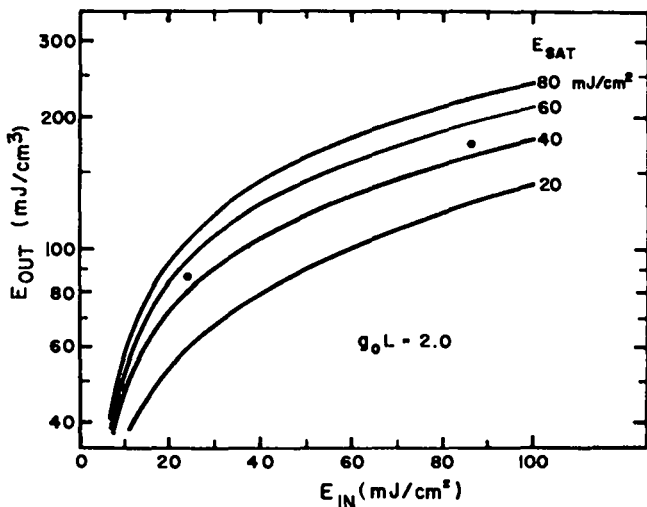


Fig. III-23.

Output energy flux predicted by the Frantz-Nodvik theory for a single pass through an amplifier with a g_0L of 2.0. The data points represent the energies measured at the end of each pass through the Lumonics-600. Beam areas were 25 cm² on the first pass and 56 cm² on the second and third passes.

REFERENCES

1. R. W. Hellwarth, J. Opt. Soc. Am. 67, 1 (1977).
2. A. Yariv and D. M. Pepper, Opt. Lett. 1, 16 (1977).
3. J. Marburger, Appl. Phys. Lett. 32, 372 (1978).
4. R. L. Abrams and R. C. Lind, Opt. Lett. 2, 94 (1978).
5. B. Ya. Zel'dovich, V. I. Popvichev, V. V. Regul'skii, and F. S. Faizullov, Zh. Eksp. Teor. Fiz. Piz. Red. 15, 160 (1972) [translation: Sov. Phys. JETP 15, 109 (1972)]; O. Yu. Nosach, V. I. Popovichev, V. V. Ragul'skii and F. S. Faizullov, Zh. Eksp. Teor. Fiz. Piz. Red. 16, 617 (1972) [translation: Sov. Phys. JETP 16, 435 (1972)].
6. V. I. Bespalov and V. I. Talanov, Zh. Eksperim. Teor. Fiz. Pis'ma Red. 3, 471 (1966) [translation: JETP Lett. 3, 307 (1966)]; R. Y. Chiao, P. L. Kelley, and E. Garmire, Phys. Rev. Lett. 17, 1158 (1966).
7. R. L. Carman, R. Y. Chiao, and P. L. Kelley, Phys. Rev. Lett. 17, 1281 (1966).
8. D. Korff, S. L. Glickler, and J. D. Daugherty, Bull. Am. Phys. Soc. 23, 156 (1978).
9. D. Bloom and G. C. Bjorklund, Appl. Phys. Letts. 31, 592 (1977); P. F. Liao, N. P. Economou, R. R. Freeman, Phys. Rev. Lett. 39, 1473 (1977); S. M. Jensen and R. W. Hellwarth, Appl. Phys. Lett. 32, 166 (1978); D. M. Bloom, P. F. Liao, and N. P. Economou, Opt. Lett. 2, 58 (1978); P. F. Liao and D. M. Bloom, submitted to Opt. Lett.; P. F. Liao, D. M. Bloom, and N. P. Economou, submitted to Appl. Phys. Lett.
10. V. Wang and C. R. Giuliano, Opt. Lett. 2, 4 (1978).
11. N. F. Pilipetskii, V. V. Ragoul'skii, V. V. Shkrounov, and B. Ya. Zel'dovich, presented at 1977 Vavilov Conference, Novosibirsk, USSR (1977).

12. A. Gondhalekar, N. R. Heckenberg, and E. Holzhauser, *Phys. Lett.* **46A**, 229 (1973).
13. J. J. Wynne, *Phys. Rev.* **178**, 1295 (1969).
14. F. Skoberne, compiler, "Laser Fusion Program—July 1-December 31, 1977," Los Alamos Scientific Laboratory report LA-7328-PR (December 1978).
15. H. C. Volkin, "Calculation of Short-Pulse Propagation in a Large CO₂-Laser Amplifier," submitted to *J. Appl. Phys.* for publication.
16. C. R. Phipps, Jr., and S. J. Thomas, *Opt. Lett.* **1**, 93 (1970).
17. M. D. Montgomery, R. L. Carlson, D. E. Casperson, S. J. Czuchlewski, J. F. Figueira, R. F. Haglund, Jr., J. S. Ladish, and S. Singer, *Appl. Phys. Lett.* **32**, 324 (1978).
18. D. H. Gill and B. E. Newnam, paper Th07, Inertial Confinement Fusion Conference, San Diego, California, February 7-9, 1978.
19. H. Claasen and A. J. Zielen, *J. Chem. Phys.* **22**, 707 (1954).
20. A. R. Chraplyvy, thesis, Cornell University, 1978 Materials Science Center Report 2903 (unpublished).
21. L. Allen and J. H. Eberly, *Optical Resonance In Two-Level Atoms*, Wiley (1975).
22. W. W. Rigrod, *J. Appl. Phys.* **34**, 2602 (1963).
23. A. S. Barker, Jr., and A. J. Sievers, *Rev. Mod. Phys.* **47**, Suppl. No. 2, S1 (1975).
24. H. W. Mocker and R. J. Collins, *Appl. Phys. Lett.* **7**, 270 (1965).
25. A. J. Demaria, *Electronics*, September 16, 1968, p. 112.
26. A. J. Alcock and A. C. Walker, IQEC—VIII, Technical Digest, 61 (1974).
27. E. Yablonovitch and J. Goldhar, *Appl. Phys. Lett.* **25**, 580 (1974).
28. R. K. Ahrenkiel, J. F. Figueira, C. R. Phipps, Jr., S. Thomas, D. Dunlavy, and A. Sievers, submitted for publication to *Appl. Phys. Lett.*
29. E. Yablonovitch, *Phys. Rev. A* **10**, 1888 (1974).
30. F. Skoberne and E. Stark, "Laser Fusion Program, January 1-June 30, 1977," Los Alamos Scientific Laboratory report LA-6982-PR (April 1978). F. Skoberne, "Laser Fusion Program, July 1-December 31, 1978," Los Alamos Scientific Laboratory report LA-7328-PR (December 1978).
31. T. F. Deutsch, *Opt. Lett.* **1**, 25 (1977).
32. J. D. Black, E. Yablonovitch, N. Bloembergen, and S. Mukamel, *Phys. Rev. Lett.* **38**, 1131 (1977).
33. H. Stafast, W. E. Schmid, and K. L. Kompa, *Opt. Commun.* **21**, 121 (1977).
34. R. V. Ambartzumian, Yu. A. Gorokhov, V. S. Letokhov, and G. N. Makarov, *Zh. Eksp. Teor. Fiz.* **69**, 1956 (1975) [Translation *Sov. Phys. JETP* **42**, 993 (1975)].
35. D. O. Ham and M. Rothschild, *Opt. Lett.* **1**, 28 (1977).
36. A. V. Nowak and J. L. Lyman, *J. Quant. Spectrosc. Radiat. Transfer* **15**, 945 (1975).
37. R. S. McDowell, H. W. Galbraith, C. D. Cantrell, N. G. Nereson, and E. D. Hinkley, *J. Mol. Spectros.* **68**, 288 (1977).
38. R. S. McDowell, H. W. Galbraith, B. J. Krohn, and C. D. Cantrell, *Opt. Commun.* **17**, 178 (1976).
39. C. K. Rhodes, A. Szöke, and A. Javan, *Phys. Rev. Lett.* **21**, 1151 (1968), F. A. Hopf, C. K. Rhodes, and A. Szöke, *Phys. Rev.* **B1**, 2833 (1970).

40. C. K. N. Patel and R. E. Slusher, *Phys. Rev. Lett.* **19**, 1019 (1967).
41. Recent reviews include: J. P. Aldridge, J. H. Birely, C. D. Cantrell, and D. C. Cartwright, *Physics of Quantum Electronics, Vol. IV*, S. F. Jacobs, M. Sargent, III, M. O. Scully, and C. T. Walker, Eds., Addison Wesley, 1976, p. 57; V. S. Letokhov and C. B. Moore, *Sov. J. Quantum Electron.* **6**, 259 (1976); R. V. Ambartzumian and V. S. Letokhov, *Acc. Chem. Res.* **10**, 61 (1977); S. Kimel and S. Speiser, *Chem. Rev.* **77**, 437 (1977); C. D. Cantrell, S. M. Freund, and J. L. Lyman, *Laser Handbook, Vol. IIIb*, M. L. Stitch, ed., North Holland (in press).
42. J. L. Lyman, J. W. Hudson, and S. M. Freund, *Opt. Commun.* **21**, 112 (1977).
43. J. L. Lyman, B. J. Feldman, and R. A. Fisher, *Opt. Commun.* **25**, 391 (1978).
44. R. V. Ambartzumian, Yu. A. Gorokhov, V. S. Letokhov, and G. N. Makarov, *Opt. Commun.* **20**, 119 (1977).
45. P. Kolodner, C. Winterfield, and E. Yablonovitch, *Opt. Commun.* **20**, 119 (1977).
46. M. Rothschild, W. S. Tsay, and D. O. Ham, *Opt. Commun.* **24**, 327 (1978).
47. D. M. Cox, *Opt. Commun.* **24**, 336 (1978).
48. J. L. Lyman, S. D. Rockwood, and S. M. Freund, *J. Chem. Phys.* **67**, 4545 (1977).
49. V. M. Akulin, S. S. Alimpiev, N. V. Karlov, A. M. Prokhorov, B. G. Sartakov, and E. M. Khokhlov, Paper Q-8, Tenth International Quantum Electronics Conference, Atlanta, Georgia, May 29—June 1, 1978.
50. *Handbook of Chemistry and Physics*, 47th ed., Robert C. Weast, ed., Chemical Rubber, Cleveland, 1966, p. D113.
51. A. V. Nowak and J. L. Lyman, *J. Quant. Spectrosc. Radiat. Transfer* **15**, 945 (1975).
52. P. L. Houston and J. I. Steinfeld, *J. Molec. Spectros.* **54**, 335 (1975).
53. T. P. Cotter, Los Alamos Scientific Laboratory, private communication, 1978.
54. L. M. Frantz and J. S. Nodvik, *J. Appl. Phys.* **34**, 2346 (1963).

IV. TARGET EXPERIMENTS AND MILITARY APPLICATIONS

In an integrated program of target experiments, theory, and target design, we are establishing a fundamental understanding of laser-target interactions, particularly of the relevant plasma physics and hydrodynamics. Experimental and theoretical efforts have addressed the scaling of consistent models to higher laser intensities. Emphasis has been placed on the development and demonstration of experimental techniques needed to determine conclusively the performance of present and future targets. A modest experimental effort is directed toward military applications.

LASER FUSION EXPERIMENTS

Introduction

The reproducibility of target performance has improved remarkably with the introduction of precise alignment and focusing techniques. This improved reproducibility now allows confirmation or rejection of physics models with a minimum number of laser shots.

One model, which has been confirmed over a range of 1000 in laser intensity, is the dependence of hot-electron temperature and associated fast-ion velocities on intensity. The data confirm the scaling of T_{hot} with the third root of the intensity, up to an intensity of 10^{16} W/cm² where the hot-electron density is expected to exceed critical density for 10.6- μm illumination.

Use of infrared microscopes and aperture transmission techniques has demonstrated that large-aperture (30-cm) reflective optics now available can provide focal spot sizes and intensities within five times the diffraction-limit or better from a full high-power laser chain. This was achieved with a final focusing mirror of $f/2$ aperture. Slower optics promise performance even more nearly diffraction limited.

Spatial and spectral resolution of Ne x-ray lines from DT/Ne-filled microballoons have been analyzed to obtain peak fuel temperature and density measurements. Straight-edge and aperture imaging techniques along with Stark profile fitting confirm that significant breakup of the glass pusher

and subsequent leaking of the fuel does not occur in exploding-pusher experiments.

Consistency of Target Behavior with ir-Microscope Alignment (D. V. Giovanielli)

Two infrared microscopes¹ using pyroelectric vidicon readouts were installed at the TBS. Each microscope was aligned to look directly into a laser beam and was focused at the target center position. The focused beams could be viewed directly at low power and each was aligned to an accuracy of ± 15 μm with respect to the target. The observed best-focus position, as determined by the ir microscope, agreed to within a beam-waist dimension with the best-focus position determined with a mask (modified Hartmann) test.

Microscope alignment was used in a series of exploding-pusher experiments employing glass microballoons with initial radii of 80 to 97 μm , initial wall thicknesses of 0.9 to 1.1 μm , and initial DT or DT/Ne fill densities of 2.03 to 2.48 mg/cm³.

Data obtained during the thirteen shots in the series are listed in Table IV-I. The risetime of the low-energy x-ray pulse emitted (center energy, 270 eV; width, 70 eV) followed the laser pulse risetime in the range of 200 to 500 ps base-to-peak.

Two four-channel x-ray spectrometers, each at $\sim 45^\circ$ to one of the beams, produced spectra in the 0.45- to 1.5-keV photon energy range. In this range, the integrals of the spectra resulted in a conversion efficiency of incident laser light into x rays of $(1.2 \pm 0.2) \times 10^{-3}$. The uncertainty limits are within one

TABLE IV-I

DATA FROM A SERIES OF EXPLODING-PUSHER EXPERIMENTS

<u>Shot Number</u>	<u>Laser Pulse Base-to-Peak Risetime (ps)</u>	<u>270-eV X-Ray Pulse Risetime (ps)</u>	<u>Ratio of X Ray To Laser Risetime</u>	<u>Ratio of North Side to South Side X-Ray Conv. Eff. (0.45 to 1.5 keV)</u>	<u>Ratio of Max Ion Velocities - North Side to South Side</u>	<u>Neutron Yield (10⁹)</u>
28060701	200 ± 30	500 ± 20	1.0	1.34	0.988 ± 10%	1.3 ± 1.1
28060702	1000	---	---	---	1.06	1.6 ± 1.1
28060902	230	---	---	0.99	0.929	2.6 ± 1.3
28060904	330	360	1.09	1.04	1.026	3 ± 1.3
28060905	230	290	1.26	1.06	1.006	3.9 ± 1.4
28060906	230	210	0.91	0.99	1.026	6.3 ± 1.5
28061302	---	500	---	1.03	0.96	1.5 ± 1.3
28061303	230	290	1.26	1.19	1.34	3.5 ± 1.4
28062103	250	---	---	0.93	0.977	2.8 ± 1.3 ^a
28062201	275	---	---	0.73	1.115	0 ± 1.3 ^a
28062602	---	---	---	0.70	1.03	0.3 ± 1.2 ^a
28062603	---	---	---	0.82	0.78	1.5 ± 1.3 ^{a,b}
28062604	200	---	---	0.97	1.04	4.2 ± 1.4 ^{a,c}
		Averages =	1.10	0.98	1.021	
		Std. Dev. =		0.18	0.125	

^a9% of atoms in fuel were neon.

^bBoth beams focused 100 μm beyond ball center.

^cBoth beams focused 200 μm beyond ball center.

standard deviation for the data obtained. The calibrations of the instruments were known to an accuracy of better than $\pm 20\%$. Table IV-I shows the ratio of conversion efficiency measured on the two sides of each microballoon. The average of this ratio is 0.98, again with an uncertainty of less than 20%.

Evaluation of Laser Target Performance by Ultrafast Ion Measurement (Tai Ho Tan)

Measurement of the ultrafast ions emitted from the high-power laser-produced plasmas yielded important information concerning the detailed mechanisms of laser-matter interactions.^{1,2} We present results that show that simple and accurate measurements of ultrafast ion velocities are one of the most powerful means for diagnosing high-power laser performance. Data collected over a wide energy range (up to 500 J) from the two LASL CO₂ laser facilities revealed that, for any target, the measured fastest ion velocity correlates directly with the laser irradiance on target. Furthermore, the hot-electron temperature can be inferred. Excellent agreement of the data with theoretical modeling suggested strongly that the ponderomotive force enhances resonant absorption by steepening the density profile. Therefore, CO₂ laser energy can be deposited at much higher densities than previously supposed, with the result that energy absorption by the target is fairly independent of laser wavelength at high power. This has indeed been confirmed by recent absorption measurements.³ Analysis of exploding-pusher targets shots showed that neutron yield is a direct function of fastest ion speed. Also, that implosion and yield are optimum only when the maximum velocities of the ions emitted in two opposite directions are the same (within measurement error).

Measured fastest ion velocities as a function of laser energy are plotted in Fig. IV-1. These ions were detected with fast scintillator-photomultiplier detectors during experiments at our TBS and Helios. Flat targets consisted of different materials (Z-values from 1 to 92), with different thicknesses (10 mm to several mm), sizes, and shapes; whereas spherical targets included glass microballoons, plastic balls, nickel balls, and gold-coated balls. The data show no dependence on the type of target used.

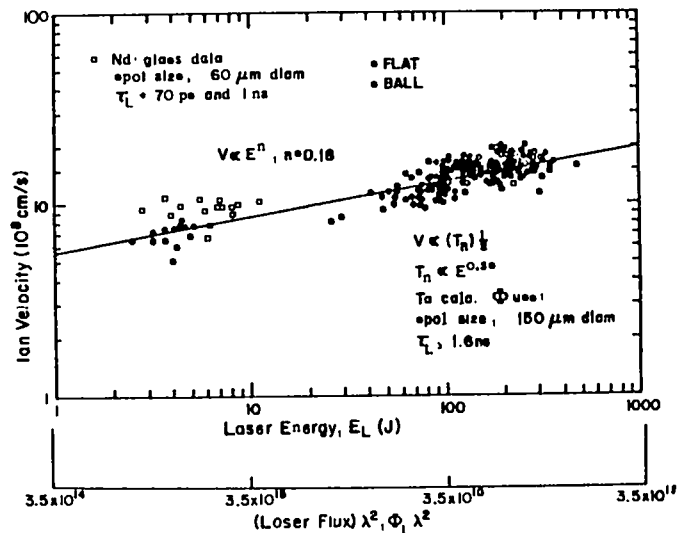


Fig. IV-1.
Plot of fastest ion velocity vs laser energy, E_L ;
laser flux, Φ_L .

The salient feature of the data-point distribution is the monotonic increase of ion velocity as a function of laser energy in this logarithmic plot. The relationship can be expressed in the form $V_1 \propto E^n$.

Because both focused spot size and laser pulse length of all these shots were the same, the power exponent is also the same if the velocity is plotted against the laser power density, i.e., $V_1 \propto \Phi^n$. An exponent of $n = 0.18$ appears to describe the data very well. Note that the dispersion of the data points is due to the specific nature of the typical target shots. Variations in several parameters can significantly affect the ion speed but cannot be determined always from shot to shot. These parameters include: risetime and pulse length of the laser; size of focused spot on target; presence of hot spots in the beam; and low-level precursor energy. In an isothermal model for plasma expansion, the fastest ion velocity can be estimated explicitly and shows almost linear dependency on the ion sound speed.⁴ Therefore, the fastest ion velocity is also a measure of hot-electron temperature, i.e., $V_1 \propto \sqrt{T_e}$ (hot). Hence

$$T_e \propto \Phi^{2n} \propto \Phi^{0.38}$$

Using a focused spot diameter of $150\ \mu\text{m}$ and $1.6\ \text{ns}$ in laser pulse length, the value of $\phi\lambda^2$ is indicated on the abscissa. It has been shown by particle-in-cell (PIC) simulation⁵ that

$$T_e \propto (\phi\lambda^2)^{1/3}$$

when laser energy is coupled to the target by the resonant-absorption mechanism with a steep density profile near the absorption region due to the presence of the laser radiation pressure. The excellent agreement between experiments and simulation results strongly implies the validity of the absorption model we used in our simulation work. It also illustrates clearly the importance of the isothermal expansion model in describing the behavior of laser-produced plasmas.

The few data points collected in previous Nd:glass laser experiments with the same detector system fit the pattern of the CO_2 data very well when plotted as a function of $\phi\lambda^2$. This further supports the contention that the absorption processes in laser-plasma interactions are only very weakly dependent on wavelength.

Note that the fastest ions observed were experimentally determined to be protons regardless of target material used. This fact is assumed to have been caused by hydrocarbon target-surface contamination from vacuum-pump oil. Figure IV-2 shows measured ion velocity as a function of target material at almost the same laser irradiance on target for each data point taken. The behavior of the ion velocity as a function of target Z-value shows that the hot-electron temperature for a specific laser irradiance is not sensitive to the kind of targets with which the laser interacts. This fact is not very surprising because the electron density does not vary significantly for different materials.

An important conclusion to be drawn from our data is finding that the fastest ion velocity can be used effectively to diagnose the laser irradiance of the target. This is demonstrated in Fig. IV-3, which shows a histogram of the ratio of ion velocities. In each shot, the two ion velocities were measured by two different detectors viewing the ion emission from the opposite surfaces of a DT-filled microballoon target. The data show that if this ratio is within 10 to 15% of unity, neutron production can be expected; otherwise, no neutron production is seen. This correlation is very important in laser fusion

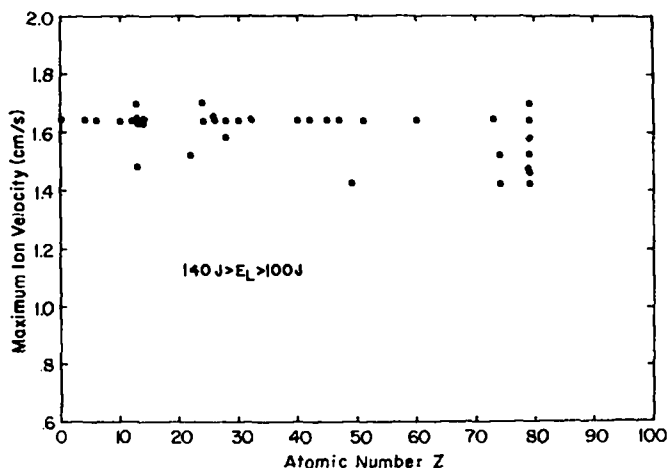


Fig. IV-2.

Plot of maximum observed ion velocity as a function of target material.

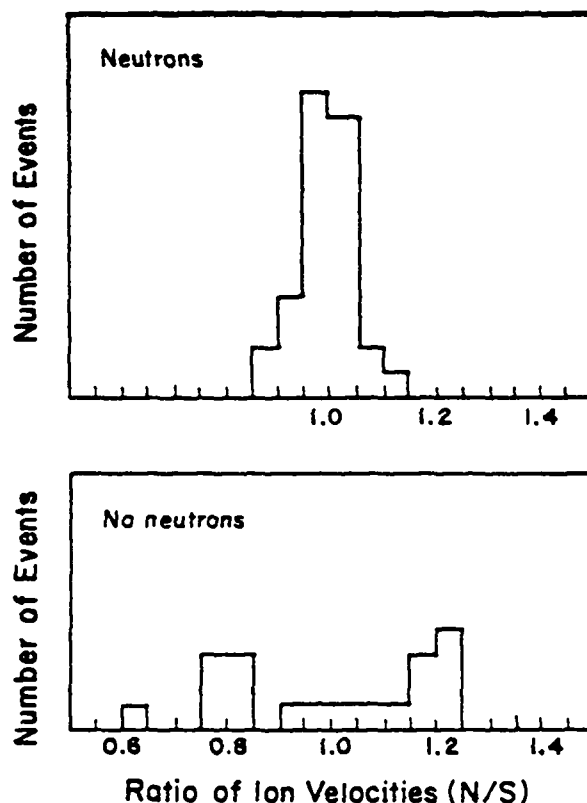


Fig. IV-3.

Histogram of sample GMB shots plotting events with neutron yield and without yield against the ratio of ion velocity.

work. It may reflect the fact that laser irradiances on target must be balanced properly for symmetrical target compression to occur.

Finally, in the exploding-pusher mode, the neutron yield increases as a function of ion velocity, hence the absorbed laser flux also increases. However, the exact relationship between yield and ion velocity or laser energy depends sensitively on pulse risetime and pulse length, as well as on the efficiency with which the absorbed energy is transported to the portion of the pellet that is not directly exposed. In short, the relationship depends on the coupling efficiency of the absorbed energy to the implosion process that heats the fuel ions. Therefore, measurement of ion velocity can serve as a means to determine how efficient this coupling process really is for a specific set of laser and target parameters.

Characterization of TBS Focal Spots Using a Transmission Infrared Microscope (D. Kohler, P. D. Goldstone, J. P. Carpenter, and L. Sprouse)

General. Two experiments were conducted on the TBS to measure the focal-spot distributions before and after installation of new paraboloidal focusing mirrors. The spots produced by the original focusing mirrors were irregular and had weak satellites. The diameters of these spots were estimated to be ~ 75 to $90 \mu\text{m}$ FWHM.

After new parabolas were installed and the mirrors in the south beam remounted to remove large astigmatic aberrations, the transmission infrared microscope (TIRM) and the autocollimating mask test (ACMT or Hartmann test) were used to align the axes of the parabolas through the target position and to align the incident beam axes with the parabola axes. The new focal spots, as observed with the TIRMs, were round and had diameters of $\sim 50 \mu\text{m}$ FWHM. Optimum parabola alignment and focus, as determined by the TIRM and the ACMT, were in good agreement. Peak irradiance appeared to increase by a small factor relative to the earlier measurement, although no quantitative irradiance measurements were made.

The TIRMs are sensitive enough to detect the oscillator output without preamplification. However, consistent beam steering of $\sim 40 \mu\text{rad}$ was observed in the preamplifiers, which would complicate target

alignment if only the oscillator pulse were used. Additionally, we found that a hole grating used as an attenuator caused no obvious distortion of the spot.

We estimated that the TIRMs could place the focal spot on the center of a spherical target within $\sim 20 \mu\text{m}$. However, interference effects due to the use of a small pulsed CO_2 laser for backlight illumination of targets prevent the TIRMs from being used to judge the focal position of a target.

Finally, we noted that the focal spots break up into an irregular collection of spots within a few hundred microns of the optimum focus, so that a large, uniform low-irradiance spot cannot be obtained by defocusing. The depth of focus of the beams and of the TIRMs are both estimated to be $\sim \pm 150 \mu\text{m}$.

Transmission ir Microscope (TIRM). The infrared microscope used in our TBS experiments is shown schematically in Fig. IV-4. Its primary components are an ir television camera and a lens (L) that look directly at the focus of the CO_2 laser beam. A direct image of the focal spot can be observed on a television monitor, and the signal amplitude can be measured on a waveform monitor. Alternatively, an object at the target position (T) may be illuminated from behind, and its shadow can be seen on the TV screen. Two identical TIRMs are used for the two beams.

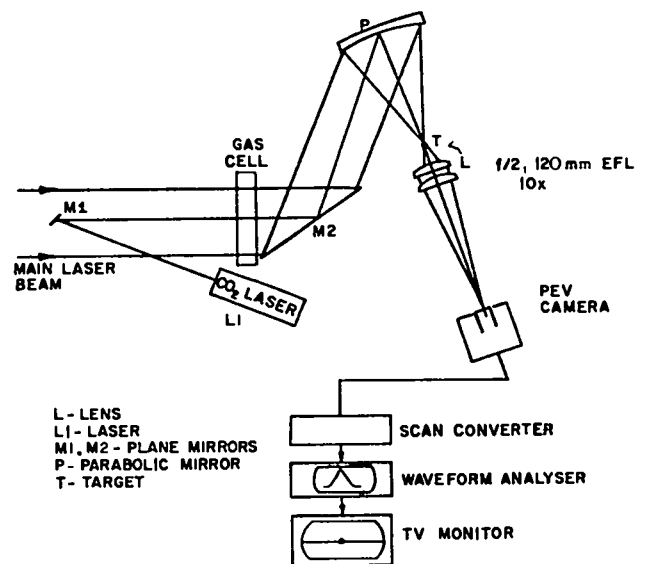


Fig. IV-4.
Transmitting ir microscope (TIRM) system.

The TV cameras are of a special design with very low noise and a large dynamic range. The pyroelectric vidicon (PEV) tubes in the cameras had been used before, had a dynamic range of nearly 100, and were quite linear over that range.⁸⁻⁸ These cameras were the first to be entirely designed around the PEV tubes and have not yet been developed to a point where they are completely satisfactory.

The cameras and tubes are sensitive enough to detect less than a microjoule in the focal spot of the beam or less than a millijoule spread over the face of the tube. A pulse containing a few millijoules ($\sim 1/10$ the energy of a front-end pulse at the target position), is sufficient to damage the tube so that the pulse must be attenuated severely to protect the TIRM.

The laser beam was attenuated as needed by Gas Mix 804 (SF_6 + Freon) in a cell at the entrance to the target chamber. Observations were usually made by using the pulse from the TBS front end (oscillator and two preamplifiers), that normally contains 20 to 40 mJ in a 1.5-ns pulse. Because of a slight imbalance in either the camera gains or the sensitivities of the two TIRM tubes, the north-beam gas cell was filled with ~ 75 torr of Mix 804, and the south-beam cell with ~ 105 torr of the mix. This corresponds to small-signal transmissions through the gas cells of 7.8×10^{-6} and 1.8×10^{-6} , respectively.

The lens (L) was a germanium doublet with a focal length of 120 mm and an $f/2$ aperture, which images a 2-mm field onto the PEV tube with a magnification of ~ 10 . The lens was designed to be nearly diffraction-limited, but in practice it had some wedge and could resolve only $\sim 50 \mu\text{m}$. The lenses were mounted on retractors that are operable under vacuum so that they were out of the way during high-power shots. The camera was protected by a shutter interlocked with the retractor mechanisms.

Objects at the target position were illuminated by the beam from a small pulsed CO_2 laser. An EG&G 411 pulser with some extra capacitance was used to pulse the head from a Sylvania 941 laser. The beam, containing ~ 1 mJ, is small enough so that diffraction keeps it from being focused by the parabola to a small spot. Hence, a shadow of the object at the target position is imaged on the PEV tube. The focal spot as detected by the TIRM may be steered so that its image coincides with the center of a target, previously determined by backlighting the target. Thus, the TIRM is a direct and sensitive alignment tool.

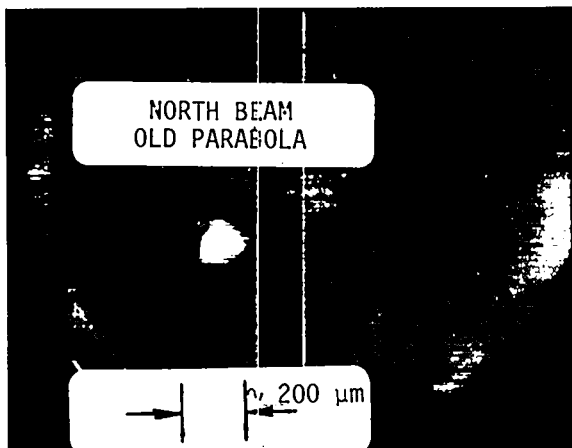
The small laser beam was inserted along the axis of the main beam by a small mirror (M1). This mirror was attached to the mask that is used for the ACMT or Hartmann test⁹ and was removed during high-power shots and for observation of the focal spot.

Characterization of Focal-Spot Distributions Using Original Parabolas. Measurements were performed with the primary objective of characterizing the focal-spot distributions before replacing the focusing parabolas with the new diamond-turned parabolas. A secondary objective was to determine if the oscillator pulse alone could be used for alignment purposes, or if the full front-end pulse (as used in ACMT) was required.

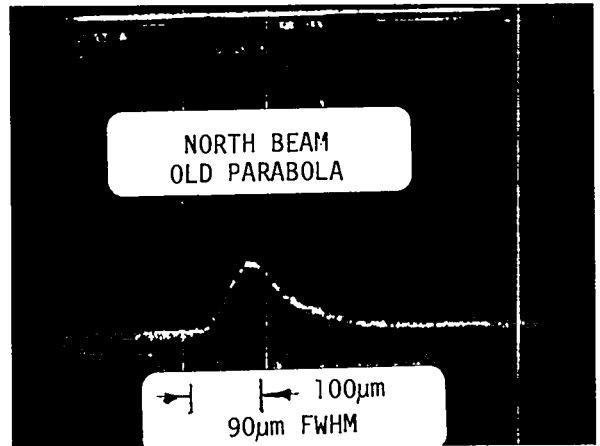
The images of the focal spots produced by the original parabolas are shown in Fig. IV-5. These photographs of images, made by the north and south TIRM cameras, were displayed on different monitors and therefore should not be closely compared. The spots below and to the right of the image in Fig. IV-5c and the peak in the waveform-analyzer trace to the right of the main peak (Fig. IV-5d) are tube defects that should be ignored. The satellites to the left of the main spots in both photographs are apparently real. It can be seen that the cores of the spots are irregular, with widths of $\sim 90 \mu\text{m}$ FWHM for the north spot and of $\sim 80 \mu\text{m}$ FWHM for the south-beam spot.

The oscillator pulse could be observed by the microscope, providing adjustments were made in the amount of absorber gas present in the beam path. The spot was then observed with, first, one and then two stages of preamplification added. As can be seen in Fig. IV-6, the spot did not distort, but was displaced downward by $\sim 20 \mu\text{m}$. This beam steering is small and extremely consistent (i.e., the spot position does not change measurably from shot to shot); however, it makes use of the oscillator alone for alignment on targets somewhat cumbersome.

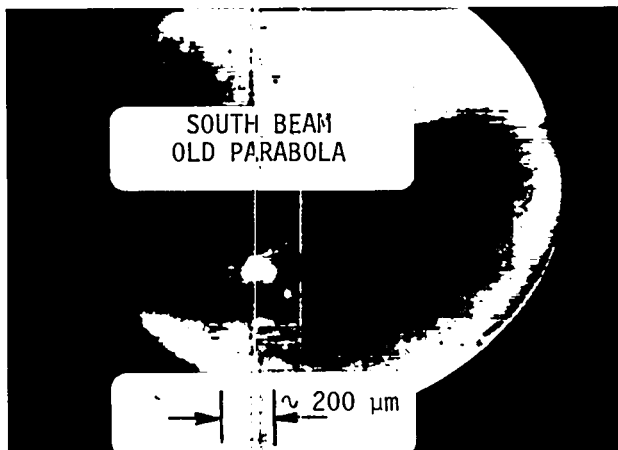
Focal-Spot Distributions Following Installation of New Parabolas. Measurements were made by using the TIRM to optimize the alignment of the new parabolas and to measure the profile of the focal spots. Before these measurements the TIRM was optimized by adjusting the lens position for best focus on a $32\text{-}\mu\text{m}$ pinhole at the target position (smallest image). The focal position of this pinhole (position



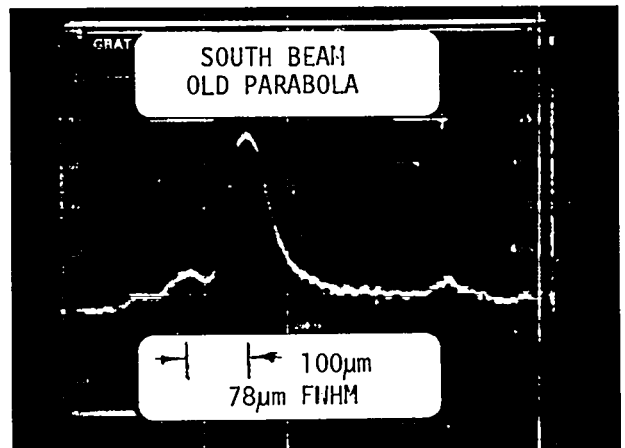
(a)



(b)



(c)



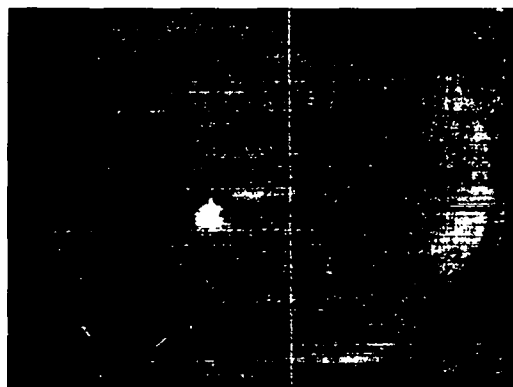
(d)

Fig. IV-5.

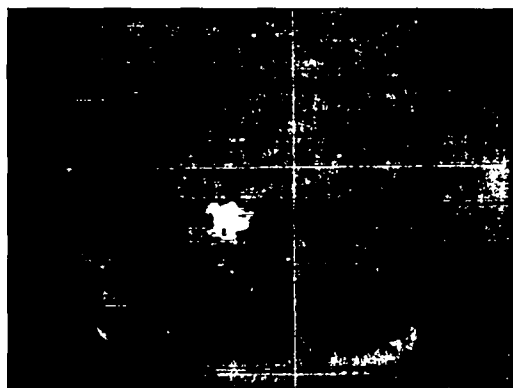
TIRM views of focal spots obtained with old parabolas, with the dual-beam modules and the chamber depressurized. Oscilloscope traces show the video signal on one horizontal line through the brightest part of the spots. Spot widths are FWHM of the scope traces for which the contrast (γ) is undetermined; (a) and (b), north beam; (c) and (d), south beam.

along the beam axis) was adjusted carefully in the target fabrication laboratory to be within a few micrometers of the ACMT surrogate target (Hartmann ball) center. In addition, adjustments were made to the position of the Hartmann balls on the target wheels, and to the kinematic mount in the target chamber, to place the center of the Hartmann

balls directly over the pivot point at the center of the chamber. This permitted the target wheels to be rotated about the pivot point with no change in target focal position. The images of the pinhole produced after these adjustments were $\sim 44 \mu\text{m}$ FWHM on the south-beam TIRM, and $\sim 50 \mu\text{m}$ FWHM on the north TIRM.



(a)



(b)



(c)

Fig. IV-6.

TIRM views of the north-beam focal spot with (a) the oscillator alone, (b) oscillator and one preamplifier, and (c) oscillator and two preamplifiers (pit pulse). The spot appears to be displaced downward about 20 μm by the preamplifiers.

Photographs of the monitor images of test objects, e.g., of a pointer, a 200- μm glass microballoon, a 128.3- μm mesh, and double crosshairs with a 160- μm spacing between centers, are shown in Fig. IV-7 with the TIRM focus correctly adjusted.

When the above adjustment procedure was followed, there remained a significant discrepancy between the optimal parabola pan adjustment as determined by the ACMT and the TIRM for the south beam. Because the mirror mounts in the south beam were known to cause mirror distortions, we assumed that phase errors in the beam might be misleading the ACMT and limiting beam quality. The mirrors were then removed, remounted to minimize aberrations, and replaced. After remounting, differences between optimal parabola alignment and focus as determined by the ACMT or TIRM were within experimental uncertainties.

Photographs of the spots at various out-of-focus positions for optimal parabola alignment are shown in Figs. IV-8 and -9. This "best" alignment was obtained by alternating between the TIRM and ACMT, using the TIRM last for fine adjustments.

Views of the optimal in-focus spots are shown in Fig. IV-10. The widths of the spots are not significantly larger than those of the image of a small pinhole: 55 μm FWHM for the north-beam spot and 50 μm FWHM for the south-beam spot. (The peak to the right of the south-beam spot is a defect in the south TIRM camera and should be ignored.) Thus, the spots are significantly tighter now than with the original parabolas. Without calibrated cameras, however, a true measurement of the Strehl ratio must be obtained from an encircled-energy measurement.

Attempts to Measure Focal Spot on Full-Power Shots. Attempts were made to measure the focal spot during a full-power shot by using a hole grating with an attenuation of 10^7 . However, noise pickup from the trigger generators and, possibly, the main discharge upset the timing of the sweep voltages in the camera during the frame of interest. Although the ACMT cameras were not similarly affected, changes in cabling, grounding, and synchronization circuits did not correct the problem. A solution appears to require significant changes to the camera circuitry, or shielding of the camera body.



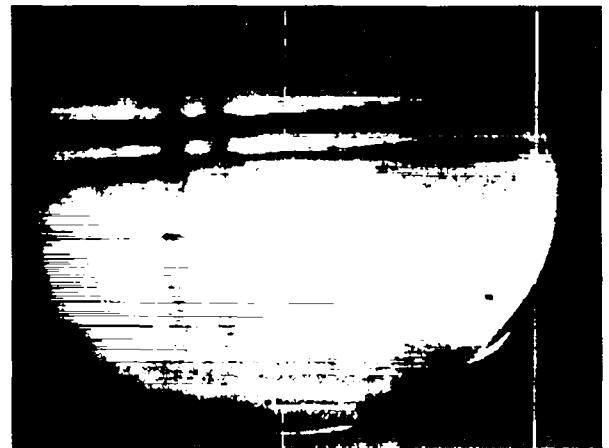
(a)



(b)



(c)



(d)

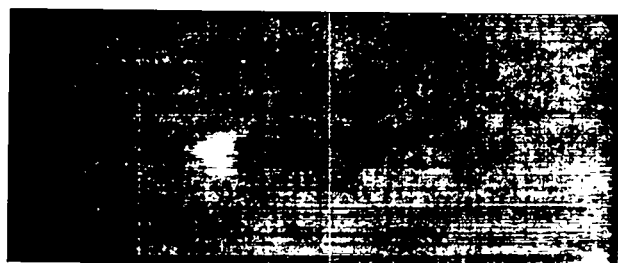
Fig. IV-7.

Photographs of monitor for north TIRM, showing images of a pointer, an $\sim 200\text{-}\mu\text{m}$ GMB, a $128.3\text{-}\mu\text{m}$ mesh, and double crosshairs with $160\text{-}\mu\text{m}$ center-to-center spacing between the vertical wires.

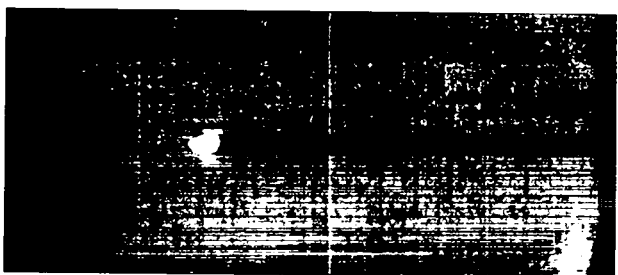
Conclusions. Our experience with the TIRM systems indicates that the microscopes should be of significant help in the alignment of laser beams on targets. The ACMT and TIRM systems are complementary, and much was gained by switching back and forth between the two systems in the process of finding the optimal parabola alignment.

Alignment time, and time between shots, is presently reduced by the following procedure. The

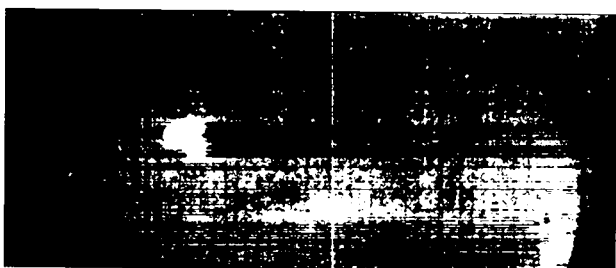
ACMT is used to carefully check beam focus and to verify that no significant pan or tilt errors in parabola alignment exist. The TIRM is then used to determine the positions of all the targets on the wheel by use of the illumination laser. Before each shot, the TIRM is used to adjust the pointing of the beams for the target to be shot. The focus adjustment should not require checking more than twice per day.



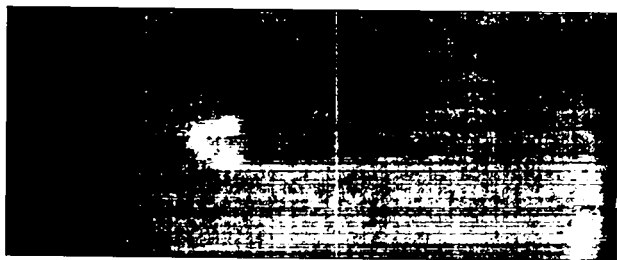
(a)



(b)



(c)



(d)

Fig. IV-8.

TIRM views of north beam near focus with the new parabola. (a) $\sim 800 \mu\text{m}$ inside focus, (b) $\sim 400 \mu\text{m}$ inside focus, (c) $\sim 400 \mu\text{m}$ outside focus, (d) $\sim 800 \mu\text{m}$ outside focus. Compare Fig. IV-9.



(a)



(b)



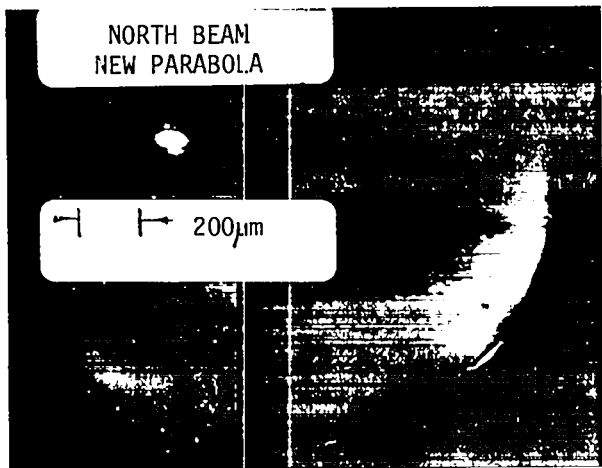
(c)



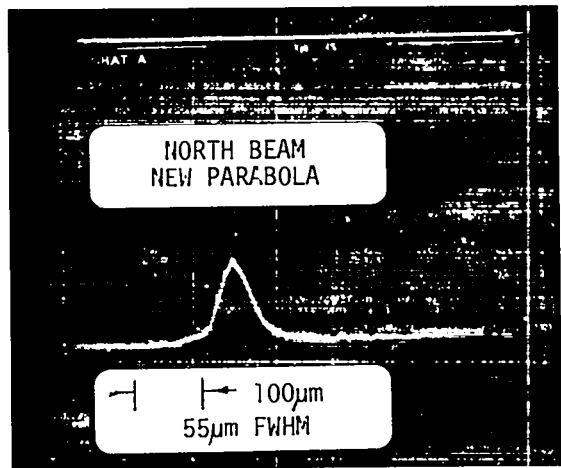
(d)

Fig. IV-9.

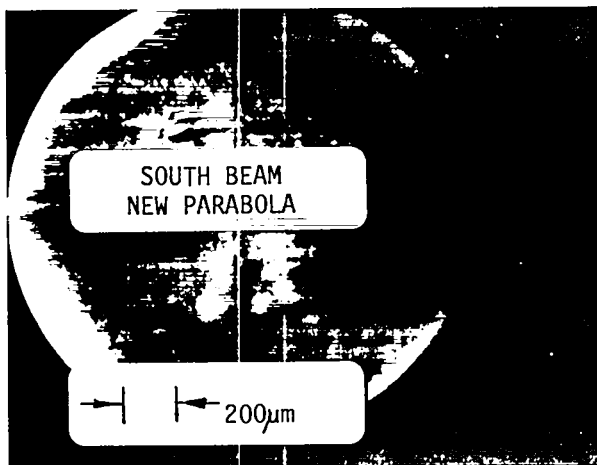
TIRM views of south beam near focus with the new parabola. (a) $\sim 1 \mu\text{m}$ inside focus, (b) $\sim 500 \mu\text{m}$ inside focus, (c) $\sim 500 \mu\text{m}$ outside focus, (d) $\sim 1 \mu\text{m}$ outside focus. Compare Fig. IV-10.



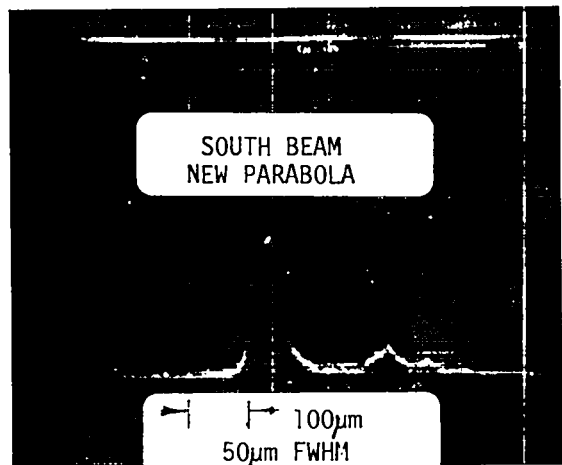
(a)



(b)



(c)



(d)

Fig. IV-10.

TIRM views of focal spots; (a) and (b), north beam; (c) and (d), south beam. Compare Fig. IV-8.

Note that the above procedure assumes that the target wheel is of good quality; i.e., that the position of targets is repeatable as the wheel is rotated and returned to the original orientation. If the wheel is "sloppy" and target position is not repeatable within $\sim 20 \mu\text{m}$, no alignment technique can be guaranteed to better accuracy than this.

Our measurements indicate that the TBS focal spots have widths of $\sim 50 \mu\text{m}$ FWHM, comparable to the TIRM point spread function width. No beam breakup or hot spots were observed within several hundred micrometers of best focus. Our data tend to indicate a significant improvement in Strehl ratio (peak irradiance) over previously measured values.

Encircled-Energy Measurement (J. J. Hayden, I. Liberman, V. K. Viswanathan)

General. Encircled-energy measurements were made on the TBS. During preparations for measuring the transmission through pinholes of various sizes (50, 100, 200, 400, and 800 μm in diameter), several points on alignment stability were noted.

- Target positions on Wheel II were not repeatable to better than $\pm 20 \mu\text{m}$.
- Target positions change when forces are applied to the target chamber (people leaning on or getting into it). The target does not return to its original position when the force is removed.
- Alignment stability on the south beam was very good.
- An unexplained discrepancy existed on the north beam between the Hartmann and ir vidicon alignments. Focus between the two methods differed by $\sim 500 \mu\text{m}$.
- During the north-beam full-machine shots, an alignment instability was noted. At one time the pointing had moved about 150 μm within 10 min.
- The energy split-off reading in the front end did not correlate well with the energy reaching the inside of the target chamber.

Experimental Technique. The pinholes were aligned by using both the Hartmann ball technique and the TIRM. After Hartmann alignment, the pinhole was backlit and viewed on the TIRM. After the position of the pinhole had been marked on the TV monitor, front-end pulses were viewed by the TIRM, and final pointing adjustments were made to place the front-end pulse in the center of the pinhole.

Energy passing through the pinhole was measured on a small calorimeter. Shot-to-shot energy variations were measured on a microjoulemeter, which was driven by energy reflected from the target-chamber input salt window. After transmission data had been taken, a blank space on the target wheel was rotated into position and total beam energy was measured. For full machine shots using the 10^6 hole plate attenuator, total beam energy was measured by using the 400- μm pinhole to block all undesirable orders generated by the hole plate.

We observed that two types of breakdown affected transmitted energy: air breakdown and surface

breakdown. The original intent was to run measurements in air at atmospheric pressure, but more reproducible results were obtained by making measurements in vacuum. However, surface breakdown of the pinhole material, when permitted to occur, still affected measurements.

Results. Table IV-II shows values of transmitted energy as a function of pinhole size for the two beams. No breakdowns were observed in taking these data. The data do not fit calculations based on typical aberrated beams. However, our best calculations indicate a Strehl ratio for the north beam of 0.23 and of 0.3 for the south beam. The data taken with the full machine had lower transmission values than data taken the previous week because of the alignment problems mentioned earlier. However, the transmission of the front end only was measured at the same time, and no degradation of the beam caused by firing the power amplifier was detected. On the contrary, energy passing through the 100- μm pinhole was 19% higher when the full machine was fired.

In addition, we measured the transmission with intentional surface breakdown of pinhole material. The measurements listed in Table IV-III show that for the 100- μm pinhole, energy transmitted drops from 75% without breakdown to $\sim 41\%$ with breakdown.

Conclusions. The focal-spot quality was improved considerably over that of a few years ago. The Strehl ratio improved from 0.07 to between 0.23 and 0.30 and the spot diameter decreased from $\sim 250 \mu\text{m}$ to under 100 μm . This improvement can only be attributed to replacing the paraboloidal focusing mirrors and remounting the large mirrors with decreased mounting distortions.

The Hartmann test alone is not capable of providing pointing precision under 25 μm because the basic assumption that the surrogate ball and target are coincident is not true due to target-wheel jitter. This problem should not exist in Helios because of the change in insertion mechanisms and verification by the autocollimating microscopes.

At times the alignment drift (150 μm in 10 min) is intolerably large with any alignment technique. Improving the stability of optics support components in the target chamber and amplifier is recommended.

TABLE IV-II

TBS TRANSMITTED ENERGY AS A FUNCTION OF PINHOLE SIZE WITHOUT BREAKDOWN

Fraction of Machine Fired	Pinhole Diameter (μm)	North Beam		South Beam	
		Transmitted (%)	Energy Level (μJ)	Transmitted (%)	Energy Level (μJ)
Front End ^b	50	20	224	26	75
" "	100	75	537	86	341
" "	200	100	338	88 ^a	463
" "	400	---	---	100 ^a	1226
" "	800	---	---	100 ^a	1573
Full Machine	100	57	854	---	---
Front End	100	48	216	---	---

^aData taken in air.

^bIncludes oscillator and preamplifiers.

TABLE IV-III

TBS TRANSMITTED ENERGY AS A FUNCTION OF PINHOLE SIZE WITH BREAKDOWN

Fraction of Machine Fired	Pinhole Diameter (μm)	North Beam	
		Transmitted (%)	Energy Level (μJ)
Front End	100	42	2215
" "	100	41	3522
" "	100	36	5213
" "	100	46	5936
Front End	200	84	1058
" "	200	94	2693
" "	200	90	6775
" "	200	85	9732

A beam of uniform intensity will have the smallest focal spot relative to any other profile having the same f number if the phase errors are small and identical. Based on limited data in firing the entire machine, and thus creating a more uniform energy

distribution, the above effect was observed and corroborates previous experimental and theoretical findings that the final amplifier does not introduce observable optical phase distortion.

Compression Measurements of Neon-Filled GMBs Irradiated by CO₂ Laser Light (K. B. Mitchell, D. B. van Hulsteyn, G. H. McCall, Ping Lee, H. R. Griem*)

Seeding GMB targets filled with deuterium-tritium (DT) mixtures with neon has received considerable attention recently in the laser fusion community, because the neon affords a method for measuring target compression.^{10,12} Yaakobi et al.,¹⁰ irradiating neon-filled targets with a four-beam Nd:glass laser, observed Stark-broadened neon lines that indicate electron densities of $7 \times 10^{22}/\text{cm}^3$. Key et al.,¹¹ reported spatially and spectrally resolved Stark-broadened neon lines emitted from GMBs imploded by a two-beam Nd:glass laser. Electron densities of $1.7 \times 10^{23}/\text{cm}^3$ were obtained. We at LASL investigated spatially resolved, Stark-broadened neon lines produced in our two-beam CO₂ laser experiments. In particular, we compared the compression as determined by measuring the neon core size to the compression indicated by fitting the observed line profiles to those expected from Stark broadening.¹⁸

The targets used in the experiment were 180- μm (nominal)-diam GMBs with 1.1- μm wall thickness filled with DT-neon mixtures at pressures ranging from 0.7 to 10 atm. The neon mass density in all cases was 0.9 $\text{mg}/\text{cm}^3/\text{atm}$ as opposed to the DT density of 0.225 $\text{mg}/\text{cm}^3/\text{atm}$; i.e., neon atoms constituted 10% of the total number of gas molecules. The TBS laser produced from 0.1 to 0.8 TW on target with a pulse length of 1.2 ns FWHM.

A flat thalium-acid-phthalate (TAP) crystal (2d = 25.75 Å) spectrometer with two (24- and 65- μm -wide) slits was used to obtain time-integrated, spatially resolved spectra over the range of 9.7 to 14.7 Å. The slits provide spatial resolution while the crystal gives spectral resolution. The spatial magnification of the spectrograph was 3.05X, and the rocking angle of the crystal was 3 arc-min (0.87 mrad) over the wavelength range of interest. Kodak RAR 2490 film¹⁴ was used to record single-shot exposures.

A spatially resolved x-ray spectrogram from an 8.6-atm DT-neon filled target is shown in Fig. IV-11. The slit width in this case was 65 μm . The observed features include neon and sodium lines in first order and silicon lines in second order. The silicon and

*Department of Physics and Astronomy, University of Maryland.

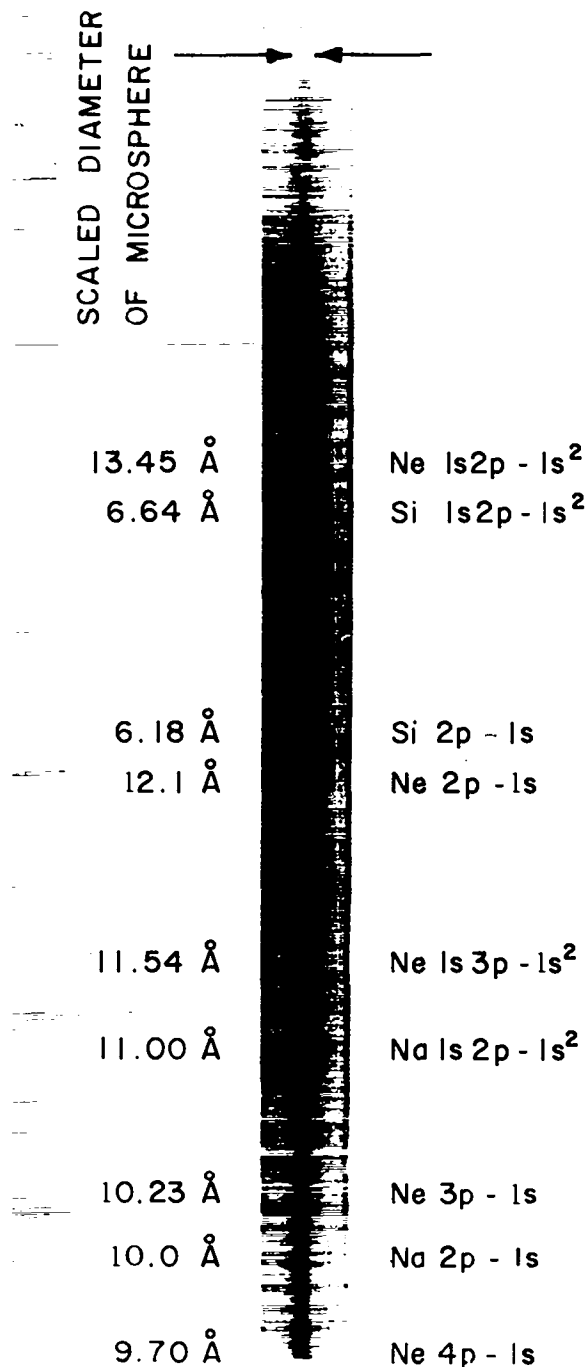


Fig. IV-11.

Spatially resolved x-ray spectrogram from a GMB target. The helium-like silicon and sodium lines have a spatial extent of about 180 μm , the diameter of the target. All the neon lines in the center of the spectrogram have a spatial extent of 45 μm .

sodium helium-like lines have a spatial extent of $\sim 180 \mu\text{m}$, which is the diameter of the target. All the neon lines appear in the center of the spectrogram and have a spatial extent of $\sim 45 \mu\text{m}$. This result provides direct and unambiguous evidence of compression.

These spatial differences can be seen more graphically in the microdensitometer scans shown in Fig. IV-12. The lower trace is a scan through the center of the spectrogram (i.e., through the core of the plasma). The upper trace is at the edge of the spectrogram and, therefore, scans the corona of the plasma. Helium-like lines of sodium and silicon dominate in the corona of the source. Hydrogen-like lines of silicon and neon are present only in the core. Furthermore, the continuum is observable only in the core.

Intensity ratios of silicon and neon lines indicate that the core is nearly 100 eV hotter than the corona.

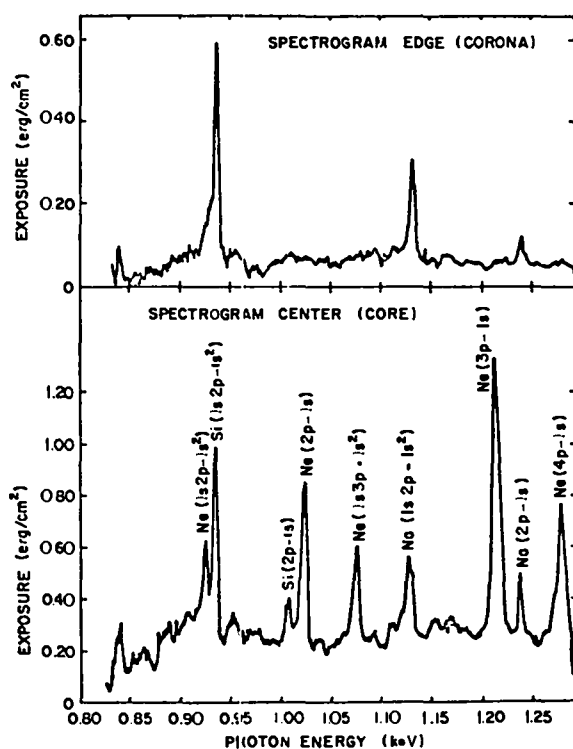


Fig. IV-12.

Microdensitometer trace gives a scan through the edge of the spectrogram, i.e., the corona of the plasma. The lower trace is a scan through the center of the spectrogram, i.e., the core of the plasma. Note the position dependence of various lines.

Analysis of neon-like ratios yields core temperatures in the range of 350 to 400 eV when opacities of neon lines are taken into account.

To evaluate the physical size of the source, it is necessary to scan perpendicularly to the direction of spectral dispersion. Unfortunately, the determination of the spatial distribution of the compressed core from this scan is complicated by the fact that the slit width is about equal to the source diameter. However, before considering the effect of finite slit width, it is important to convert film density to x-ray intensity and to subtract the continuum background. Once these responses have been taken into consideration, the effect of slit width upon x-ray intensity on the film, $I(x)$, is given by

$$I(x) = \frac{1}{2\delta} \int_{x-\delta}^{x+\delta} S(x') dx', \quad (\text{IV-1})$$

where $S(x)$ is the spatial intensity distribution from the source, $\delta = w(1 + M^{-1})/2$, w is the slit width, M is the magnification, and diffraction is neglected.

The source distribution, $S(x)$, can be determined, in principle, by differentiating Eq. (IV-1), but noise in the data makes this approach impractical. Instead, a least-squares fit of an assumed source function to the data was performed by using Eq. (IV-1) directly. We found that the fit was not sensitive to the form of the assumed function, but the geometry of the spectrograph and the image distribution suggested a function with intensity proportional to the length of a chord of a cylinder in the viewing direction. This function was perturbed by a polynomial to give a trial source distribution of the form

$$S(x) = [1 - (x/R)^2]^{1/2} \sum_{i=0}^n C_i x^i. \quad (\text{IV-2})$$

Figure IV-13 shows the result of this procedure. The solid curve is the intensity distribution at the film in the spatial direction, the dashed curve is the source function, $S(x)$, from Eq. (IV-2), and the dotted curve is the result of substituting Eq. (IV-2) into Eq. (IV-1). For this case the diameter of the compressed region is $64 \pm 2 \mu\text{m}$. This approach can be used to determine the diameter of the compressed core to an

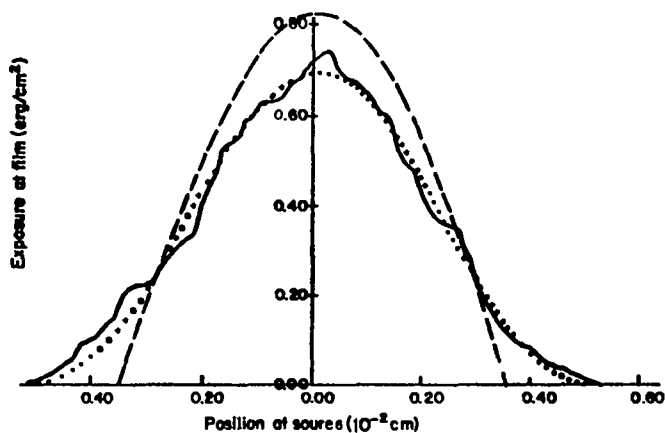


Fig. IV-13.

Determination of intensity distribution, $S(x)$, across the source for the neon $L\beta$ line. The solid curve is a microdensitometer scan along the spatially resolved direction of a neon $L\gamma$ line. The dotted curve is a reasonable estimate of $S(x)$, and the dashed curve is the "best fit" to experimental profile using Eq. (IV-1). The source size in this case is $64 \pm 2 \mu\text{m}$.

accuracy of 10% or better. Hence, the volume can be determined to within 30%. Table IV-IV summarizes the results.

Another significant feature of the spectra is the presence of Stark-broadened neon lines. Figure IV-14 shows a microdensitometer trace of a neon Lyman beta line taken in the spectral direction. The dotted and dashed curves are "best fits" to the experimental-line profile based on calculations of Griem and Kepple.¹⁸ Doppler effect, finite source size, and crystal rocking angle have been folded into the Stark profile. The dotted curve is for the case

where the opacity at line center, τ_{max} , is 0; the dashed curve corresponds to $\tau_{\text{max}} = 1$. It can be seen that both curves fit well at the wings and both imply an electron density of $1.9 \times 10^{22}/\text{cm}^3$; the final DT density is $1.0 \times 10^{22}/\text{cm}^3$, which is $\sim 20\%$ of DT liquid density. A Stark profile fit of the Lyman gamma line indicates a similar electron density, but the opacity at line center was only 0.3. With a temperature $T_e \sim 350 \text{ eV}$, the calculated densities of Ne X and Ne XI are found to be $3.0 \times 10^{20}/\text{cm}^3$ and $7.5 \times 10^{20}/\text{cm}^3$, respectively. Note that the observed Stark width of $21 \text{ m}\text{\AA}$ dominates the observed line width, while Doppler broadening, crystal rocking angle, and the effect of finite source size contribute only 2.0, 6.0, and $0.5 \text{ m}\text{\AA}$, respectively.

Self-consistent calculations of self-absorption¹⁶ indicate that the opacities at line center (τ_{max}) are 30, 1, and 0.3 for the Lyman α , β , and γ lines, respectively. The dominant broadening mechanism for the $L\alpha$ line is thus self-absorption, where $L\beta$ and $L\gamma$ are nearly optically thin and broadened primarily by the Stark effect.

In the Stark-broadening method of electron density measurement, an accurate fit to the wings of a line is very important,¹⁹ because the theory is quite accurate for this region of the profile. An estimated error of 25% or less due to noise and possible asymmetries in the actual lines usually exists in fitting the calculation to the experimental line profile.

The technique of source-size measurement and the Stark-broadening methods are compared in Table IV-IV for three shots with different laser powers on target. The neon densities deduced from the source size agree very well with the Stark results for all three shots. This agreement is a good indication that the extrapolation of the electric microfield

TABLE IV-IV

COMPARISON OF SOURCE-SIZE METHOD AND STARK-BROADENING CALCULATIONS FOR MEASURING COMPRESSED NEON DENSITIES

Shot	Target Fill DT + Ne (atm)	Laser Power (W x 10 ¹¹)	Initial Diam (μm)	Final Diam (μm)	Neon Density Volume Measurement ($\text{cm}^{-3} \times 10^{20}$)	Neon Density Stark Broadening ($\text{cm}^{-3} \times 10^{20}$)	Volume Compression (Stark)
RR-11	8	3.24	189	68	4.2 ± 1.3	5.8	30
RR-21	8	4.52	185	56	7.1 ± 2.0	9.5	48
RR-26	7	8.22	181	50	8.1 ± 2.4	7.9	46

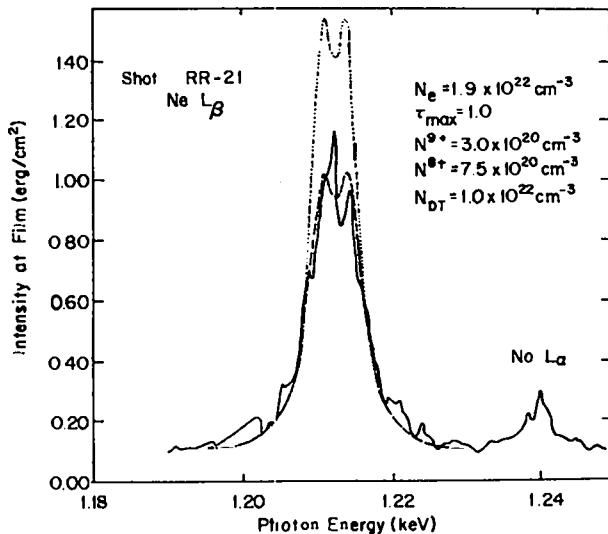


Fig. IV-14.

Density determination: Fitting of a Stark profile (dashed and dotted curve) for $N_e = 1.9 \times 10^{22} \text{ cm}^{-3}$ to the experimental line profile (solid curve). The dotted curve is for the case where the optical depth at line center, τ_{max} , is zero. The dashed curve is for the case $\tau_{\text{max}} = 1$.

effect used in Stark-broadening calculations to high densities ($\sim 10^{22}/\text{cm}^3$) is reasonable. Note that volume compression is relatively independent of laser power. This agrees well with the exploding-pusher model,¹⁶ which assumes that the fuel and the pusher are in thermal equilibrium.

MILITARY APPLICATIONS OF LASERS AND RELATED STUDIES

Introduction

In the first half of 1978, activity in the two-beam Nd:glass laser facility increased considerably. Not only were all the previous experiments continued, but new efforts were added, most notably the calibration and testing of the GEAR fast x-ray camera (described in the Diagnostics Section), and preparations for a visiting National Bureau of Standards group to do far-ultraviolet spectroscopy of refractory metals irradiated by a focused laser beam. Laser reliability and performance have been

improved significantly, which is most important because all available time is committed months in advance.

The remainder of this section will treat in detail the following subjects:

- Operation of and modifications to the Nd:glass laser facility,
- Laser equation-of-state measurements,
- Laser-driven high-pressure-shock studies,
- Multiburst simulation,
- Opacity experiments, and
- Modification of material properties by strong shocks.

Nd:Glass Laser Facility—Operation and Modification (A. Engelhardt, R. Robertson, I. V. Johnson, M. E. Powers)

A total of 687 target shots were logged, 554 of which were of good quality, i.e., delivering useful energy to the target (5 to 47 J/beam). The success ratio was thus 81%. An additional 50 shots through the entire system were made for alignment and equipment checks. The majority of these 737 shots were of 300-ps duration (FWHM) and for one beam only. Eight shots were made with two beams at 70 ps and 22 shots with one beam at 70 ps.

The amount of energy split into B- and C-beam lines was adjusted to increase the energy input to the B-beam relative to the C-beam. A 70% reflecting mirror produced a nearly balanced output of the two beams and compensated for the larger amplification in the C-line, which is on the 30% transmitting side of the splitter mirror.

Changing the pulse width from 300 ps to the minimum of 70 ps was accomplished simply by removing an etalon from the oscillator cavity; replacing this etalon stretched the pulse width once more to 300 ps. The etalon is a 2-mm-thick fused quartz disk with 20% reflective coatings on each side.

Design and fabrication of an improved safety interlock system was nearly completed. A more restrictive system was needed because of the increased traffic through the laser area to the new computer facility next door. Each hazardous operation is enabled by its own set of input conditions, which are logical combinations of door and manual switches, beam blocks, and commands from the

laser operator's console. Modular construction allows changes in procedures or rules to be accommodated easily.

Design of new mounts for the Pockels cells of the single-pulse switchout portion of the laser was started. These mounts will permit precise alignment of the Pockels cells and will thereby improve the discrimination ratio between the switched-out pulse and the rest of the oscillator train.

An improved dye cell to replace the one in the oscillator cavity was being fabricated. This cell will improve the dye-flow pattern and should improve oscillator reliability. However, the main reliability problem stems from the spark-gap and Pockels-cell unit and from the failure to switch out a pulse consistently.

Laser Equation-of-State Measurements (J. Solem, L. Veese)

Our results to date are summarized as follows. By using a streak camera, we can see the light which appears at the back of an aluminum foil that has been shocked by a laser pulse of 20 to 30 J (1.06- μ m wavelength, 300-ps-long pulse, 100- to 200- μ m-diam spot). The risetime of the luminosity is less than the 50-ps resolution of our present instruments, indicating that the shock front must be less than 0.7 μ m thick. The shock intensity appears to dissipate as the shock moves through the material, as thicker foils produce dimmer streaks of light. After the shock arrives at the back of the foil, the surface remains hot for some time, leaving on the streak-camera image a tail, from whose motion we can infer the motion of the shocked material. We measured shock velocities of 1.3×10^9 cm/s for laser pulses of 3×10^{14} W/cm² striking 13- μ m-thick foils.

Laser-Driven High-Pressure Shock Studies (L. Veese, J. Solem, A. Lieber)

Because we were unable to obtain a high-speed GEAR streak camera for our laser-induced equation-of-state work, we spent several weeks using a slower

LASL-built camera to do development work. We determined that fiber-optics coupling of the target to the camera is presently feasible because of low light levels. Also, we spent considerable time checking a report from LLL¹⁷ indicating that shock waves are much more intense in targets of their design (1-mm-diam foils suspended on fibers) than in ours (foils covering a 6-mm-diam hole in a heavy backing). The suspected cause of the difference was energy propagating radially in our targets, weakening the shock wave. We could not find evidence for much change in shock intensity as a function of foil diameter, but we did notice considerable heating of the edges of the small foils, perhaps from ion currents near the target. This edge heating may have obscured the shock breakthrough in the Livermore experiments.

Multiburst Simulation (S. N. Stone, M. D. Wilke, and G. E. Barasch)

General. Laser microfireball experiments started previously to simulate the nuclear multiburst environment were continued and were expanded to include simulations of nuclear attacks on underground systems (missile silos, MX trenches).

Shocks in Air.

(1) $0 < t < 1$ ns. The two-dimensional camera diagnostic processing was used to compute laser energy deposition onto the thin-wall plastic-shell targets we use to produce microfireballs in low-pressure air. When the targets, 0.5 mm in diameter with a 4- μ m-thick wall, were irradiated, the laser-induced plasma was highly asymmetric at the end of the 0.3-ns laser pulse. Plasmas of higher density and velocity were created on the part of the wall irradiated by the laser beam. The computed plasma configuration agreed essentially with the fireball configuration observed at later times ($\gtrsim 1$ μ s) by emission photography. In addition, calculations predicted that 30% of the incident laser-beam energy is absorbed in the target plasma, in good

agreement with the 20 to 30% deduced from the fireball expansion radius-vs-time characteristics.

(2) $1 \text{ ns} < t < 200 \text{ ns}$. A fast photodiode was used to measure visible-light emissions from laser-driven microfireballs from initiation to 200 ns. For 15- to 20-J sparks in 580-torr air (sparks are caused by breakdown near the laser focus, without a material target), a minimum in emitted light power was observed at ~ 30 ns. This minimum time is in fair but surprising agreement with predictions of minimum-time scaling laws derived from full-scale atmospheric nuclear fireballs. We are considering a physical interpretation of the observed optical minima.

(3) $t > 0.2 \mu\text{s}$. Radius-vs-time plots for computed and observed laser-induced microfireball shock fronts in 1- to 50-torr air are in good agreement at times ($\geq 1 \mu\text{s}$) when the shock-entrained air mass is large compared to the target mass. Before such times, perturbing effects of the target mass were identified. Equivalent early-time source-mass-induced perturbations were documented for nuclear fireballs.

A critical test of multidimensional fireball codes can be obtained by comparing computed and measured air density profiles behind the shock front of laser-driven microfireballs. Specifically, we have to compare the profiles computed for late times (5 to 50 μs) and large radii (1 to 4 cm) with those derived from interferograms. The preliminary results show that the computed and measured profiles have the same shape, although the computed peak densities are $\sim 50\%$ higher than the observed values.

Shocks in solids. Preliminary studies were conducted of shocks propagating in Plexiglas slabs, in glass tubing, and across air-to-solid interfaces. Holographic interferometry and multiframe shadowgraphy, developed to diagnose air shocks, are the diagnostic methods employed. An interferogram taken several microseconds after laser irradiation of a point at the surface of a 4-cm-thick slab of Plexiglas is shown in Fig. IV-15. The shock fronts are visible as fringe discontinuities, both in the air outside the block and in the block, where reflections from the back and side walls are also visible. In addition

to the circular shocks, the fringe patterns show the presence of a narrow, strongly disrupted region propagating into the block from the irradiated surface. The cause of this effect is not understood. In future work, holes can be drilled in the Plexiglas blocks to simulate missile silos and trenches.

Opacities of Metal Plasmas (N. H. Hoffman, L. W. Miller, and J. M. Mack)

We used a television camera and videotape system to record the output of a high-speed streak camera viewing the back side of aluminum foil laser targets. Our long-range goal is to measure relative opacities of hot, dense metal plasmas by using the limb-darkening technique. This technique was discussed briefly in Los Alamos Scientific Laboratory report LA-7328-PR (1977) and is covered in more detail in another report.¹⁸

Most of our work was performed with foils whose thickness is $12.5 \mu\text{m}$ (0.5 mil), although some shots were made with 18- (0.75-) and 25- μm (1.0-mil) foils. Thus we fulfilled the condition that the laser spot size ($\sim 150 \mu\text{m}$) be much greater than the foil thickness, so that the initial plasma is planar.

Because the plasma is planar, we must view it along a number of different lines of sight to observe the limb-darkening. A straightforward way is to construct at least two identical observing systems, each with a different viewing angle with respect to the plasma normal. An example of such an arrangement is shown in Fig. IV-16. Streak cameras provide spatial and temporal resolution, which are required to allow for beam nonuniformity and to discriminate against unwanted light. Television cameras and videotape recorders are convenient and sensitive data-recording media.

We constructed one such line of sight for our present observations (Fig. IV-17), using a Hadland Imacon 700 streak camera and a Cohu 4400 low-light-level SIT TV camera. An IVC videotape recorder, a videodisk unit, and two small TV monitors, obtained in house, completed the setup.

The Imacon was operated at a streak rate of 1 ns/mm. Its photocathode had an S-20 response. It was triggered by a portion of the laser oscillator pulse, which was switched out before passing

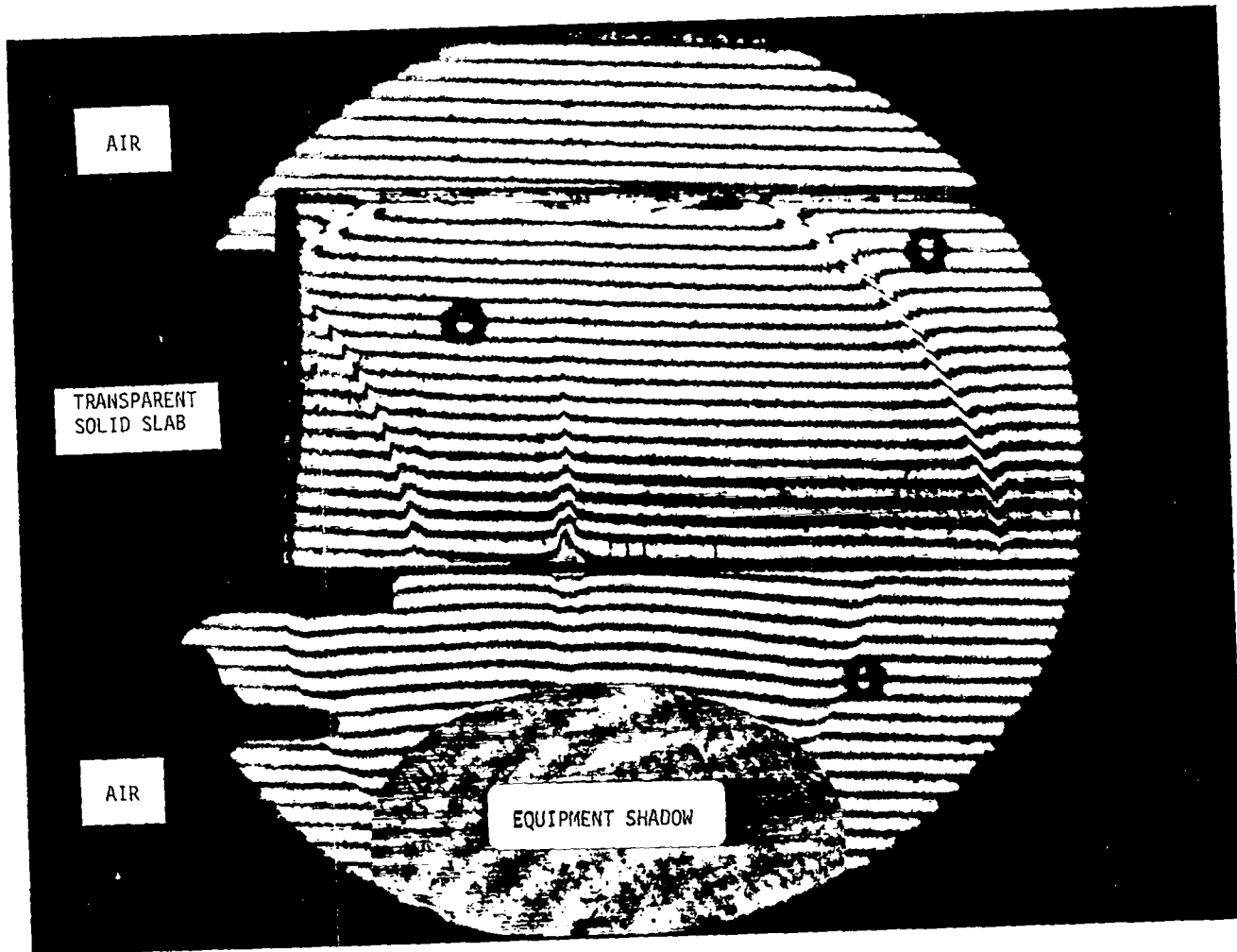


Fig. IV-15.

Weapon effects simulation in solids by laser-induced shocks. A 27-J, 300-ps Nd:glass laser pulse was incident from below through 20-torr air. The f/4 beam was focused on the lower surface of the 4-cm-thick Plexiglas slab. The 30-ns pulsed ruby laser holographic interferogram exposure was recorded 15 μ s after shock initiation. The three small open circles are fiducial marks.

through the main laser amplifiers. The trigger pulse passed through a single small YAG amplifier and then to a trigger photodiode that generated an electrical pulse to trigger the Imacon.

The TV camera was modified to allow manual gain adjustment. We operated it at maximum gain.

The TV camera was about 10 times more sensitive than Polaroid ASA 10 000 film, which we also tried as a recording medium, using a Hadland film back with lens coupling.

The TV camera was allowed to free-run, without synchronization between the laser pulse and the

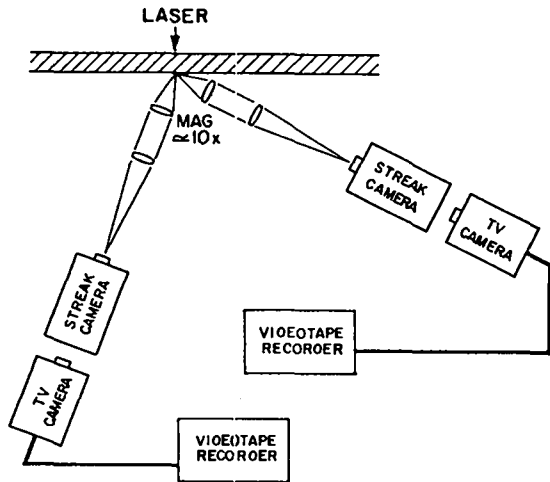


Fig. IV-16.

Simple scheme for detecting the existence of limb darkening in a planar plasma.

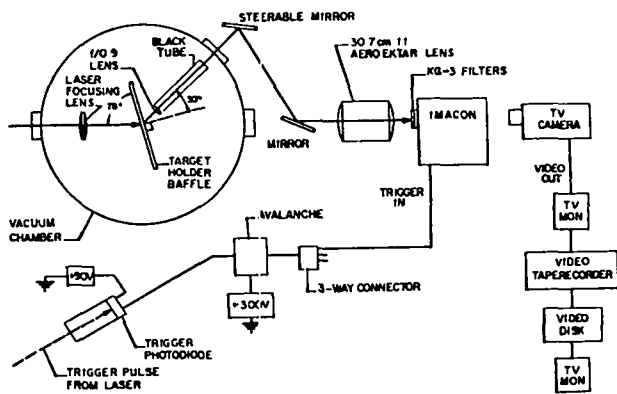


Fig. IV-17.

Experimental layout for observing back side of laser target. See text for discussion.

readout of TV frames. Thus, the pulse sometimes occurred in the middle of a readout. This was inconvenient although not critical; in the future we will externally blank the readout until after the pulse.

The system was sensitive enough to provide a ten-fold magnification of the image of the backside plasma and still record a usable signal. Thus, if the plasma is $150 \mu\text{m}$ across, its image is $\sim 1.5 \text{ mm}$ across at the Imacon photocathode. Because the dynamic spatial resolution of the Imacon is probably from 3 to 5 line pairs/mm,¹⁹ we have from 4 to 8 resolution elements across the plasma. This allows us to measure

the center-to-edge brightness variation due to laser-beam nonuniformity.

Magnification was achieved by placing a small f/0.9 lens of $\sim 3\text{-cm}$ focal length inside the vacuum chamber so that the plasma was at its focus. The collimated light exited the chamber and was refocused onto the Imacon photocathode by a large lens of 30.7-cm focal length. Extensive light-baffling covered the entire line of sight to exclude scattered front-side light. The exterior mirrors could be removed easily to give us a 15° viewing angle instead of the 30° angle shown.

The videotape recording of the streak-camera data was digitized and then written out on magnetic binary tape for further reduction. A TV monitor photograph of a typical streak-camera record is shown in Fig. IV-18. The time axis increases downward and the spatial axis runs horizontally. The rectangle at the top of the frame is the static image of the photocathode recorded before the Imacon is triggered.

The streak is characterized by a bright flash at its origin followed by a fainter tail. The variation in brightness across the streak indicates nonuniform

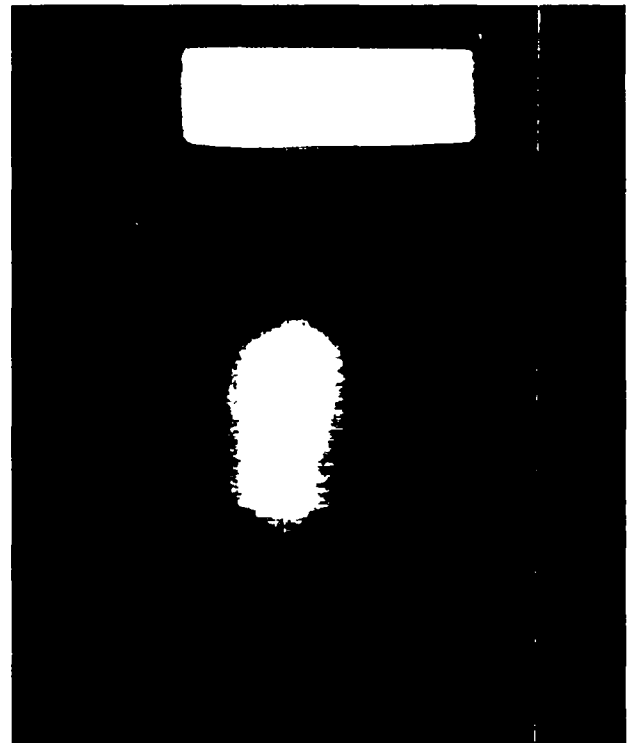


Fig. IV-18.

TV monitor photograph of a TV frame of videotape data.

heating of the plasma. The Nd:glass laser shot contained 26 J and had a pulse width of 300 ps FWHM; the target was 12.5- μm -thick aluminum foil. The viewing angle was 30°. The laser beam axis formed a 15° angle with the target normal. The exposure was made in white light; the observational band was determined by the S-20 photocathode response and the KG-3 laser light filters protecting the *Imacon*. The streak was $\sim 200 \mu\text{m}$ across and ran for $\sim 10 \text{ ns}$.

More detail is apparent in the contour plot of the same TV frame shown in Fig. IV-19. This plot was produced from the digitized data using the TV reduction codes developed by Gow.²⁰ The contours show levels of constant video amplitude. The initial flash has a roughly circular core $\sim 100 \mu\text{m}$ across. The shape of the core is apparent because we did not use a slit to reduce spatial smearing along the time axis. Thus, both time and space information appear along the vertical axis, as indicated by the vertical arrow showing the time and space scale. The total field of view is ~ 600 by $800 \mu\text{m}$. In future shots we may use a slit to reduce the field of view in one dimension, permitting higher time resolution. Alter-

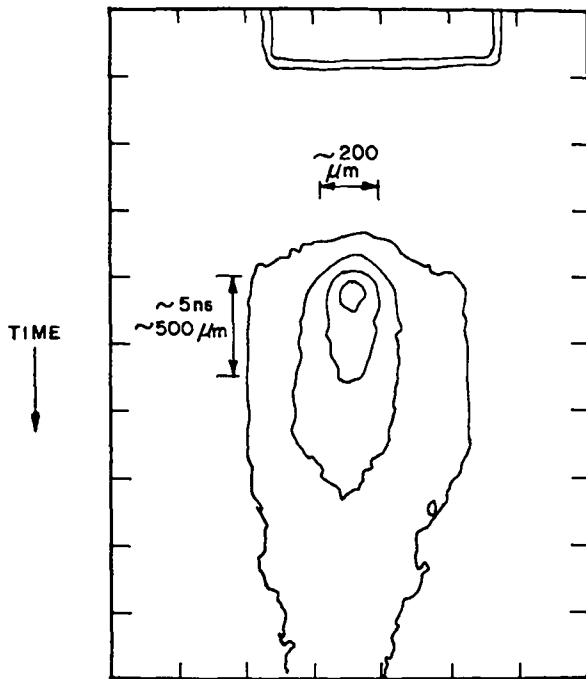


Fig. IV-19.

Contour plot of the TV frame shown in Fig. IV-18. Contours of constant video amplitude are shown.

natively, demagnifying the plasma image also permits higher time resolution, at the expense of space resolution.

To observe limb darkening, we need a relative-intensity calibration of the observing system, which can be performed by using a xenon flashlamp as a source and introducing various degrees of neutral-density attenuation. To measure temperature as a function of optical depth we need an absolute calibration, for which the calibrated xenon flasher may be useful.

To begin measuring limb darkening, one might simply assemble a second identical observing system as shown in Fig. IV-16. A more elegant procedure is to construct an optical device, which allows several different views of the plasma to be recorded on a single streak camera.

Such an arrangement is shown in Fig. IV-20. This arrangement permits viewing the target simultaneously along the target normal and at an angle of 30° to the normal. Note that both views form the same angle with the laser beam and therefore will not detect intensity variations due to an angular correlation between the laser beam and the emitted radiation. (Such a correlation can be easily investigated with the same arrangement.) The two optical paths are identical. The light acceptance cone is $\sim f/2$, which will give sufficient resolution of

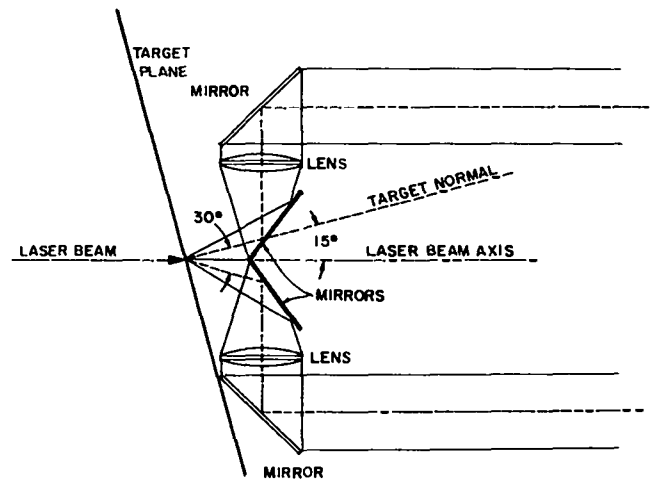


Fig. IV-20.

A possible design of an optical arrangement to permit viewing two angles along a single line of sight.

the direction of the emitted radiation and will also collect an amount of light sufficient to measure with the Imacon-TV system.

An arrangement such as this, perhaps with an additional optical path to permit viewing the target at an angle of $\sim 60^\circ$ from the normal, should be adequate to demonstrate the existence of the limb-darkening effect. Because this effect may occur at angles considerably less than 90° from the normal, there may be no need for observations at or near grazing angles, which would be more difficult.

Use of Laser Beams to Study Strong Shocks in Materials (J. M. Mack and J. Petrovic)

General. About 15 separate experiments were conducted on our Nd:glass laser with various target materials (aluminum foils, aluminum oxide, silicon nitride, silicon carbide) to ascertain whether high-power lasers could induce strong-enough shocks through these materials to cause material changes that could be determined after the fact. Figure IV-21 summarizes this program.

Laser Shock of Metals (Aluminum). The stress-strain characteristics of laser-shocked 1100 aluminum did show deviation from similar proper-

ties of the standard sample, but such changes were not dramatic. However, we feel that improved experimental technique will expose these kinds of transformations better. Electron-microscopic analysis of these aluminum samples clearly indicated significant alteration of the microstructure, which was evident in a dramatic increase of dislocation density. The dislocation density could possibly be used to indicate the average pressure of the laser shock wave traversing the sample. Knowledge of the average pressure is crucial to the correct interpretation of microstructural alterations and therefore will be given appropriate weight in subsequent studies.

Laser Shock of Ceramics. Three common high-strength ceramic materials, Si_3N_4 , SiC , and Al_2O_3 , were exposed to shock with our Nd:glass laser to see how well these brittle materials would withstand the laser shock conditions. The ceramic targets were in the form of rectangular bars because the ceramic strength after laser exposure could be determined by fracturing the bars in four-point bending, a common method of strength determination for ceramic materials.

The Si_3N_4 and SiC exposures were 6.3 by 12.2 mm in cross section by 25.4 mm long (0.25 by 0.5 by 1.0 in.) and the Al_2O_3 specimens were 6.3 by 6.3 mm in cross section by 38.1 mm long (0.25 by 0.25 by 1.5 in.). Laser energies ranged from 24 to 32 J, and the pulse time was 300 ps. The laser beam was focused on the front surface of the specimen, producing a spot size of 150 to 200 μm . No overlays were placed between the specimen surface and the laser beam. The specimens were backed by a brass plate.

In one case a rectangular Si_3N_4 bar specimen was completely fractured in half by the laser pulse. The fracture surface of the specimen showed an extensive rough region of substance fractures produced by the laser pulse. The fact that the specimen fractured in half indicated that large tensile stresses were produced in the specimen by the exposure.

Another Si_3N_4 specimen received two laser pulses, but did not fracture apart completely. Some material removal occurred at the laser spot, and large fractures initiated from this region but did not propagate completely through the specimen. Similar behavior was observed for SiC , although the SiC showed a larger amount of surface removal and spalling at the laser spot than did the Si_3N_4 .

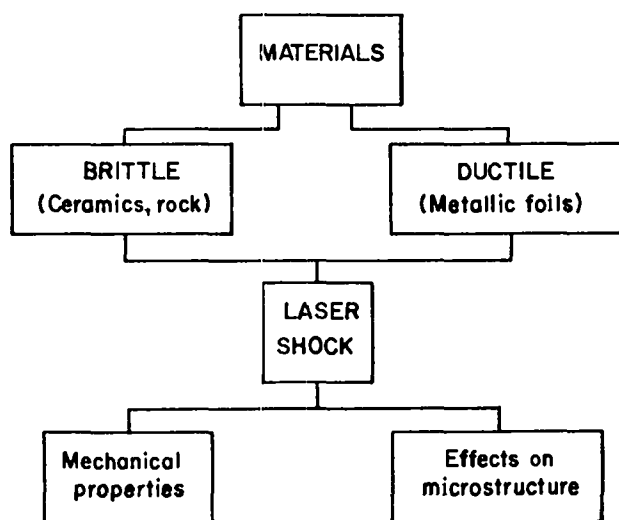


Fig. IV-21.

Program investigating effect of laser shocks in various materials.

TABLE IV-V

BEND TEST RESULTS ON LASER SHOCKED CERAMICS

<u>Bend Test No.</u>	<u>Material</u>	<u>Four-Point Bend Strength (psi)</u>	<u>Laser Shot No.</u>	<u>Laser Energy (J)</u>
1	Si ₃ N ₄	83 520	Unshocked	
3	Si ₃ N ₄	15 780	10	23.64
2	SiC	52 580	Unshocked	
4	SiC	15 310	8	32.31
6	Al ₂ O ₃	24 470	Unshocked	
7	Al ₂ O ₃	14 880	7	29.63

All laser-shocked specimens fractured from the site of the laser exposure.

We also exposed Al₂O₃ to the laser beam. In general, the Al₂O₃ was less affected by the laser shock than either the Si₃N₄ or SiC. Material removal at the laser spot was minimal, and no surface cracking from the laser spot was evident.

Effects of laser exposure on subsequent mechanical strength are tabulated in Table IV-V. Fracture strengths of both unshocked and laser-shocked specimens were measured in four-point bending. The fact that all laser-shocked specimens fractured in bending from the site of the laser exposure indicates that the material had been damaged mechanically by the laser pulse. The most severely degraded material was the Si₃N₄, followed by the SiC, while the Al₂O₃ was least degraded in mechanical strength by the laser pulse. All laser-exposed strengths for the three materials were about the same. The reasons for the differences in strength degradation among the three materials are unclear, although they might be entirely related to surface absorption of the laser pulse, because both the Si₃N₄ and SiC are black, whereas Al₂O₃ is white. In terms of resistance to a pulsed laser exposure at 1.06 μm, the Al₂O₃ was the most resistant material, showing little effect on either surface properties or mechanical strength, with no laser-induced cracking observed.

In summary, this laser-shock technique does produce the desired magnitudes of material alterations. We need detailed studies of the mechanical and microstructural effects on materials of interest.

The feasibility study was completed, and no major future effort is planned.

REFERENCES

1. T. H. Tan, G. H. McCall, A. Williams, and D. Giovanielli, "Laser Interactions and Related Plasma Phenomena," Fourth Workshop, Rensselaer Inst. (Plenum Press, New York, 1972), 4B, 677.
2. E. Stark and F. Skoberne, "Laser Fusion Program at LASL, January 1—June 30, 1976," Los Alamos Scientific Laboratory report LA-6510-PR, p. 78 (November 1976).
3. V. M. Cottles, Bull. Am. Phys. Soc. 22, 3K3, 1090 (1977).
4. J. G. Crow, P. L. Auer, and J. Allen, J. Plasma Phys. 14, Part 1, 65 (1975).
5. D. Forslund, K. Lee, and J. Kindel, PRL 39, 284 (1977).
6. D. R. Kohler and P. B. Weiss, "Use of Pyroelectric Vidicons for Measurements on CO₂ Laser Systems," in Proc. Topical Meeting on Inert. Confin. Fusion (Opt. Soc. Am., 1977, Publication 78CH1310-2QEA).

7. P. B. Weiss and D. R. Kohler, "Characterization of Pyroelectric Vidicons for Use with Pulsed CO₂ Lasers," *J. Opt. Soc. Am.* **67** (10), 1445 (1977).
8. D. R. Kohler and P. B. Weiss, "Measurements at 10.6 Microns with Pyroelectric Vidicons," *J. Opt. Soc. Am.* **67** (10), 1445 (1977).
9. J. P. Manning, Q. G. Klingler, C. J. Stump, and I. Liberman, "CO₂ Laser Fusion Target Alignment," *Proc. Topical Meeting on Inert. Confin. Fusion (Opt. Soc. Am., 1977, Publication 78CH1310-2QEA)*.
10. B. Yaakobi, D. Steel, E. Thorsos, A. Hauer, and B. Perry, *Phys. Rev. Lett.* **39**, 1562 (1977).
11. M. H. Key, R. G. Evans, D. J. Nichols, F. O'Neill, P. T. Rumsby, I. N. Ross, W. T. Toner, P. R. Williams, M. S. White, C. L. S. Lewis, J. G. Lunney, A. Moore, J. M. Ward, D. Brown, P. Carter, T. A. Hall, T. P. Hughes, P. Salter, E. Frabrikesi, A. Flaven, J. Murdoch, and J. Kilkenney, Rutherford Laboratory, Central Laser Facility report RL-77-122/B (September 1977).
12. D. S. Bailey, University of California Research Laboratory report UCRL-79861 (1977).
13. H. R. Griem, M. Blaha, and P. C. Kepple, submitted to *Phys. Rev.*; see also P. C. Kepple and H. R. Griem, Naval Research Laboratory report 3634 (1978).
14. R. F. Benjamin, P. B. Lyons, and R. H. Day, *Appl. Opt.* **16** 393 (1976).
15. R. D. Cowan and G. H. Dieke, *Rev. Mod. Phys.* **20**, 418 (1948).
16. D. V. Giovanielli and C. W. Cranfill, "Simple Model for Exploding Pusher Targets," Los Alamos Scientific Laboratory report LA-7218-MS (May 1978).
17. R. J. Trainor, J. W. Shaner, J. M. Averbach, and D. W. Phillion, "Laser-Generated Shock-Wave Experiments in Metals Above ITPa," *Bull. Am. Phys. Soc.* **23**, 105 (1978).
18. N. M. Hoffman, L. W. Miller, J. M. Mack, "The Limb-Darkening Opacity Experiment Using a Laser-Heated Plasma," Los Alamos Scientific Laboratory report LA-7484-MS (October 1978).
19. G. E. Barasch and M. G. Duran, Los Alamos Scientific Laboratory, personal communication, January 1978.
20. C. E. Gow, EG&G, Inc., personal communication, January 1978.

V. LASER FUSION THEORY AND TARGET DESIGN

Our theoretical support activities are closely coupled to our experimental efforts, with the intent of gaining a fundamental understanding of laser target interactions, particularly of the relevant plasma physics and hydrodynamics. The close coupling of theory and experiments has made it possible to eliminate theories that are not supported by experiment. In general, basic studies have shown that the design difficulties associated with long wavelengths are less severe than believed earlier, and that breakeven target designs are attainable even in the presence of a hot-electron spectrum. These results have significantly increased our confidence that scientific breakeven can be demonstrated with our efficient, inexpensive CO₂ lasers.

THEORETICAL SUPPORT AND DIRECTION

Introduction

The supporting physics section continued its efforts in analyzing electron transport, the processes involved in laser-light absorption and corona expansion, and in evaluating various diagnostics techniques. Two new theories of electron transport were developed and are being evaluated: the reduced-source method and the two-component method. To obtain maximum absorption symmetry in Helios laser target experiments, a program was written to compute the illumination and absorption asymmetries for various spot and target sizes. The emission of various harmonics from the target was analyzed to evaluate the value of that diagnostic tool. The effects of space charge on ion pinhole diagnostics were also assessed, and alterations in the expanding plasma corona due to the presence of various ion charge states were investigated.

Coronal Expansion With Multiple Charge States (D. Forslund)

The structure of the supersonic expansion of the outer low-density regions of a laser-irradiated pellet is known to depend sensitively on the laser inten-

sity¹ and on the electron distribution function.² In addition, various charge states in the expanding plasma can further complicate the expansion process. Indeed, experiments have shown that several different charge states are typically present and that the ions are accelerated at different rates,^{3,4} possibly because the acceleration rate of the ions in the ambipolar field is proportional to Z/M if ion-ion collisions are sufficiently weak. Once the different ion species begin to separate they are susceptible to an ion-ion streaming instability,⁵ which may have a variety of nonlinear consequences. We investigated the conditions under which various ion charge states can separate in velocity and analyzed the resulting ion-ion streaming instability. This induced turbulence may alter the spectrum of fast ions and may even alter the absorption or scattering of the incident laser light.

In a plasma with several ion species, each with a different Z/M , as mentioned above, the ambipolar electric field tends to accelerate these different species relative to one another. If the collisions between these species are sufficiently weak, the species will indeed separate in velocity. The cold-ion-fluid equations describing this process are

$$\frac{\partial v_j}{\partial t} + v_j \frac{\partial v_j}{\partial x} = \frac{eZ_j E}{M_j} + \sum_k v_{jk} (v_k - v_j), \quad (V-1)$$

$$\frac{\partial n_j}{\partial t} + \frac{\partial}{\partial x}(n_j v_j) = 0 \quad (\text{V-2})$$

$$E = -\frac{1}{n_e} \frac{\partial p_e}{\partial x}; \quad n_e = \sum n_j, \quad (\text{V-3})$$

where n_j is the electron density associated with the ion species j , v_j is the j th species velocity, and ν_{jk} is the slowing down collision frequency between species j and k . If the collision rates are sufficiently low, we can drop the ν_{jk} terms in Eq. (V-1). Just how low these rates have to be will be discussed later. In our case we can simplify Eqs. (V-1) and (V-3) by means of the similarity variable $\xi = x/t$. Although the similarity solutions for a two-component plasma have been discussed in considerable detail,⁶ we find that we can derive a simple set of equations, which allows us to treat an arbitrary number of ion species. The basic similarity equations are

$$(v_j - \xi) \frac{\partial v_j}{\partial \xi} + \frac{eZ_j}{M_j} \frac{\partial \phi}{\partial \xi} = 0, \quad (\text{V-4})$$

$$(v_j - \xi) \frac{\partial n_j}{\partial \xi} + n_j \frac{\partial v_j}{\partial \xi} = 0, \quad (\text{V-5})$$

$$\frac{\partial \phi}{\partial \xi} = \frac{1}{n_e} \frac{\partial p_e}{\partial \xi}, \quad (\text{V-6})$$

where $n_e = \sum n_j$. For these homogeneous equations we have the overall constraint

$$\sum_j \left(1 - \frac{Z_j}{M_j} \frac{\partial p_e / \partial n_e}{(v_j - \xi)^2} \right) n_j = 0. \quad (\text{V-7})$$

Equations (V-4) through (V-6) can be equivalently written

$$\frac{\partial n_j}{\partial \phi} = \frac{eZ_j}{M_j} \frac{n_j}{(v_j - \xi)^2}, \quad (\text{V-8})$$

$$\frac{\partial v_j}{\partial \phi} = -\frac{eZ_j}{M_j} \frac{1}{(v_j - \xi)^2}, \quad \text{and}$$

$$e \frac{\partial \phi}{\partial \xi} \left[\sum_j (1 - 3\alpha_j) n_j \alpha_j - n_e \frac{\partial T}{\partial \phi} \right] = \sum_j \frac{2n_j \alpha_j T}{(v_j - \xi)}, \quad (\text{V-9})$$

where $\alpha_j \equiv Z_j T / M_j (v_j - \xi)^2$. With Eq. (V-7) as an initial condition, Eqs. (V-8) and (V-9) can be integrated to obtain the rarefaction-wave solution. Note that for an isothermal electron distribution the second term in brackets is zero, whereas for non-isothermal distributions it may give rise to rarefaction shocks.²

We do not intend to investigate the many aspects of the solutions to these equations, particularly because the two-species problem has been so carefully treated in Ref. 6. However, we will discuss a particular solution to these equations, which will illustrate some basic features. We consider a two-ion-species plasma with a Z/M ratio of 5. The light ion species is taken to have an electron density of 0.1 of the total. In Fig. V-1 we show a plot of density as a function of the similarity variable ξ for both species. Note the sharp drop in the density of the heavier species at $\xi = 7.5$, a feature discussed in Ref. 6. In Fig. V-2 we show the velocity of both species as a function of ξ . Note that just before the cutoff of the heavier species, the lighter species moves faster than in the absence of the heavier species. This may result in an observable structure in the fast ions correlated with the heavier ions.

Let us consider the conditions under which the collision terms in Eq. (V-1) must be retained. More specifically, let us attempt to determine when the variously charged species begin to separate in velocity. For a two-ion-species plasma the relative velocity $u \equiv v_2 - v_1$ in the collisional regime is, from Eq. (V-1),

$$u = \left(\frac{Z_2}{M_2} - \frac{Z_1}{M_1} \right) \frac{eE}{\nu}, \quad (\text{V-10})$$

where $\nu \equiv \nu_{12} + \nu_{21}$. When u exceeds the thermal velocity of one of the ion species, the collision frequency with that species as a target begins to decrease. Therefore, the runaway condition is given approximately by $u = v_{T1}$ or $u = v_{T2}$, where v_{Tj} is the thermal velocity $(Z_j T_j / M_j)^{1/2}$. One chooses the term that gives a larger electric field. Because $E \sim eT_e / L$ where L is the density scale length, the critical runaway condition may be written as

$$L \leq \left(\frac{Z_2}{M_2} - \frac{Z_1}{M_1} \right) T_e \times \min \left(\frac{1}{\nu_{21} v_{T1}}, \frac{1}{\nu_{12} v_{T2}} \right), \quad (\text{V-11})$$

where

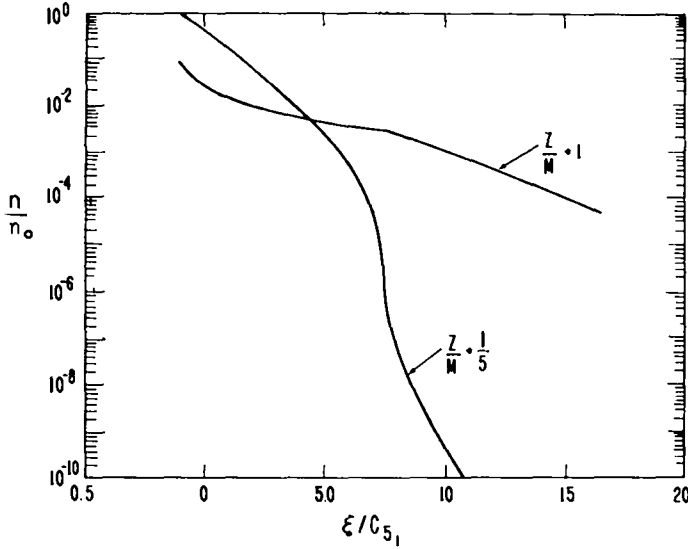
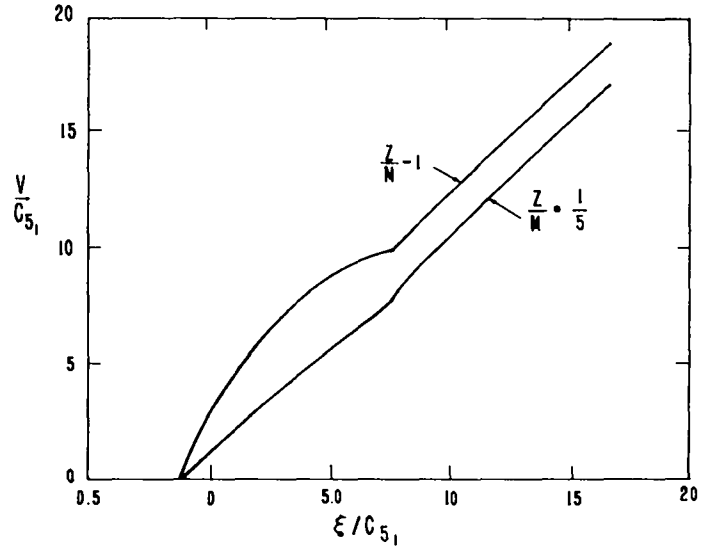


Fig. V-1.

Ion density for each of two ion species as a function of the similarity variable ξ in units of the lighter ion speed of sound. The ratio of Z/M for the two species is 5.

Fig. V-2.

Ion velocity for each of two ion species as a function of the similarity variable ξ for the same parameters as in Fig. V-1.



$$v_j = 6.7 \times 10^{-2} n_\alpha Z_i^2 Z_j^2 \ell n \lambda \frac{1}{\mu_i} \left(1 + \frac{\mu_i}{\mu_j} \right) T^{-1} \text{ cm/s}^2 ; \quad (\text{V-12})$$

$\mu_j = M_j/M_p$; T is in eV; and n is in cm^{-3} . From this latter expression one can readily see that even at a relatively low density of heavy ions, these ions will dominate the drag between species. We can also see that for $T_s \approx 1 \text{ keV}$, $T_i \approx 100 \text{ eV}$, $n_j \sim 10^{19}$, $Z_j = 6$, the scale length must be less than a few microns if the ion species are expected to separate. Thus, the primary regions of separation will occur in regions of sharp density gradients, i.e., at rarefaction shocks.² Because the strongest rarefaction shock may occur

at the critical density,¹ most species may separate just outside the critical-density region. In the absence of rarefaction shocks the adiabatic cooling of the ions during expansion would result in an increase in coupling at lower densities rather than a decrease.

A careful investigation of the resulting ion-ion instability in the critical-density region shows that it is a convective instability with the most unstable mode growing at large angles to the flow direction, with a spatial growth rate of about

$$\text{Im } k \sim \frac{1}{\lambda_D} \left(\frac{n_2}{n_0} \frac{c_{s2}^2}{u^2} \right)^{1/3}, \quad (\text{V-13})$$

where n_2 is the lower density ion component, C_{s2} is the speed of sound of that species, and u is the relative drift velocity between the two species. Numerical simulations of the instability verify this rapid spatial growth rate and show saturation at ion wave levels of $\delta n/n \sim 0.1$ to 0.2 . The dominant non-linear process is the heating of the ions until $T_1 \sim T_e/3$ in the direction of the unstable waves. There is only a small amount of momentum coupling between the ion species. The large ion waves are localized in space due to the rapidly dropping density of the heavier ion species. The effect of this turbulence on the absorption and scattering of the incident laser light is under investigation.

Two-Component Hot-Electron Transport in Self-Consistent E- and B-Fields (R. J. Mason)

Energy is carried from the critical surface to deeper regions of a laser pellet by hot-electron transport. This process involves the scattering of hot electrons by ions and cold background electrons. The absorption of these electrons into the background is a result of Coulomb drag and their motion through self-consistent E- and B-fields. An accurate description of this transport is essential to modeling the x-ray emission from two-dimensional targets, to their hydrodynamic stability, to fast-ion blowoff, to preheat, and, ultimately, to their two-dimensional implosion hydrodynamics.

The simplest, so-called double-diffusion, approach treats the hot and cold electrons as two distinct counter-diffusing fluids governed by

$$\frac{\partial n_{h,c}}{\partial t} = -\nabla \cdot \vec{j}_{h,c} + \dot{s}_{h,c} - \dot{l}_{h,c}; \quad \dot{s}_h = -\dot{s}_c, \quad \dot{l}_h = -\dot{l}_c, \quad (V-14)$$

$$\begin{aligned} \vec{j}_{h,c} &= -\frac{\vec{\nabla} p_{h,c}}{m\nu_{h,c}} - \frac{en_{h,c}}{m\nu_{h,c}} \vec{E} - \frac{\vec{j}_{h,c}}{\nu_{h,c}} \times \frac{e\vec{B}}{mc}, \quad \vec{j}_{h,c} \\ &= n_{h,c} \vec{u}_{h,c}, \end{aligned} \quad (V-15)$$

$$\nu_{h,c} = \nu_{h,c} \left[1 + \beta \frac{|j_{h,c}^u|}{n_{h,c} v_h} \right]; \quad \beta = 1/\sqrt{3}, \quad (V-16)$$

$$\vec{j}_h + \vec{j}_c = -\frac{c}{4\pi e} \vec{\nabla} \times B, \quad (V-17)$$

$$\frac{\partial B}{\partial t} = -\vec{v}_c \times \vec{E}. \quad (V-18)$$

Laser deposition is ascribed to the first overdense cell that would be encountered by the beams. The temperature of the hot electrons T_h is set by the laser intensity. The inertia terms are dropped and replaced by the flux limit factors (V-16) relating ν^* and ν . The $j_{h,c}^u$ terms describe the "unlimited" currents predicted for the next cycle with $\beta = 0$. The limiters fix the electron speeds at $\sqrt{3KT_{h/m}}$, mocking up the inertial limit on hot electrons and the cold response to an \vec{E} field retaining the hot electrons.

Equations (V-14) through (V-18) are solved for each computational time step by splitting technique, which first fixes B . Then, rearrangement of the momentum equation, Eq. (V-15), transforms B into $(1 + \omega^2\tau_{h,c}^2)^{-1}$ and $\omega\tau(1 + \omega^2\tau_{h,c}^2)^{-1}$ factors in which ($\omega = eB/mc$, $\tau = 1/\nu^*$), multiplying the diffusion coefficients. The \vec{E} field is eliminated from Eq. (V-15) with the aid of Amperes' law, Eq. (V-17). The cold density is eliminated with quasi-neutrality, i.e., $n_c = Zn_1 - n_h$. The modified Eqs. (V-14) and (V-15) then provide a single diffusion-like equation for the hot electrons, which is solved by an ADI scheme. In this equation \dot{S}_h is the laser source rate and \dot{L}_h is the rate of particle loss by collisional absorption; T_h is the isothermal, and T_c is locally increased in accordance with hot absorption into the cold electrons. With the new \vec{E} consistent with the new n_h and j_h values, we then use Eq. (V-18) to obtain B .

In test runs we examined the importance of various physics elements in the model. A partially ionized gold foil, $Z_e = 43$, was considered. This foil was $40 \mu\text{m}$ thick with a $450\text{-}\mu\text{m}$ half-length and a free-electron density $n_t = 2.2 \times 10^{24} \text{ cm}^{-3}$. An exponential density ramp from an earlier prepulse precedes the foil by $160 \mu\text{m}$ and drops from 10^{21} cm^{-3} to the background density of $3 \times 10^{16} \text{ cm}^{-3}$. The background extends to the backside of the foil. Mirror boundary conditions are imposed on n_h at the edges of a $500\text{-by-}500\text{-}\mu\text{m}$ calculational area (50 cells horizontal by 10 cells vertical). A glass laser is incident from the right, penetrating to the first cell beyond the ramp. The illumination extends from $y = 0$ to $50 \mu\text{m}$, corresponding to a $100\text{-}\mu\text{m}$ beam diameter; the intensity I is $3 \times 10^{16} \text{ W/cm}^2$. Also, $T_h = 20 \text{ keV}$ and, initially, $T_c = 0.5 \text{ keV}$.

Figure V-3 depicts the case for $B = 0$ at $t = 20 \text{ ps}$. In the calculations for the left-hand frames (a), the

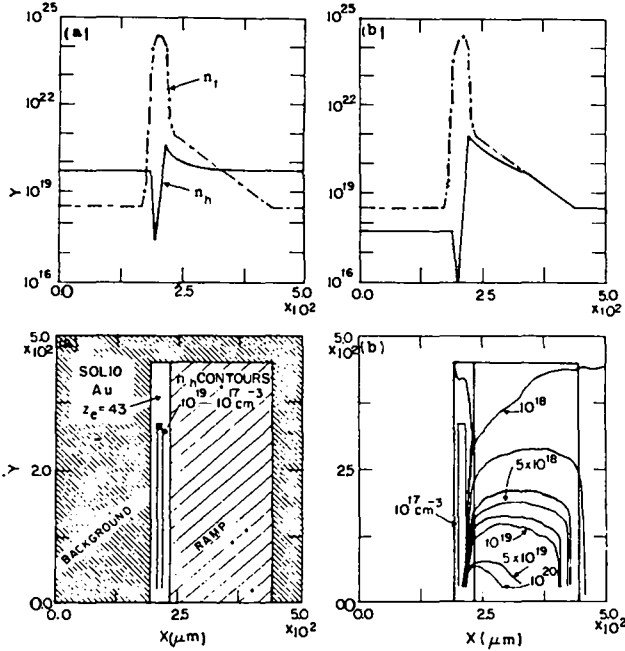


Fig. V-3.

Hot-electron density configuration at 20 ps with $B = 0$. Upper frames: axial hot-electron density n_h and total electron density $n_1 = Z_e n_i$. Lower frames: n_h contours relative to a gold foil, density ramp, and $3 \times 10^{16} \text{ cm}^{-3}$ background. Run (a): no E , charge, or flux limitation; Run (b): these features are "on." Run (a) shows unacceptable results that $n_h > n_1$ and $u > c$; obvious improvements in Run (b).

hot electrons were subject only to scattering and absorption [$\vec{E} = 0$ and $\nu^* \rightarrow \nu$], which exclude them from the foil center. Their range is enormous in the background plasma, $\lambda = (v_h/\nu_h)/\Delta x \gtrsim 10^3$, and n_h , therefore, is nearly uniform at the edges, where the lack of charge limitation permits the unphysical result that $n_h > Zn_i$. The right-hand frames (b) show the effects of including \vec{E} , as well as flux and charge limitation. Density now propagates to the back side at roughly $\sqrt{3} v_h \sim 100 \mu\text{m/ps}$, and the hot density is constrained to $n_h < n_i$.

The effects of B are displayed in Fig. V-4. For Run (c), Eqs. (V-17) and (V-18) were used, but the $\vec{j} \times \vec{B}$ terms in Eq. (V-15) were dropped, i.e., $\omega\tau_{h,c} = 0$. The net effect on n_h is insignificant—compare (b) and (c). The field, however, is substantial. It first appears as contours enclosing the edge of the laser

spot. It then spreads up along the critical surface, around, and down the backside of the foil. Principally, the field is directed into the page, with a maximum intensity of 8 MG at the spot edge. In Run (d), $\omega\tau_{h,c} \neq 0$, but the transverse current components, i.e.,

$$j_{hx} \sim \frac{-1}{\omega\tau_h} \left[\frac{1}{v_m} \frac{\partial p}{\partial y} + \frac{en_h E_y}{v_m} \right] \quad (\text{V-19})$$

are suppressed.⁷ The hot electrons below $n_h = 10^{19} \text{ cm}^{-3}$ are now strongly confined to the spot region, and B spreads toward the laser, instead of laterally. The B maximum is reduced to 2 MG. Finally, Run (e) presents results for the full system, Eqs. (V-14) through (V-18). The results are similar to those in (d); B_{max} is still 2 MG, but now both the n_h and B contours exhibit a tendency to arc away from the laser beam at low densities, which is consistent with B tracking the self-consistent curved trajectories of the suprathermals before their absorption in the cold background.

Figure V-4(f) shows the results of changing from gold to CH_2 , $Z_e = 2.67$. By $t = 2.5$ ps, hot electrons have broken through the backside of the foil and a prompt B -field appears on the steeper backside with a maximum intensity of 0.7 MG, centered 75 mm beyond the spot edge, and out of the page. The front-side field extends into the page and is only 0.4 MG strong. By $t = 20$ ps the front and back fields are each 2.0 MG, and 0.5-MG field maxima are distributed along the horizontal foil edge at $y = 450 \mu\text{m}$. These and the corresponding maxima in (d) and (e) will diminish in cylindrical geometry and under the more gradual n_i gradients of partial ionization. The prompt, backside field may be amenable to field coil measurement under both Nd and CO_2 illumination.

For equal $I\lambda^2$ values we find somewhat larger B -fields in CO_2 runs, whereas, generally, for $I\lambda^2 < 10^{17} \text{ W}\cdot\mu\text{m}^2/\text{cm}^2$ the field $B \gtrsim 4$ MG. For $I > 10^{16} \text{ W/cm}^2$ the CO_2 calculations (i.e., ramp density from 10^{19} to $3 \times 10^{18} \text{ cm}^{-2}$) are complicated by the fact that all the axial electrons rapidly become suprathermal, so that flow from the axis is charge-limited, with $\vec{j}_h = -c/4\pi e\vec{\Delta} \times \vec{B}$. The field then appears to be created in the laser deposition region and to be convected out and upward along the density ramp by the $\vec{\Delta} B^2$ term.

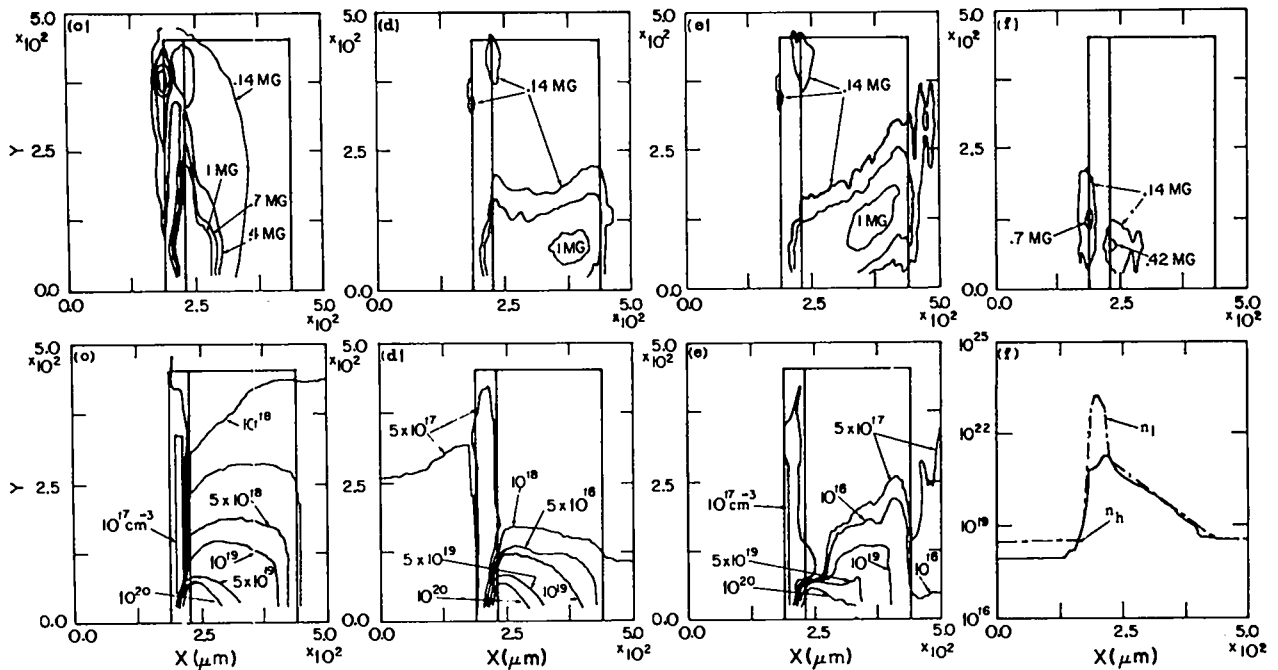


Fig. V-4.

Results at 20 ps with $B \neq 0$. Upper frames: B-field contours. Lower frames: n_h contours for runs (c) through (e), and axial densities, run (f). Run (c), $\omega_{\tau_{h,c}} = 0$. Run (d), $\omega_{\tau_{h,c}} \neq 0$, but transverse $\vec{\nabla}P \times \vec{B}$ currents neglected. Run (e), full-model solution. Run (f), results for a plastic foil at $t = 2.5$ ps showing the prompt rear-surface B-field from hot electrons.

Illumination of and Absorption in Laser Fusion Pellets (A. J. Scannapieco and H. Brysk)

An important aspect of the laser fusion problem is the illumination of spherical targets and the absorption of laser light.

In numerous experiments we studied the absorption by flat targets, and a few tests were performed on spherical targets.⁶⁻¹² Extensive theoretical results on absorption are available for flat targets, but little work has been done on spherical targets.^{13,14} However, because typical target radii are at least an order of magnitude larger than the wavelength, the absorption at a point on the sphere can be modeled by that on the local tangent plane. The problem then reduces to a pure geometrical exercise. Calculations were carried out for spherical targets used in our CO₂ laser systems, i.e., the single-beam CO₂ laser system (SES) and the Helios.

For generality, the program is set up to compute illumination and absorption for a laser system of N-beams arbitrarily distributed around the pellet.

Each beam is assumed to have a Gaussian cross section of intensity. Diffraction-limited optics are used rather than geometrical optics. Polarization effects are included. The basic absorption mechanism is considered to be resonant absorption. The absorbed energy is calculated from a theoretical computation of resonant absorption by a plane, and also from a modified model that purports to account for surface dimpling and rippling and for other effects (and, not incidentally, is adjusted to agree with experimental results).

Basically, two aspects of the problem were studied: the percentage of energy absorbed, and, for multibeam systems, the symmetry of the illumination and energy absorption. Although many parameters exist, which we could have varied, we restricted our first investigations to studying the effects of varying the radius of the target with respect to the laser spot size, and of varying the position of the laser focus relative to the center of the pellet. Later, we will study the effects of defocusing the beams and of changing the relative polarization

directions in multibeam systems. Three conclusions can be drawn from our studies. (1) Good agreement with experiments on spherical targets was obtained; (2) the pellet radius and beam focus positions can be tuned to enhance absorption; (3) the symmetry of illumination can be enhanced at the price of a penalty in energy absorbed, but the symmetry of the energy absorbed is not enhanced thereby.

A computer code was developed to carry out these studies. To set up a typical problem we have to define (1) the number of laser beams, (2) the θ and ϕ coordinates of the center of each focusing mirror in the system, (3) the distance from the pellet center to the center of each mirror, (4) the focal distance from each mirror, (5) the scale length of the Gaussian beam at the minimum spot position and at the mirror, (6) the direction of each beam relative to the center of the pellet, (7) the intensity at the center of each beam at its mirror, (8) the unit polarization vector at the center of each beam, and (9) the radius of the critical surface for the pellet.

Some results from our investigations are shown in Figs. V-5 through -8, and Table V-I.

Figure V-5 is a plot of percent energy absorbed vs the parameter R/L (i.e., the ratio of critical surface radius to minimum laser spot size) using the theoretical resonance absorption curves for P- and S-polarization with and without surface structuring.

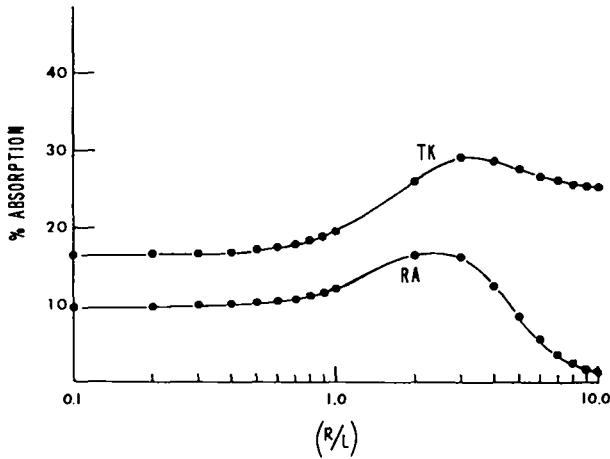


Fig. V-5.

Absorptivity for laser focused at center of spherical target. Abscissa is ratio of target radius to focal-spot radius. The lower curve is for pure resonance absorption; the upper one is for the Thomson-Kruer modification.

The curve marked RA was obtained by using the theoretical curves for P- and S-polarization without surface structuring, whereas the curve marked TK was obtained from the curves for P- and S-polarization with surface structuring. The maximum amount of energy absorbed for the RA curve is 19%, whereas the maximum for the TK curve is 29%.

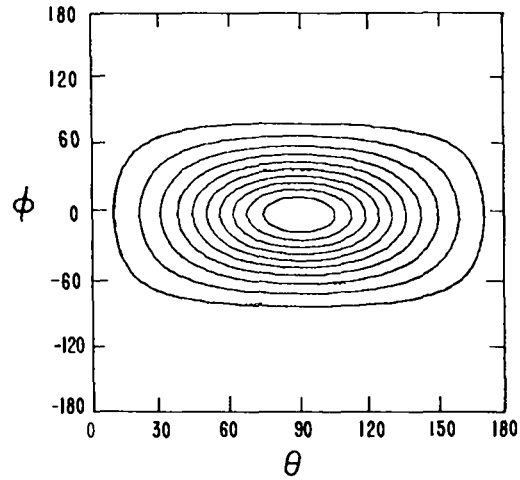


Fig. V-6.

Isodensity contour plot for illumination by SBS for beam focused at center of target the same size as focal spot ($R/L = 1$).

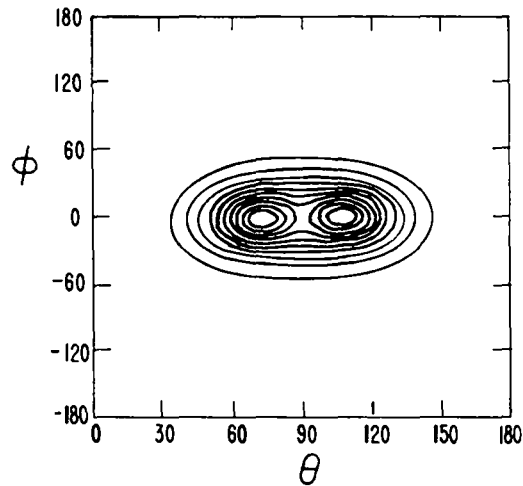


Fig. V-7.

Same as Fig. V-4 except for energy deposition instead of illumination. The arrow indicates the polarization direction (along $\phi = 0$).

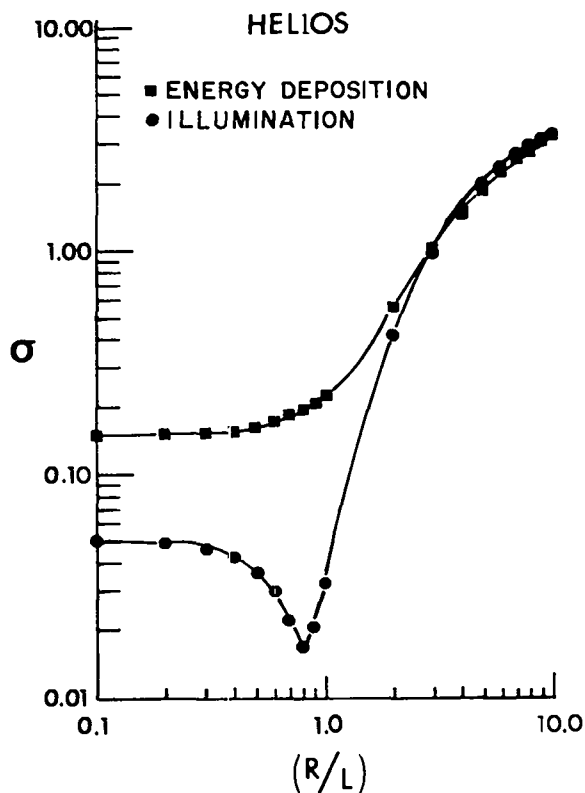


Fig. V-8.

Standard deviation of target coverage by Helios as function of target/focal-spot size ratio. The circular points are for illumination; the squares for energy deposition.

In an actual laser-target interaction history, the radius of the critical surface as well as the intensity of the laser pulse are functions of time. To calculate a percentage of energy absorbed by the pellet, we performed a weighted time integral of curve TK.

Cottles, et al.¹² carried out a series of experiments on glass microballoons and measured the percentage of energy absorbed as $\sim 25\%$. Cottles' experiments were in the parameter range $1 \leq (R/L) \leq 18$. If we refer to the TK curve of Fig. V-5, we see that within the range $1 \leq (R/L) \leq 10$, the average value for percentage of energy absorbed is $\sim 25\%$, whereas for $(R/L) > 10$ the curve asymptotes to $\sim 25\%$. Agreement is excellent.

An interesting phenomenon suggests itself when we study the contour plots of intensity and energy absorbed vs θ and ϕ in Figs. V-6 and -7. When the position of minimum laser spot size coincides with the center of the pellet, the maxima of energy ab-

TABLE V-I

ABSORPTION AT VARIOUS DISPLACEMENTS δ OF FOCUS FROM TARGET CENTER (%)

R/L	0	1	2	3	4	5
1	19.45	17.48	12.61	7.25	3.28	1.16
2	26.13	25.35	22.70	17.97	12.10	6.75
3	29.15	29.65	30.22	29.06	25.20	19.30
4	28.81	29.90	32.28	34.04	33.56	30.35
5	27.77	28.95	31.87	35.02	36.83	36.37
6	26.88	27.95	30.76	34.25	37.21	38.63
7	26.62	27.17	29.64	32.98	36.28	38.72
8	25.85	26.61	28.72	31.71	34.95	37.80
9	25.59	26.22	28.00	30.61	33.61	36.52
10	25.42	25.94	27.44	29.71	32.42	35.21

Note: R is the target radius, L the focal-spot radius; δ is the displacement of the focus from the target center, in units of L, along the polarization direction. The absorptivities are normalized to the illuminations at $\delta = 0$.

sorbed do not coincide with the maxima of laser intensity, but occur in lobes displaced along the polarization vector direction on either side of the position of maximum intensity. This lobe pattern occurs because the optimal absorption of P-polarized light occurs at an incidence angle of 23° and not 0° . Therefore, if we tilt the beam axis along the polarization direction so that the maximum beam intensity hits the pellet critical surface at the optimal angle of incidence, the percentage of energy absorbed should increase. That this indeed does occur is seen in Table V-I.

The data show the percentage of energy absorbed as a function of (R/L) and δ , where δ represents the displacement of the beam axis along the polarization direction from the center of the pellet. This displacement δ is in units of L, the minimum laser spot size. The percentage absorbed is normalized to the illumination at $\delta = 0$.

It is immediately seen that a pellet designed with a critical surface in the parameter range $6 \leq (R/L) \leq 7$, would increase the amount of energy absorbed by the pellet by 40% if the beam axis were displaced by a δ of five. One possibility for tuning the critical-surface radius to the laser spot size would be to coat

the pellet with a graded layer of very low density foam. Another advantage of tilting the beam is to decrease the specular reflection back toward the laser amplifier, thus reducing the problem of parasitics.

Because Helios has eight laser beams, it is reasonable to inquire about the symmetry of illumination and of power absorbed as a function of the parameter R/L . Figure V-8 is a plot of σ_I and σ_E (the normalized standard deviations of intensity and energy absorbed, respectively, as a function of R/L). The squares represent σ_E and the circles represent σ_I .

There is a definite value of R/L for which the illumination symmetry is optimized. On the other hand, the symmetry of the power absorbed decreases monotonically with increasing R/L .

The best symmetry of power absorbed is obtained for targets in the parameter range $(R/L) < 1$. However, in this case the total energy on target will decrease because a portion of the beam will miss the target, and the percentage of total energy absorbed will be small, as seen in Fig. V-5. Further, we would be unable to make use of the increased absorption due to a displacement of the laser beam axis that occurs for $(R/L) > 1$, as described in Fig. V-8.

In practice, the symmetry of the power absorbed is enhanced by conduction and hot-electron transport, which tend to symmetrize the energy absorbed at the critical surface. This is borne out experimentally in x-ray pinhole pictures that show a quite symmetric implosion even for a single beam on a ball-and-plate target.¹⁶ There is also theoretical evidence that the critical surface expands uniformly during a pellet implosion.¹⁶ It is, therefore, more important to optimize the energy absorbed rather than to try for small gain in the symmetry of absorption.

Harmonic Generation from Critical Surface (B. Bezzerides, D. W. Forslund, and D. F. Dubois)

Recent experiments report the observation of an extended series of integral harmonics in the direct backscatter spectrum of $10.6\text{-}\mu\text{m}$ radiation incident on planar targets.¹⁷ As a result of this work we have begun to reinvestigate the harmonic emission problem to determine its usefulness as a quan-

titative diagnostic tool. In our work we assume that the harmonic output is due to the nonlinear, adiabatic motion of electrons arising from large-amplitude electrostatic waves generated in the neighborhood of the critical surface by resonant conversion of the incident light wave. We derive here an integral expression for the harmonic output in terms of the harmonic currents. We then show how the currents are related to the first harmonic wave amplitude in the neighborhood of the critical surface.

Normalizing the simulation code WAVE to the experiments, we plan to use the first harmonic amplitude from the simulation to calculate the higher harmonics. This result will be compared with experiments, testing our assumption that resonance absorption is indeed the dominant absorption mechanism. This procedure will be a more or less direct test because the higher harmonics depend on the detailed structure of the resonantly excited first harmonic wave.

For the canonical geometry of resonance absorption as shown in Fig. V-9 it is straightforward to show from the wave equation that the magnetic field $\underline{B}^{(n)} = \hat{x}B^{(n)}$ is given by the solution of

$$\frac{d^2}{dz^2} \bar{B}^{(n)}(z) + I^{(n)}(z)\bar{B}^{(n)}(z) = \frac{S^{(n)}(z)}{\sqrt{\epsilon_n^{(n)}}}, \quad (\text{V-20})$$

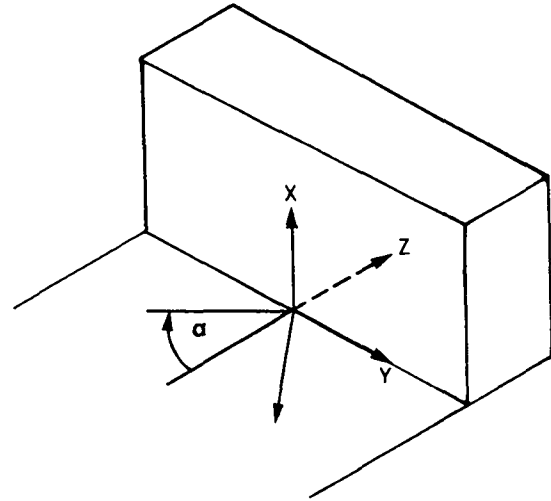


Fig. V-9.

Light incident on a slope polarized in the plane of incidence.

where

$$B^{(n)}(z) = \sqrt{\epsilon_n} \bar{B}^{(n)}, \quad k_n^2 = n^2 k_0^2 (\epsilon^{(n)} \sin^2 \theta),$$

$$I^{(n)}(z) = \left[k_n^2 - \frac{3}{4} \left(\frac{\epsilon_n}{\epsilon_n} \right)^2 = \frac{1}{2} \left(\frac{\epsilon_n}{\epsilon_n} \right) \right],$$

and the source is given by

$$S^{(n)}(z) = -\frac{4\pi}{c} \left(\nabla \times \underline{j}_0^{(n)} + \underline{v}_0^{(n)} \times \frac{\nabla \epsilon^{(n)}}{\epsilon^{(n)}} \right).$$

We solve Eq. (V-20) by forming the Green's function for the corresponding homogeneous equation whose boundary conditions are determined by the density profile. Transparency to ω light leads to outgoing conditions at $\pm\infty$, whereas nontransparency to ω implies that only boundedness can be imposed at $+\infty$.

In the more general case for a linear profile, the solutions can be constructed in terms of the Airy functions $A_1(\eta^{(n)})$ and $B_1(\eta^{(n)})$, where $\eta^{(n)} = (nk_0 L)^{2/3} z/L$ and the reflection coefficient $b^{(n)}$ off the n th critical surface. The solution for $B^{(n)}$ becomes

$$B^{(n)}(z) = \int_{-\infty}^{\infty} dz' \left(\frac{\epsilon^{(n)}(z)}{\epsilon^{(n)}(z')} \right)^{1/2} G(z, z') S^{(n)}(z') \quad (V-21)$$

Because the resonantly converted first harmonic wave is localized about the critical surface, we can assume that $\underline{j}_0^{(n)}$ is similarly localized. Then, in the wave zone,

$$B^{(n)}(z) = -\frac{2\pi}{c} \frac{1}{\sqrt{1 - \frac{1}{n^2}}} \frac{e^{-iznk_0 \alpha}}{\alpha} \left\{ \sin \theta j_{Oz}^{(n)}(-nk_0 \alpha) + \alpha j_{Oy}^{(n)}(-nk_0 \alpha) - i b^{(n)} (\sin \theta j_{Oz}^{(n)}(nk_0 \alpha) - \alpha j_{Oy}^{(n)}(nk_0 \alpha)) \right\}, \quad (V-22)$$

where

$$\alpha^2 = 1 - \frac{1}{n^2} - \sin^2 \theta$$

It is clear from Eq. (V-22) that the harmonic output is a measure of the Fourier transform of the currents $\underline{j}_0^{(n)}$. Thus, the $B^{(n)}$ fields act as a diagnostic on the harmonic currents in the neighborhood of the critical surface.

To obtain the currents, it is convenient to enter the oscillating frame by applying the transformation

$$f = F(\underline{v} - \underline{u}) \quad (V-23)$$

in the Vlasov equation, where \underline{u} is the oscillating velocity in the high-frequency field. If we take the first two velocity moments, we have

$$\frac{\partial N}{\partial t} + \nabla \cdot (\underline{u}N + \underline{p}) = 0, \quad (V-24)$$

and

$$\begin{aligned} \frac{\partial}{\partial t} \underline{p} + N \left[\frac{e}{m} \underline{E}_\perp + \nabla \cdot \frac{1}{2} (\underline{u} \cdot \underline{u}) \right] + \nabla \cdot \underline{\Pi} \\ = -(\nabla \cdot \underline{u}) \cdot \underline{p} - \underline{p} \cdot \nabla \cdot \underline{u} - \underline{u} \cdot \nabla \underline{p}, \end{aligned} \quad (V-25)$$

where

$$\begin{aligned} N &= \int d^3 v F(\underline{v}), \quad \underline{p} = \int d^3 v \underline{v} F(\underline{v}), \quad \text{and} \quad \underline{\Pi} \\ &= \int d^3 v \underline{v} \underline{v} F(\underline{v}). \end{aligned} \quad (V-26)$$

Because $n \geq 2$, the ponderomotive term in Eq. (V-25) dominates the convective term π , Eqs. (V-24) and (V-25) may be iterated to obtain any $\underline{j}^{(n)}$. For example,

$$-e^{-1} \underline{j}^{(2)} = \int d^3 v f \underline{v} = N^{(0)} \underline{u}^{(2)} + N^{(1)} \underline{u}^{(1)} + \underline{p}^{(2)}, \quad (V-27)$$

and from Eq. (V-25) with

$$\begin{aligned} \underline{j}_0^{(2)} &= \underline{j}^{(2)} - N^{(1)} \underline{u}^{(2)}, \\ \underline{j}_0^{(2)} &= -e N^{(1)} \underline{u}^{(1)} - \frac{iN^{(0)}}{4\omega} \nabla \cdot (\underline{u}^{(1)} \cdot \underline{u}^{(1)}). \end{aligned} \quad (V-28)$$

Substituting Eq. (V-26) into Eq. (V-22), we obtain $B^{(2)}$ in terms of the field $E^{(1)}$. Once $B^{(2)}$ is known, we may obtain $u^{(2)}$, $N^{(2)}$, and $P^{(3)}$ from (V-24) and (V-25). Then we can form $j_0^{(3)}$ to obtain $B^{(3)}$. Of course, this iterative scheme becomes prohibitively complex for $n > 3$, but up to $n = 3$, it should be possible to perform the necessary normalization and comparison with experiment.¹⁷

Space Charge Effects in Laser Plasma Particle Diagnostics (S. J. Gitomer and H. Brysk)

In laser plasma particle diagnostics, the plasma incident upon the various measuring instruments is delimited by a narrow pinhole or aperture. Ehler¹⁶ has estimated the Debye length of a laser plasma from measurements using a graded sequence of apertures. Typical Debye lengths (1 μm to 1 mm) can be comparable to the size of the pinhole in particle detectors. Thus, single-particle effects may be important. In particular, we consider the possibility that, because of an image force within the aperture, the plasma will issue from the aperture with a net charge. This charged beam would then be subject to space-charge spreading due to its own electric field. We treated both aspects of this problem in an approximate analysis that is then applied to actual measurements. We found, in particular, that this mechanism can account for the enlargement of the ion image reported by Slater¹⁹ in a pinhole-camera experiment that otherwise suggested anomalous behavior in the source plasma.

The details of this work were published.²⁰ We found a simple scaling law for the enlargement of an ion pinhole image under the influence of space-charge effects. The fractional expansion r/b (where r is the image radius and b the pinhole radius) is given by

$$r/b = v^{3/2} N^{3/4} L^{1/2} b^{1/2} d \quad , \quad (\text{V-29})$$

where v is the ion velocity, N is the electron number density incident upon the pinhole, L is the length of the pinhole, and d is the distance between the pinhole and the film.

Monte Carlo Transport of High-Energy Electrons (J. Comly)

General. Two different problems, each involving the transport of electrons having energies in the range of a few kilovolts to a few hundred kilovolts, and each playing an important role in the LASL CO₂ laser fusion program, have been studied with our Monte Carlo transport codes.

- Modeling calculations for the electron beam controlled CO₂ discharges in the Helios and Antares power amplifiers predict that there are sufficient parameters at our disposal to greatly reduce any detrimental gain inhomogeneities.
- Computations of the penetration of high-temperature electron distributions (representing those generated in the CO₂ laser target interaction) through thick layers of materials have provided not only test cases for numerical simulations but also data of direct use in target design.

Antares Operation at 100 kJ. To prevent damage to optical components when operating at the 100-kJ level, each of the Antares power amplifier beams must have an energy density that is very uniform over its full transverse area; this requires a properly uniform gain distribution within the discharge region. Our calculations show that the following operating conditions will achieve this uniformity: a primary beam at 280 keV, passing through a 2-mil-thick titanium foil into a 0:1:4::He:N₂:CO₂ mixture at 1800 torr, with an average discharge field of 18 kV/cm (beyond a 4-cm-wide drift space to the discharge cathode grid). The primary beam current density at the foil is V-shaped as a function of θ , the angle about the cylindrical amplifier axis, with the current density at the edges of the electron beam foil ($\pm 10^\circ$ from the sector midline) being 10 times the current density at the sector midline. The electron beam current density could be shaped by varying the gaps in the foil-support structure.

Figure V-10 shows the relative ionization density produced by the primary electron beam in one 30° sector of the discharge, as calculated by the Monte Carlo transport code, SCTDEP, for the above conditions. Contours are shown at the maxima (+), and at the 1/2, 1/4, 1/8, and 1/16 levels. The nonuniform

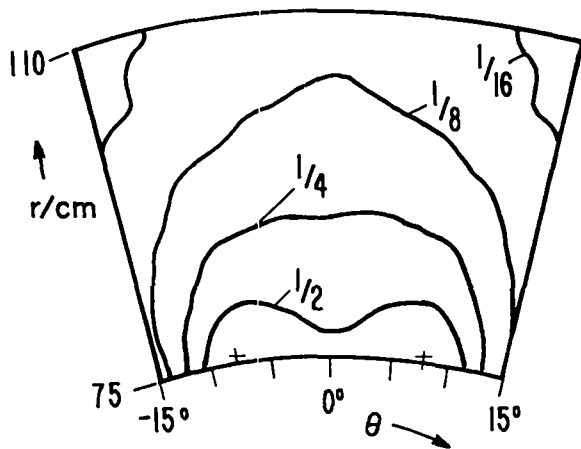


Fig. V-10.

Calculated ionization density in an Antares amplifier sector, under 100-kJ operating conditions; the contours are labeled with the density relative to the maxima (+).

ionization is needed; it allows a uniform energy extraction by compensating for several other effects: the geometry-produced nonuniformity of the discharge current density, the nonlinear discharge conductivity, the field dependence of the CO_2 kinetic rates, and the geometry of the laser pulse path. Efforts are continuing to improve the various codes²¹ required to calculate these effects, as well as the Monte Carlo transport code;²² however, the modifications are expected to produce only a small perturbation on the calculated energy extraction. The conclusion remains that the Antares amplifiers are capable of producing the full 100-kJ output.

Deep Target Penetration by High-Energy Electrons. In many CO_2 laser fusion target designs, it is necessary to provide shielding to prevent the high-energy electrons (produced near the laser absorption position) from depositing too much energy in the DT fuel. Even for a simple shielding calculation, such as described below, the problem is made difficult by the need to determine accurately a small residual energy, which remains after electrons penetrate thicknesses of matter nearly equal to their range.

Figure V-11 shows results of a residual energy calculation, using a one-dimensional Monte Carlo transport code; energy loss and scattering cross sections were those of solid, "cold" materials, and there were no electromagnetic fields. The half-space ($x >$

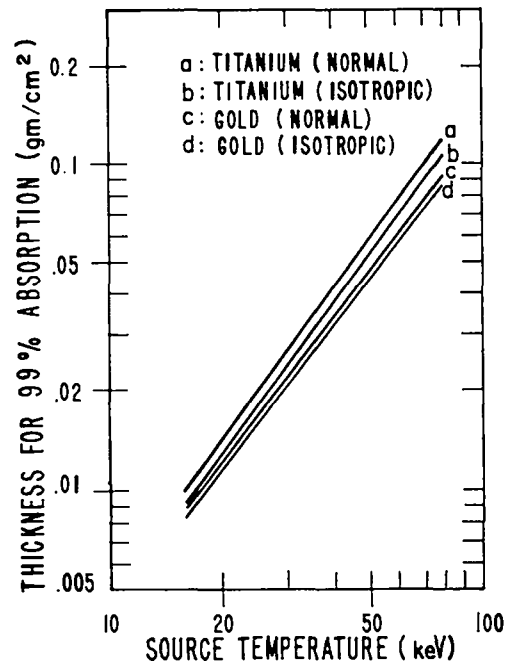


Fig. V-11.

Material thicknesses needed for 99% shielding, with Maxwellian electron source distributions. (Within the scatter inherent in the Monte Carlo technique, the calculated points fit the straight lines shown.)

0) was filled with homogeneous material, either titanium or gold, and an electron source was present at $x = 0$. Electrons were followed until they were stopped; any leaving toward $x < 0$ were reflected back into the problem. The source always had an energy spectrum corresponding to a three-dimensional Maxwellian, although the angular distribution was either isotropic or normal to the boundary. The figure shows, as a function of source temperature, the thickness of material (in g/cm^2) that absorbed all but 1% of the energy. In a true shielding situation, the material beyond the shield would contribute a backscattering, which would differ from the shield material itself, somewhat affecting the curves.

As would be expected, the normal incidence source isotropizes in the gold more quickly than in the titanium, as shown by the offsets in the curves for different source distributions. However, it is also apparent that the Z-number of the shield only weakly affects the shielding effectiveness under

these conditions; this result has not been fully explained. Investigations are under way to rule out numerical effects and to determine the influence of the "straggling" distribution on these results. It may also be necessary to include the "density effect" and the transport of knock-on electrons in determining the far tail of the absorption distribution; neither was included in these calculations. Finally, it is also expected that a more realistic source spectrum (extending only to some limited energy) would scale differently in Z .

A Hybrid Method for the Numerical Solution of the Electron Transport Equation: The Reduced-Source Method (G. S. Fraley, K. Lee, M. A. Strosio)

General. One of the major difficulties encountered in transporting suprathermal electrons produced by laser plasma interaction²⁹⁻²⁷ is due to the rapidly varying mean free path of the suprathermal electrons. The mean free path λ_{mfp} is related to the suprathermal velocity v and the background electron density n_e , through $\lambda_{mfp} \sim v^4/n_e$. For typical laser-produced plasmas, λ_{mfp} varies over ten orders of magnitude from the underdense region outside the critical surface to the overdense region inside the critical surface. An adequate treatment of suprathermal electron transport must yield accurate solutions in the long mean-free-path (free-streaming) limit as well as the short mean-free-path (diffusive) limit.

Previous attempts to treat suprathermal electron transport have used a wide variety of numerical schemes. (1) The multigroup diffusion method, where the distribution function is taken as a truncated angular expansion of Legendre polynomials, has been used in several treatments of suprathermal electron transport (SET);²⁸⁻³¹ these algorithms are suitable in short mean-free-path regions but are inadequate in the free-streaming limit. (2) In addition, Monte Carlo treatments of SET are available.^{28,32-36} The Monte Carlo treatment is, of course, adequate for all mean free paths; however, it is generally acknowledged that this method requires a relatively large number of numerical operations. (3) The method of discrete ordinates, where the transport equation is evaluated in a set of discrete angular directions, has been applied to SET and re-

quires fewer numerical operations than Monte Carlo transport.³⁶⁻⁴¹ This method is difficult to include in a Lagrangian hydrodynamics code. (4) Progress was made in SET by using a two-dimensional, two-fluid diffusion treatment that is certainly adequate in the diffusion regime.³² (5) A hybrid model, which attempts to treat each velocity group in a given hydrodynamic cell by either diffusion or free-streaming equations, was developed.⁴² This model does not provide transport solutions that are independent of the mean free path that is chosen to separate the long and short mean-free-path regimes. In addition, it is necessary to restrict the source distribution in ways that may not be consistent with the existence of plasma instabilities such as the Weibel instability.^{43,44} (6) The transport of long mean-free-path electrons in the region of resonant fields was accomplished by performing a "bounce-average."⁴⁵ Appropriate methods of interfacing this analysis with the transport in the short mean-free-path regime are unclear. (7) A relativistic transport equation⁴⁶ was cast in the multigroup diffusion form.⁴⁷

All methods of treating SET have their own regime of validity. The most general method is Monte Carlo transport; however, there is a clear need to reduce the number of required computations. A method capable of (a) reducing the number of numerical operations required and (b) yielding the accuracy of a full Monte Carlo scheme was used in the area of radiation transport.^{48,49} This method, the Reduced-Source Method (RSM), is discussed in the context of SET. Specifically, we will present the transport equation appropriate to SET and will provide a general discussion of the reduced-source method; the reduced source will be derived for a special case. Finally, we will present a preliminary iteration scheme for the inclusion of electric fields.

Suprathermal Electron Transport Equation. The equation describing the transport of suprathermal electrons has frequently been taken to be a Fokker-Planck approximation to the Boltzmann equation.^{28,39,60} In this treatment, the Boltzmann equation for the distribution function $f(r,v,t,\mu)$ is taken as

$$\frac{\partial f}{\partial t} + \mu v \frac{\partial f}{\partial r} + \frac{v(1-\mu^2)}{r} \frac{\partial f}{\partial \mu} + \frac{\vec{F}}{m_e} \frac{\partial f}{\partial \vec{v}} = \left(\frac{\delta f}{\delta t} \right)_{coll} + S, \quad (V-30)$$

for the case of spherical geometry in one dimension. In Eq. (V-30), $\mu = \cos \theta$, where θ is the angle between the velocity and radius vectors, and r, v, t are the radius, suprathermal velocity, and time, respectively; S is the source of suprathermal electrons and \bar{F} is taken as $e\bar{E}$ to include the possibility of electric-field generation. The collision operator $\delta f/\delta t_{\text{coll}}$, in the limit where collisions are dominated by small-angle scattering and the suprathermal-suprathermal interaction is assumed to be small, becomes the Fokker-Planck operator.

$$\left(\frac{\delta f}{\delta t}\right)_{\text{coll}} = \frac{-4\pi e^4}{m_e^2} \ln \Lambda \left\{ \frac{n_e}{v^2} \frac{\partial f}{\partial v} + \frac{n_e}{2} \frac{(Z+1)}{v^3} \frac{\partial}{\partial \mu} (1 - \mu^2) \frac{\partial f}{\partial \mu} \right\} . \quad (\text{V-31})$$

In Eq. (V-31), n_e is the cold-electron density, Z is the charge of the cold ionic background, $\ln \Lambda$ is a Coulomb logarithm, and e and m_e are the electron charge and mass, respectively. Note that Ref. 39 contains a sign error in the leading term of the Fokker-Planck operator. Defining the flux of particles, $\phi = vf$, Eqs. (V-30) and (V-31) may be combined to give

$$\begin{aligned} \frac{1}{v} \frac{\partial \phi}{\partial t} + \frac{\partial \phi}{\partial r} + \frac{(1 - \mu^2)}{r} \frac{\partial \phi}{\partial \mu} - \frac{e|E|}{m_e} \left(\frac{\mu}{v} \frac{\partial \phi}{\partial v} - \frac{\mu \phi}{v^2} \right) \\ = \left(\frac{\xi}{2} \right) \frac{1}{v^3} \frac{\partial \phi}{\partial v} - \left(\frac{\xi}{2} \right) \frac{\phi}{v^4} \\ + \left(\frac{\xi}{2} \right) \frac{(Z+1)}{2v^4} \frac{\partial}{\partial \mu} (1 - \mu^2) \frac{\partial \phi}{\partial \mu} + S , \end{aligned} \quad (\text{V-32})$$

where

$$\left(\frac{\xi}{2}\right) = - \frac{4\pi e^4 n_e}{m_e^2} \ln \Lambda .$$

In our discussion of the reduced-source method, it is convenient to cast Eq. (V-32) into the form

$$L(\phi) = S \quad (\text{V-33})$$

where

$$\begin{aligned} L(\phi) = & \left(\frac{1}{v} \frac{\partial}{\partial t} + \mu \frac{\partial}{\partial r} + \frac{(1 - \mu^2)}{r} \frac{\partial}{\partial \mu} \right. \\ & - \frac{e|E|}{m_e} \left\{ \frac{\mu}{v} \frac{\phi}{v} - \frac{\mu}{v^2} \right\} - \frac{\xi}{2} \frac{1}{v^3} \frac{\partial}{\partial v} + \frac{\xi}{2} \frac{1}{v^4} \\ & \left. - \frac{\xi}{4} \frac{(Z+1)}{v^4} \frac{\partial}{\partial \mu} (1 - \mu^2) \frac{\partial}{\partial \mu} \right) \phi . \end{aligned} \quad (\text{V-34})$$

Derivation of Reduced Source for Special Conditions. The basic philosophy of the reduced-source method has been discussed in detail in Refs. 48 and 49. It is assumed that an approximate solution to Eq. (V-33) has been obtained by *any* convenient means, e.g., multigroup diffusion. Let this approximate solution be ϕ_A . Then,

$$L(\phi) - L(\phi_A) = S - S_A = S_R , \quad (\text{V-35})$$

where S_R is the reduced source and S_A is the approximate source corresponding to ϕ_A . From Eq. (V-36) the reduced source may be written as

$$S_R = S - L(\phi_A) . \quad (\text{V-36})$$

Letting $\delta = \phi - \phi_A$, we obtain for a linear operator L ,

$$L(\delta) = S_R . \quad (\text{V-37})$$

(The operator L of Eq. (V-34) is *not* linear because the self-consistent electric field depends on the particle flux ϕ . This point will be discussed later.) From Eqs. (V-36) and (V-37) the basic idea of the reduced-source method is apparent: an approximate solution ϕ_A is obtained by *any* convenient method and is used to calculate the reduced source S_R , which is taken as the source in Eq. (V-37). Equation (V-37) is solved by the Monte Carlo method. For cases where ϕ_A is a good approximation to the exact solution, it follows that $S_R = S - S_A \ll S$; hence, the Monte Carlo solution of Eq. (V-37) requires many fewer numerical operations for an accurate solution than does Eq. (V-33). This last observation follows

from the fact that the number of Monte Carlo simulation particles required for a solution of given accuracy is proportional to the square of the source.

Multigroup diffusion generally provides an accurate solution to ϕ in the short mean-free-path regime. In particular, the multigroup-diffusion solution is expected to be accurate in the overdense region of the plasma, but is, of course, suspect in the plasma corona.

In the rest of this discussion, we consider the special case where ϕ_A is approximated by the multigroup-diffusion method. In this case it is possible that ϕ_A is a poor approximation to ϕ in the corona and we expect the Monte Carlo solution of Eq. (V-37) to require essentially the same number of numerical operations as a full Monte Carlo treatment. It is possible that an accurate solution for ϕ_A could be obtained in the corona by the techniques of Ref. 45. This possibility is being considered, but is not discussed here.

The multigroup-diffusion technique in the P_1 -approximation is applied by assuming a solution of the form

$$\phi_A = \phi_0 + \phi_1 \mu \quad , \quad (V-38)$$

where the expansion has been truncated after the P_1 term. Upon taking the first moment, $1/4\pi \int () d\Omega$, and second moment, $\int 1/4\pi () \mu d\Omega$, of Eq. (V-34) with $\phi = \phi_A$, one obtains

$$\begin{aligned} \frac{1}{v} \frac{\partial \phi_0}{\partial t} + \frac{1}{3} \frac{\partial \phi_1}{\partial r} + \frac{2}{3} \frac{\phi_1}{r} - \frac{e|E|}{3mv} \left(\frac{\partial \phi_1}{\partial v} - \frac{\phi_1}{v} \right) \\ - \frac{\xi}{2} \frac{1}{v^3} \frac{\partial \phi_0}{\partial v} + \frac{\xi}{2} \frac{1}{v^4} \phi_0 = \langle S \rangle \quad , \quad (V-39) \end{aligned}$$

$$\begin{aligned} \frac{1}{v} \frac{\partial \phi_1}{\partial t} \frac{\partial \phi_0}{\partial r} - \frac{e|E|}{mv} \left(\frac{\partial \phi_0}{\partial v} - \frac{\phi_0}{v} \right) - \frac{\xi}{2} \frac{1}{v^3} \frac{\partial \phi_1}{\partial v} \\ + \left(\frac{Z+2}{2} \right) \frac{\xi}{v^4} \phi_1 = 3 \langle \mu S \rangle \quad , \quad (V-40) \end{aligned}$$

where

$$\langle S \rangle = \frac{1}{4\pi} \int S d\Omega \quad , \quad \langle \mu S \rangle = \frac{1}{4\pi} \int S \mu d\Omega \quad ,$$

and we have used

$$\begin{aligned} \frac{1}{4\pi} \int d\Omega = 1, \quad \frac{1}{4\pi} \int \mu^2 d\Omega = \frac{1}{3}, \quad \frac{1}{4\pi} \int \mu^3 d\Omega = 0, \\ \frac{1}{4\pi} \int \mu d\Omega = 0, \quad \text{and} \quad \frac{\partial \phi}{\partial \mu} = \phi_1 \quad (V-41) \end{aligned}$$

in obtaining the moments. Equations (V-39) and (-40) represent, respectively, the first and second moments of the transport equation. These equations are rewritten as

$$\begin{aligned} \tau = \langle S \rangle - \frac{1}{v} \frac{\partial \phi_0}{\partial t} - \frac{1}{3} \frac{\partial \phi_1}{\partial r} - \frac{2}{3} \frac{\phi_1}{r} \\ + \frac{e|E|}{3mv} \left(\frac{\partial \phi_1}{\partial v} - \frac{\phi_1}{v} \right) \quad , \quad (V-42) \end{aligned}$$

$$\rho = 3 \langle \mu S \rangle + \frac{e|E|}{mv} \left(\frac{\partial \phi_0}{\partial v} - \frac{\phi_0}{v} \right) \quad , \quad (V-43)$$

where $\tau(\rho)$ is defined by comparison with Eq. (V-39) [Eq. (V-40)]. From Eqs. (V-33) and (V-36) with $\phi = \phi_A$, one obtains

$$\begin{aligned} S_R = S - \left[\frac{1}{v} \frac{\partial \phi_0}{\partial t} + \mu^2 \frac{\partial \phi_1}{\partial r} + \frac{(1 - \mu^2)}{r} \phi_1 - \frac{e|E|\mu}{mv} \right. \\ \left. \left(\frac{\partial \phi_0}{\partial v} - \frac{\phi_0}{v} \right) - \frac{e|E|}{mv} \mu^2 \left(\frac{\partial \phi_1}{\partial v} - \frac{\phi_1}{v} \right) + \tau + \rho \right] \\ = \left[S - \langle S \rangle - 3\mu \langle \mu S \rangle \right] + (\mu^2 - \mu_0^2) \left[\frac{\phi_1}{r} - \frac{\partial \phi_1}{\partial r} \right] \\ + (\mu^2 - \mu_0^2) \frac{e|E|}{mv} \left(\frac{\partial \phi_1}{\partial v} - \frac{\phi_1}{v} \right) \quad , \quad (V-44) \end{aligned}$$

where $\mu_0^2 = 1/3$. This reduced source for the electron transport equation differs from that derived for radiation transport^{46,49} in three respects: (1) an anisotropic source must be included, as represented by the presence of the first three terms in Eq. (V-44). (2) The electric field must be included in all

self-consistent one-dimensional formulation, as is manifest in Eq. (V-44) by the presence of the terms containing $|E|$; and (3) the remaining terms in Eq. (V-44), other than electric-field or source terms, differ from the corresponding radiation transport reduced source as a result of the basic differences in the electron and radiation transport equations. The electric fields in Eq. (V-44) have been treated purely formally to this point. That is, the electric field has been taken as given independently of the particle flux ϕ . This is, of course, not the case and this must be corrected by iteration of the electric field as a function of the particle flux.

Preliminary Iteration Scheme for Inclusion of Electric Fields. The electric field depends on the current J_H associated with the suprathermal electron flux, and in turn, on the cold return current J_c . The first step in the proposed iteration scheme is to use the multigroup diffusion approximation to ϕ , namely ϕ_A , to calculate $|E^n| = |E(\phi_A)|$. This value of $|E|$ is then inserted into L and Eq. (V-37) is solved by the Monte Carlo method. The new value of $\phi, \phi^{(1)}$ is then used to calculate $|E^1| = |E(\phi^{(1)})|$. This iteration is repeated until

$$\left| |E^n| - |E^{n-1}| \right| < \epsilon_1, \quad (\text{V-45a})$$

$$|\phi^n - \phi^{n-1}| < \epsilon_2, \quad (\text{V-45b})$$

where n refers to the index defining the iteration and ϵ_1 and ϵ_2 represent user-defined convergence criteria.

Conclusion and Summary. The reduced-source method provides a consistent method of treating SET in both the short and long mean-free-path regimes of a laser-produced plasma. In addition to reducing the time required by a full (but accurate) Monte Carlo simulation, this method provides a way of interfacing different methods of solution. We restricted our discussion to the case where an approximate solution is obtained by the multigroup diffusion approximation. In this case the transport solution in the plasma corona is suspect, and we expect to provide an essentially full Monte Carlo treatment in the corona.

The reduced-source method is by no means limited to this treatment. For example, a promising

approach being investigated is based on using a multigroup diffusion solution of ϕ_A in the short mean-free-path regime and a "bounce-averaged" solution for ϕ_A in the long mean-free-path regime where resonant fields and the reflecting plasma sheath play major roles in suprathermal electron transport.

Above, we presented a general discussion of the reduced-source method for SET and gave an example that obtains when ϕ_A is determined by multigroup diffusion. This is not necessarily the best scheme available. We are investigating other techniques of applying the reduced-source method to SET.

TARGET DESIGN

Introduction

Recent target design efforts have been directed primarily toward classified targets for Helios and Antares. Two classes of unclassified targets are still being actively pursued, however. A comprehensive analysis of exploding-pusher designs for Helios is nearing completion, and a sequence of targets bridging the gap between these exploding pushers and targets designed for the 20-times-liquid-density milestone have been proposed. These targets should play a useful role in normalizing diagnostics used to provide convincing evidence of the densities achieved.

High-Compression Targets (Sirius B) for Helios (R. Kopp)

One of the early stated goals of the Helios system is to achieve compressed-fuel densities of about 4 g/cm^3 (the 20-times-liquid-density experiment). As described in LASL report LA-7328-PR, the attainment of high densities with existing and contemplated laser systems requires pellet implosion in the ablative mode. Thus, target preheat during laser illumination must be carefully controlled (shielded) to ensure that subsequent compression of the fuel will occur nearly adiabatically from an initially low temperature.

Fuel preheat generally results from hot-electron thermalization and soft x-ray absorption (radiative

preheat). Both the hot electrons and the x rays are generated in the outermost pellet layers during laser illumination. At the anticipated Helios energies (5 to 10 kJ), preheat by hot electrons is the dominant process. Of the classes of target that can readily be fabricated and tested at present, those that promise the best performance, in terms of neutron yield and net fuel compression, consist of a glass microshell of 100 to 150 μm radius, filled with several tens of atmospheres of DT gas, and surrounded by a thin (few microns) pusher of high-Z material (e.g., nickel or molybdenum) and a thick low-density ablator (CH or CH_2). The ablator acts as a hot-electron preheat shield and the high-Z pusher performs a similar function for the radiative preheat.

Unfortunately, the large opacity of the high-Z pusher, required for efficient radiative shielding, also effectively traps soft x rays produced in the fuel region at maximum compression and prevents their detection. This severely limits the usefulness of conventional soft x-ray techniques for diagnosing target performance. In a short-term effort to ease these diagnostics problems, extensive design calculations were carried out for targets in which the high-Z pusher had been omitted. These targets contained only the minimum amount of glass necessary to contain the fuel at the desired pressure, and their CH-ablator thicknesses ΔR_{CH} ranged from 0 to 150 μm .

Figure V-12 shows the expected neutron yield and maximum (average) fuel density for a sequence of calculations for these "pusherless" targets. This particular sequence considered a 1- μm -thick GMB of 100- μm radius filled with 100 atm of equimolar DT, upon which various thicknesses (ΔR_{CH}) of plastic had been deposited. The transition from exploding-pusher behavior (high yield, low density) to ablative characteristics (lower yield, high density) is clearly shown by such a display. The laser illumination assumed for this sequence of calculations consisted of a 5-kJ triangular pulse with a 200-ps risetime (peak power, 8.33 TW) of which 20% was absorbed by the target.

From calculations such as these we are confident that the behavior of targets irradiated by Helios can be followed well into the ablative regime, thus laying the groundwork for subsequent experiments on targets in which high-Z pushers are reintroduced (the pusherless targets discussed here only marginally reach the desired density of 20-times liquid).

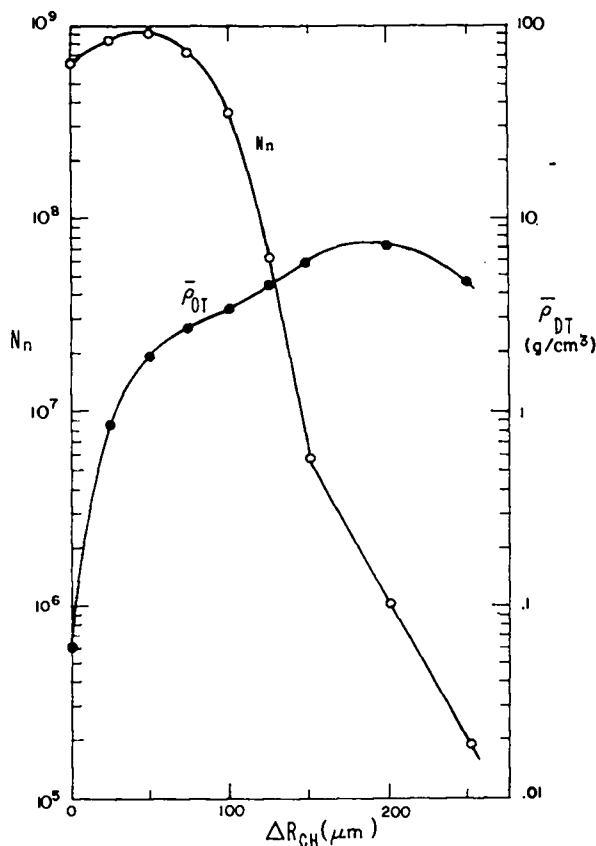


Fig. V-12.

Neutron yield N_n and compressed fuel density ρ_{DT} for the ablative targets described in the text, as a function of CH-ablator thickness ΔR_{CH} . The targets are filled with pure DT at an initial pressure of 100 atm.

The addition of neon to the pellet fuel region is known to afford still another useful diagnostic technique, namely, x-ray spectroscopy of the resulting line emissions. Order-of-magnitude estimates of the resonance-line opacities of highly ionized neon in the compressed cores of the above targets suggest that no more than a few tenths of a percent (by number) neon additive to the fuel is needed to produce abundant line emission for this technique. This fact is fortunate, because recent calculations (see Fig. V-13) as well as recent experiments on exploding-pusher targets with the TBS strongly indicated that the neutron yield may decline rapidly as neon is added to the fuel.

Ablatively driven laser fusion targets are expected to be inherently more sensitive to nonuniformities

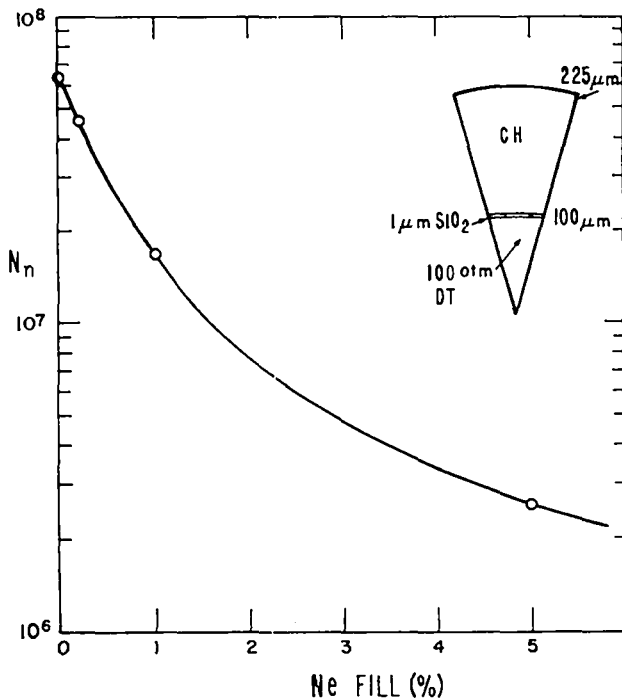


Fig. V-13.

Neutron yield for 100-atm DT-filled ablative targets ($\Delta R_{CH} = 125 \mu\text{m}$ as a function of Ne addition (at. %).

of, e.g., shell thickness and laser illumination, than are exploding-pusher targets, because the lateral redistribution of deposited energy is less efficient for the former and they are more susceptible to hydrodynamic instabilities during implosion. To gain a quantitative idea of the degradation of implosion symmetry to be expected under various conditions of illumination nonuniformity, several two-dimensional simulations of typical high-density (Sirius-B) target configurations were carried out. Two of these will be mentioned; in each case the target was a GMB of 100- μm radius, 1- μm thickness, filled with 100 atm (DT + 5% neon), with a 100- μm CH ablator. As before, the laser-pulse energy was 5 kJ, and the absorption fraction was set at 0.20.

In the first case all beam energies were equal, but the light incident on the "right" side of the target (in, say, four of the eight beams) was retarded by 50 ps relative to that incident on the left side (i.e., by $\sim 4\%$ of the implosion time). This delay represents the maximum degree of beam nonsimultaneity to be expected in the Helios system. The upper plot of Fig. V-14 shows the computer mesh for the pellet

core region near the time of maximum compression. Note that the fuel region (within the innermost shaded region) is still roughly spherical, but is displaced $\sim 8 \mu\text{m}$ along the z-axis toward the side of retarded illumination. A shift of this amount should be observable on x-ray pinhole pictures, assuming that emission from the fuel region can be seen at all. The neutron yield and fuel compression for this case are barely diminished from that given by one-dimensional simulations at the same energy, indicating that beam nonsimultaneity of the maximum degree anticipated for Helios should have little effect on overall target performance (see Table V-II).

The effects of beam energy imbalance could be more serious, because the individual beams on Helios may vary considerably in energy relative to one another from shot to shot, and in an unpredictable manner. In our second simulation, all eight beams arrived simultaneously at the target, but the four beams incident on the "left" side (which are assumed to spread their energy uniformly over this side) carried 17% more energy than the four beams incident on the right (all eight beams still totaling 5 kJ, however). The mesh distortion at maximum compression for this case is comparable (Fig. V-14b) to that in the previous example, and the yield remained about the same. Again, the major effect was the displacement of the fuel region to one side, in this case away from the more strongly illuminated surface, as one would intuitively expect.

Two-dimensional simulations involving stronger illumination and greater target asymmetries will provide useful guidelines to acceptable laser system and target fabrication tolerances. In addition, some experimental data already exist from the TBS relating to the displacement of the pellet core, as seen in soft x rays, as a result of unequal beam energies and/or beam nonsimultaneity. We will, therefore, repeat in the near future some of the above calculations for exploding-pusher targets using conditions appropriate for the TBS.

Stability of Laser Fusion Targets, Study and Results (A. J. Scannapieco)

The laser fusion targets currently being considered are analytically intractable. We have therefore chosen a computational approach to investigate the problem of stability, comparing our results with analytic solutions whenever possible.

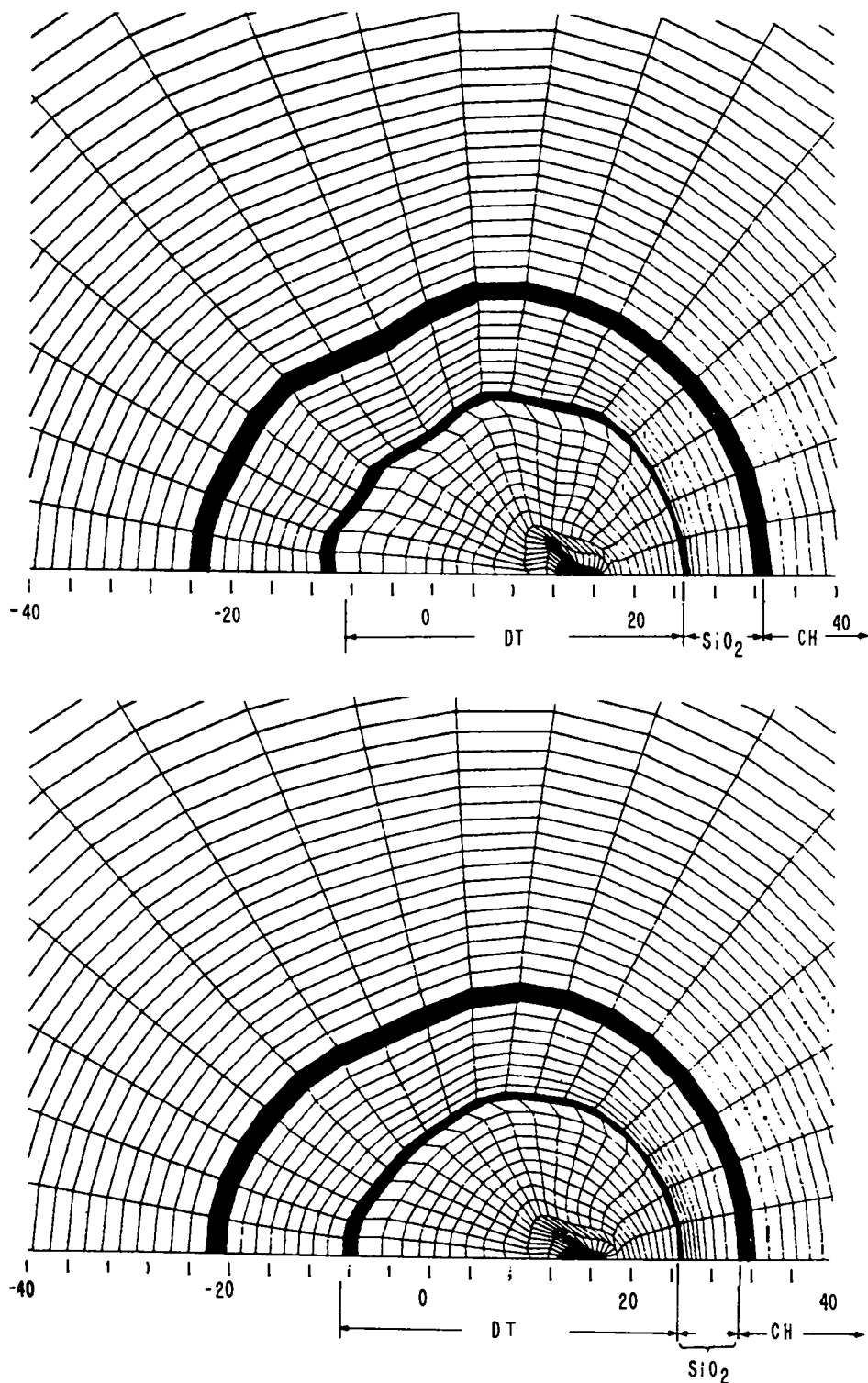


Fig. V-14.

Lagrangian mesh plots of pellet core region near the time of maximum fuel compression. (a) Equal laser beam intensities, but irradiation from right arrives 50 ps later than that from left; (b) simultaneous beam arrival times, but energy impinging from left is 17% higher than that from right; in both cases the axis of symmetry (z axis) is the abscissa (scale is in micrometers).

TABLE V-II

COMPARISON OF ONE-DIMENSIONAL AND TWO-DIMENSIONAL SIMULATIONS

$R_{GMB}, 100 \mu\text{m}; \Delta R_{CH}, 100 \mu\text{m};$
 Fill, 100 atm (DT+Ne)

	One-Dimensional	Two-Dimensional	
		50-ps Time Delay	17% Intensity Imbalance
Neutron number	2.9×10^7	2.6×10^7	3.0×10^7
Maximum fuel density	6.1 g/cm^3	5.7 g/cm^3	5.7 g/cm^3

Our computational approach first considers the linear phase of instability growth in the fusion pellet. After a linear stability analysis is performed, which contains all the relevant laser pellet physics, we can apply the following procedure to the pellet design. If the pellet maintains its structural integrity linearly, the pellet will work and the stability study of the pellet is complete. However, if the pellet does not maintain its structural integrity linearly, then a nonlinear analysis must be performed, because the nonlinear saturation and possible stabilizing effects. It may also be necessary to consider the nonlinear and turbulent phases to increase the design parameter space available to fusion targets.

Our linear stability studies use calculations that exist in two forms: a one-temperature version and a three-temperature version.

The implosion of a fusion pellet can be described by a closed set of fluid moment equations. The particular set of equations chosen dictates what physics will be treated in the linear stability code. The fluid equations shown in Tables V-III and -IV are those from which the set of perturbed fluid equations used in the one- and three-temperature versions of the calculations were obtained.

The two sets of equations differ in the treatment of energy transport. The single equation for energy transport in the one-temperature calculation is replaced by the three coupled-energy equations in the three-temperature calculation. In the latter, the energy is transported by three species (i.e., elec-

TABLE V-III

ZEROTH-ORDER MOMENT EQUATIONS PERTURBED TO FORM FIRST-ORDER MOMENT EQUATIONS SOLVED IN ONE-TEMPERATURE CALCULATIONS

$$\frac{dR}{dt} = \underline{v}(R, t)$$

$$\frac{\partial \rho}{\partial t} + \underline{v} \cdot (\rho \underline{v}) = 0$$

$$\left(\frac{\partial \underline{v}}{\partial t} + \underline{v} \cdot \underline{\nabla} \underline{v} \right) = - \underline{\nabla} P$$

$$\left(\frac{\partial \epsilon}{\partial t} \right)_{\rho} \frac{dT}{dt} = \left[\frac{P}{\rho^2} - \left(\frac{\partial \epsilon}{\partial \rho} \right)_{T} \right] \frac{d\rho}{dt} + \frac{1}{\rho} \underline{v} \cdot \underline{\nabla} \cdot \underline{K} \underline{\nabla} T + \frac{\dot{q}}{\rho}$$

$$P = P(\rho, T)$$

trons, ions, and radiation) rather than by one (a neutral fluid) as in the one-temperature calculation.

Results were obtained from one-temperature calculations for the 20-times-liquid-density target designed for Helios and for a multishell, high-aspect-ratio target.

The target is shown schematically in Fig. V-15. If we concentrate our attention on the two surfaces of

TABLE V-IV

ZERO-TH-ORDER MOMENT EQUATIONS SOLVED IN CYLINDRICAL PARTICLE LAGRANGIAN CODE, THE EQUATIONS FROM WHICH THE SET OF FIRST-ORDER EQUATIONS SOLVED IN THE THREE-TEMPERATURE CALCULATIONS IS DERIVED

$$\frac{dR}{dt} = \underline{v}(R, t)$$

$$\frac{\partial \rho}{\partial t} + \nabla \cdot (\rho \underline{v}) = 0$$

$$\rho \left(\frac{\partial v}{\partial t} + \underline{v} \cdot \nabla v \right) = - \nabla P$$

$$\left(\frac{\partial \epsilon_e}{\partial T_e} \right)_\rho \frac{dT_e}{dt} = \left[\frac{P_e}{2} - \left(\frac{\partial \epsilon_e}{\partial \rho} \right)_{T_e} \right] \frac{d\rho}{dt} + \frac{1}{\rho} \nabla \cdot k_e \nabla T_e$$

$$+ A_{ie}(T_i - T_e) - A_{er}(T_e - T_r) + \frac{g_e}{\rho}$$

$$\left(\frac{\partial \epsilon_i}{\partial T_i} \right)_\rho \frac{dT_i}{dt} = \left[\frac{P_i}{2} - \left(\frac{\partial \epsilon_i}{\partial \rho} \right)_{T_i} \right] \frac{d\rho}{dt} + \frac{1}{\rho} \nabla \cdot k_i \nabla T_i - A_{ie}(T_i - T_e) + \frac{\dot{g}_i}{\rho}$$

$$\left(\frac{\partial \epsilon_r}{\partial T_r} \right)_\rho \frac{dT_r}{dt} = \left[\frac{P_r}{2} - \left(\frac{\partial \epsilon_r}{\partial \rho} \right)_{T_r} \right] \frac{d\rho}{dt} + \frac{1}{\rho} \nabla \cdot k_r \nabla T_r + A_{er}(T_e - T_r) + \frac{\dot{g}_r}{\rho}$$

$$P = P_e(\rho, T_e) + P_i(\rho, T_i) + P_r(\rho, T_r)$$

the high-Z pusher, we obtain the results shown in Fig. V-16, which plots the number of e-foldings vs time for the ablator-pusher interface (solid line) and for the fuel-pusher interface (dashed line). The vertical lines at 1.2, 3.1, and 4.2 ns represent, respectively, the onset of shock passage through the pusher, the acceleration turnaround at the fuel-pusher interface, and the time of maximum compression.

The stabilization or negative growth seen occurs mainly because of damping due to thermal conduction when the Taylor mode is purely oscillatory.

Mode growth is small (i.e., $\gamma\tau \gtrsim 1$) up until the acceleration turnaround at the fuel-pusher interface. After this acceleration turnaround, mode growth becomes large (i.e., $\gamma\tau < 1$). The maximum value of $\gamma\tau$, for this mode, at the fuel-pusher interface, at peak compression is ~ 5 .

By using the value of $\gamma\tau$ at peak compression, obtained by one-temperature calculation, one can predict that at maximum compression the high-Z pusher will thicken to $\sim 7 \mu\text{m}$. Therefore, if we assume that the surface perturbation has to grow to

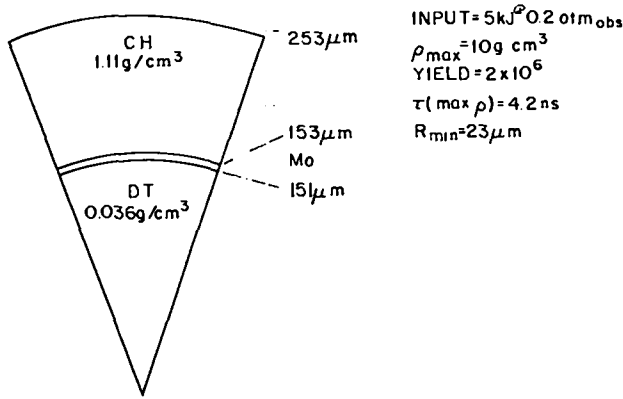


Fig. V-15.
RIGEL 20-times-liquid-density target for Helios.

the thickness of the shell before shell disruption occurs, then the maximum initial surface imperfection, for this mode, that will maintain shell integrity is ($\xi_0 = 7 \mu\text{m}/e^5 =$) $0.05 \mu\text{m}$.

One cannot realistically expect such surface smoothness because the perturbation growth will be nonlinearly damped to a value less than that predicted by calculation. However, we now know what degree of surface smoothness will guarantee shell integrity against the growth of the mode studied. A complete study, however, would require a set of characteristic modes associated with each shell of the pellet.

We also see that from a stability standpoint it is far better if the pellet reaches design compression while the pusher is still accelerating the fuel.

Several phenomena that have been observed analytically and in other numerical simulations have also been observed in our studies. Besides the classical Taylor mode growth, we have also observed shock reversal of perturbations,⁵¹ non-Taylor (Plesset-Birkhoff)^{52,53} growth of modes, shock damping and growth of perturbations,⁵⁴ and convergence instability.

Another example of the results obtained with the one-temperature calculation is shown in Figs. V-17 and -18 for a multishell high-aspect-ratio target. The two figures represent different interfaces between a high-Z and low-Z material in the pellet, and plot the ratio of perturbation amplitude to initial perturbation amplitude (ξ/ξ_0) vs time (in 10^{-8} s). The dots represent results of a two-dimensional

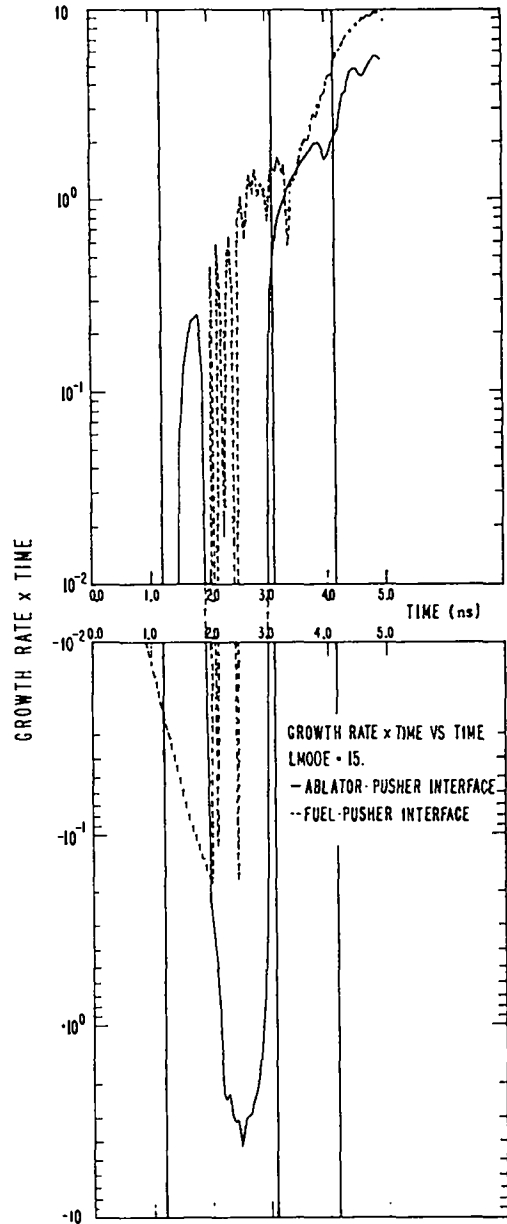


Fig. V-16.
Plot of number of perturbation e-foldings vs time for RIGEL target. Solid line: growth rate at ablator-pusher interface; dashed line: growth rate at fuel-pusher interface.

simulation of the pellet initialized with a given mode, whereas the squares show the results obtained by a one-temperature calculation for the same mode using a one-dimensional zeroth-order state for the same pellet.

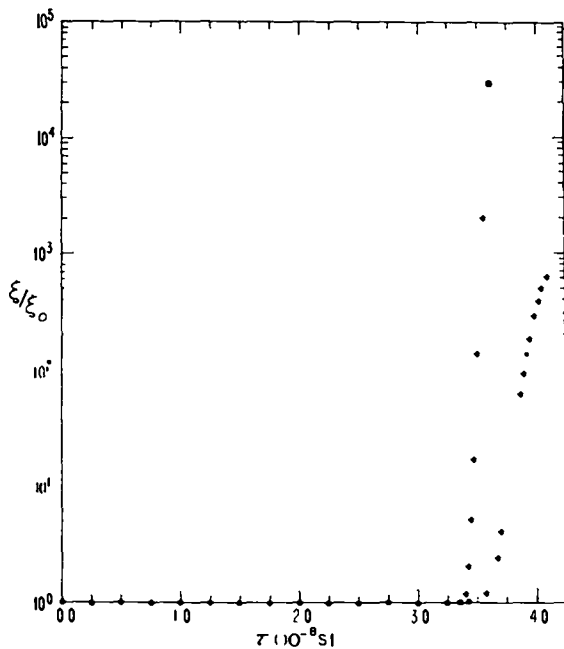


Fig. V-17.

Plot of perturbation amplitude vs time at a Taylor unstable interface of a high-aspect-ratio target. The ordinate is normalized to the initial perturbation amplitude. Circles show results of a two-dimensional simulation, and squares represent results obtained with one-temperature calculations for the same pellet. The spherical harmonic studied had an L -value of 60.

We see that the time for the onset of instability predicted by the one-temperature calculation corresponds exactly to the time of onset generated in the two-dimensional run. However, in each case the growth predicted by the one-temperature calculation is always higher than that predicted by the two-dimensional code, as can be expected for several reasons. First, the nonlinear saturation present in the two-dimensional simulation does not exist in the linear one-temperature calculation. Second, the two-dimensional calculation contains stabilizing effects due to energy transport and deposition that are not contained in the one-temperature calculation.

Thus far we have concerned ourselves with the linear aspects of the stability problem. However, many of the phenomena of interest occur in the nonlinear regions of the instability history and, possibly, even in the late-time turbulent phase of in-

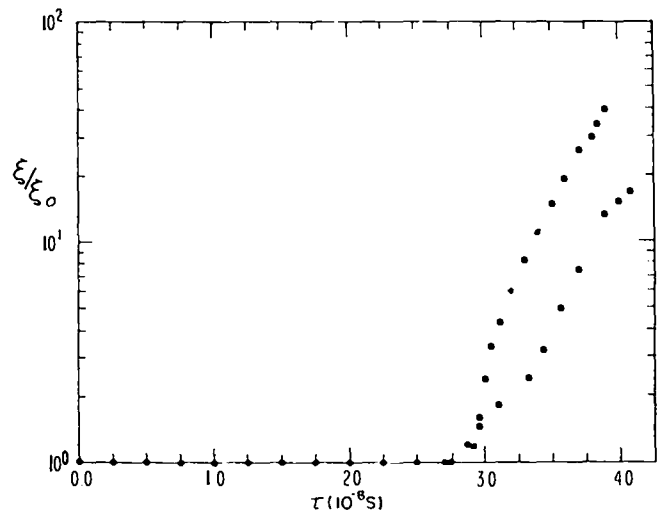


Fig. V-18.

Same as Fig. V-17 except at a different Taylor unstable interface. Ratio of densities at this interface is smaller than that in Fig. V-17 and the temperature is higher.

stability development. We must, therefore, extend our understanding of the linear theory somehow to these latter stages.

Our nonlinear stability studies revolve around several codes. To understand the nonlinear evolution of fluid instabilities we are using these codes to solve the full set of fluid equations rather than solving a perturbed first-order set of these equations. The following are some of the questions we hope to answer.

- What are the spectral and flow characteristics, and the saturation levels of perturbations when they have grown to a level at which they can no longer be considered perturbations?
- How does a turbulent mix region evolve at the material interfaces of our targets after the nonlinear phase of the evolution of the instability is over, and, moreover, does the mix always become turbulent during pellet evolution?
- If the mix is turbulent, can we characterize the shear flow set up by the nonlinear phase of the instability that feeds the turbulence?
- Is there a difference in the evolution of turbulence in converging spherical geometries as opposed to planar geometries?
- Can we predict the nonlinear evolution from an understanding of the linear evolution?

To answer some of these questions, we created a rectangular, variable-mesh, two-dimensional Eulerian hydrocode that solves the fluid equations shown in Table V-III.

Figures V-19 through -21 were taken from three frames of a motion picture produced with this code. The initial state of the system is shown in Fig. V-19; we see contour plots of density, temperature, and x and y momentum. The scales are highly distorted,

being $2 \mu\text{m}$ in x and $200 \mu\text{m}$ in y. A thermal source is applied at $y = 200 \mu\text{m}$ that drives the rectangular slab. A perturbation of $1 \mu\text{m}$ in wavelength was applied to the density. Figure V-20 clearly shows the development of Taylor spikes after 1.5 ns, which exhibit an aspect ratio of 20:1. We also see a fanning out of the spikes as they protrude into the higher-temperature regions. Figure V-21 shows the development of the Taylor instability on the inside

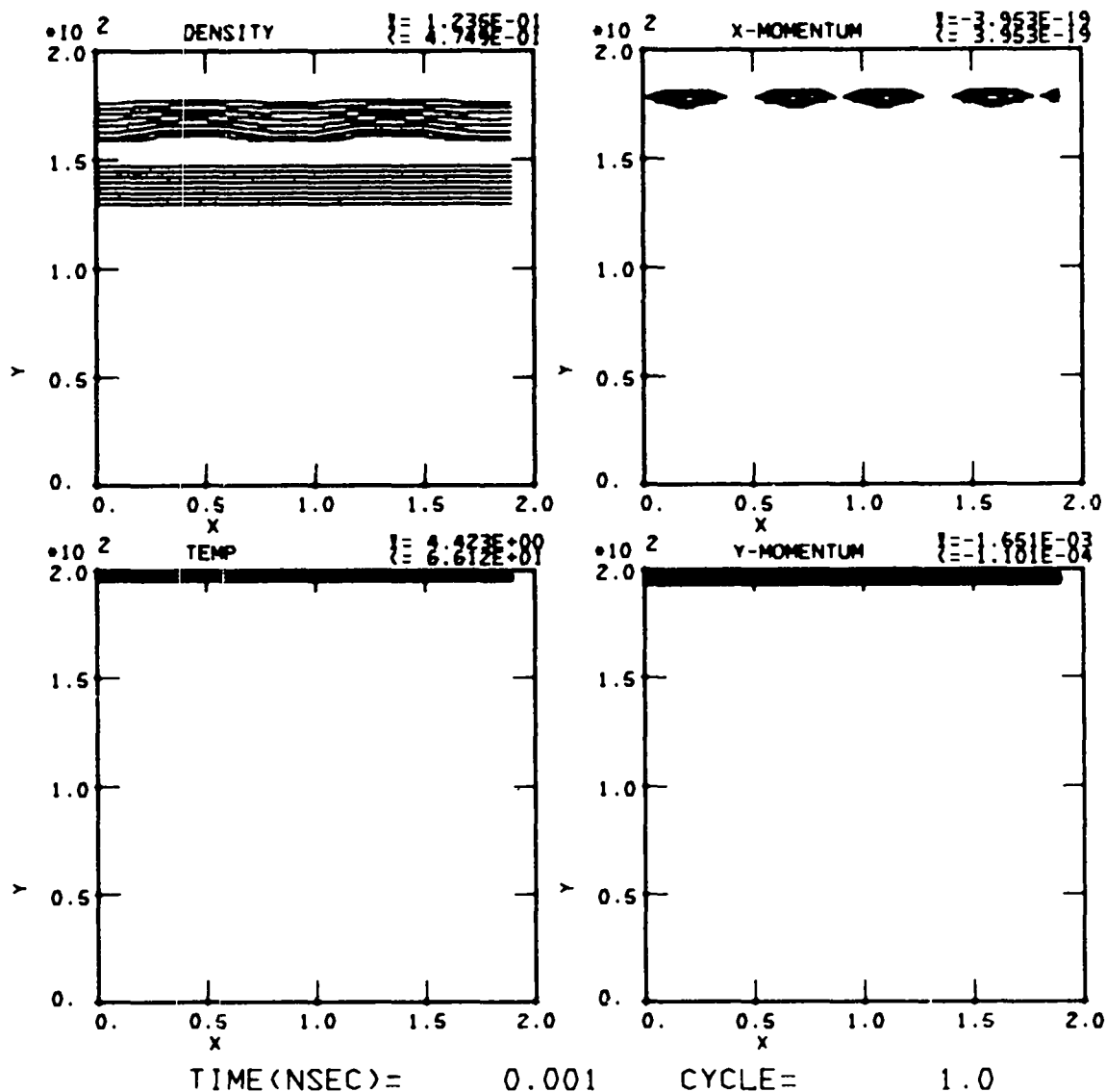


Fig. V-19.

Frame from a moving picture made with a two-dimensional hydrocode. Contour plots of density, temperature, x-momentum, and y-momentum are shown at 0 ns. A two-wavelength initial perturbation was applied to the density, and a temperature source that increases to a value of 333 eV in 1 ns was applied along the $y = 200\text{-}\mu\text{m}$ boundary. Note that the scale is highly distorted (2 by $200 \mu\text{m}$).

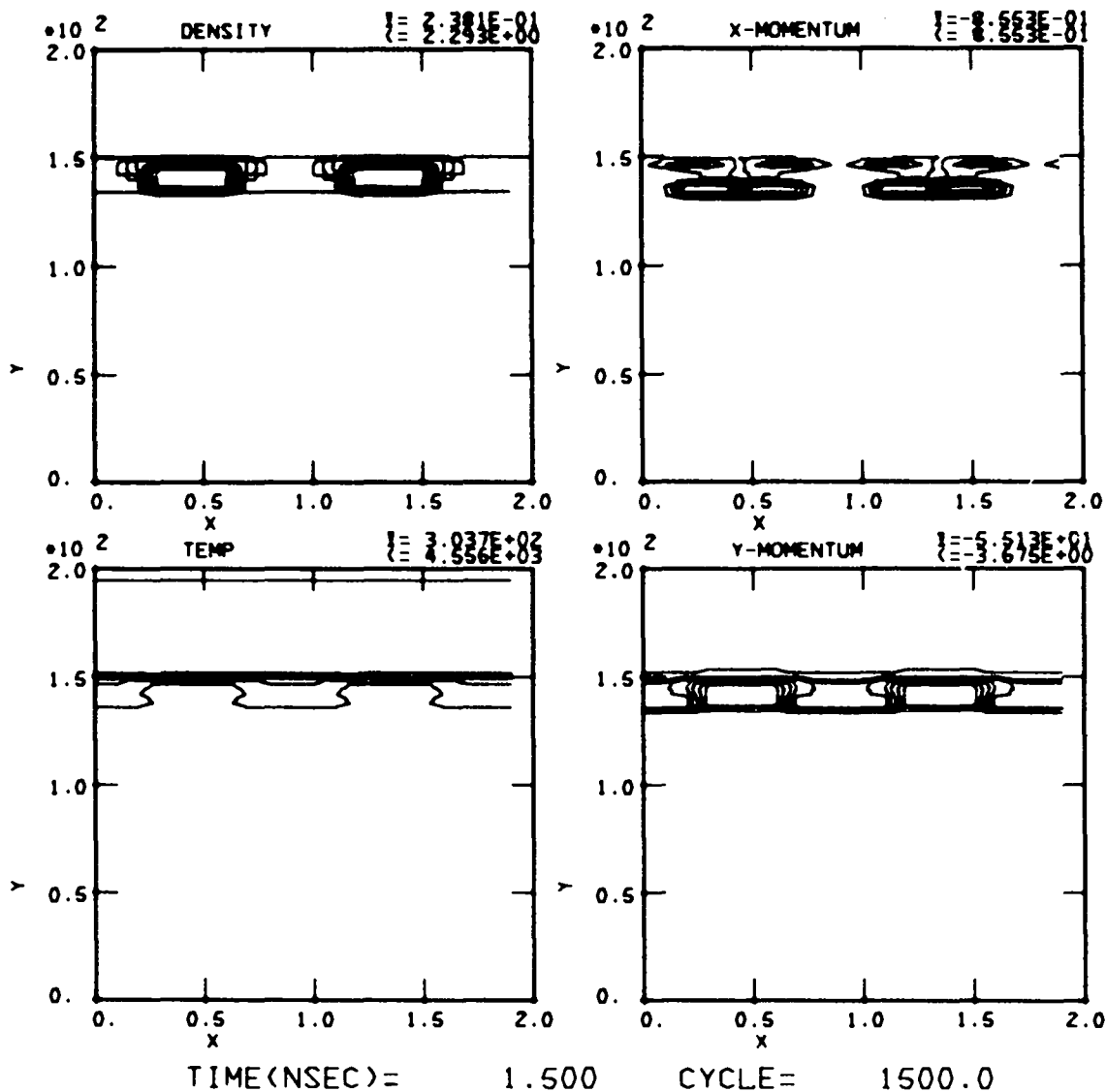


Fig. V-20.

Same as Fig. V-19 except at 1.5 ns. Note shell compression, full development of Taylor spikes, and flaring of spikes in the higher temperature regions. Aspect ratio of spikes, 40:1.

of the slab as it begins to decelerate. It decelerates because there is a symmetry boundary at $y = 0$, which causes the pressure between the two colliding slabs to increase.

Thus, a simulation of the Taylor instability was carried out into the far nonlinear region; but mode growth, saturation, and transition to turbulence remain to be studied. Mode growth and saturation are buried in the density profiles shown in Figs. V-20 and -21. To extract this information, a fast Fourier transform of the density profiles was performed and

the model structure of the profiles as a function of time was obtained. The results for the original initial mode and its first harmonic are shown in Fig. V-22. At first, the amplitude of the original mode remains constant because the thermal wave has not yet reached the slab. However, at ~ 6 ns the thermal wave reaches the slab and begins to accelerate the slab ablatively. At this time the original mode begins to grow and higher harmonics are generated. The linear-growth phase and the saturation for both the original mode and its first harmonic are clearly

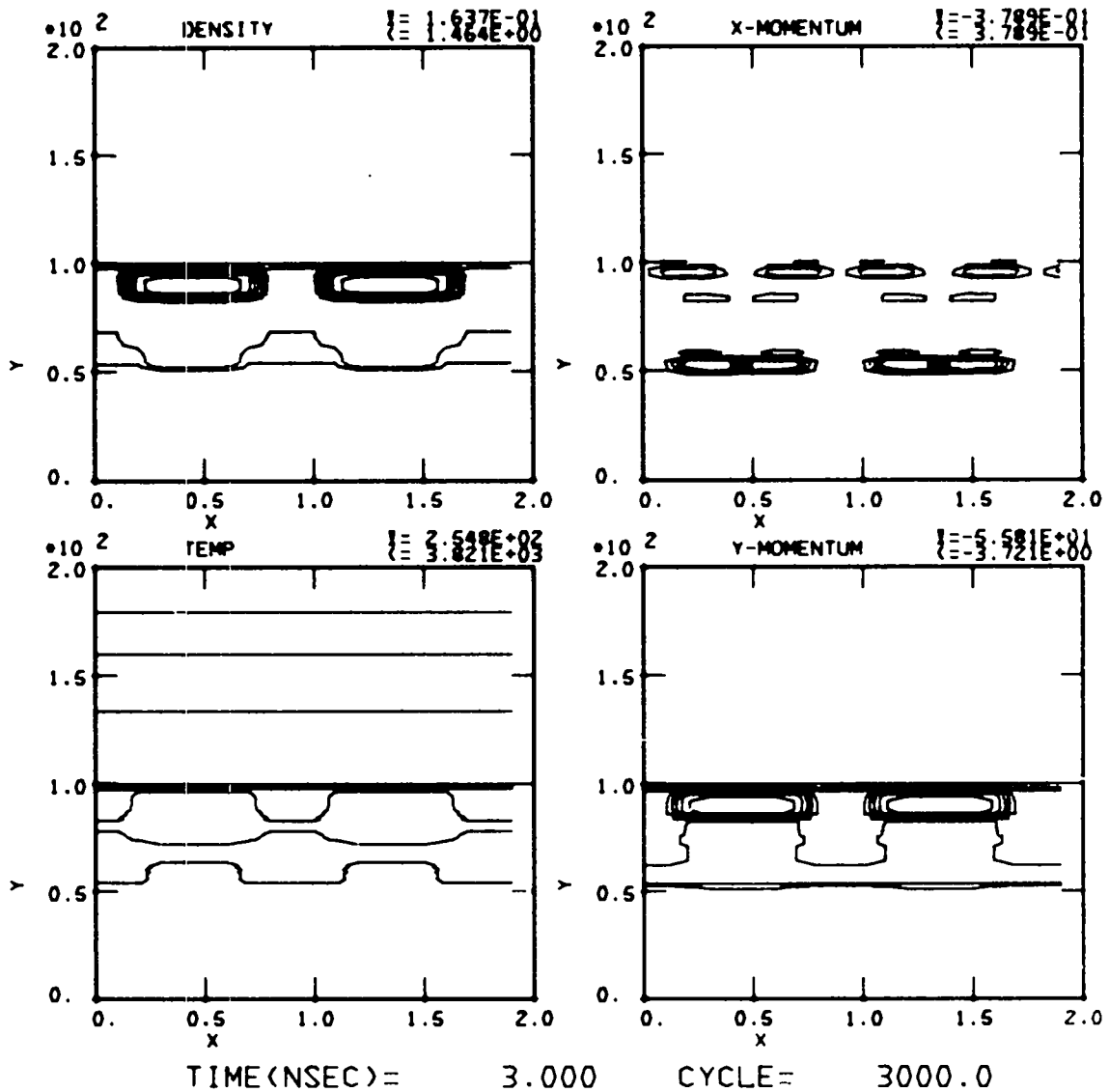


Fig. V-21.

Same as Fig. V-19 except at 3.0 ns. The slab has moved down and is decelerating. As the slab decelerates, a Taylor structure begins to develop on the inside of the slab. (Symmetry boundary at $y = 0 \mu\text{m}$)

seen in Fig. V-22. Because the Taylor growth rate is proportional to the square root of the wavenumber of the mode, the growth rate of the first harmonic should be greater than that of the original mode by about $\sqrt{2}$; this is borne out in Fig. V-22, as is the fact that the modes have saturated. Our studies of saturation levels of the modes as a function, e.g., of zeroth-order gradient, scale lengths, and flow velocities are continuing.

The transition-to-turbulence problem is addressed by examining the modes developed on the sides of the Taylor spikes and the shear flow velocities along the spikes, which give rise to a Kelvin-Helmholtz instability that may drive a turbulent state. The time scale for the development of turbulence is thus given by the ratio of the wavelength of the dominant mode on the sides of the Taylor spikes divided by the shear velocity.

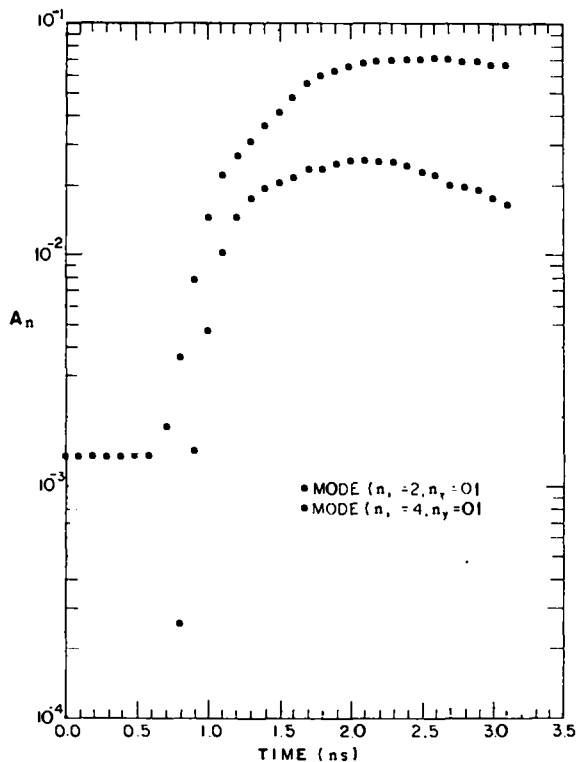


Fig. V-22.

Plot of mode amplitude A_n vs time. This plot was obtained by performing a fast Fourier transform of the density represented in Figs. V-19 through -21 at every time step, and plotting the amplitudes of the initial mode and its first harmonic. Note the time delay for the thermal shock to hit the slab before growth begins, the well-defined linear regime, and the subsequent nonlinear saturation of the modes.

Similar studies of nonlinear and transition-to-turbulence problems in spherical systems closely resembling laser-fusion pellets will be carried out with more sophisticated codes.

A LASL-developed cylindrical (R-Z) particle-Lagrangian code solves the set of fluid equations shown in Table V-IV.⁶⁶ We study the nonlinear and transition-to-turbulence problems in spherical systems because the code can handle highly contorted flows without mesh-tangling.

Our linear, nonlinear, and turbulence studies should increase our understanding of laser fusion pellet stability to a level at which the following engineering approach to the evaluation of pellet stability can be taken:

- First, a sequence of pellets is developed by using a one-dimensional mode and a particular design is chosen by the designer.
- A linear stability analysis is performed on the chosen design. If the design maintains shell integrity, the stability analysis ends, and we can be highly confident that the design is feasible. If, however, the design is unstable, we can either reject the design or proceed to the next step.
- A nonlinear stability analysis is subsequently performed. If the design maintains shell integrity after nonlinear saturation and turbulence are taken into account, the stability analysis ends, and we can be highly confident that the design is feasible. However, if the chosen design still does not maintain its integrity well enough during its implosion history, a recommendation is made to reject the design.
- Finally, if the target maintains its shell integrity, the effects of mix, turbulent pusher layers, and low-level perturbations on target performance must be evaluated.

REFERENCES

1. K. Lee, D. W. Forslund, J. M. Kindel, and E. L. Lindman, *Phys. Fluids* **20**, 51 (1977).
2. B. Bezzerides, D. Forslund, and E. Lindman, "Existence of Rarefaction Shocks in a Laser Plasma Corona," to be published in *Physics of Fluids* (1978).
3. A. W. Ehler, *J. Appl. Phys.* **46**, 2464 (1975).
4. R. DeCoste and B. H. Ripin, *Appl. Phys. Lett.* **31**, 68 (1977).
5. D. W. Forslund and C. R. Shonk, *Phys. Rev. Lett.* **25**, 281 (1970).
6. A. V. Gurevich, L. V. Pariiskaya, and L. P. Pitaevskii, *Soviet Physics JETP* **36**, 274 (1973).
7. G. B. Zimmerman, "Numerical Simulation of the High Density Approach to Laser Fusion," University of California Research Laboratory report UCRL-74811 (1973).

8. J. S. Pearlman, M. K. Matzen, *Phys. Rev. Lett.* **39**, 140 (1977).
9. K. R. Manes, V. C. Rupert, J. M. Auerbach, P. Lee, and J. Swain, *Phys. Rev. Lett.* **39**, 281 (1977).
10. R. P. Godwin, P. Sachsenmaier, and R. Sigel, *Phys. Rev. Lett.* **39**, 1198 (1977).
11. V. M. Cottles and D. V. Giovanielli, Los Alamos Scientific Laboratory unpublished data (1978).
12. V. M. Cottles, L. G. White, and A. H. Williams, "Absorption of One Nanosecond CO₂ Laser Pulses by Plane Finite Targets," 8th Annual Conference on Anomalous Absorption of Electromagnetic Waves (Tucson, 1978).
13. D. Forslund, J. Kindel, K. Lee, E. Lindman, and R. Morse, *Phys. Rev.* **A2**, 679 (1975).
14. J. J. Thomson and W. L. Kruer, *Comments Plasma Physics*, Vol. 3, No. 5, pp. 129-136 (1978).
15. J. F. Holzrichter, H. G. Ahlstrom, D. R. Speck, E. Storm, J. E. Swain, L. W. Coleman, C. D. Hendricks, H. N. Kornblum, F. D. Seward, V. W. Slivinsky, Y. L. Pan, G. B. Zimmerman, and J. H. Nuckolls, *Plasma Physics* **18**, 675 (1976).
16. M. A. Stroschio, D. B. Henderson, and A. B. Petschek, submitted to *Nucl. Fusion* (1978).
17. N. H. Burnett, H. A. Baldis, M. L. Richardson, and G. D. Enright, *Appl. Phys. Lett.* **31**, 172 (1977).
18. A. W. Ehler, *Phys. Fluids* **16**, 339 (1973).
19. D. C. Slater, *Appl. Phys. Lett.* **31**, 196 (1977).
20. S. J. Gitomer and H. Brysk, *Appl. Phys. Lett.* **32**, 616 (1978).
21. E. Stark and F. Skoberne, "Laser Fusion Program at LASL, October 1—December 31, 1976," Los Alamos Scientific Laboratory report LA-6834-PR (October 1977), pp. 14-15.
22. W. T. Leland, G. York, T. Ganley, D. Swanson, G. Loda, E. Yavornik, K. Riepe, R. Lindstrand, and J. Comly, "Antares Prototype Power Amplifier, Final Report," Los Alamos Scientific Laboratory report LA-7186 (July 1978), pp. 103-104.
23. D. W. Forslund, J. M. Kindel, and K. Lee, "Theory of Hot-Electron Spectra at High Laser Intensity," *Phys. Rev. Lett.* **39**, 284 (1977).
24. J. P. Freidberg, R. W. Mitchell, R. L. Morse, and L. I. Rudsinski, "Resonant Absorption of Laser Light by Plasma Targets," *Phys. Rev. Lett.* **28**, 795 (1972); R. P. Godwin, "Optical Mechanism for Enhanced Absorption of Laser Energy Incident on Solid Targets," *Phys. Rev. Lett.* **28**, 85 (1972); M. M. Mueller, "Enhanced Laser-Light Absorption by Optical Resonance in Inhomogeneous Plasma," *Phys. Rev. Lett.* **30**, 582 (1973).
25. D. W. Forslund, J. M. Kindel, Kenneth Lee, E. L. Lindman, and R. L. Morse, "Theory and Simulation of Resonant Absorption in a Hot Plasma," *Phys. Rev.* **A11**, 679 (1975).
26. K. G. Estabrook and W. L. Kruer, "Properties of Resonantly Heated Electron Distributions," *Phys. Rev. Lett.* **40**, 42 (1978); K. G. Estabrook, E. J. Valeo, and W. L. Kruer, "Two-Dimensional Relativistic Simulations of Resonance Absorption," *Phys. Fluids* **18**, 1151 (1975); R. L. Stenzel, A. Y. Wong, and H. C. Kim, "Conversion of Electromagnetic Waves to Electrostatic Waves in Inhomogeneous Plasma," *Phys. Rev. Lett.* **32**, 654 (1976); P. Kolodner and E. Yablonovitch, "Proof of the Resonant Acceleration Mechanism for Fast Electrons in Gaseous Laser Targets," *Phys. Rev. Lett.* **37**, 1754 (1976).
27. J. M. Kindel, K. Lee, and E. L. Lindman, "Surface-Wave Absorption," *Phys. Rev. Lett.* **34**, 134 (1975).
28. K. Lee, "Comparison of Multigroup Diffusion and Monte Carlo Electron Transport," *Bull. Am. Phys. Soc.* **22**, 1188 (1977).

29. David S. Kershaw, "Flux Limiting Nature's Own Way—A New Method for Numerical Solution of the Transport Equation," Lawrence Livermore Laboratory preprint UCRL-78378 (1976).
30. G. A. Zimmerman, "Numerical Simulation of the High Density Approach to Laser Fusion," Lawrence Livermore Laboratory report UCRL-74811 (1973); G. A. Zimmerman and W. L. Kruer, "Numerical Simulation of Laser-Initiated Fusion," *Comments in Plasma Phys. Controlled Nucl. Fusion Res.* 2, 51 (1975).
31. David Potter, *Computational Physics* (John Wiley & Sons, New York, 1953), p. 53.
32. R. J. Mason, "Hot Electron Transport in Laser Produced Plasmas," *Bull. Am. Phys. Soc.* 22, 1188 (1977); R. J. Mason, "Double-Diffusion Hot Electron Transport in Laser-Produced Plasmas," IEEE Catalog No. 78CH1357-3 NPS, p. 1A9 (1978). (Also to be published in *Phys. Rev. Lett.*)
33. C. W. Nielson, Los Alamos Scientific Laboratory, private communication, March 1978.
34. Martin J. Berger, "Monte Carlo Calculation of the Penetration and Diffusion of Fast Charged Particles," in *Methods of Computational Physics*, Vol. 1, B. Alder, S. Fernback, and M. Rotenberg, Eds. (Academic Press, New York, 1963), p. 134.
35. D. B. Henderson, "Electron Transport in Gas Discharge Lasers," Los Alamos Scientific Laboratory report LA-5154-MS (April 1973); D. B. Henderson, *J. Appl. Phys.* 44, 5513 (1973).
36. K. Boyer, D. B. Henderson, and R. L. Morse, "Spatial Distribution of Ionization in Electron-Beam-Controlled Discharge Lasers," *J. Appl. Phys.* 44, 5511 (1973).
37. B. R. Wienke, K. Lee, and W. F. Miller, Jr., "Electron Transport with Discrete Ordinates," *Bull. Am. Phys. Soc.* 22, 1189 (1977).
38. K. D. Lathrop, "Discrete-Ordinates Methods for the Numerical Solution of the Transport Equation," *Reac. Technol.* 15, (1972).
39. B. R. Wienke, "Fokker-Planck Collision Operator in One-Dimensional Geometries," in "Transport and Reactor Theory, April 1—June 30, 1977," Los Alamos Scientific Laboratory report LA-6911-PR (August 1977), p. 10.
40. B. R. Wienke and W. F. Miller, Jr., "Multigroup Discrete Ordinates and Fokker-Planck Operator," in "Transport and Reactor Theory, April 1—June 30, 1977," Los Alamos Scientific Laboratory report LA-6911-PR (August 1977), p. 12.
41. B. R. Wienke, "Spencer-Lewis Collision Operator and Small-Angle Corrections," in "Transport and Reactor Theory, July 1—September 30, 1977," Los Alamos Scientific Laboratory report LA-7025-PR (November 1977), p. 21.
42. J. Delettrez and E. B. Goldman, "Numerical Modeling of Suprathermal Electron Transport in Laser Produced Plasmas," University of Rochester report No. 36 (1976).
43. G. Kalman, C. Montes, and D. Quemada, "Anisotropic Temperature Plasma Instabilities," *Phys. Fluids* 11, 1797 (1968).
44. R. L. Morse and C. W. Nielson, "Numerical Simulation of the Weibel Instability in One and Two Dimensions," *Phys. Fluids* 14, 830 (1971).
45. J. R. Albritton, I. B. Bernstein, E. J. Valeo, and E. A. Williams, "Transport of Long-Mean-Free-Path Electrons in Laser-Fusion Plasmas," *Phys. Rev. Lett.* 39, 1536 (1977).
46. D. Mosher, "Interactions of Relativistic Electron Beams with High Atomic-Number Plasma," *Phys. Fluids* 18, 846 (1975).
47. D. S. Kershaw, "Interaction of Relativistic Electron Beams with High-Z Plasma," Lawrence Livermore Laboratory report UCRL-77047 (1975).

48. G. S. Fraley, E. J. Linnebur, R. J. Mason, and R. L. Morse, "Thermonuclear Burn Characteristics of Compressed Deuterium-Tritium Microspheres," *Phys. Fluids* 17, 474 (1974).
49. Gary S. Fraley, "The Integrated Compton Cross Section and Its Use in a Monte Carlo Scheme," Los Alamos Scientific Laboratory report LA-4592-MS (April 1971).
50. D. C. Montgomery and D. A. Tidman, *Plasma Kinetic Theory* (McGraw-Hill Book Co., New York, 1964).
51. L. A. Elliott, *Proc. R. Soc. Vol. A*, 284, 397-401 (1965).
52. M. S. Plesset, *J. Appl. Phys.* 25, 96-8 (1954).
53. G. Birkhoff, *Quart. Appl. Math.* 13, 451-3 (1956).
54. R. D. Richtmyer, *Comm. Pure Appl. Math.* 13, 297-319 (1960).
55. K. A. Taggart, Los Alamos Scientific Laboratory, private communication, 1977.

VI. LASER FUSION TARGET FABRICATION

Our target fabrication effort, supported by extensive theoretical investigations, supplies thermonuclear-fuel-containing pellets for laser-driven compression and heating experiments. These targets, which range from simple, deuterated, flat plastic films to complex, multilayered structures containing cryogenic, solid DT fuel, are optimized for use with high-power CO₂ lasers. After a target design has been created by the theoreticians, we first develop the new technologies to produce the materials, shapes, and properties desired. We then fill the target with thermonuclear DT fuel, assemble the necessary parts, and develop methods for measuring and characterizing all these properties. Finally, we insert the target in the target chamber and position it at the exact laser focal spot.

INTRODUCTION (R. J. Fries and E. H. Farnum)

Our target fabrication effort has two objectives.

- (1) We are supplying targets of current design to satisfy the needs of the experimental program. Targets of various designs are used: thermonuclear compression targets for main sequence experiments, partial and modified compression targets for target-essential experiments, a wide variety of targets for support-physics experiments, and several types of targets for military applications experiments. All are irradiated in one or the other of our laser systems.
- (2) We are developing new techniques as needed for the fabrication of future thermonuclear compression targets envisaged in the Laser Fusion Program plan. Because the design of these targets is not fixed, we must continue to investigate all the materials that have a high probability of being used in the final designs. We also are developing methods of measuring and characterizing these materials and of assembling them into required configurations.

In addition to these two goals, we provide micromachining, microassembly, and materials fabrication services to other groups.

A recent design for the Polaris-A multishell laser fusion target is shown in Fig. VI-1. Laser fusion targets have evolved slowly to this stage. Initial

targets, called Sirius, consisted of only one shell filled with room-temperature DT gas; this single shell acts as an exploding pusher in which the fuel is heated as it is compressed. Most of these shells consist of GMBs with only a few atmospheres of DT gas fill. Although these designs cannot lead to a high yield, they do produce some thermonuclear reactions and neutrons. The target is improved by adding a 100- μ m-thick layer of plastic, which is vaporized by the laser pulse causing the glass shell

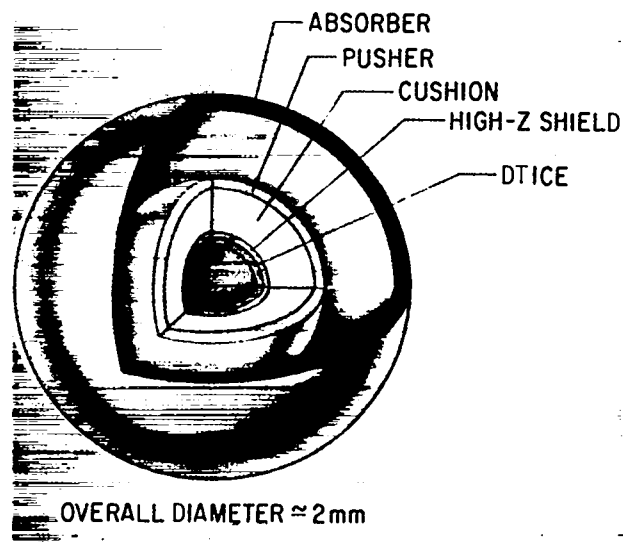


Fig. VI-1.
Polaris target design.

to implode hydrodynamically. By coating the GMB with molybdenum or other high-Z metal before plastic deposition we reduce preheat and thus make the desired adiabatic hydrodynamic compression possible. Such a design will be used to attain our 20-times-liquid-density milestone.

In our Polaris-A target, this high-Z metal coating is added as a heat shield for the fuel, the ablator layer is changed to low-density plastic foam to provide a hydrodynamic cushion, and a second pusher layer is added outside the foam.

In initial targets, we will irradiate the outer pusher shell directly, but in subsequent experiments we will add an ablator layer of low-Z material such as CH plastic. Finally, other layers will be added to provide further thermal insulation, to enhance laser absorption, and to improve hydrodynamic coupling of the laser energy to the target.

In all these targets, from the simple Sirius to Polaris, the fuel will be frozen as a solid layer of DT ice onto the inside surface of the innermost pusher shell. Calculations show that this cryogenic modification will improve the yield substantially. We are developing techniques to freeze such layers in place within the Helios target chamber. These and other targets of recent design call for the development of high-Z metal shells with diameter and wall-thickness uniformity deviations of not more than 1% and a surface smoothness tolerance of $<1000 \text{ \AA}$. They also require low-density, small-cell-size plastic foams, thick layers of plastic loaded with materials of normal or high Z, metal foams of both high and low Z, and smooth metal layers of moderate or low Z. In addition, we are developing methods to prepare alternative fuels that are solid at room temperature and contain fuel atoms at high density (e.g., polyethylene, lithium hydrides, or ammonia borane, in which the hydrogen is replaced by an equimolar mixture of deuterium and tritium). Even though the nonfuel atoms in these compounds dilute the nuclear fuel and reduce target performance, the fact that these materials are solid at room temperature may be an advantage, especially in designs that require fuel-containing layers in the outer parts of the target.

Because any target must be completely characterized to understand its performance, we have devoted much of our effort to measuring and documenting all targets we deliver and to developing new, automated high-resolution methods of characterizing target parts. We are developing a sur-

face acoustic-wave resonator/driver to sort batches of target shells for diameter and wall uniformity using the efficiency (Q-value) and frequency at which the shells bounce as an indicator of quality. We are also automating our x-ray microradiographic method for observing defects and nonuniformities in opaque shells.

TARGET FABRICATION

General

Our primary assignment in target fabrication is the assembly, delivery, and postshot analysis of targets for our three operating laser systems. We therefore devote whatever fraction of our effort is required to meet delivery requests from experimenters on these systems. In addition, we try to maintain a large and very flexible inventory of materials and techniques so that we can respond rapidly to changes in target design or specifications. As part of target assembly, we also mount and align the targets on the appropriate target-changing mechanism to eliminate the need for any further position adjustment in the target chamber. If desired, we photograph and analyze any remnants to supplement target diagnostics.

The process of target fabrication typically includes the following steps. A type of GMB is chosen that is most suitable for the desired diameter, wall-thickness, and gas-permeation characteristics. These GMBs are available from the 3M Company, KMS Fusion Inc., or LLL. The chosen microballoons are precision-screened to the desired size on an air-jet sieve, separated according to density by flotation in SF_6 gas, crushed by external pressurization (only for cases where the desired wall thickness is greater than $1.5 \mu\text{m}$), and cleaned by flotation in ethanol. The refined batch is optically preselected with an interference microscope and then filled with DT or DT:Ne gas mixtures by permeation through the wall at elevated temperature and pressure. The filled microballoons are cleaned in ethanol and examined carefully with an interference microscope. Targets passing optical inspection are examined and measured in three different planes. Coatings of metal and/or plastic are then applied to these selected microballoons. These coatings are examined in three views by x-ray microradiography to determine coating smoothness and uniformity, often

after each successive layer has been applied. In the meantime, other parts are being fabricated. For example, for the two-shell vacuum insulation target (see Fig. VI-2), we form the outer plastic shell by coating an appropriately sized copper ball bearing with plastic (by our low-pressure plasma polymerization method described below), cutting the coating into two halves using a laser knife (see Fig. VI-3), and etching the copper mandrel away in nitric acid to leave the plastic hemispheres (see Fig. VI-4). Other targets are fabricated in a similar manner. When the central fuel container is opaque, we use x-ray microradiography to determine shell uniformity.

Fabrication Activity (B. Cranfill, V. Woods, V. Gurule)

We supplied over 750 targets to our three operating laser systems and made nearly 250 parts for diagnostic devices. About 200 targets were fabricated for main-sequence experiments. Another 250 were supplied for a wide variety of target-essential and support-physics experiments including preliminary shots on the Helios laser, and over 300 were made for military-applications experiments.

We have completed the development of fabrication techniques for the current Vega-B target. We also developed a method of coating a mounted GMB with over $50\ \mu\text{m}$ of parylene for the 20-times-liquid-density milestone target. The surface smoothness of this coating is acceptable ($\pm 1\ \mu\text{m}$), but perturbations near the mounting stalk are still a problem because both the GMB and the stalk are coated in the coating process. We are trying to remove this coated stalk and to replace it with a new, uncoated one, but present separation methods do not give a smooth, spherical surface at the cutoff. We successfully fabricated glass-fiber targets for transverse-conductivity experiments by glueing $10\text{-}\mu\text{m}$ -diam glass fibers into the configuration shown in Fig. VI-5.

Gas Analysis of Laser Fusion Targets

General. To predict the performance of hydrogen-, deuterium-, and DT-filled microballoons correctly, we must be able to measure the gas fill with a high degree of accuracy. Also important are the permeation rates of the hydrogen isotopes through thin



*Fig. VI-2.
Two-shell vacuum insulation target.*

layers (shells) of a variety of coating materials at various temperatures. This information will be helpful in deciding under what conditions a given target type can be filled in real time. Permeation data at room temperature and below will also be important in selecting the best storage temperature for targets filled with the desired quantity of fuel gas.

Lead Cone Targets (J. E. Barefield II, V. Cottles, J. K. Feuerherd). Mass spectral analysis of four lead-cone targets¹ containing DT gas was completed and correlated with the results from x ray² and photon³ counting methods. Photon counting indicated a lifetime of 5 h. When the first lead-cone target was analyzed by mass spectroscopy within one lifetime after the target had been filled, a positive signal implied that the target contained DT

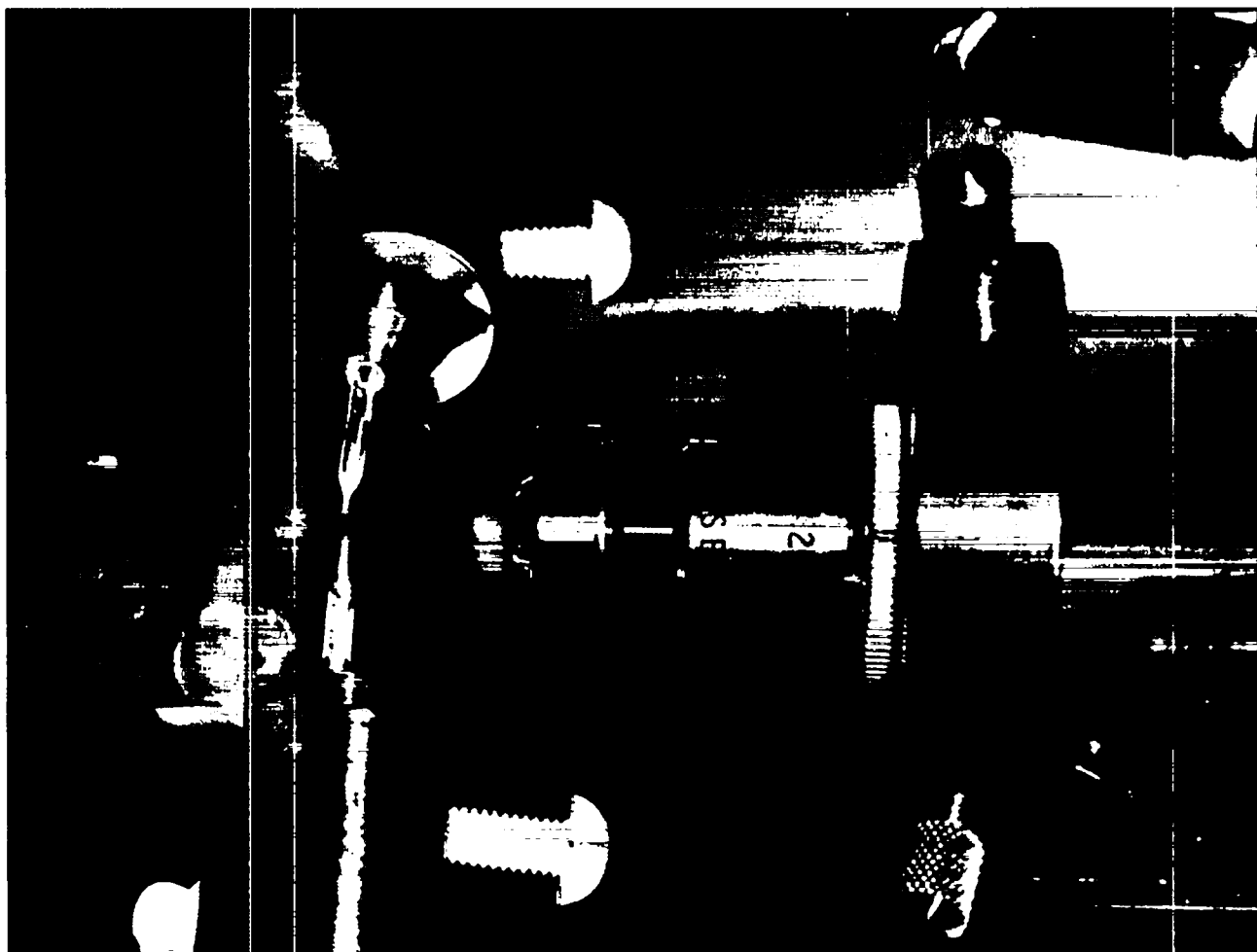


*Fig. VI-3.
Laser knife for cutting shells into hemispherical pieces.*

gas. However, no positive signals were observed for the remaining three targets, which were analyzed several lifetimes later. This result is consistent with the lifetime estimate of 5 h from the photon-counting method. Counts were observed from the x-ray counting method for all four targets, but these x-ray counts did not decrease with time.

System Modification (J. E. Barefield II, A. Mondragon). The turnaround time required to analyze individual microballoons in the mass spectrometer is determined by (1) the time required to outgas the ball crusher and (2) the time required for the pumping system to return the vacuum in the source of the mass spectrometer to its maximum

operating level (10^{-6} to 10^{-7} torr). The first problem was reduced by inserting a syringe-loaded microballoon crusher (similar to one developed at KMS-Fusion⁴) into the gas inlet section of the mass spectrometer system. In this apparatus, the microballoons are inserted in a microsyringe, which is pushed through a two-septa port. After the first septum is punctured, the microsyringe and its contents are outgassed. After the second septum is punctured, the microballoon, which is then at the mass spectrometer gas inlet port, is crushed and the gas content is measured. The second problem will be solved by installing a highly efficient vacuum system that will be pumped by a turbomolecular pump (the ultimate operating pressure of this unit is

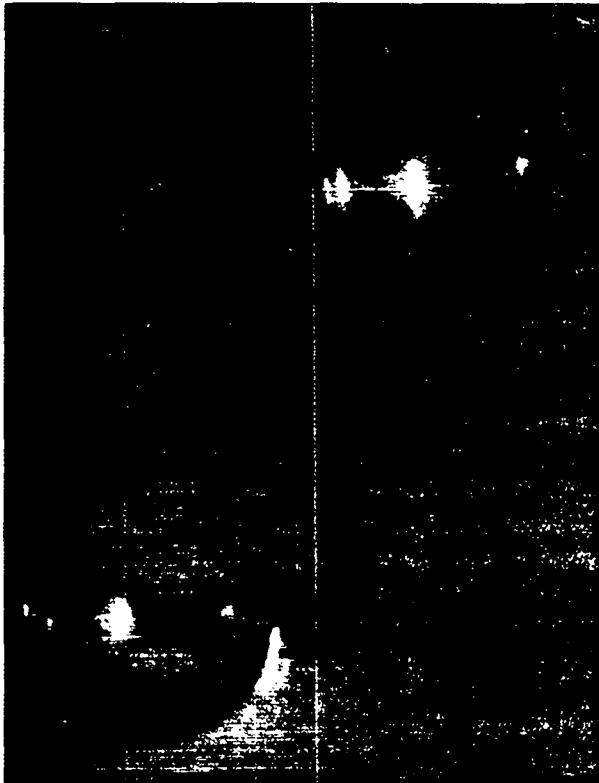
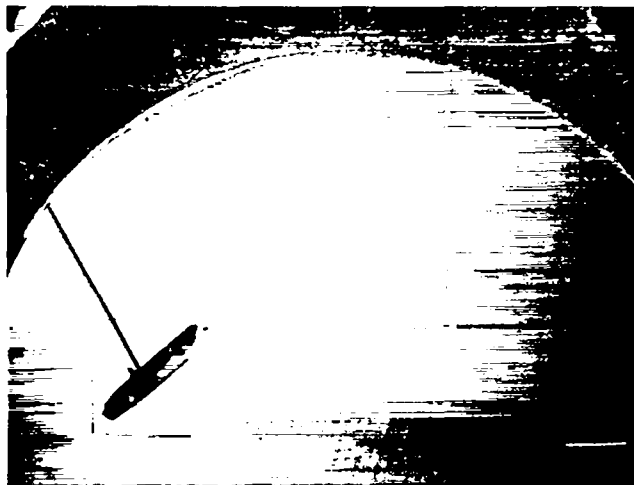


Fig. VI-4.
Hemispherical plastic shells.



→ | mm | ←

Fig. VI-5.
Photomicrograph of a transverse conductivity target. Glass fibers are $\sim 10 \mu\text{m}$ in diameter.

5×10^{-8} torr). With the small quantities of gas expected to be analyzed, the high-vacuum recovery time (in the source of the mass spectrometer) should not exceed a few minutes. The design and installation of this pumping system are essentially complete. The system will be in operation by the end of July 1978.

Microballoon Separation, Measurement, Characterization, and Fabrication

General. Almost all our DT-filled targets use a microballoon as the central, fuel-filled core. We therefore devote considerable effort to develop methods for separating, measuring, and characterizing glass or metal microballoons. In addition, we are developing techniques to alter the size and/or the quality of existing microballoons, as well as to fabricate microballoons directly.

X-Ray Microradiography (D. M. Stupin, M. Campbell, M. A. Winkler)

General. Both the size and the wall-thickness uniformity of laser-target microballoons must be measured to 1% for sphericity, between 1 to 10% for wall thickness, and between 10 to 100Å for small-scale surface defects such as dimples and warts. Optical interferometry is very useful for GMBs, but cannot be used for metal microballoons or for other opaque microballoons. For these specimens we are using micro-x-radiography. Because the yield of good microballoons in a particular batch, in general, amounts to only a few per cent or less, it is important to develop rapid methods to find the few good microballoons in each batch that satisfy the uniformity requirements. We have not discovered any batch processes other than screening and density separation that significantly improve the yield of metal microballoons. However, we have improved 10-fold the rate at which we can radiographically examine metal microballoons for quality. In addition, we demonstrated that x radiography is a sensitive method to measure wall-thickness variations in opaque plastic coatings applied to glass microballoons.

Development of a Simple Array Shaker. The 10-fold speedup in quality examinations is due primarily to an array shaker that resembles a salt shaker

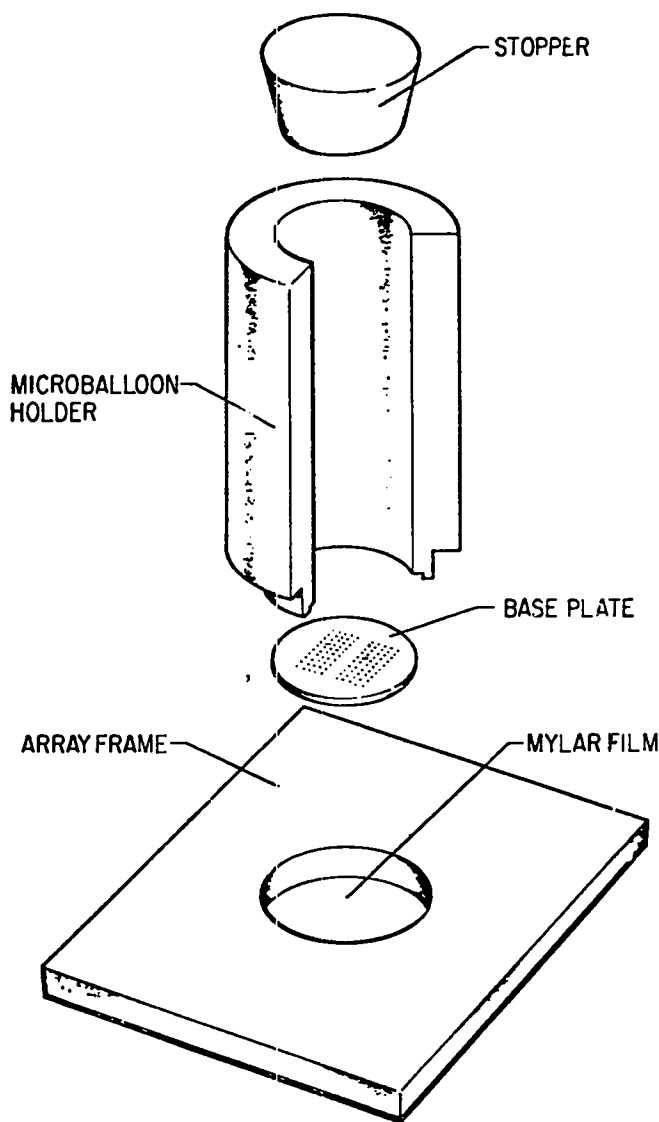


Fig. VI-6.
Microsphere array maker.

(Fig. VI-6). With this array shaker, four arrays of 400 balloons each are laid down on Mylar film in about one minute, where previously a single 100-balloon array required 1 h. To make an array, a Mylar film coated with a thin layer of vacuum grease is placed over the top of the array shaker; this assembly is inverted allowing the microballoons to fall through the holes in the shaker to the Mylar film (Fig. VI-7). When the shaker and Mylar are reinverted, a 400-sample array is left on the Mylar film.

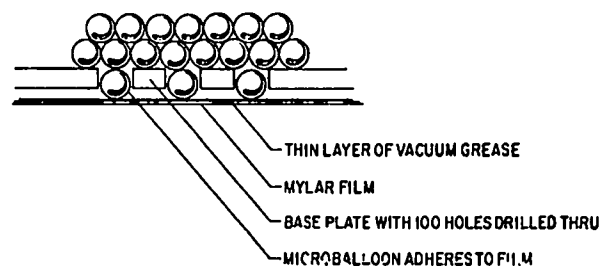
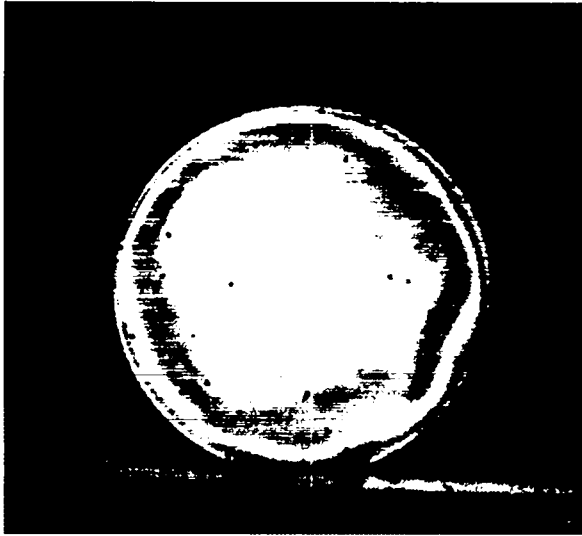


Fig. VI-7.
Detail of dispersing method for microsphere array maker.

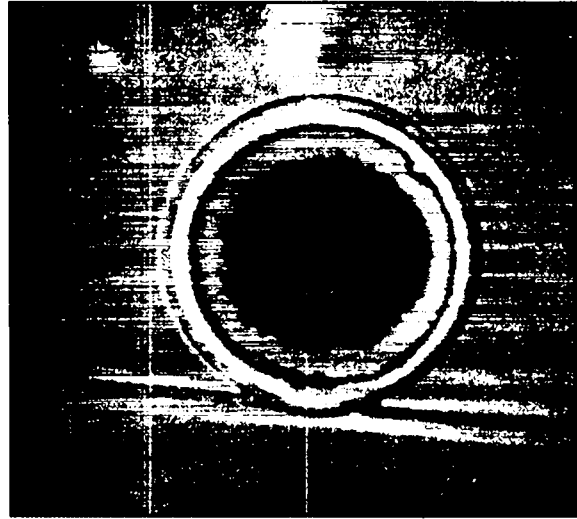
In a recent selection process, four arrays of 400 metal balloons each (1600 balloons total) were radiographed simultaneously in 10 min with a 20-kV bremsstrahlung x-ray source, and the resultant contact radiographs were scanned visually in ~10 min under a microscope. Ten thousand nickel microballoons were examined in this manner, and from this sample, 35 microballoons were selected as possibly good ones. To characterize these 35 balloons more completely, they were reradiographed at three known angles, and from these radiographs it was determined that only three specimens had wall-thickness variations of $\pm 5\%$ or less. This entire process took three weeks to complete, which is ten times faster than previously possible.

X Radiography of Plastic Coatings (D. M. Stupin, M. Campbell, R. Liepins). To improve our ability to deposit uniform plastic coatings on GMBs, we must measure the thickness and thickness uniformity of plastic coatings applied under different experimental conditions. We determined that microradiography with a 4-kV bremsstrahlung x-ray source is sensitive to thickness variations in poly(p-xylene) deposited on a $1\text{-}\mu\text{m}$ -thick glass microshell when the coating is more than $10\ \mu\text{m}$ thick.

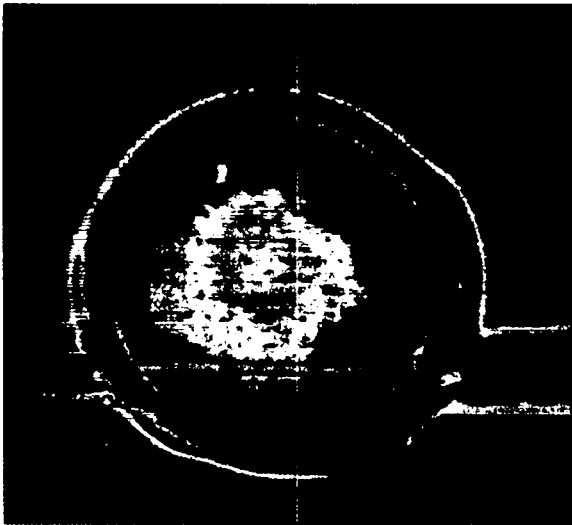
Five $100\text{-}\mu\text{m}$ -diam GMBs with an average wall thickness of $1\ \mu\text{m}$ were selected for sphericity; two had uniform walls, but the other three had very non-uniform walls when viewed in Jamin-Lebedev interference. The GMBs were glued to $10\text{-}\mu\text{m}$ -diam glass fibers, and interference images of each were made in white light in a known orientation of the GMB (Fig. VI-8). Then the microballoons were coated with $10\ \mu\text{m}$ of poly(p-xylene) and radiographed with 4-kV bremsstrahlung x radiation.



(a)



(b)



(c)

We analyzed the radiographs with an image analyzer (Fig. VI-8b) and compared the radiographs to the interferographs. Figures VI-8a and -8b show that a GMB with significant wall variation appears to have a uniform wall when coated uniformly with $10\ \mu\text{m}$ of poly(p-xylene). Therefore, the radiographic analysis of the coated GMB is sensitive primarily to the plastic coating, and the variation in the thickness of the glass wall is not significant. Figure VI-8c is a radiograph of a GMB coated nonuniformly with poly(p-xylene).

Fig. VI-8.

Analysis of plastic coating uniformity on GMBs by x-ray radiography.

- (a) GMB in interference microscope. Nonuniform wall is evident;*
- (b) same GMB, x-ray radiograph, after coating with plastic; nonuniform wall of GMB does not distort image of uniform plastic coating;*
- (c) x-ray radiograph of a GMB coated with a nonuniform layer of plastic.*

Surface Acoustic Wave Separation Techniques (W. Bongiani, Rockwell Int.)

Commercially available microballoons of both glass and metal are generally of very poor quality, with as few as one in 10^8 possessing the sphericity and wall-thickness uniformity required for laser fusion targets. We have therefore developed elaborate procedures to separate the few high-quality microballoons⁵ in batch processes, and we are continuously striving to improve these separation and recovery techniques.

We are evaluating the use of surface acoustic waves (SAW) in separating microballoons according to their size and geometric perfection. This method analyzes the acoustic response of the wall of the microballoon. At sufficiently high power levels, this acoustic response gives rise to a net displacement whose velocity leads to automated separation.

The four characteristic parameters of a microballoon (radius, wall thickness, and the variations in each), can be expressed in the more readily observable parameters of outside diameter, mass, and variation of mass about a center of gravity. Ideally, it would be desirable to use surface acoustic waves to measure each of these last three parameters independently to any degree of accuracy. Unfortunately, these parameters couple to one another and set an upper bound on the accuracy that can be obtained on any one variable. For example, a GMB with an infinitely thin wall could resonate only at a single frequency, that is, it would have an infinitely narrow bandwidth. Any deviation from symmetry or any flaw would scatter energy into other modes (i.e., other frequencies) that could be readily observed. A real microballoon has a definite wall thickness and therefore has a finite bandwidth. This bandwidth is inversely related to the aspect ratio given by the radius divided by the wall thickness.

Any flaw in a real microballoon must have a vibration mode that falls outside the natural bandwidth to be observed. Thus, it follows that a quality sorter, which selects on the basis of resonance, can only approach the resolution given by the aspect ratio. For example, a sorter of given efficiency (Q-value) will produce thin-walled microballoons of poor quality along with thicker-walled ones of good quality. To maximize the number of good ones it is necessary to select for diameter and wall thickness first. Microballoons can be sorted for diameter by sieving, and sieved microballoons can be sorted for thickness by observing their drift velocities when they are driven by SAWs below their resonance frequency.

We measured the power level of the surface acoustic wave needed to remove a microballoon from a surface and compared these values with our calculations. The drift velocity of a microballoon along a surface was calculated by extending our original theory and including the effect of electrostatic charge. Theoretically, we should be able to separate GMBs with average wall thicknesses differing by no more than 0.5%. Once the wall

thickness is determined, a second resonance sorting should determine wall uniformity to the same level of accuracy.

All mechanical parts for a continuous SAW microballoon processor were constructed and tested. These included a microballoon feeder that placed GMBs, one at a time, on the sorter and a laminar-flow pickoff device that collected the GMBs from the sorter.

Initial results with 100- μ m-diam microballoons were disappointing. A batch of 3M Company's B18A GMBs that had been screened and washed in ethanol moved only very short distances on the SAW surface plate. A second batch of B18A GMBs that had not been washed showed somewhat better motion but still would not move freely. The inhibited motion during the initial experiment was probably caused by excessively high humidity. High humidity has always plagued microballoon handling, presumably because adsorption of water on the GMB adds surface-tension forces that become predominant at humidity levels significantly above 50%. Humidity control might solve the sticking problem. We do not consider this problem an insurmountable obstacle to future work because we can increase the amplitude of the SAWs with high-power transducers and rf sources that are available and drive the GMB off the surface.

INORGANIC COATINGS DEVELOPMENT

General

Because nearly all future targets will require layers and shells of metal or plastic, we continued the development of a wide variety of coating techniques. Metal coatings were applied by the wet chemical methods of electro- and electroless plating, by chemical vapor deposition (CVD), by physical vapor deposition (PVD), and by sputtering. We focused our attention on high-quality coatings and on the coating and recovery of a small number (~100) of preselected glass or metal microballoons.

Electroless Plating (S. Armstrong, A. Mayer)

Two main problems are encountered when scaling down the electroplating process previously

developed.⁶ The first is related to the plating fixture and to recovering all the targets placed into it for a plating run, and the second is related to the fact that plating problems arise when trying to plate small quantities of substrates in which the ratio of surface area to solution volume is small.

The greatest progress was made in fixture development. To retain a small number of GMBs in the plating chamber, we scaled down the original bulk plater and selected materials for the moving parts with compatible thermal-expansion coefficients that would maintain the small clearances during electroless nickel-plating. The plating chamber was made from Pyrex glass with ground flat ends. Both ends of the glass chamber were threaded, which allowed us to capture the balls between two nylon end screens after the chamber was assembled into the threaded alumina cylinder and threaded Lexan top plate. The stationary piston was made from Teflon. The latest plating apparatus is shown in Fig. VI-9. Recovery rates of 90% and better have been typical with this plating fixture.



Fig. VI-9.

Electroless plating fixture designed to plate less than 100 microspheres in a plating run.

The second major problem in coating small numbers of spheres was our inability to achieve acceptable electroless deposits. In the past we were able to deposit uniform coatings of electroless nickel on CVD-metallized glass spheres in bulk quantities of $\sim 100\,000$, or more. However, the same process (Shipley's Niculoy 22, a Ni-P-Cu tertiary alloy) on 10 to 100 metallized spheres, produced unacceptable results. In most instances a thin ($<1\text{-}\mu\text{m}$) initial layer of copper was deposited on the majority of the substrates, which rendered the surface noncatalytic to nickel deposition. In other cases, voids were observed in the coatings. However, multiple CVD nickel deposits, approaching a total thickness of $1\ \mu\text{m}$, followed by hand-sorting to select spheres with continuous coverage, appeared to solve the problem of voids in the coating. We are still investigating why an initial copper layer was deposited on the spheres that caused the subsequent cessation of catalytic metal deposition. The small ratio of surface area to bath volume in the case of small loads may be the cause, because we always obtained normal plating in larger loads. Work towards solving this problem is in progress.

Electroplating (S. Armstrong, A. Mayer)

A small number of high-quality Be-Cu bearings, $500\ \mu\text{m}$ in diameter, were electroplated with $10\ \mu\text{m}$ of bright gold. The mandrels were then dissolved through $25\text{-}\mu\text{m}$ -diam holes drilled in the gold plating, by alternately pressurizing and evacuating the acid leaching bath. We hope to be able to reseat the $25\text{-}\mu\text{m}$ holes by laser or electron-beam welding, thus forming a faultless freestanding gold shell.

Rising-Bubble Process for Manufacturing Hollow Micro- and Macrospheres (S. Armstrong)

All current processes of producing hollow microspheres are similar: they are batch processes in which small, solid particles of the shell material containing a blowing agent are passed through a hot zone, where they expand into bubbles. Because the material composition must be carefully chosen to give the desired properties for bubble formation, options for tailoring the physical properties of the shell to target design requirements are severely restricted.

In our experiments we aimed at demonstrating the feasibility of plating gas bubbles generated and introduced into a plating bath. This concept involves the generation of a carefully controlled gas bubble containing a reducing or destabilizing agent that would cause metal plating to occur at the bubble's surface. Theoretically, the bubble could consist of any type of gas with just sufficient destabilizing agent to initiate the plating process.

Simple experiments demonstrated the feasibility of the idea. In these experiments the gas bubbles were generated by the action of a colloidal tin-palladium catalytic solution on cadmium and aluminum metal. A metallic shell formed over the bubble, which was shown to be tin. Using this method, we may be able to make metal microballoons from a wide variety of materials.

Chemical Vapor Deposition (CVD) (W. McCreary, D. Carroll)

The CVD process involves the reduction, either thermal or chemical, of a metal-containing compound at the surface of a substrate. For the CVD process to be useful as a technique for fabricating laser fusion targets, it must produce a uniformly thick, fully dense coating with a nearly perfect surface finish.

In the CVD area we emphasized the characterization of fluid beds and the development of methods for coating small numbers of preselected GMBs in the size range of 100 to 300 μm . The coating thickness desired was between 1 and 10 μm with a wall-thickness uniformity of 10% and a surface smoothness of 0.1 μm . We also tried to deposit very thin, adherent, CVD nickel coatings as the metalization layer on GMBs to allow subsequent electroless plating.

We were able to reproducibly coat GMBs with ~ 1 μm of CVD nickel, although several coating runs were sometimes required to obtain this thickness. Recovery was as high as 90%, and surface quality was good (Fig. VI-10). Attempts to deposit thick, smooth nickel coatings have not been successful. The low flow rates required to prevent blowout of the light GMBs resulted in low coating rates, and thus in long run times for thick coatings. Usually, CVD nickel runs must be terminated after 15 to 30 min due to sluggish bed action, so that multiple runs are

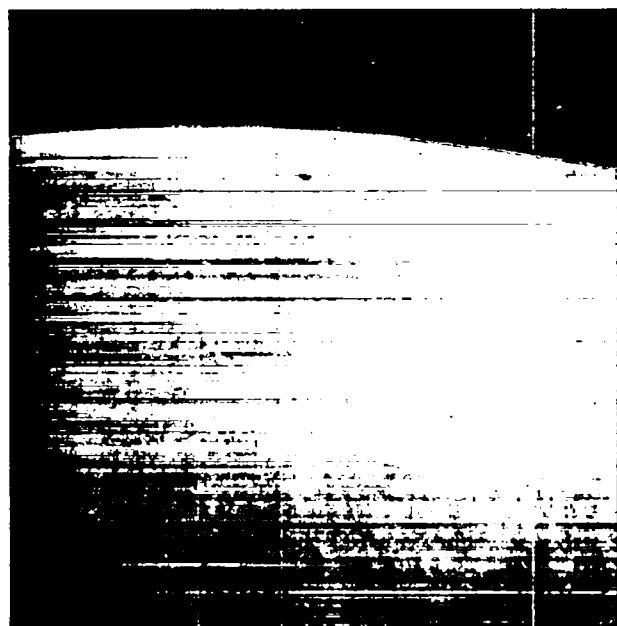


Fig. VI-10.

Scanning electron micrograph of CVD nickel coating, 1.2 μm thick on glass microballoon; 2500 X.

required, with the yield of GMBs being reduced in each run. Additionally, rough and nodular metal begins forming as the thickness increases.

Attempts to deposit CVD tungsten coatings onto small quantities of preselected GMBs were also unsuccessful. The major difficulty is that at the low flow rates required to prevent microballoon blowout, the reaction kinetics are changed. The $\text{WF}_6 + \text{H}_2$ reaction is not well-enough understood to allow us to reestablish the conditions required to regain the surface quality we normally obtain.

Sputter Coatings (A. T. Lowe, C. Hosford)

We continued our development of sputter coatings on microspherical mandrels. These efforts concentrated on GMBs and solid copper spheres in the diameter range of 200 to 500 μm and on high-Z metals such as gold, molybdenum, and tungsten. Previously, we had discovered that a small batch of GMBs could be sputter-coated with molybdenum or tungsten while agitated on a vibrating table. The vibration frequency had to be swept to keep the

spheres in motion and even then, only metals with a high elastic modulus could be plated without causing the spheres to stick to the vibrating table. We can presently deposit $\sim 1\text{-}\mu\text{m}$ -thick coatings of molybdenum, tungsten, and palladium onto large batches of GMBs with average surface defects of $\sim 0.1\ \mu\text{m}$. Attempts to increase coating thickness failed because the additional vibration needed to keep the heavier spheres in motion broke the spheres. In addition, larger vibration amplitudes further degraded the coating surface finish. Therefore, we discontinued work on the vibrating table and concentrated our efforts on a microsphere levitator.

A gas-jet microballoon levitator was developed at Bjorksten Research Laboratory in attempts to levitate and heat a GMB to improve its surface finish.⁷ The GMB is levitated on a laminar gas flow and, because the sputter deposition process requires a low pressure-gas background, we incorporated the levitator into the sputtering apparatus. Sputter-depositing metal onto levitated, rotating microspheres eliminated any collisions that deteriorated the surface finish of GMBs coated on the vibrating table and should produce more uniform coatings of a wider range of materials. The main disadvantage of the levitator is the small number of GMBs (presently only one) that can be levitated at one time. This number is somewhat smaller than desired for coating "small batches" of preselected GMBs.

The levitator is made from a commercially available collimated hole structure (CHS) (a closely packed array of parallel $50\text{-}\mu\text{m}$ -diam tubes with a dimple machined in the upper surface) as shown schematically in Fig. VI-11. This CHS provides a gas bed upon which the GMB floats with the machined dimple providing lateral stability.

The levitating gas also supplies part of the sputtering medium. With $500\text{-}\mu\text{m}$ -diam copper spheres at pressures of 10 to 20 torr, nearly all the sputtering gas is supplied by the levitator, but for the lighter GMBs, the levitation-gas flow must be supplemented by additional sputtering gas.

Initially, levitating a GMB in the vacuum chamber was a difficult task. GMBs levitated in air could not be kept suspended during pumpdown because of the large pressure differentials in the bell jar and because of the required rapid adjustments to the levitating gas flow. Two techniques have worked with limited success. First, a vacuum chuck was in-

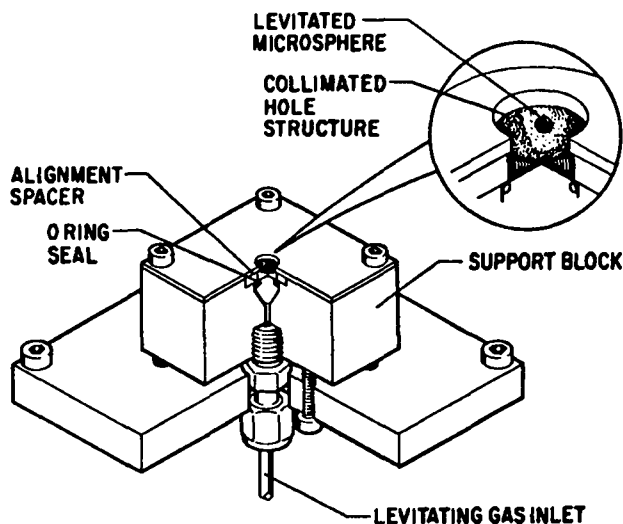


Fig. VI-11.

Gas-jet levitator employing a collimated hole structure.

stalled above the CHS, which is used to hold the GMB in place during pumpdown. When the system is ready the GMB is dropped into the dimple of the CHS with a combination of positive air pressure and mechanical vibration on the probe. Secondly, we had some success in lifting the GMB off an inactive CHS with a puff of gas. Because the gas flow required to levitate the GMB is insufficient to overcome the adhesion forces between the GMB and the CHS, we added a small, additional pulse of gas flow to begin levitation. A schematic of the gas control system for the vacuum chamber, of the vacuum chuck, the levitator main stream, and the levitator gas puff is shown in Fig. VI-12. Each pressure and vacuum system is independently controlled and monitored. In addition, we used several types of static eliminators to try to overcome electrostatic attraction between the GMB and the CHS before pumpdown. If the GMB has a large electrostatic charge and if the majority of this charge is not removed before pumpdown, no amount of vibration or gas puffing will remove the GMB from the CHS surface in a controlled manner.

Static problems are minimized when using solid copper-sphere substrates, and initial results with gold deposited on levitated copper spheres are encouraging. A $2.5\text{-}\mu\text{m}$ -thick gold coating (shown in Fig. VI-13) shows a uniformity of better than 10%.

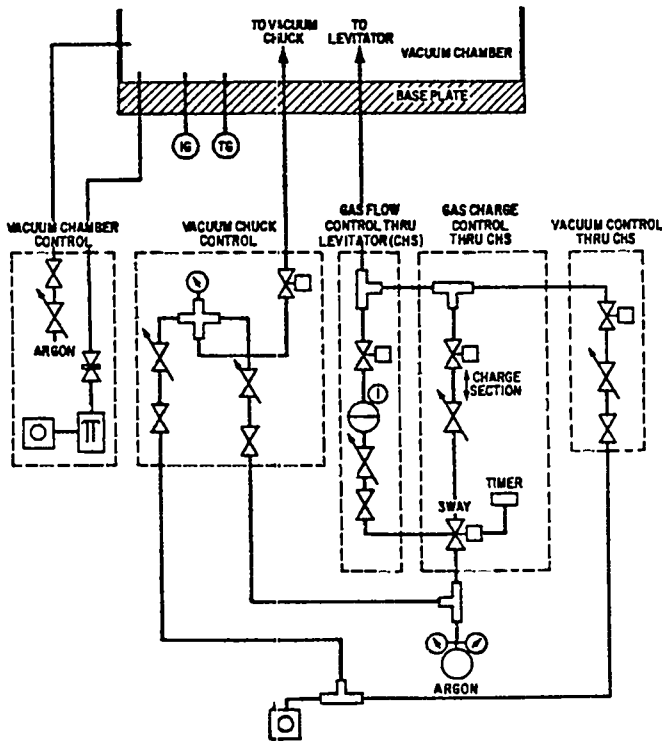


Fig. VI-12.

Gas control systems for gas-jet levitator.

GMBs were also levitated in vacuum and sputter coated for short times. However, the GMBs soon became unstable in the rf plasma and returned to the CHS surface where they became stuck. We are trying to understand why plasma coating affects the GMB levitation and are attempting to determine the smoothness and thickness of the coatings we can apply.

Strength Measurements on Shells (J. V. Milewski)

The mechanical strength of target shells determines the maximum amount of fuel gas that can be loaded into a target and thus limits target design. To provide this design information and to help develop stronger shells and materials, we built a microballoon tensile tester to measure the mechanical strength of a microspherical object. This method consists of potting slightly less than half of a shell, whose diameter and wall thickness had been measured, onto a tensile rod grip with high-strength epoxy; aligning the grip in the tensile testing ap-

paratus to a mating grip attached to a microload cell; potting and curing the other half of the shell to this mating grip, as shown in Fig. VI-14; and recording the tensile load required to pull the grips apart. Shell diameter and wall thickness are remeasured on the broken pieces by optical microscopy to verify initial nondestructive measurements.

A detailed stress analysis was performed to determine the error caused by the bending stress that results if the potting is not exactly at the equator of the hemisphere. Results are summarized in Fig. VI-15, which shows measurement error caused by that fraction of the shell diameter that remains unpotted. This fraction is easily controlled to 0.2 diameters, which causes an error of only 3%. Furthermore, the fraction can be measured before breaking the shell and the proper correction can then be applied to the data.

Mandrel Development (S. Butler)

Work toward making mandrels for metal microballoons continued. This effort should produce microspheres that can be (1) coated with nickel by CVD and (2) removed through the coating leaving a shell strong enough for further coating. The resulting product is a freestanding metal microballoon, with the inside diameter dependent upon the mandrel size and the wall thickness determined by the coating process.

The droplet generator,⁸ described in LASL report LA-7328-PR, was modified to allow heating of the reservoir and capillary or orifice so that molten materials may be dropped. Also, the capillary was replaced with a larger tube terminating in an orifice that allows viscous liquids to be driven out of the generator reservoir at lower pressures. Breakup of the liquid jet was stimulated by both transverse and axial vibrations on the tube.

Drops ranging in diameter from 550 μm to 1 mm were made of a high-temperature wax (melting point, 382 to 386 K). The material was heated to 403 to 423 K (viscosity, ~ 130 cP), dropped, and cooled in the ambient air as it fell. Even with a fall distance of ~ 3 m, obtained by directing the stream horizontally, only the smallest drops in this size range solidified before impacting the collector.

Spheres of this high-temperature wax withstood the low-temperature (353 K) CVD nickel process,



Fig. VI-13.

Photomicrograph of 2.5- μm -thick gold coating on a 500- μm -diam Be-Cu sphere; 2000 X.

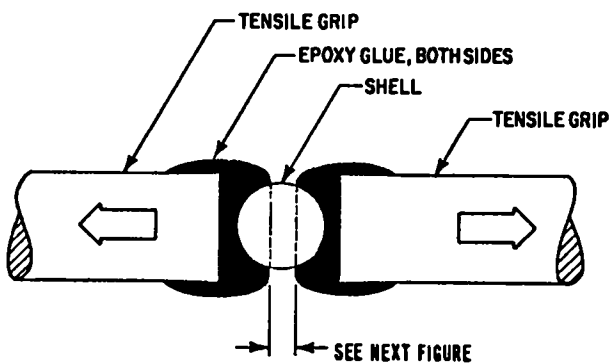


Fig. VI-14.

Close-up illustration of shell potted and ready for tensile testing.

but as yet a suitable coating, allowing dissolution of the wax without destroying the coating, was not achieved. Work is continuing, and if the material is suitable, the droplet size range will be extended by using smaller orifices and faster cooling with a cold gas or with helium.

The apparatus is also capable of dropping a molten inorganic salt, sodium nitrite (melting point, 556 K), but work with this material awaits availability of a fume hood.

ORGANIC COATINGS DEVELOPMENT

General

Many of our multilayered laser fusion targets use an outer shell of low-density, low-Z material as an

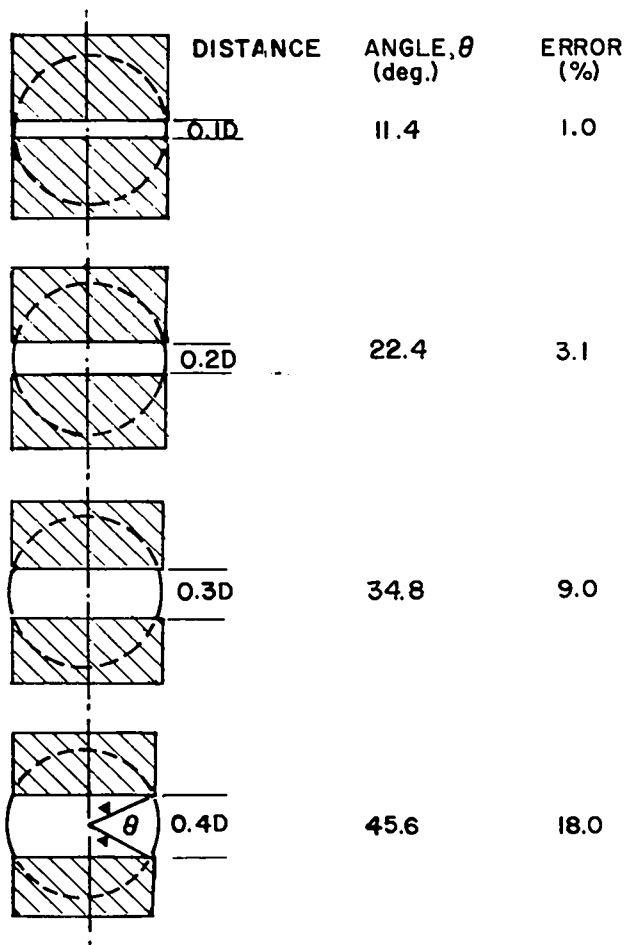


Fig. VI-15.

Tensile stress error due to unpotted depth expressed as a fraction of diameter. Unpotted distance can be measured before testing and correction applied to data.

absorber/ablator layer. This layer absorbs energy from the incident laser, is heated and vaporized, and streams away from the pusher shell causing the pusher shell to implode via the rocket reaction forces. For target pellets that do not depend on the strength of this absorber/ablator to contain the fuel-gas pressure, we generally use plastic. We also frequently provide freestanding cylindrical and spherical shells of plastic as targets and for special diagnostic measurements. These latter specimens are generally fabricated by coating appropriate mandrels, which are then dissolved in acid to leave the freestanding plastic shells, but we are also trying to make plastic shells by using our droplet generator described earlier. Finally, because the Polaris-A

target requires a shell of low-density small-cell-size plastic foam, we are developing techniques for shaping this foam into spherical shells that can be placed around target cores.

Gas-Phase Coatings (R. Liepins, M. Campbell, A. T. Lowe)

General. The primary problems encountered in coating GMBs with plastic are obtaining uniform coating thicknesses and high surface smoothness. Of the three general coating approaches—solid, liquid, and gas phase—the gas-phase coating approach gave the most promising results. Two gas-phase techniques were investigated: (1) a low-pressure plasma process, and (2) a vapor-phase pyrolysis process, i.e., the Parylene process.

The primary requirements for coatings on laser fusion targets are sphericity and uniformity of better than 1% and smoothness or defects less than 1000 Å. Our work to date indicates that the low-pressure plasma process is capable of approaching such requirements.

Low-Pressure Plasma Process (LPP)

Introduction. To meet these specialized laser fusion target requirements, a capacitively coupled LPP coater was developed several years ago. Typically, the coater was operated at several hundred volts at 1 kHz across the parallel, flat-plate electrodes. An important feature of this coater was its ability to bounce the GMBs in the glow discharge and thus to expose their entire surface randomly to the coating medium. Thus, uniform coatings of thicknesses up to 8 μm could be obtained. However, two important properties remained to be determined: (1) the maximum uniform coating thickness and (2) the best possible surface smoothness obtainable in the instrument.

Parametric Study. All previous work had been done on bouncing GMBs. Because the LPP coatings flaked at increased thicknesses it was of interest to investigate the feasibility of coating mounted GMBs. Specifically, we wanted to know what coating thicknesses and surface smoothnesses were possible if the GMBs were stationary rather than bouncing. A brief parametric study revealed that mounting the GMBs permitted us to deposit thicker

coatings and to obtain coatings considerably smoother than comparable coatings on bounced GMBs (see Fig. VI-16).

Both effects are probably a result of eliminating the mechanical damage to the coating caused by bouncing and by positioning the GMBs in the negative glow region between the electrodes during the entire run.

Sample Support Effect. The samples were mounted in five different configurations shown in Fig. VI-17. Both sample-support configuration and electrical conductivity have a pronounced effect upon the kind of coating obtained. The support configuration primarily affects the sphericity and concentricity of the coating and, to a lesser extent, the coating deposition rate (and thus, coating thickness obtainable). For highest sphericity and concentricity the ring configuration (Fig. VI-17d) or an

equidistant four-post configuration (Fig. VI-17e) are preferred.

The electrical conductivity of the support structure affects the deposition rate, but with no noticeable effect upon sphericity, uniformity, or surface smoothness. The higher the electrical conductivity between the microballoon and the bottom capacitor plate, the faster the deposition rate. This rate more than doubles, from 270 to 592 $\text{\AA}/\text{min}$, when an all-insulator support is changed to a fully conducting one. A typical rate for bounced GMBs at identical operating conditions is 258 $\text{\AA}/\text{min}$. All sample-support effects can be explained with the effect of the electrostatic charge buildup on the support structure.

Current Effect. In addition to sample-support effects, the plasma current also has an important effect upon the deposition rate. This effect is illustrated in Table VI-I. The plasma current, like the



(a)



(b)

Fig. VI-16.

Scanning electron micrograph.

(a) bounced GMB coated with $2.7 \mu\text{m}$ of *p*-xylene (LPP); 10 000 X.

(b) mounted GMB coated with $3.5 \mu\text{m}$ of *p*-xylene (LPP); 10 000 X.

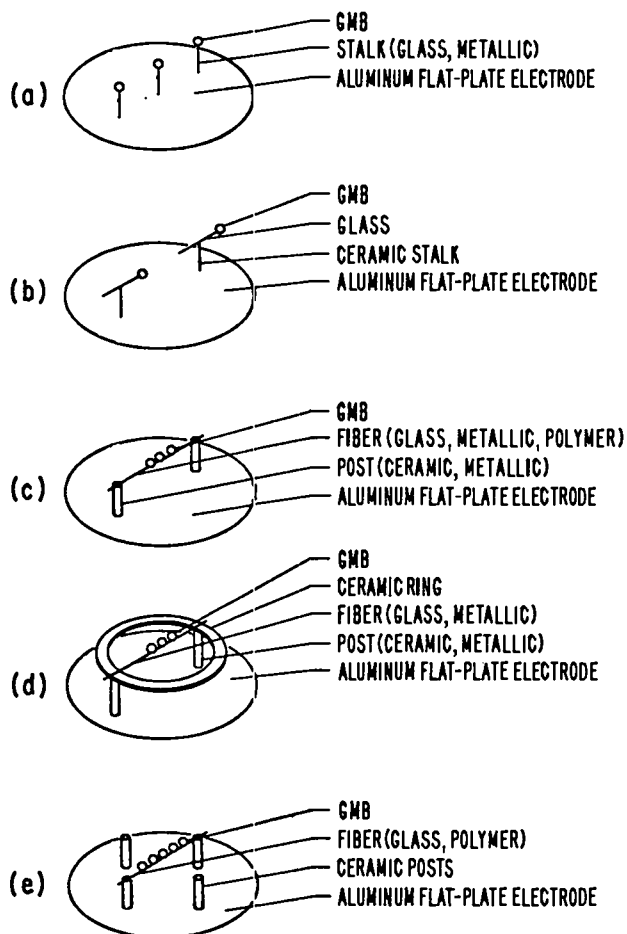


Fig. VI-17.

Sample configurations used in studying *p*-xylene deposition on GMBs.

- (a) vertical position
- (b) horizontal position
- (c) fiber and end-post configuration
- (d) fiber and ring configuration
- (e) fiber and four-post configuration.

sample-support configuration, had no significant effect on sphericity, uniformity, or surface smoothness.

Uniformity vs Coating Thickness. The best uniformities for various coating thicknesses obtainable with *p*-xylene in our LPP instrument are listed in Table VI-II. These coatings were obtained with either the ring or the four-post sample-support configurations. The reported coating thicknesses are the averages of four measurements, and the Δ thicknesses are the differences between the highest and the

TABLE VI-I
EFFECT OF PLASMA CURRENT
ON LPP DEPOSITION RATE

Current (mA)	Deposition Rate ($\text{\AA}/\text{min}$)
0.50	133
0.75	203
1.00	243
1.50	391
2.00	418
3.00	571
4.00	816
5.00	1057

TABLE VI-II

UNIFORMITY VARIATIONS IN LPP
COATINGS ON SUPPORTED GMBs

Δ Thickness (μm)	Average Thickness (μm)
0.0	7.2
0.3	11.9
0.4	13.9
0.6	18.0

lowest measurements in the set of four. Coatings thicker than $18 \mu\text{m}$ have been obtained; however, the Δ thicknesses increased then rather abruptly.

Other Effects. Increasing the *p*-xylene partial pressure in either the presence or absence of argon increased the deposition rate proportionately, but without any noticeable effect upon sphericity, uniformity, or surface smoothness of the coating. Doubling the *p*-xylene flow rate at the same partial pressure had no noticeable effect upon the quality of the coating and only a small effect upon the deposition rate. Furthermore, applying the coating under flowing *p*-xylene or *p*-xylene plus argon or under static conditions made no noticeable difference as far as coating sphericity, uniformity, or surface smoothness were concerned. Use of chloroform,

bromoform, or iodoform as plasma additives produced no noticeable changes in surface smoothness.

Smooth Surface Coatings. To achieve smooth surfaces we developed an approach of chemically controlling the surface as it is formed, in which we repeatedly introduced small amounts of air to the chamber during the run. The pulses of air seemed to minimize the accelerated-growth sites and to promote overall surface smoothing. A typical surface obtained by this technique is shown in Fig. VI-18.

Perdeuterated p-Xylene Coatings. In our study of neutrons of "strange origin" we sometimes require targets of perdeuterated polymeric shells. To form these targets, we adapted our LPP technique for the preparation of coatings from which the shells are made. Perdeuterated p-xylene is deposited onto beryllium-copper spheres that are then laser-cut and leached out to yield the polymeric shells. The coatings are deposited at no-flow conditions to minimize the consumption of the perdeuterated

monomer. Coatings of excellent concentricity and sphericity with thicknesses of 2.33 and 2.54 μm were prepared.

Vapor Phase Pyrolysis Process (VPP) (R. Liepins, M. Campbell)

General. To extend our capability in the preparation of thick coatings with precise control of coating thickness and surface smoothness we also developed the VPP process. In principle, the process has no coating-thickness limitation and inherently leads to a conformal coating of high surface smoothness and uniformity. The coating material possesses high mechanical strength, good thermal stability, and high resistance to most solvents and chemicals.

Our work on Parylene coatings can be separated into three phases. Phase 1 consisted of building the system and of conducting a brief parametric study of the operating variables; Phase 2 comprised the construction of a low-temperature chamber and the first low-temperature coating work; and Phase 3 saw the construction of a cold chamber with wider temperature and gas-flow capability to accomplish thicker coatings.

Phase 1. A schematic of the initial Parylene processor was shown in LASL report LA-7328-PR. The coatings were applied at room temperature in a 10-l glass bell jar at a vacuum of at least 0.1 torr. We investigated the effect of process variables on coating rate and quality, i.e., of vaporizer temperature, pyrolyzer temperature, operating pressure, and dimer charge weight. (The operating pressure is the pressure obtained at thermal equilibrium when the dimer is being vaporized through the system.)

We found the efficiency of coating formation independent of

- vaporizer temperature in the range of 393 to 563 K,
- pyrolyzer temperature in the range of 888 to 918 K, and
- operating pressure in the range of 0.020 to 0.10 torr.

Coating thickness was directly proportional to the dimer charge weight, which was the only variable of those investigated with any effect on thickness. A 2.0-g dimer charge gave a 3.7- μm coating in the most favorable sample position inside the bell jar.

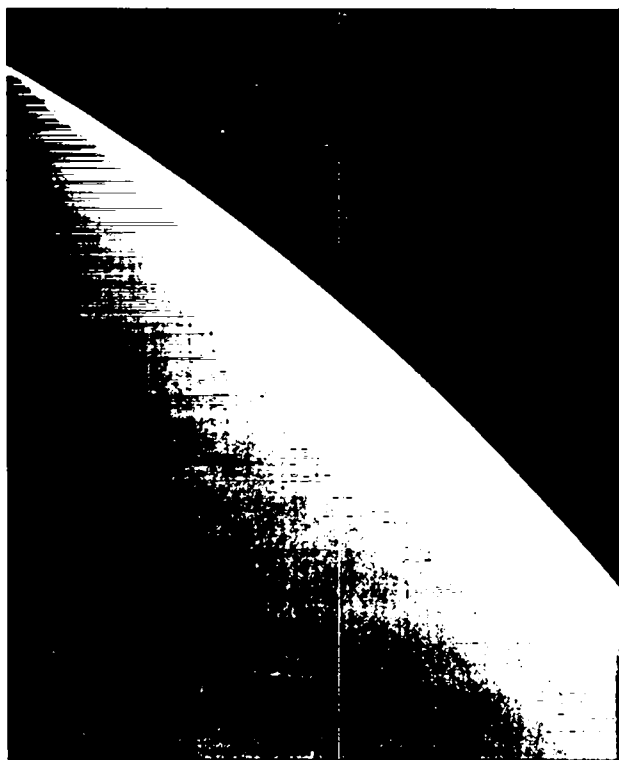


Fig. VI-18.

Scanning electron micrograph of an 11- μm p-xylene coating (LPP) on a GMB; 10 000 X.

Because the coating thickness depended linearly on the dimer charge weight, we estimated that a 52-g charge would be required to obtain the desired 100- μm coating. Aside from the prohibitive cost of such a coating, we could not vaporize and pyrolyze such a large charge in our instrument.

Scanning electron microscopy indicated that the surfaces of these Parylene coatings were smoother than LPP coatings of similar thickness on bunched GMBs (see Figs. VI-16a and -19).

Phase 2. For the next phase, we built a vaporizer furnace, redesigned and enlarged the sample port, and incorporated a cold chamber inside the bell jar. A schematic of the new processor is shown in Fig. VI-20. Coatings made in this processor at 283, 273, and 252 K showed no degradation in surface finish or strength, but displayed a marked increase in coating rate at the lower temperatures. The following rates were achieved for a 2-g dimer charge.

Temperature ($^{\circ}\text{C}$)	Coating Thickness (μm)
21 (room temp.)	3.7 (no cold chamber)
10	9 (with cold chamber)
0	20
-21	25

Also, a 4-g charge yielded a 49- μm coating at 252 K, which shows that the coating thickness in the new processor is still directly proportional to the dimer weight.

However, the new deposition chamber did introduce a new experimental variable. Coating thickness and surface smoothness both depended on the vertical position of the sample in the cold chamber. The thickest coatings with the roughest surfaces were obtained near the top of the chamber, with the thinnest coatings and smoothest surfaces at the bottom. The effect of sample position on surface smoothness is illustrated in Fig. VI-21. Because the thickest films had the roughest surfaces, surface smoothness may simply be dependent on the coating rate. This effect is being investigated.

Phase 3. We redesigned the Phase-2 processor to increase the capability of depositing thick coatings and to improve their surface smoothness. A cold chamber of larger capacity with a larger temperature gradient and with baffles to control the gas flow was constructed and put into operation.



Fig. VI-19.
Scanning electron micrograph of a mounted GMB coated with 4.8 μm of Parylene; 10 000 X.

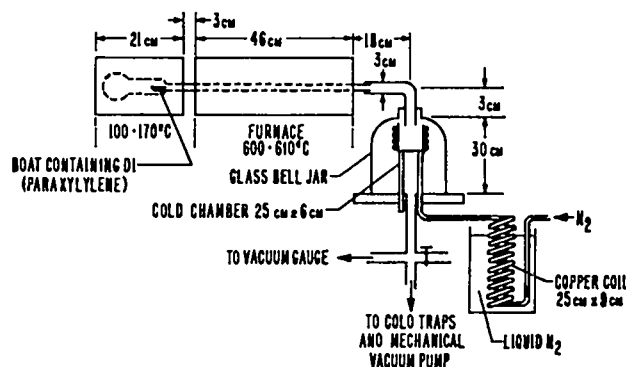


Fig. VI-20.
Latest Parylene processor with a cold chamber for microballoons.

POLYMER SHELL FABRICATION (S. Butler)

Preliminary efforts were made to fabricate polymer shells by using the droplet generator technique described above. In this process polymer-solution droplets fall through a heated column in



(a)



(b)



(c)

Fig. VI-21.

Scanning electron micrograph of mounted GMBs coated with Parylene at 252 K:

- (a) this GMB was mounted at the top of the cold chamber; 48- μ m coating; 4000 X.*
- (b) this GMB was mounted in the middle of the cold chamber; 28- μ m coating; 4000 X.*
- (c) this GMB was mounted at the bottom of the chamber; 10- μ m coating; 4000 X.*

which the solvent evaporates leaving a polymer shell.^{9,10} We built a heated column designed for 120- μm -diam shells and measured the temperature profile at several temperatures. We also studied the properties of droplet formation for the polymer (initially polymethylmethacrylate in acetone) by forming, charging, and deflecting drops of the solvent.

POLYMER FOAM DEVELOPMENT

General

Several advanced laser fusion target designs require $\sim 250\text{-}\mu\text{m}$ -thick spherical shells of low-density foam (0.05 to 0.3 g/cm^3) with very small cells (1 to $2\text{ }\mu\text{m}$). Ideally, the foams should consist only of carbon and hydrogen. However, to increase the chances for producing the desired foams, we also used polymers containing nitrogen and/or oxygen atoms. This broadened the choice of polymers greatly. Heavy metals and other elements with atomic numbers higher than 20 are generally considered undesirable, although some designs call for low-density foams loaded with high-Z metal. Because the foams should have a uniform structure throughout, cell size and density should be uniform.

CH_2 Microfoam (R. Liepins, M. Campbell)

Pure polyethylene foam $(\text{CH}_2\text{CH}_2)_n$ represents a "best choice" for low-density foam development because it exhibits a very low average atomic number and because the starting density is quite low (0.93). Our approach to polyethylene foam is a modification of one developed at Exxon,¹¹ which uses radiation crosslinking followed by solvent leaching.

Our approach involves radiation crosslinking of two types of materials: (1) a polymer that has been "diluted" with a radiation-insensitive, polymer-compatible material, and (2) a water-extended polyester emulsion developed for us by Monsanto Research Corp. In principle, this approach permits the irradiation of these materials either in the form of a film or as a coating on a GMB, later followed by foam formation. In the "diluted" polymer case, radiation causes molecular crosslinking where the crosslink density depends on radiation dose. Following irradiation, the uncrosslinked part of the

polymer along with the diluent are extracted with a hot solvent which, after drying, leaves behind a cellular structure. In the water-extended polyester case the microemulsion is preformed and then cast as a film or applied as a coating. We hope to stabilize this preformed microstructure by radiation crosslinking before drying. This may prevent the microcells from coalescing, which has plagued previous wet chemical methods of stabilization.

Our initial work consisted of determining the relationship of radiation dose to crosslink density for high- and low-density polyethylene and for an ethylene/propylene copolymer. We molded the polymers into thin sheets and irradiated samples from these sheets in evacuated (10^{-5} -torr) glass ampules with cobalt-60 gamma radiation. Total doses of 1 to 30 mrad were tried. Evaluation of these foams is still in progress.

Water-Extended Polyester (WEP) Foam Development (J. L. Schwendenmen, Monsanto Research Laboratories)

We tried various ways to decrease the cell size of WEP resins. Mainly, our work centered on adding a reactive monomer (styrene) to reduce the viscosity of the emulsion, and on introducing an added surfactant to the resin/water emulsion to reduce cell size and to improve cell uniformity.

The use of styrene reduced the emulsion viscosity slightly. However, it did not result in any reduction in cell size. Figure VI-22 shows a WEP/styrene foam.

Both nonionic and anionic surfactants were also tested. A range of hydrophile/lyophile balance numbers (HLB) for the surfactants was investigated. The anionic surfactants caused the emulsions to break before the required amount of water had been added. A variation of the HLB number for the nonionic surfactants was not effective in reducing cell size. As a result of these failures, we suspended our activity on WEP emulsions and concentrated our efforts on cellulose acetate foam.

Cellulose Acetate Foam Development (J. L. Schwendenmen, Monsanto Research Laboratories)

Eight samples of cellulose acetate foam were prepared. These foams represented varying concentrations of cellulose acetate dissolved in a mixed

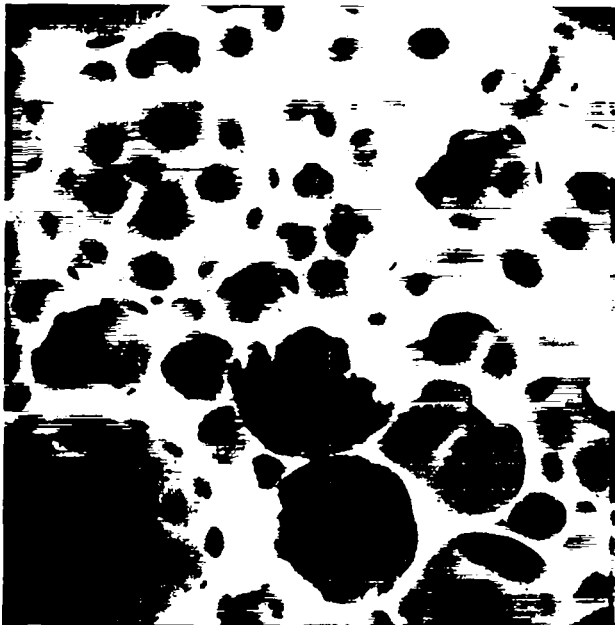


Fig. VI-22.

Scanning electron micrograph of the best WEP/Styrene foam produced. 2000 X, 1 cm = 5 μ m.

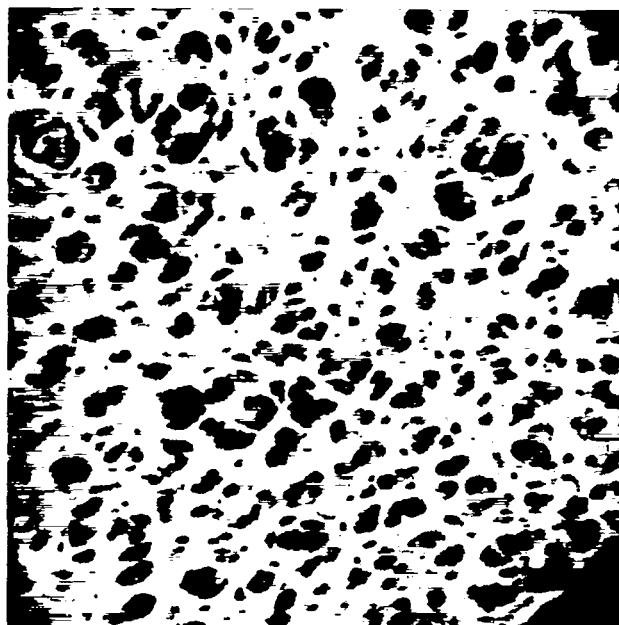


Fig. VI-23.

Scanning electron micrograph of a cellulose acetate foam; 5000 X, 1 cm = 2 μ m.

solvent (formamide and acetone), and a given quantity of cellulose acetate (10%) dissolved in several different mixed solvents. The foams are apparently quite open in structure and have cells in the range of 2 μ m in size. Figure VI-23 shows one such foam.

The foams were prepared in the form of sheets that can probably be used to form hemispherical shells in a positive-pressure or vacuum mold. Special tooling will permit hemispherical shells to be formed from foam films. Both positive-pressure and vacuum molds are being made. The molds previously used with emulsions were reworked to give a tighter closure of the molds and one set of molds was provided with Teflon mold faces.

DEVELOPMENT OF NEW MATERIALS

General

We continued our development of new high-density fusion fuels that are solids at room temperature. These materials are deuterated and tritiated compounds with a very high DT atom ratio. Although the DT density is high, nonfuel atoms generally dilute the fuel, absorb energy, and degrade

target performance. An exceptional case is the compound ${}^6\text{LiD}_{0.76}\text{T}_{0.26}$ in which the ${}^6\text{Li}$ fissions to form tritium during the burn. However, even with other compounds, convenient physical properties often outweigh the disadvantage caused by diluent atoms and make these compounds useful for fusion fuel. For example, in targets requiring layers of fuel on both the outside and inside surface of an inner shell in a multishell target, the layer on the outside surface could be made of a solid fuel compound. Otherwise, it may be impossible to fabricate the target.

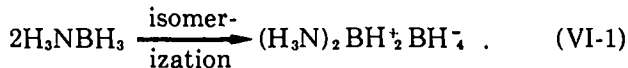
Ammonia Borane (R. A. Geanangel, University of Houston)

Introduction. We had discovered previously the following significant results in the evaluation and development of ammonia borane as an inertial confinement target material.¹²

- The decomposition of ammonia borane in the liquid state can be minimized (~ 0.2 mol per cent hydrogen loss per minute) by maintaining 1000 psi of hydrogen pressure in the target fabrication vessel.

- Heating ammonia borane briefly above its melting point in a stirred, unreactive fluid such as dodecane in the presence of 600 to 1000 psi H₂ yields microspheres and microballoons potentially suitable as laser fusion targets.
- To give satisfactory results, the ammonia borane must first be zone-sublimed, giving a fibrous product (melting point, 383 to 385 K), which is then mechanically chopped into small pieces used as feedstock.
- Fabrication conditions (temperature, time, stirring rate) were determined that produce substantial numbers of microballoons.
- Methods for using vacuum microspheres to recover microballoons from the fabrication mixtures were developed.
- An electron microscopic investigation of early samples of microballoons showed them to be somewhat irregular with diameters ranging from 160 to 300 μm and wall thicknesses of 2.2 to 7.0 μm.

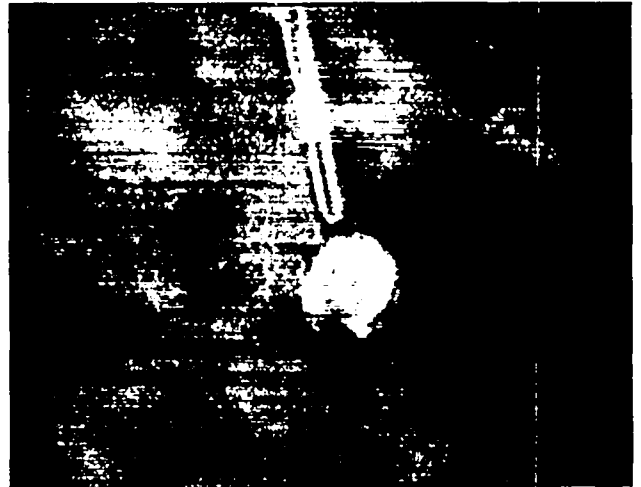
Ammonia Borane Preparation. Investigation of samples of purified ammonia borane stored one to two months at room temperature showed significant melting-point degradation. Evidently, H₃NBH₃ experiences solid-state decomposition without significant hydrogen loss. A probable explanation for this decomposition is that isomerization (Eq. VI-1) to bis(ammonia)-dihydridoboron(III) tetrahydroborate is occurring,



A substantial activation energy is probably available for the isomerization reaction in the solid state so that it may be possible to preserve the purity of H₃NBH₃ simply by refrigeration.

Microscopic Examination of Microballoons. Several representative microballoons were isolated from a series of fabrication runs and mounted on short glass stalks with epoxy cement for optical and scanning-electron microscopy. Examples are shown in Fig. VI-24.

During preparation for SEM investigations we discovered extensive cracking as gold was sputtered onto the surface of ammonia-borane microballoons. We confirmed that cracking was caused by an expansion of 10 to 20% during sputtering.



(a)



(b)

Fig. VI-24.

Photomicrographs of ammonia borane microballoon at different magnifications: (a) at 40 X; (b) 70 X.

The heat of atomization of gold, which is released as the gold is deposited, along with other heating effects, may raise the temperature of the microballoons to near 373 K, where decomposition is known to set in. Omitting the coating step will represent only a minor problem in SEM observation of shells because silver paint can be used to minimize charging effects and because the contrast of the uncoated balloons is sufficient for reasonable viewing. However, this effect bears additional study because

pusher coatings for later stages of target evaluation will almost surely be desirable. Slower deposition rates and/or the use of other metals with smaller heats of atomization might alleviate the problem.

CRYOGENIC TARGET DEVELOPMENT

General

Laser fusion targets fueled with cryogenic, liquid or solid, DT offer the advantage of high initial fuel density without the disadvantage of diluent atoms being present, as they are in room-temperature solids having a high hydrogen density, e.g., lithium in Li(DT), carbon in $[C(DT)]_n$, or boron and nitrogen in NH_3BH_3 . Calculations indicated that the yields from targets fueled with liquid or solid DT can be considerably higher than those from targets of the same design, but fueled with high-pressure DT gas. We therefore actively pursued the development of cryogenic targets despite the significant experimental complications encountered in their fabrication and in their use in laser-target interaction experiments. We are also testing a cryogenic insertion mechanism for loading and cooling these targets in the Helios target chamber. In a modest program of determining basic hydrogen properties we measured the compressibility and thermal expansion coefficient of the cryogenic deuterium-tritium system.

Cryogenic targets receiving greatest attention are uniform, hollow shells of solid or liquid DT condensed onto the inside surface of a glass or metal microballoon that serves as the pusher shell. We made substantial progress, in developing techniques to condense the DT into a uniformly thick layer on the inside surface of GMBs and in measuring the thickness uniformity of the DT shell. We also cycled multishell targets to cryogenic temperatures and measured cryogenic layer uniformity for different configurations.

Fast Isothermal Freezing (FIF) (J. R. Miller)

The investigation of any possible limitations of the FIF technique for producing uniform, solid DT layers in target fuel cores continued. As reported in LASL reports LA-6616-PR and LA-6834-PR, the FIF method forms layers of solid DT on the inner surface

of bare GMB fuel cores with a uniformity that is better than can be determined interferometrically ($\pm 10\%$ variation in layer thickness). Because laser fusion targets of advanced design have multiple shells and multiple layers around the cryogenic fuel core, we began the investigation of inherent limitations that may apply to the FIF technique.

Two-shell targets were studied extensively. A 0.5- to 1.0-mm-diam glass shell, assembled around a 100- μ m-diam fuel core filled with 10 ng of DT fuel was investigated (see Fig. VI-25). Special care was taken in selecting the outer glass shell for wall-thickness uniformity. This care was necessary to prevent a nonuniform outer shell from degrading the interferometric measurements of the uniformity of the solid DT layer inside the fuel core. Two-axis interferometric measurements showed that the outer shell increases the cooling rate of the fuel core, causing the formation of solid DT layers as uniform as those produced in bare fuel cores. The study is continuing with outer shells of different sizes, masses, and materials.

Additional results from quasi-local resistance heating in the FIF technique indicated that such heating does not yield a uniform fuel layer in bare GMBs. Interferometric measurements on two

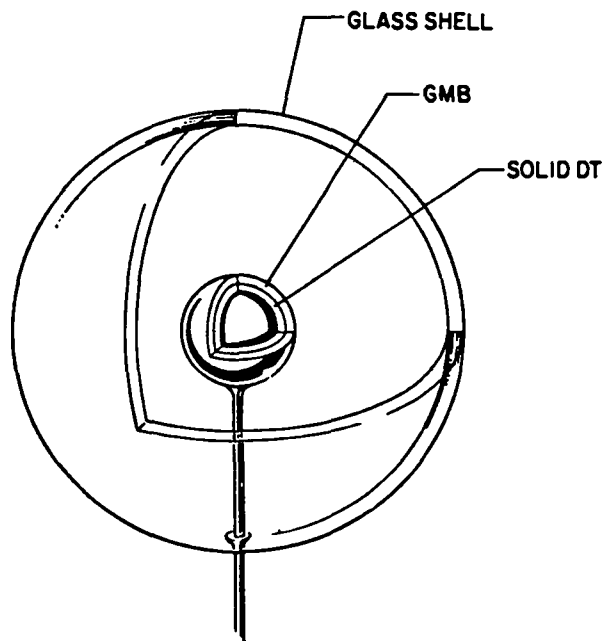


Fig. VI-25.

Two-shell target used to investigate cryogenic DT layers with the FIF technique.

orthogonal axes were used for this determination. These results ended our evaluation of FIF resistance-heating experiments.

Helios Cryogenic Target-Producing Prototype (J. R. Miller, J. Feuerherd)

Considerable progress was made on the experimental apparatus designed to produce cryogenic targets in the Helios laser system. This prototype device was fabricated, assembled, and partly tested. As reported in LASL report LA-7328-PR, targets at 300 K will be loaded and positioned one at a time into the target chamber and there frozen with the FIF technique. Tests of the thermal isolator separating the 4 K target from the room-temperature target carrier indicate a heat loss of ~ 0.2 W from the target carrier. This value is not significant from an alignment standpoint (temperature drift) because the thermal mass of the target micropositioner, carrier, and mating kinematic receiver plate is large.

Because a cryogenic target survives only a few milliseconds after it is exposed to room-temperature radiation, the cryogenic shroud used to process the target has to be retracted just before laser irradiation. Tests of a 2.54-cm-diam, air-actuated piston show that this device is too slow for our use: it retracts 4.5 cm in ~ 16 ms.

Design of a mechanism that will retract more rapidly is in progress. This second retraction system relies on atmospheric pressure to rapidly collapse an evacuated, welded-metal bellows.¹⁸ The bellows, initially magnetically latched in its extended position, collapses when the holding electromagnets are de-energized. Advantages of this mechanism over other devices include the small accelerated mass, lack of any moving fluid, accurate release timing, and simple scalability. This bellows mechanism is expected to retract the cryogenic processing shroud sufficiently fast.¹⁸

Cryogenic Target Fabrication (J. R. Miller, B. S. Cranfill, V. Woods)

Because advanced laser fusion targets are composed of various materials in complicated, geometrically exact configurations, attention has to

be given to fabrication methods. Additional constraints are imposed when these targets have cryogenic fuel cores—the target must remain intact during a 290 K temperature change. We therefore have continued our investigation of cryogenic target-fabrication techniques.

Other researchers¹⁴ reported the use of thin, drawn, rubber-cement fibers for support elements in their cryogenic targets. We studied this material for its stability and reliability in simple ball-on-fiber targets. A photograph of one rubber-fiber test fixture is shown in Fig. VI-26. As shown, thin rubber-cement fibers are stretched between parallel glass supports. A GMB is attached to the side of each fiber (no additional glue is needed or used). This assembly is lowered to cryogenic temperatures and the GMB adhesion and rotation as well as the fiber integrity are noted. Two parameters are varied in this test—the fiber diameter and the rubber-cement solvent content.

Our experimental results indicated that rubber-cement fibers are less reliable than glass fibers. Although no GMB rotation or detachment was

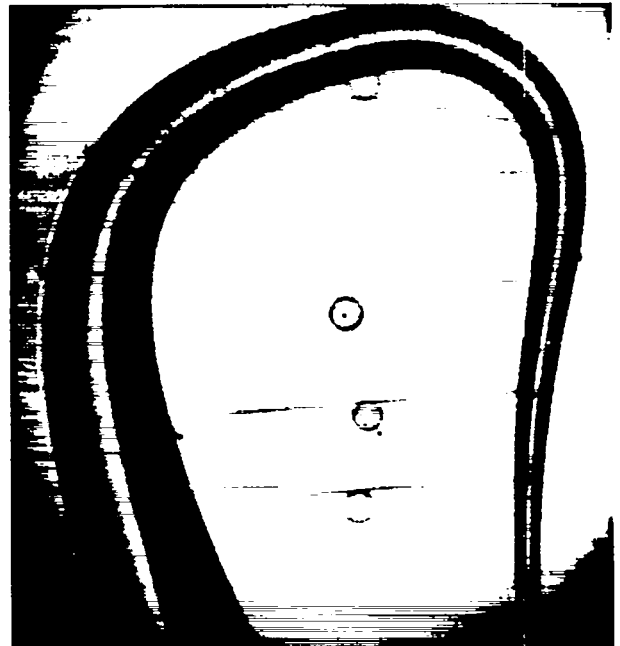


Fig. VI-26.

Photomicrograph of a cryogenic test fixture for GMB support fibers. Targets are at 4 K. Rubber fibers on the bottom are broken but are rigid from the cold temperature; 20 X.

observed, the rubber fibers tended to break. This is not necessarily a significant defect, because the fiber's temperature at failure was sufficiently low for the fiber to remain rigid.

Our tests showed that thin rubber fibers ($\leq 5 \mu\text{m}$) break less often than thick fibers ($\geq 5 \mu\text{m}$). The solvent content, although important for fiber drawing, seems to have little effect on breakage.

Measurements of Hydrogen Isotope Properties (E. Grilly)

A negative volume-thermal-expansion coefficient was measured in solid $p\text{-H}_2$ over the temperature range 14 to 15 K. The reversal of the normal positive coefficient occurred at ~ 0.1 K below the melting temperature, roughly parallel to the melting curve. If the volume anomaly is associated with a phase transition, the change in pressure with temperature (dP/dT) should be positive. Indeed, we observed that the negative volume change was accompanied by a release of heat, which is consistent with $dP/dT > 0$. Finally, we measured the pressure (P) in the liquid-solid mixture that occurred while freezing (P_r) and melting (P_m) during a compression-decompression cycle at a fixed temperature T_1 . We started with all liquid, went to all-solid (at several atmospheres above P_r), and returned to all-liquid. If a volume decrease is induced in the compressed solid by a small temperature increase but not removed during an identical decrease, then $P_m < P_r$. However, no volume decrease occurs in the solid at $P > P_r$, and while $P_m > P_r$ initially, $P_m < P_r$ several hours later.

The results of these experiments strongly suggest a structural change in solid H_2 , which has a martensitic character. Further pressure-volume-temperature experiments will continue on DT mixtures.

REFERENCES

1. E. Stark and F. Skoberne, "Laser Fusion Program at LASL, October 1—December 31, 1976," Los Alamos Scientific Laboratory report LA-6834-PR (October 1977).
2. R. Jay Fries and E. H. Farnum, *Nucl. Instrum. Methods* **126**, 285 (1975).
3. V. Cottles, H. R. Maltrud, E. H. Farnum, and R. J. Fries, "Nondestructive Assay of Fuel Content in Laser Fusion Targets by Fluorescent Photon Counting," Paper 10B-10, Post Deadline Section, 18th Annual Meeting of the Plasma Physics Division of the American Physical Society, San Francisco, California, November 15-19, 1976.
4. M. A. Ebner and W. B. Rensil, *Rev. Sci. Instrum.* **46**, 1290 (1975).
5. R. Jay Fries and E. H. Farnum, "Laser Fusion Target Fabrication: A Status Report, 30 April 1974," Los Alamos Scientific Laboratory report LA-5703-SR Rev. (February 1975).
6. A. Mayer and D. S. Catlett, *Plating and Surface Finishing*, March 1978, 432.
7. S. A. Dunn, "Expansional Concentration of Glass Microballoons," Bjorksten Res. Labs., Madison Wisconsin, Final Report on Contract LP7-96759-1.
8. N. R. Lindblad and J. M. Schneider, *J. Sci. Instrum.* **42**, 635 (1965).
9. C. D. Hendricks and S. Babil, *J. Phys. E: Sci. Instrum.* **5**, 905 (1972).
10. KMS Fusion Inc., *Final Report* (1977) Section 12.2.
11. Gerald M. Halpern and Hyo-Gun Kim, Proc. Topical Meeting on Inertial Confinement Fusion, February 1978 (San Diego, California).
12. R. A. Geanangel, *Progress Report*, DOE, ORO-5176-6 (December 1977).
13. Don Musinski, KMS Fusion Inc., personal communication, May 10, 1978.
14. Ye. G. Gamilii, A. I. Gromov, A. I. Isakov, L. A. Krupinina, Yu. S. Leonov, F. I. Matveeva, Yu. A. Merkul'ev, A. I. Nikitenko, Ye. R. Rychkova, and G. V. Sklizkov, *Akademiia Nauk SSSR, Fizicheskii Institut Imeni P.N. Lededev, Trudy*, **94**, 29-60 (1977) [Translated—LA-TR-78-21].

VII. TARGET DIAGNOSTICS

The tiny volume and brief duration involved in the laser fusion process create needs for new diagnostic techniques having spatial and temporal resolutions in the submicrometer and 1- to 100-ps regime, respectively. These needs are being met with a vigorous program of diagnostics in such areas as laser calorimetry, charged-particle and neutron detection, x-ray spectrometry, and subnanosecond streak camera development.

INTRODUCTION (D. V. Giovanielli)

Continued development of neutron-yield diagnostics has extended our minimum detectable level to less than 10^8 without significant background or noise contaminations. Further development of sophisticated detection techniques may lead to neutron-imaging diagnostics with spatial resolutions of 10-20 μm usable with total source yields of 10^{14} or less.

A variety of x-ray diagnostics have been developed for use at the Helios target facility. A spectral range of 30 eV to more than 100 keV will be covered with high-resolution, spatially resolved spectroscopy available in the 180-eV to 2.5-keV region. Two-dimensional imaging capability now exists and will be extended to the very soft and hard portions of the spectrum. Backlighting and shadowgraphy techniques are being developed for diagnosis of high-Z pusher geometries and fuel density measurements.

The variety of imaging techniques available can be greatly increased if care is taken to deconvolve the imaging aperture correctly. With multiple two-dimensional views, considerable insight can be gained regarding target symmetry and energy transport.

The multiline, diffraction-limited target irradiation facility is nearing completion. The oscillator for this system allows pulse shaping with a wide dynamic range and with both long-term and short-term stability. This system will be used for precise target measurements that do not require very high irradiance on target ($<10^{16}$ W/cm²) and that will benefit from rapid turnaround time.

NEUTRON DIAGNOSTICS

Li⁶ Detector for Neutron Yield Measurement in Laser Fusion (T. Tan, A. Williams, W. Bowman)

We have investigated a neutron detector assembly consisting of a thin Li⁶ glass scintillator, a photomultiplier, and a moderator for total yield measurement in laser fusion events (Fig. VII-1). Because of a very high thermal neutron cross section, a 2-mm-thick Li⁶ glass scintillator corresponds to an interaction path length. A burst of neutrons produced from the laser target is slowed down and

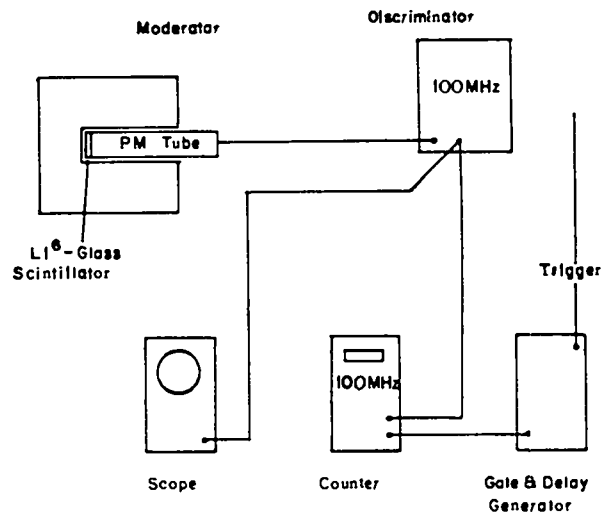


Fig. VII-1.

Detector configuration of associated counting electronics.

spread out in time by the moderator over a few milliseconds so that each neutron interacting within the Li⁶ can be counted individually. Each interaction is promptly followed by the emission of a triton and an alpha particle, which registers nearly a constant pulse height on the photomultiplier output. A fast electronic system capable of counting up to 10⁶ interactions in the detector within a few milliseconds is used (Fig. VII-1). The dynamic range of this detector can be tailored to suit many experimental requirements. For example, at 15 cm from the target, one single count corresponds to a total yield of 40. This detector is, therefore, uniquely suited for some of the early high-compression experiments with ablatively imploded targets. At very high yield, where pileup of pulses becomes a problem, the photomultiplier output may be integrated.

An important quality of this detector is the amazingly low noise level under normal circumstances. Typically, the background count for a period of several milliseconds is one or less. However, under intense x-ray radiation during a laser target shot, this background could be significantly higher. Fortunately, we were able to solve this problem by proper shielding of the scintillator and the photocathodes.

The investigation was carried out as a joint effort between LASL and Sandia Laboratories.

Interaction of Neutrons with Atomic Rydberg States (R. L. Carman and C. K. Rhodes)

Atomic Rydberg states may serve as a sensitive new method for detecting systems possessing a magnetic moment. For inelastic collisions of fast neutrons with appropriate excited states, cross sections on the order of 10⁻¹⁶ cm² are estimated.

It has been demonstrated¹ that certain excited atomic states will exhibit inelastic scattering channels arising solely from the electromagnetic properties of fast neutrons and that the characteristic cross sections for these processes are several orders of magnitude larger than those associated with nuclear forces. This new effect originates largely from the combined interaction of three factors. These are (1) the enormous electric susceptibility associated with Rydberg states,² (2) the apparent electric dipole moment \vec{p} arising from a Lorentz transformation of the neutron magnetic dipole $\vec{\mu}$ as perceived by an

observer at rest with respect to the rapidly moving neutron, and (3) a collisional mechanism that enhances the contribution of large impact parameter events. The latter issue, incidentally, is known to be an important aspect of the collisional behavior of H(2s) metastables³⁻⁵ and H₂(E, F, ¹Σ_g⁺) states.⁶

An observer at rest with respect to a neutron moving with velocity \vec{v} experiences an electrical disturbance proportional to

$$\vec{p} \cong \frac{\vec{v}}{c} \times \vec{\mu} = \frac{g\epsilon}{2M_n} \left(\frac{\vec{v}}{c} \right) \times \hat{\mu} \quad (\text{VII-1})$$

to first order⁷ in \vec{v}/c where g is the neutron g -value, M_n is the mass of the neutron, and $\hat{\mu}$ is a unit vector pointing along $\vec{\mu}$.

To estimate the cross section for the interaction of a neutron with a Rydberg atom X(n, ℓ) in the process

$${}_0n^1 + X(n, \ell) \rightarrow {}_0n^1 + X(n, \ell \pm 1), \quad (\text{VII-2})$$

our analysis is similar to that used by Bethe⁸ for charged-particle excitation with the potential arising from the dipole given in Eq. (VII-1). In this manner we find that the cross section $\sigma(n, \ell, E)$ is

$$\sigma(n, \ell, E) = \left(\frac{81}{32\pi} \right) g^2 \left(\frac{E}{Mc^2} \right) \left(1 - \frac{\Delta E}{E} \right)^{1/2} n^2 (n^2 - \ell^2) \lambda_c^2, \quad (\text{VII-3})$$

in which the triple (n, ℓ, E) designates the principal quantum number n , the orbital quantum number ℓ , and the center-of-mass collision energy E . In Eq. (VII-3), λ_c is the electron Compton wavelength and ΔE represents the energy difference between the initial (n, ℓ) and final ($n, \ell \pm 1$) states in such a way that

$$\Delta E \equiv E(n, \ell) - E(n, \ell \pm 1). \quad (\text{VII-4})$$

The cross section for this process increases linearly with collision energy E in the regime for which $E \gg \Delta E$ and, therefore, is greatest for the more energetic neutrons, in contrast to the typical nuclear scattering case. Numerically, for a 14-MeV neutron in collision with a Rydberg system for which $n = 30$ and $\ell = 2$, the cross section given by Eq. (VII-3) is $\sim 5 \times 10^{-17}$ cm², a value in the range typical for many atomic phenomena.

Given the interaction described above, it is possible to configure a neutron detection apparatus which is (1) selectively sensitive to fast neutrons, (2) capable of spatial resolution on the scale of less than $10\ \mu\text{m}$, and (3) able to detect polarized particles. A system capable of this function is illustrated in Fig. VII-2. The scattering process, Eq. (VII-2) is detected selectively by the mechanism of field ionization, a procedure that has been thoroughly demonstrated⁹ in sodium.

X-RAY DIAGNOSTICS

X-Ray Diagnostics for Helios (K. B. Mitchell)

Four instruments were developed as x-ray diagnostics for target experiments on Helios. First, a dual-purpose spectrograph having two film transports was designed, fabricated, and installed in the target chamber. This instrument will obtain time-integrated x-ray spectra over a broad energy range from 0.80 to 4.8 keV and space-resolved spectra over a limited energy range. The broad coverage is achieved by using two convex crystals of rubidium

acid phthalate (RAP) and pentary thritol (PET) each having a 50-mm radius of curvature. The x-ray emission from an essentially point-source plasma is diffracted from each crystal at a different wavelength range. The spectra are displayed side by side on the same film. Space-resolved spectra are obtained by use of a dual slit perpendicular to the dispersion direction of a third crystal, whose spatial image is recorded on a separate film. The one-dimensional spatial image has a magnification of 4X. The two slits used have different widths so as to obtain both source brightness and intensity. A choice of flat or parabolic crystals is available to cover three different energy regions.

Three spectrometers were designed to obtain time-integrated spectral intensities of x-ray continua and intensities of specific x-ray line emissions. All three instruments used fluor-photomultiplier detectors with outputs to CAMAC-gated charge-sensitive digitizers. These output data are recorded and analyzed in the PDP-11/70 computer.

The first of these instruments is a spectrometer with a five-channel K- or L-absorption-edge filter to measure the spectral intensities ($\text{J}/\text{sr}\cdot\text{keV}$) of x-ray continua at 0.45, 0.78, 1.45, 2.6, and 4.5 keV. This

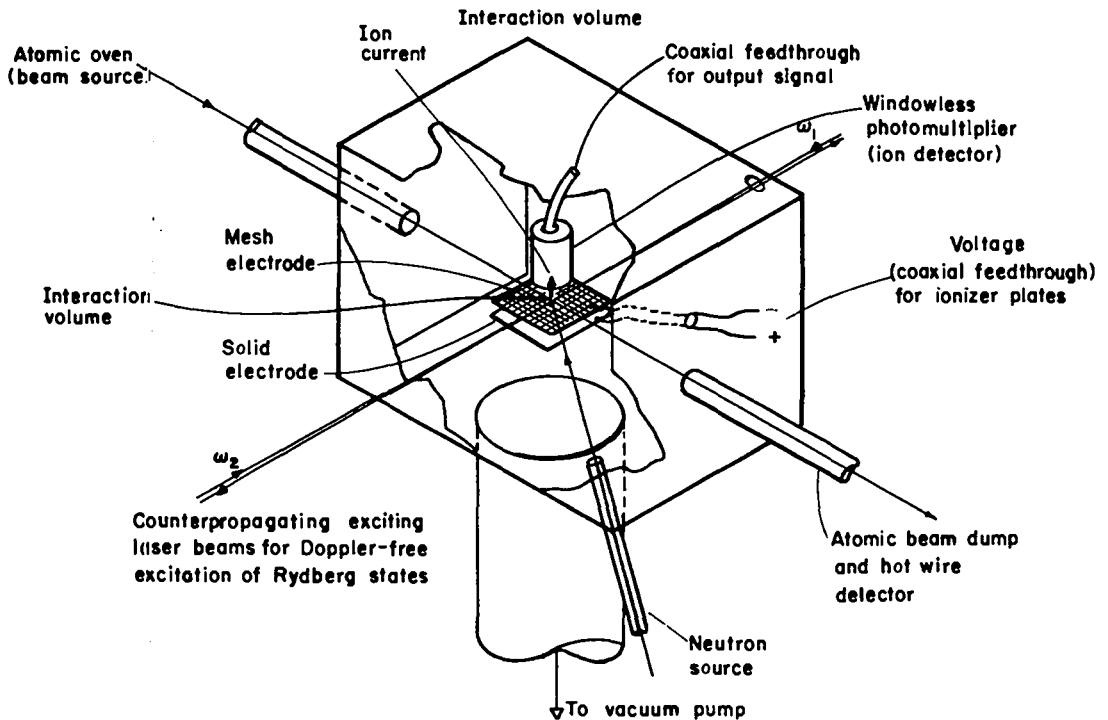


Fig. VII-2.

Schematic of neutron detection apparatus showing the atomic beam, the laser beams, and the field ionization mesh electrode.

instrument is very similar to one in use for x-ray measurements on our TBS. Fabrication and calibration of this system are complete.

A six-channel Bragg crystal spectrometer was designed and fabricated to measure the intensity (J/sr) for specific x-ray lines. One of the six channels will be used to measure the spectral intensity of x-ray continua at 270 eV. The system permits the selection of individual channels to monitor different lines of interest depending on the specific measurements of the experiment. At present, detectors are calibrated for the (2p-1s) and (1s2p-1s²) silicon lines. We will also monitor the K-lines of silicon and pusher materials. Alignment tests were conducted during evaluation of the Helios target chamber. Modifications were made to the mounting plate to maintain an optical alignment of the crystals with respect to the target to within one arc minute. The electrical noise from two detectors, measured when all eight laser beams were fired during the first integrated system test, was a very acceptable 20 mV.

Finally, we are developing a three-channel, matched-pair K-edge absorption-filter spectrometer to measure the spectral intensity at 9.6, 24, and 70 keV. These x-ray continuum measurements will be made to evaluate the hot-electron problem through measurement of T_H for plasmas produced by 10.6- μm radiation at high laser powers. The matched-pair absorption-filter instrument will give more definitive results than a standard K-edge filter spectrometer. The spectral response of a K-edge-filter/fluor combination is in a narrow band at the energy of about twice the energy of the K-edge. The signal from the K-edge band and the broadband from such a system will be at best about equal for a relatively flat x-ray spectrum, as expected for high-energy x-ray emission. The matched-pair system will record the signal (I) from a standard K-edge absorption-filter spectrometer and a signal (II) from a K-edge filter combined with a series of lower-Z blocking filters to eliminate the response at the K-edge. The final response of the system (K-edge band only) is obtained by subtracting the signals (I-II).

Calculations have shown that we can reduce the transmission at the K-edge to $\sim 5\%$ by the blocking filters and still match the broadband response of the standard K-edge filter. The entire system has been designed and fabricated. Calibrations and fluor evaluations are in progress.

Instrument Development—Cesium Fluoride Scintillators (D. G. Gerke, D. W. Lier, R. H. Day) J-Division; (P. Lee) L-Division

The usefulness of cesium fluoride (CsF) scintillators for detection of x rays in the range of 1 to 100 keV was tested on our TBS. The attractions of CsF scintillators are their high attenuation coefficient ($z = 55$) and short decay constant ($\tau \sim 5$ ns FWHM).

The efficiencies of a CsF scintillator and of NEIII plastic (plus 5% doping) are compared in Fig. VII-3. The advantage of CsF over NEIII scintillators for high-energy x-ray detection is quite obvious. The decay time of a CsF scintillator is relatively short when compared to NaI scintillators, $\tau \sim 200$ ns FWHM. The short decay constant allows a short integration time that can eliminate electrical noises generated during laser-plasma interaction. A typical oscilloscope trace of CsF scintillator-photomultiplier (PM) tube output from a GMB irradiated with out TBS is shown in Fig. VII-4. The filter material in this case was 3-mil-thick tantalum whose x-ray absorption-point energy (K-edge) is 10 keV. The FWHM of the pulse is 8 ns. The response time of the PM tube is 4 ns.

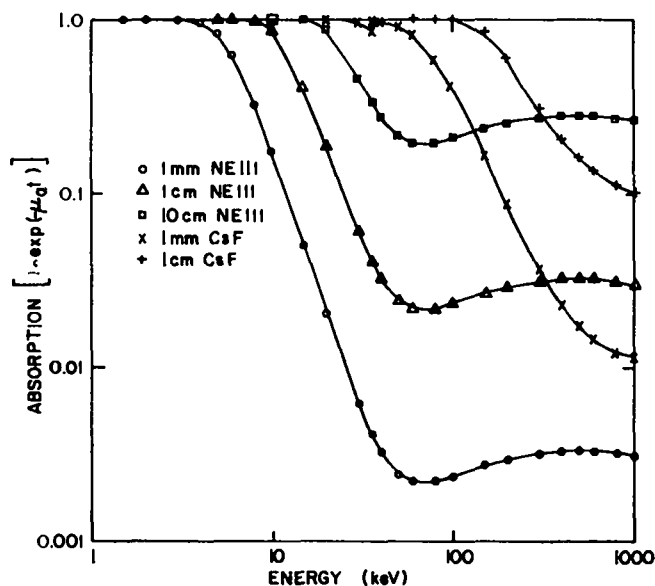


Fig. VII-3.

Efficiency of CsF scintillators compared with the efficiency of scintillators made of NEIII plastic with 5% doping.

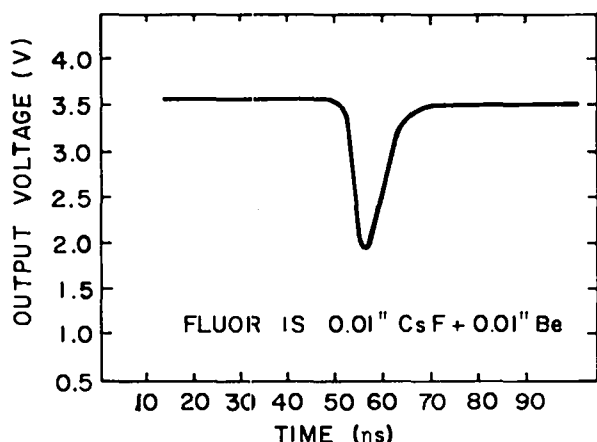


Fig. VII-4.

Typical oscilloscope trace of CsF scintillator-photomultiplier tube output from an irradiated glass microballoon.

The main disadvantage of the CsF scintillator in comparison to NaI(Tl) scintillators is their light output, which is about two orders of magnitude smaller than that of NaI(Tl). However, in a high-flux environment with enormous electrical noise, the short decay time of CsF may often outweigh its relatively poor light output.

Testing of GEAR X-Ray Streak Camera (P. D. Rockett, J. S. McGurn)

General. Two General Engineering and Applied Research (GEAR) Pico-X x-ray streak cameras were received in March 1978. These optically triggered units promise a 200-ps temporal window with an 8-ps/mm sweep rate, a <30-ps jitter, and a resolution of 3 line pairs/mm. Each unit is equipped with a proximity focused streak tube containing a collimating microchannel plate that permits compact packaging as seen in Fig. VII-5. Camera 1 produces an 18-mm streak record, whereas Camera 2 produces a 25-mm streak record.

Camera Calibration. Rather than proceed blindly with the use of the camera, we decided to calibrate the absolute spectral sensitivity in the 1- to 20-keV region. The photocathode of the Pico-X camera consists of a 1-mil beryllium substrate coated with 150 Å of gold, operated in the transmission mode. Henke et al. have done the most com-

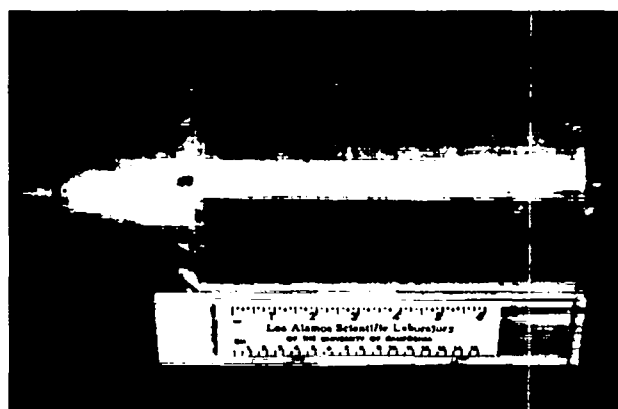
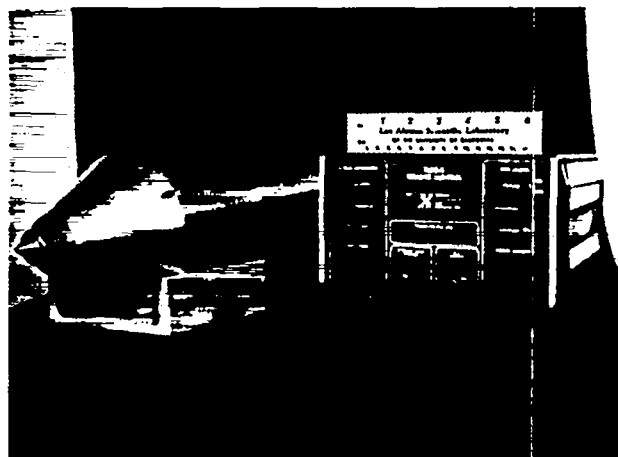


Fig. VII-5.

GEAR x-ray streak camera.

(a) Streak-camera head with control panel.

(b) Camera head sitting in U-channel cradle.

plete experimental studies of x-ray-induced photoemission and have found most of the secondary electron yield peaked at 1 to 2 eV with a FWHM of 4 to 8 eV.^{10,11} These slow secondaries are emitted isotropically, regardless of incident x-ray angle. The fundamental shape and location of the secondary spectrum varies little with cathode material or with incident photon energy. Day et al. have shown that the total number yield is indeed material-dependent.¹² Day observed that photocathode quantum efficiency was about 10 times higher in an evaporated gold film than it was in an aluminum cathode. He also found a considerable dependence of yield on surface condition in the gold samples, as have other researchers.¹¹ In view of these data and the lack of any measurements of secondary yield and spectrum vs cathode thickness, absolute spectral

calibration appeared necessary. With such data in hand we will be able to make definitive statements regarding plasma temperature and spatial emissivity, based on temporally resolved x-ray measurements.

A simple model of spectral sensitivity was used to guide the calibration. One assumes that all the energy of a stopped photon is converted into slow secondaries. Photons are assumed to be stopped with a standard $1 - \exp[-\mu(E)t]$ dependence, where E = incident photon energy, $\mu(E)$ = absorption coefficient, and t = photocathode thickness. The conversion efficiency, $f(E)$, from photons to electrons, must of course, vary with energy, as the Compton effect increases with energy. The yield Y will, therefore, vary as $Y \propto E[1 - \exp(-\mu t)] f(E)$ or $Y \propto E \mu(E) f(E)$. Because $f(E)$ appears to be a slowly decreasing function of E , and is not well characterized, our model will look only at $Y \propto E \mu(E)$. A plot of $E \mu(E)$ (including beryllium window transmission) appears in Fig. VII-6.

The model shows little sensitivity below 1.5 keV and a surprising rise in sensitivity near 15 and 82 keV. Sharp breaks in the curve are due to M, L, and K gold edges, respectively.

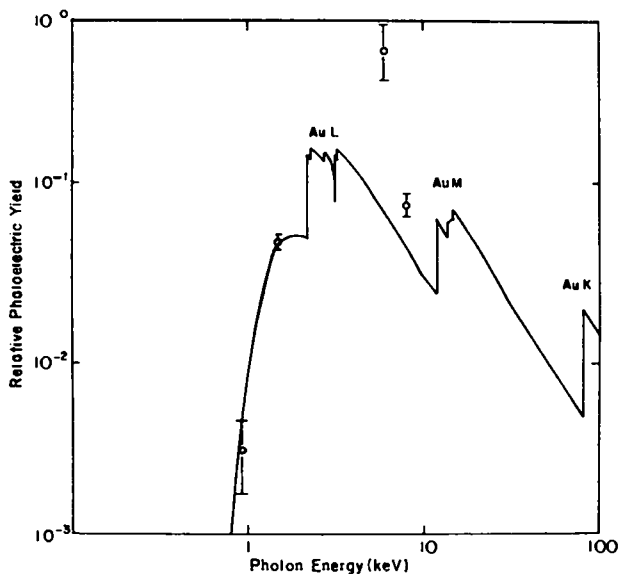


Fig. VII-6.

Model of relative photoelectric yield, Y , for gold vs photon energy based on $Y \propto E \mu(E)$, including the transmission of a 1-mil beryllium window. Circles correspond to experimental data points.

Absolute calibration of the streak-tube sensitivity in a dc mode was partially completed with calibrated Henke tube sources. Spectral sensitivity was measured as recording-film density/photon flux (photons/cm²) as a function of photon energy in keV. The results in Fig. VII-6 show data taken at 930 eV (Cu L), 1.5 keV (Al K α), 6.4 keV (Fe K α), and 8.05 keV (Cu K α). The data were normalized to the model at 1.5 keV. Note that the empirical calibration shows an increased relative sensitivity at 6 and 8 keV compared to the photocathode model. Henke has shown that the slow secondary photoelectrons have the same spectral distribution, regardless of incident photon energy, from 270 to 8.05 keV.^{10,11} Thus, there is no reason to believe that conversion of electrons to light within the streak tube would affect this measurement. The discrepancy may be due to the cathode thickness (150 Å) coupled with its use in the transmission mode. Other data points are planned at Ti K α and Mo K α to improve our understanding of the camera's spectral sensitivity.

Previous time-resolved measurements of the x-ray spectral output during GMB implosions were made at LLL with an uncalibrated photocathode.¹⁸ The results were interesting, but questionable regarding relative spectral sensitivity of the streak tube. Our calibrations should add sufficient information for accurate observations of the plasma thermal temperature and of the high-energy spectral component.

Triggering Experiments. The ability of the Pico-X camera to streak and to record an x-ray image has been verified on our Nd:glass laser. The only problem preventing immediate use on a CO₂ laser system is one of triggering.

The standard trigger supplied with the camera is an optically triggered solid-state (Mylar) spark gap. This gap is the key to providing a rapidly rising voltage ramp to the streak plates. The spark gap had only been used at a wavelength of $\lambda = 1.06 \mu\text{m}$ with 70-ps or shorter pulses. In comparison, our typical CO₂ pulses have a length of 1.2 ns FWHM with a risetime from 10 to 30% of ~ 225 ps.

The spark gap was removed from the camera and was tested for both triggering jitter and delay between an incident 10.6- μm pulse and the gap electrical breakdown. Previous results obtained with a 70-ps Nd:glass pulse at 1.06 μm were a delay of <200 ps and a jitter of <20 ps. A 37-mm f/1,

antireflection-coated ZnSe lens replaced the stock 25-mm $f/1$ glass focusing objective. Both lenses could produce diffraction limited focal spots. Preliminary measurements of freestanding 1-mil Mylar showed that 10 mJ of 10.6- μm light was necessary to burn a clean hole. Beginning at 5 mJ incident and running up to 180 mJ in a clean TEM₀₀ beam, the Gigawatt Test Facility (GWTF) provided a test CO₂ pulse. The spark gap was charged to 5 kV (similar to its charge in the Pico-X), and both the CO₂ pulse and the gap voltage were combined on a single fast-scope channel.

The results were disappointing. Jitter was high, ± 5 ns, and the formative time delay was large, ~ 5 ns. This delay was minimum for ~ 40 mJ incident. As the incident energy neared and exceeded 100 mJ, air breakdown was clearly visible and jitter soared. The breakdown physics appeared quite different at 10.6 μm than at 1.06 μm . Breakdown seemed to be a thermal process rather than an electron avalanche process. There are several possible explanations for this result.

The GWTF pulse shape was nearly symmetrical with a 1.2 ns FWHM and a 400-ps risetime from 10 to 90%. (In comparison, TBS or Helios risetimes are 180 to 250 ps.) The slow risetime may partially explain the poor gap performance. To date, the Mylar spark gap has not been tested for jitter with a 1.06- μm pulse exceeding 70 ps FWHM. Air breakdown thresholds are 10 times lower for 10.6 μm than they are for 1.06- μm radiation.¹⁴ Thus, premature air breakdown may refract the incident beam and raise the jitter. Finally, diffraction limits the focal-spot diameter to $2.44 (f\text{-number}) \lambda$; that is, to 10 times larger than 1.06- μm focus. This reduces incident intensity by a factor of 100 and minimizes changes for initiating avalanche breakdown.

To begin collecting data with the Pico-X, triggering will be performed electronically. A trigger unit is being purchased from GEAR, which will provide an 8 to 10-ns record across 25 mm with ± 100 -ps jitter and 120-ps resolution. The camera should be taking data by November 1978. Faster triggering schemes are being investigated as a parallel effort on the second camera.

X-Ray Microscope (W. Friedhorsky)

The region of high spatial resolution ($\sim 1 \mu\text{m}$) for an axisymmetric x-ray microscope (XRM) is limited

to a very shallow focal plane (10 μm deep for a 10X, 1.5° grazing-angle system). Very accurate focus of the XRM is thus required for full exploitation of its capabilities. Two approaches are apparent to address the focusing problem. (1) The XRM can be focused directly with x rays. This must be done in vacuum because of the low energy (~ 1 keV) of the x rays reflected by the XRM, and requires an intense miniature source as well as an x-ray detector with real-time data readout. (2) The alternative method, which we have chosen to develop, is to focus at optical wavelengths. The XRM, being a purely reflective system, is achromatic, focusing at the same position optically and at x-ray wavelengths. However, the focal-plane image of the XRM is severely blurred by diffraction at optical wavelengths. (The diameter of the diffraction core corresponds to 10 μm at the object plane.) Optical focus must therefore be obtained with a photometric system that allows accurate location of the peak of a broad diffraction pattern.

A proposed optical focusing system, which was successfully tested in breadboard form, is shown in Fig. VII-7. Light from a helium-neon laser is focused on a pinhole, and the pinhole is then imaged by the XRM. When the plane mirror is at the focal point of the XRM, the focused beam is returned to the XRM and refocused through the pinhole. Moving of the mirror from the plane of focus causes the flux returning through the pinhole to fall off according to the axial distribution of the refocused image. Part of the returning flux is split off by the beam splitter and measured by the detector. The breadboard test showed that the returning flux fell to half-maximum when the XRM was moved from best focus by 400 μm . A phase-locked detection scheme involving modulation of the returned signal by vibration of the plane mirror seems likely to allow accurate ($\pm 5 \mu\text{m}$)

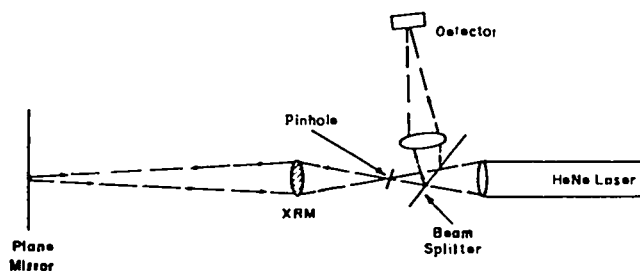


Fig. VII-7.
Schematic focus mechanism for x-ray microscope (XRM).

location of the peak of the axial intensity distribution. Hardware for the phase-locked detection scheme is on order.

Ray-traced design studies for future microscopes continued. The XRM ray-trace program was modified for operation on the PDP-11/70 computer.

The performance of high-magnification XRMs, which might be required for a low-resolution detector such as the streak camera, was evaluated. For a given grazing angle, object distance, and optical length, the resolution of the XRM at the object plane was found to be independent of magnification.

The high-energy cutoff of the XRM is set by the grazing-angle θ of the surface. Current XRM prototypes have $\theta = 1.50^\circ$, and a correspondingly high-energy cutoff of 1.5 keV. A microscope with a grazing angle of 0.5° (with x-ray response up to 5 keV) would have an effective solid angle $1/27$ that of a 1.5° optic with the same resolution. Thus, high-energy response in an XRM can only be achieved at a substantial cost in efficiency.

Fresnel Zone-Plate Imaging in X-Ray Region (P. Rockett, P. Lee)

A binary Fresnel zone plate (FZP) was used in the same mount as the uniformly redundant array (URA) to compare image quality. The plate was $2.6 \mu\text{m}$ in diameter with a minimum ring width of $18.5 \mu\text{m}$. It contained 38 rings made of $3\text{-}\mu\text{m}$ gold foil. When placed in the camera mount, theoretical spatial resolution in the first-order image was $26 \mu\text{m}$. A FZP image was produced of a GMB implosion on the TBS, and the coded image was reconstructed in helium-neon light (Fig. VII-8). Note the reconstruction artifacts and relatively low image quality. Whereas the support stalk is barely visible, a compressed core can be seen. Although light-gathering ability is less than that of the URA, the optical reconstruction technique offers several advantages. In particular, reconstruction in higher diffraction orders promises improved resolution. We plan both the use of a smaller FZP with $6\text{-}\mu\text{m}$ theoretical resolution and reconstruction in the third order to broaden our x-ray imaging capability.

X-Ray Shadowgraphy (D. B. van Hulsteyn, P. Lee)

A technique for observing the compression of a target by measuring x-ray attenuation through the

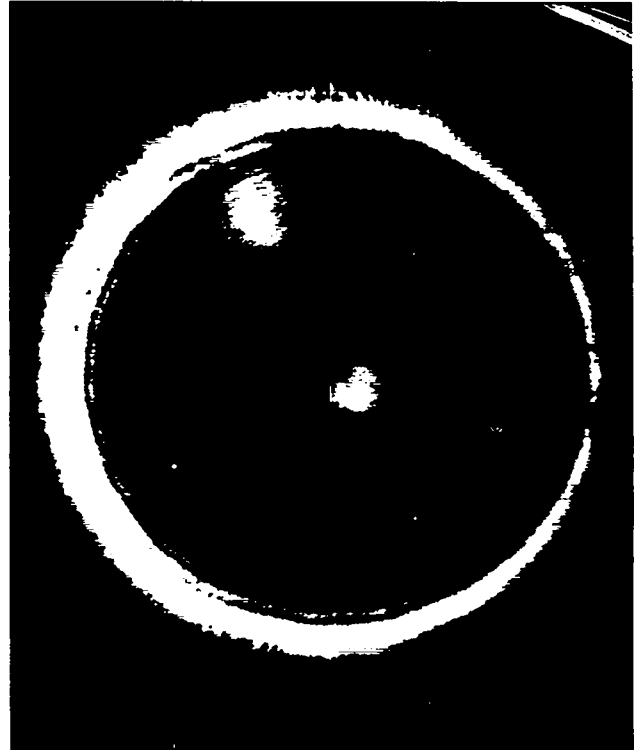


Fig. VII-8.

Reconstructed Fresnel zone plate image of a GMB implosion.

target is required, particularly for ablative-compression experiments. We will describe a simple slit-crystal backlighting scheme that can serve as a framing camera capable of taking one or more shadowgraphs at predetermined times during the implosion. The most significant advantage of a device using this concept is that it filters most of the x rays emitted by a hot object. This aspect is important, because it would otherwise be difficult to distinguish the signals produced by the backlighting source from those emitted by the imploded target.

The technique presently being developed is depicted in Fig. VII-9. Here a backlighting source of x rays is produced when a laser pulse irradiates a material of atomic number Z . If no imploded target is present, the slit-and-crystal combination forms two-dimensional spatial images of the lines emitted by the source. In practice, because of the position of the target relative to the backlight, only one line can be used for shadowing, and this line must be narrow, sufficiently intense, and well-separated from its neighbors.¹⁶ These criteria must be fulfilled for good spatial resolution in the direction of dispersion.

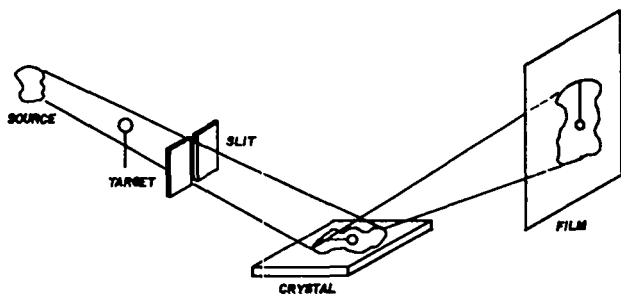


Fig. VII-9.

Backlighting camera showing the relative orientations of backlighting source, target, slit, crystal, and film.

A shadowgraph of the target can be produced if the target is aligned with the selected line from the backlight and is physically smaller than the emitting region. Furthermore, the target must be opaque to the line and, when imploded, must produce little radiation in the same spectral region. Consequently, the selection of a backlighting material will depend upon the composition of the target.

The concept of backlighting for laser target diagnostics is not new. It was described by Lieber,¹⁶ tested on cold targets by van Hulsteyn and Benjamin,¹⁷ and developed for a practical application by Key and coworkers.¹⁸ In these latter cases the images were obtained by pinhole-camera optics. However, when the emission from the target is significant, the situation becomes complicated. Filtering must be introduced to pass the signal from the source and to attenuate the radiation from the target. To produce the shadowgraph, the target must at the same time be opaque to the x rays from the backlighting source. In many applications, it may be impossible to find source, filter, and target materials that fulfill all these requirements.

One proposed technique to separate the backlight from the self-emission is to use a crystal in conjunction with a pinhole.¹⁹ This approach can indeed perform this function and also yield good resolution. Alignment, however, is quite difficult, and the field of view in the dispersive direction is limited by the fact that the film can see only a region of the target comparable with the pinhole size.

The system described in Fig. VII-9 avoids the field-of-view problem by replacing the pinhole with a slit. It might appear, at first, that this would also

eliminate spatial imaging in the direction of dispersion. A simple analysis, however, shows that this information is not lost and that the resolution is determined by the rocking angle of the crystal and by any line broadening that might exist in the backlighting source.¹⁶

The slit-crystal imaging, which has been discussed elsewhere,²⁰ is presented in Fig. VII-10 for clarification. Emission from a single point A produces a series of spectral lines (plus continuum) on the film. The length of the lines is dictated by slit size and geometric magnification, whereas the width is determined by the crystal rocking angle and line broadening. From the set of lines we select one, e.g., the narrowest, the most intense, the most well separated, or some compromise of these factors, and denote its image of A by A'.

Correspondingly, there is an image, C', of point C, which is displaced in the dispersive direction by the projected distance between A and C. Point B, separated from A in the direction perpendicular to the dispersion produces an image B' on the film, while D' is the image of D.

Another possible scheme using the imaging properties of curved crystals, described by von Hamos,²¹ has been described with Nagel.²² This device, which is more difficult to fabricate, will have much higher collection efficiency and is being considered as an alternative to the slit-and-crystal arrangement.

The imaging described in Fig. VII-10 differs from standard optics in three respects. First, the pinhole image is a 180° rotation of the object, whereas the crystal introduces a mirror inversion along the

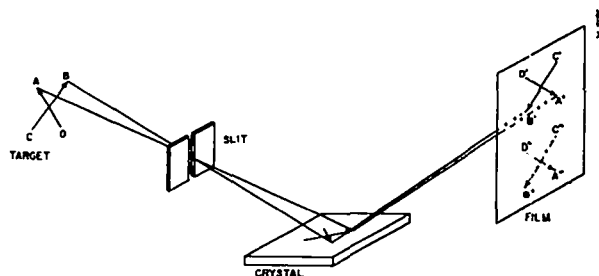


Fig. VII-10.

Two-dimensional imaging using the slit-and-crystal arrangement. Only two non-overlapping images are shown. The effect of resolution and magnification in the two spatial directions is not shown.

transverse direction. Secondly, although the solid angle subtended by the slit-crystal may be comparable with that of the pinhole, the signal recorded is weaker because the image is created from a single line rather than from the entire spectrum. Finally, for the slit-and-crystal scheme the magnifications are different in the two directions and may be controlled individually. Transverse to the dispersion, the magnification depends upon the ratio of the film-to-slit vs the slit-to-object distance, whereas along the dispersion this quantity depends upon the angle at which the x-ray signal hits the film.

A graphic illustration of slit-crystal imaging is presented in Fig. VII-11. A photograph of a target of crossed $5\text{-}\mu\text{m}$ SiO_2 fibers before being irradiated with a single beam of our TBS laser is shown in Fig. VII-11a. Whereas Fig. VII-11b shows the x-ray photographs taken with a $20\text{-}\mu\text{m}$ pinhole camera from behind the target. Figure VII-11c is the x-ray photograph produced by the target on a spectrograph with a $58\text{-}\mu\text{m}$ slit. This particular device, which used a flat TAP crystal ($2d = 25.75 \text{ \AA}$), was situated 60° to one side of the target. The images observed in Fig. VII-11c are from helium-like and hydrogen-like lines of silicon in second order. The most striking feature of this photograph is the absence of the bright spot that shows up in Fig. VII-11b. Note also that the $1S^2 \rightarrow 1S2p$ image is clear and well separated from its neighbors, and that the resolution along the dispersion is of the order of $50 \mu\text{m}$.

A second example is shown in Fig. VII-12. In Fig. VII-12a we see a pinhole photograph of a microballoon irradiated by both beams of our TBS laser; the typical features of the glowing halo and the intensely radiating core. Figure VII-12b shows a spectrographic image taken with a device located directly opposite the pinhole. The crystal, in this case, was EDDT ($2d = 8.808 \text{ \AA}$), with the spectrograph slit set at $25 \mu\text{m}$. The magnifications along and transverse to the dispersion were both set equal to 1.4 for the $1S^2 \rightarrow 1S2p$ line so as to preserve its shape. A comparison of Figs. VII-12a and -12b reveals that the halo regions are comparable in shape, size, and orientation. On the other hand, the spectrograph shows no bright central region, indicating that the core contains very little helium-like emission. We note, also, that no trace of hydrogen-like emission from the core was visible on the film, suggesting that for this particular shot the intense radiation in this region was due to continuum.

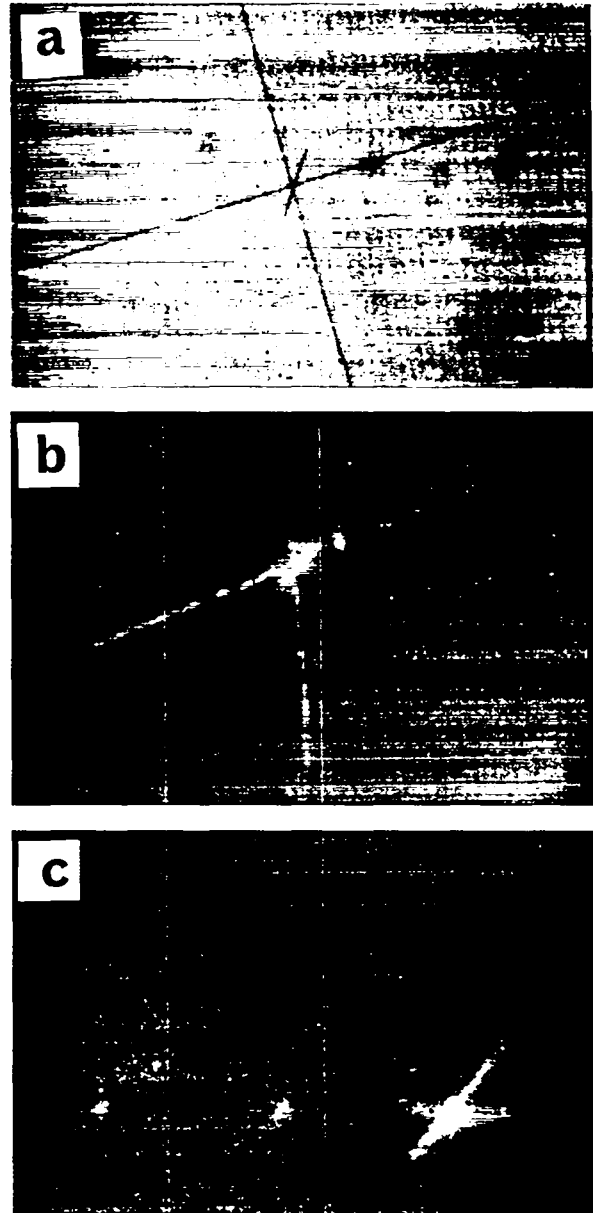


Fig. VII-11.

Crossed $5\text{-}\mu\text{m}$ fibers. (a) Actual target before it was irradiated. (b) $20\text{-}\mu\text{m}$ pinhole photograph taken from behind the target. (c) Spectrographic image of the same event; note the absence of the bright spot that appears in (b). The most intense image is due to the $1S^2 \rightarrow 1S2p$ transition; weaker images are due to the $1S \rightarrow 2p$ and $1s^2 \rightarrow 1s3p$ lines.

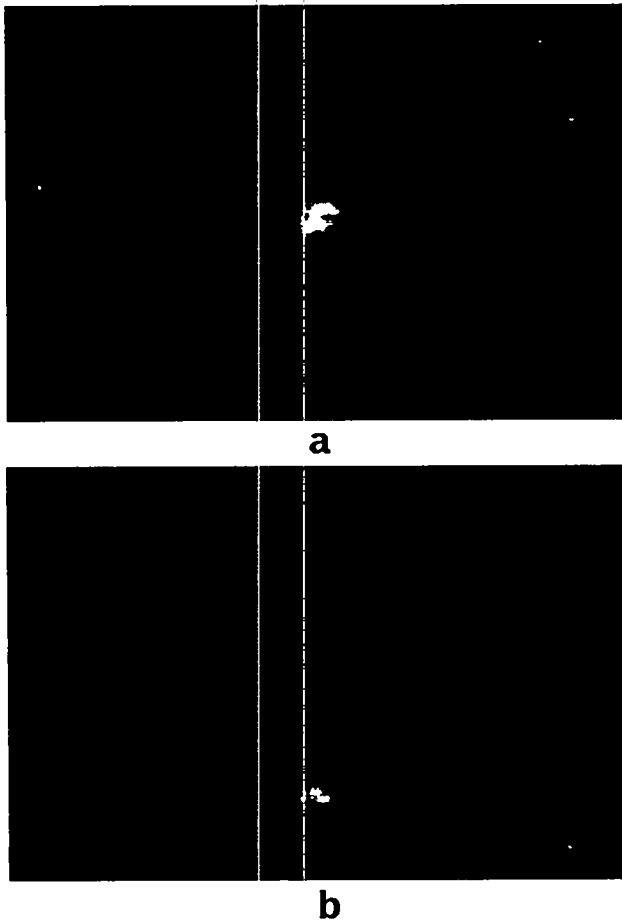


Fig. VII-12.

Imploded glass microballoon. (a) Pinhole image filtered by $12.5 \mu\text{m}$ of beryllium. (b) $1S^2 \rightarrow 1S2p$ image of the same event. The absence of the bright central spot from (b) indicates that this core may be due to continuum. The tail in (b) is produced by satellite lines and by continuum.

Having established that imaging is feasible, it remains to specify the backlighting element, Z_B , assuming that the constituents of the target are known. For the sake of argument, let us suppose that the target is hot, because otherwise conventional backlighting techniques^{17,18} would be more reasonable. Three major considerations, then, dictate the choice of Z_B . First, there is the chemical and physical nature of the element itself; strontium, for example, could be ideal in all other respects but might be undesirable as a target because of its

pyrophoric nature. Second, the efficiency of line production is Z -dependent;²³ it must be known whether or not the desired line from the source is sufficiently intense to produce an image that is stronger than the background state. If the target is hydrogen-like, for example, it can produce a shadow only if the backlighting emission is sufficiently energetic to remove the remaining electron. The cross section for this process is highest if the line from the source is slightly greater than $13.6 Z_T^2$ eV, where Z_T is the atomic number of the target.

Geometrical Single-Aperture Imaging and Wide-Aperture Deconvolution (M. M. Mueller)

Because the bulk of x-ray image data from laser fusion targets is obtained with pinhole or slit apertures, an in-depth study was conducted to provide improved rational bases for the optimum design of single-aperture imaging systems as well as for the deconvolution of the data to obtain information about imploded targets. The results of this study are too complex and diverse to be discussed here in reasonable depth. However, a recent report²⁴ covers both the analytical and numerical results in considerable detail.

Analytical solutions for the image irradiance distribution were obtained for a uniform disk source irradiating a screen through either a slit or a circular aperture. For the structured sources of more direct interest to laser fusion, we developed a two-dimensional convolution algorithm to handle arbitrary asymmetrical configurations. Thus, rather realistic simulations of single-aperture imaging can now be provided. Such simulations are particularly useful in developing deconvolution methods, as well as in optimizing the design of imaging systems. Because of the complexities of convolution, the imaging results—particularly when slit apertures are used—are sometimes surprising and always instructive.

A plot of apparent radiance from a source model composed of a uniform spherical shell of emission surrounding an eccentric homogeneous ball of emission is shown in Fig. VII-13. (The coordinates of the source plane, u and v , are antiparallel to x and y , the corresponding coordinates of the detector plane.) The diameter, or width, of the aperture is denoted $2a$, whereas $2b$ denotes the source diameter. The irradiance distribution formed by a slit of halfwidth

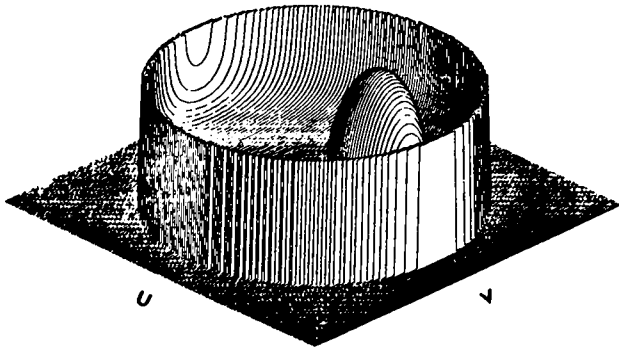


Fig. VII-13.

Radiance plot for a uniform spherical shell surrounding an eccentric homogeneous ball of emission.

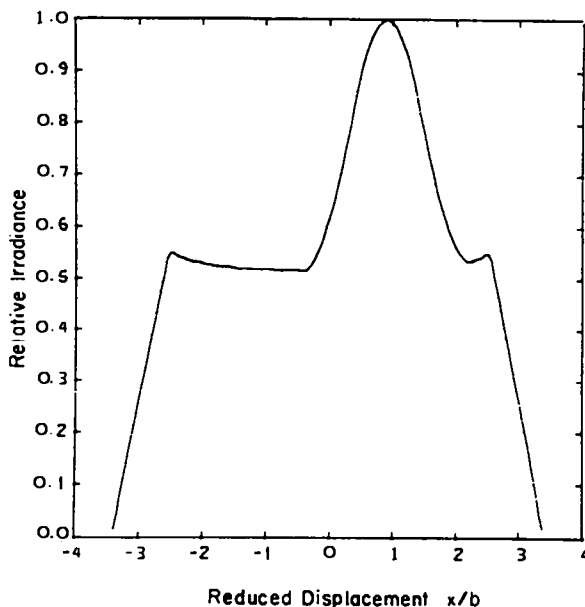


Fig. VII-14.

Irradiance distribution for the source in Fig. VII-13 with $M = 3$ for a slit with $a/b = 0.1$.

$a = 0.1b$ with a system magnification $M = 3$ is displayed in Fig. VII-14. Because the long dimension of the slit is parallel to the y axis, the convolution is in the x direction. Note that the valley within the rim of irradiance due to the shell is almost completely filled in, so that the image superficially resembles that of a roughly uniform source rather than the annular image that might naively be expected. Indeed, this effect is not due to poor resolution in the usual sense (because it also occurs with a slit of arbitrarily

narrow aperture) but is due rather to the one-dimensionality of the slit aperture. By comparison, a pinhole aperture broadens the rim, but only partially fills in the valley, so that a spherical shell produces an annular image, as shown in Fig. VII-15 for a circular aperture with $a = 0.2b$.

The two-dimensional convolution algorithm is valuable in understanding pinhole and slit images in several ways. First, it enables us to fit an assumed source model to the irradiance data by iteratively adjusting parameters pertaining to the model. Second, because the shapes of small apertures are seldom accurately circular, more realistic shapes can be used to provide improved simulations. Third, numerical simulations provide valuable checks and limits to the validity of simple methods of determining the diameter of the source or of a part thereof. For example, although simple and accurate alternatives exist, some other laboratories still use the full width at half maximum to determine the size of the compressed core of an imploded target. This produces, according to our simulations, an overestimate of the volume compression by nearly a factor of 2 for a solid core of x-ray emission.

Moreover, one of the main thrusts of this study is to point out the potential advantages of using wide apertures. Where image degradation due to diffraction is unimportant, the only significant drawback to pinhole imaging is the weak image intensity caused by the need to use a small aperture to obtain good geometrical resolution. However, one of our conclusions is that, for image data of sufficient quality to allow meaningful first derivatives, the use of very wide slits or circular apertures can become tantamount to the use of extremely narrow slits or pinholes in terms of resolving source structure.

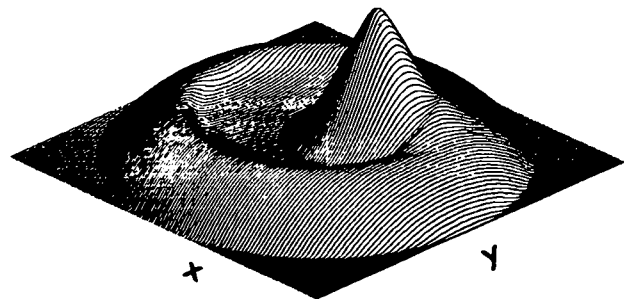


Fig. VII-15.

Irradiance distribution for the source in Fig. VII-13 with $M = 3$ for a circular aperture with $a/b = 0.2$.

Apart from the intrinsic advantages of using wide apertures (larger than the source) in some circumstances, the study of their behavior is mandatory because their employment is sometimes unavoidable. One example is the compressed central core of a laser fusion target that may be smaller than the pinhole aperture. Another example comes from x-ray spectroscopy where wide slits are often necessary because of the weak emission of certain atomic lines of interest.

A slit aperture is, of course, formed by two straight edges. In the wide-slit regime, by definition, the regions of variable irradiance passing these two edges do not overlap. Thus, the wide-slit regime is just a "knife-edge" regime with redundancy. One can show by analysis that the first derivative of a knife-edge convolution gives an image of the source radiance distribution identical to one that could be obtained with an infinitesimal slit.

Figure VII-16 displays the image of the source in Fig. VII-13 formed by a slit with $a = b$. Then the first derivative of this irradiance distribution is shown in Fig. VII-17, exhibiting the redundancy discussed. In Fig. VII-18, the mean values of the two sides of Fig.

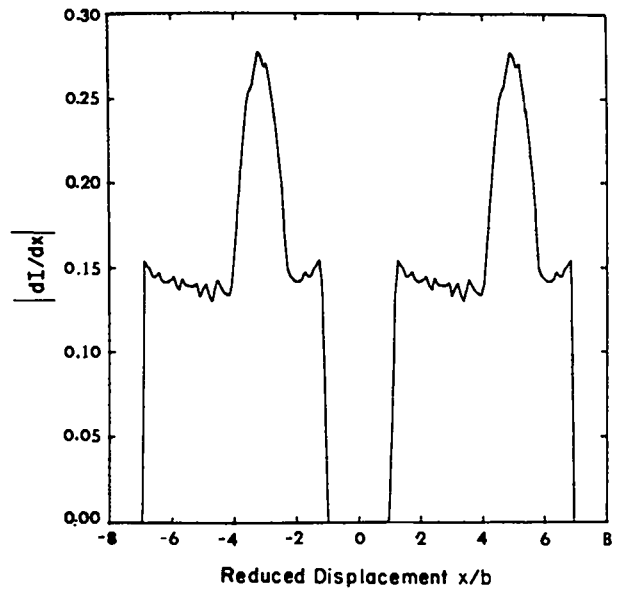


Fig. VII-17.

Irradiance derivative distribution for the source in Fig. VII-13 with $M = 3$ for a slit with $a/b = 1$.

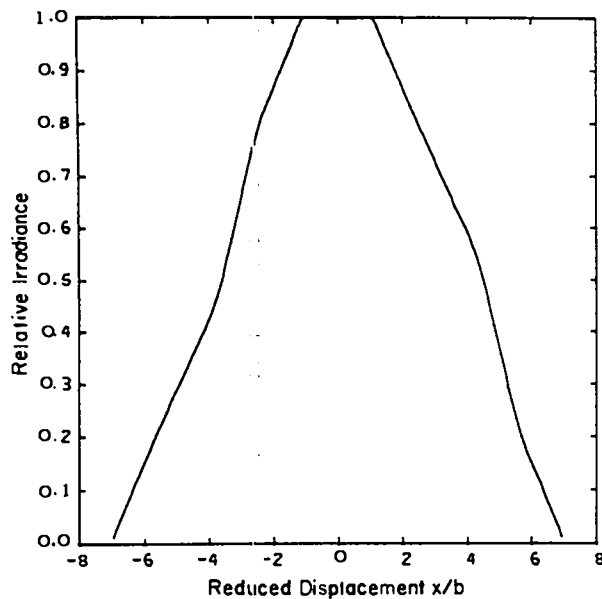


Fig. VII-16.

Irradiance distribution for the source in Fig. VII-13 with $M = 3$ for a slit with $a/b = 1$.

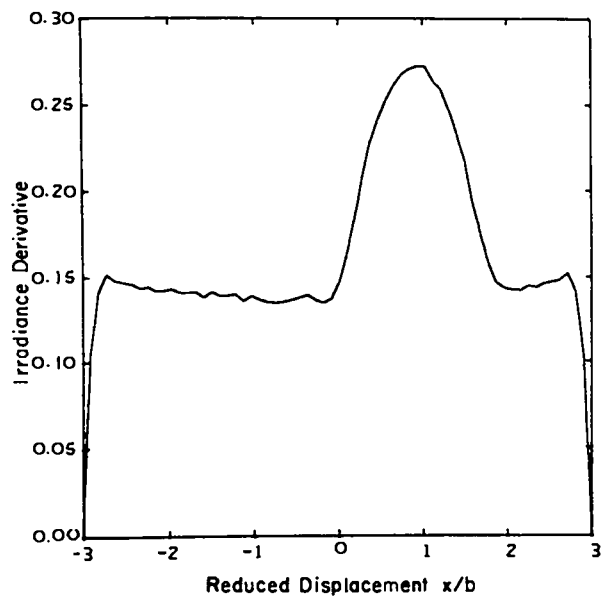


Fig. VII-18.

A replot of Fig. VII-17 giving an image identical with that from an infinitesimal slit.

VII-17 have been replotted at corresponding points to give an image identical (save for noise due to the discrete solution of the problem) to what would be seen through an infinitesimal slit. Hence, in the absence of significant data noise and diffraction, the problem of instrumental broadening has been overcome.

Performing this kind of deconvolution for images formed by wide circular apertures is, of course, complicated by the effects of curvature. However, a "decurving function" can be developed to reduce the distorted images to approximately what would be seen by an infinitesimal slit. Thus, a wide circular aperture, by providing information in many azimuthal directions, may be more potent than several slit apertures. Indeed, such a wide circular aperture, providing infinitesimal-slit-like information in a large number of azimuthal directions, is probably equivalent in principle to an infinitesimal pinhole.

POCKELS CELL DEVELOPMENT AND IMPLICATIONS (E. McLellan, F. Harrison)

Introduction

A Pockels cell of the type previously described has been used to generate CO₂ laser pulses as short as 90 ps FWHM. These short CO₂ pulses were then used to evaluate an electrical redesign of the Molecron P500 pyroelectric detector mount. The signal generated by the redesigned detector viewing the short CO₂ pulse is used to compare the performance of the LASL-built 5-GHz and Type 1776 oscilloscopes, and of the Tektronix R-7912-R transient digitizer.

90-ps Electro-optic Shutter

A 50-Ω matched-impedance crystal holder driven by a 500-kV laser-triggered spark gap was used as a full-wave shutter to generate 105-ps, and as a 3/2-wave shutter to generate 90-ps CO₂ laser pulses. The full-wave device operates as follows. When the 7- by 7- by 40-mm CdTe crystal is placed between crossed polarizers, the transmission is maximum when the applied voltage is (1/2, 3/2, 5/2...) times the full-wave voltage V_λ , and minimum at (0, 1, 2,...) V_λ . A

voltage step with amplitude equal to the full-wave voltage will cause the transmission to go from minimum to maximum and back to minimum during the voltage risetime. The 105-ps CO₂ laser pulse generated by this method is shown in Fig. VII-19.

A 3/2-wave voltage step will cause the transmission to go from minimum to maximum to minimum and back to maximum during the voltage risetime, producing an even shorter pulse if the step risetime remains constant. Fig. VII-20 shows the 90-ps CO₂ laser pulse generated by the initial minimum to maximum to minimum portion of the transmission during the voltage rise. Additional Pockels cells can be used to increase contrast ratio and to eliminate the final transmission cycle in the 3/2-wave voltage case.

Fast Pyroelectric Detector Improvements

The Molecron P500 detector consists of a 1- by 1-mm SBN pyroelectric detector element mounted in a BNC connector. Previously,²⁶ it was shown to have an electrical bandwidth greater than 5 GHz. Presently, the poor impedance matching of the detector to the BNC connector can cause some pulse distortion for pulses well below 1 ns in duration. We redesigned the detector housing to eliminate this

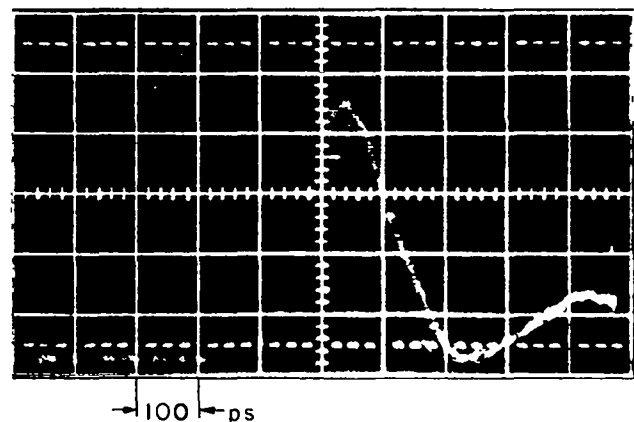


Fig. VII-19.
CO₂ laser pulse generated by full-wave voltage methods as measured on the 5-GHz scope.

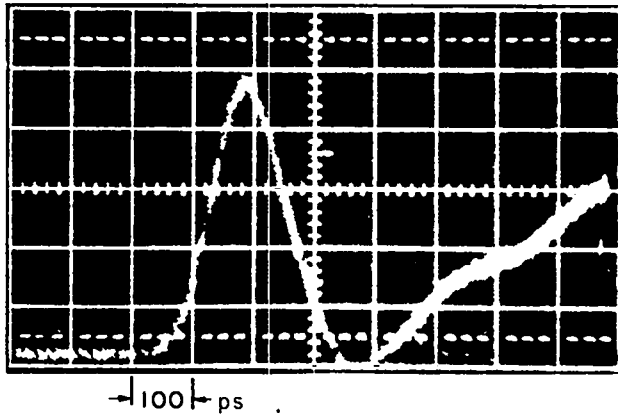


Fig. VII-20.

CO₂ laser pulse generated by 3/2 wave voltage methods as measured on the 5-GHz scope.

problem. To test the performance of the modified detector, we compared pulse shapes before and after the modifications for ~100-ps CO₂ laser pulses incident on the detector and displayed on our 5-GHz scope. In addition, a Tektronix 7612 TDR/Sampler was used to evaluate the impedance matching of the detector via 35-ps-risetime test signals.

Figure VII-21a shows the reflected step function produced by the unmodified detector and indicates that distortions can be caused by impedance mismatch for time measurements of ~0.25 ns or less. Figure VII-21c shows the 105-ps CO₂ laser pulse, described above, detected by the unmodified Molelectron P500 and displayed on the 5-GHz scope.

The detector was disassembled and the small epoxy disk on which the SBN detector is mounted was removed and mounted on an SMA connector pin. The detector and pin were then plugged into a Kings 879-4 SMA-to-BNC adapter and a large diameter wire was used to attach the connector casing to the detector ground. The TDR/Sampler-reflected step function with the detector remounted in the SMA-to-BNC adapter is shown in Fig. VII-21b. Impedance mismatch distortions have been eliminated. A BNC-to-Type-N adapter was used to attach the new mount and detector to the TDR/Sampler to determine the degradation that would be caused by such an adapter between the 5-GHz scope

and the detector. This connection introduced less than 5% distortion at 10 GHz (see Fig. VII-21b).

These data show that future work with fast detectors should use BNC rather than Type N connectors as the detector mount, because no performance gain is obtained by using Type N connectors, and these are less desirable from an operational standpoint. Figure VII-21d shows the same CO₂ pulse displayed in Fig. VII-21c, with the detector in the new impedance-matched mount.

Fast Oscilloscope Comparisons

Tests were conducted with the full-wave electro-optic shutter and modified pyroelectric detector to deduce more accurately the electrical bandwidth of the LASL-built 5-GHz scope and Type 1776 scopes and the Tektronix R-7912-R transient digitizer scope. For our purposes, the oscilloscope bandwidth was defined as follows:

$$\text{Bandwidth} = \frac{1}{2\sqrt{\tau^2 - \tau_{CO_2}^2}}$$

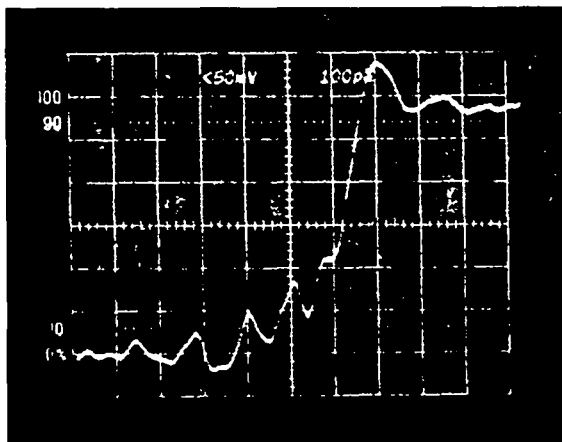
where τ is the FWHM measured on the display and τ_{CO_2} is the FWHM of the CO₂ voltage signal at the scope. Figure VII-22 shows the normalized signals generated by the short CO₂ pulse on the modified pyroelectric detector with a 1-m-long RG-223 cable connecting the detector to each of the three scopes in turn.

To obtain relative bandwidths of the scopes, $\tau_{CO_2} = 112$ ps is assumed to give the correct bandwidth for the 5-GHz scope. With the same assumption, the observed pulse shapes predict the bandwidth of the Type 1776 scope to be 2.5 GHz and that of the R-7912-R to be 2.2 GHz. These bandwidths correspond to a vertical sensitivity of 0.14 V/cm, 1.0 V/cm, and 1.7 V/cm, respectively, for the 5-GHz, 1776, and R-7912-R scopes. Figure VII-23 gives a qualitative comparison of the scope displays. The R-7912-R trace is a digitized and stored image and requires some operator interpretation.

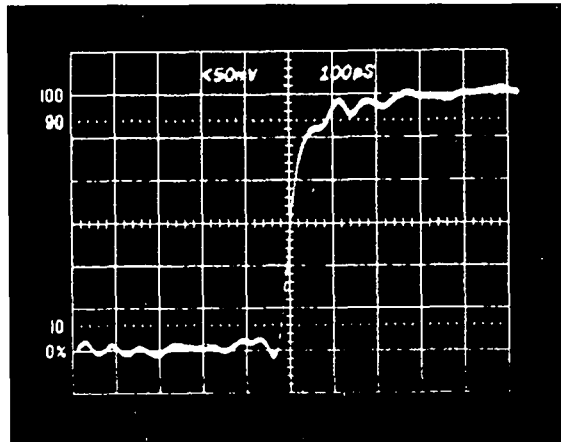
TECHNOLOGY DEVELOPMENT

Production of High-Quality Mylar Pellicles (A. H. Williams)

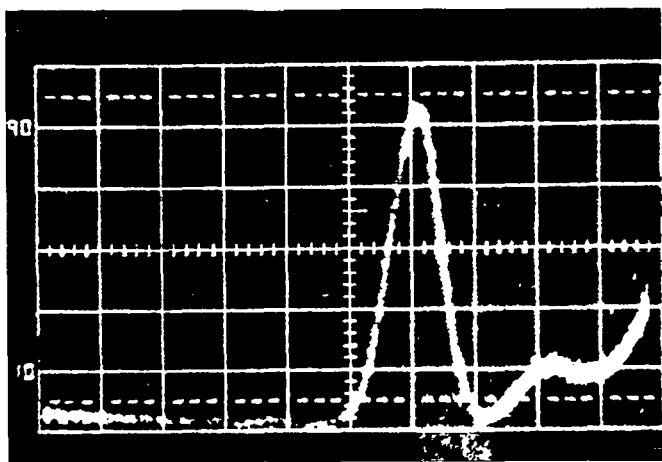
To satisfy our expanding optical and experimental requirements, we are now able to produce, in house,



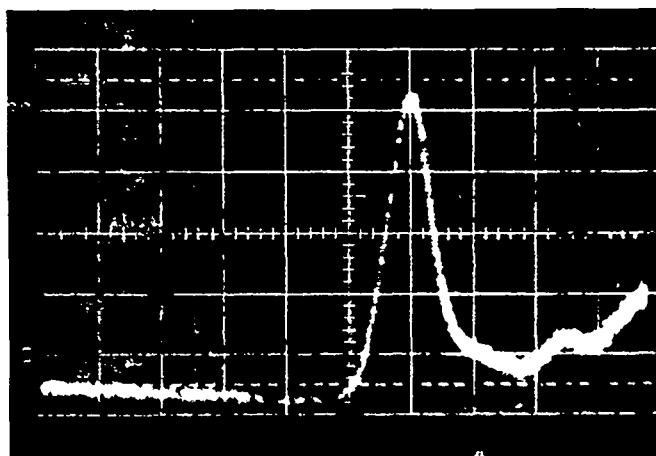
A



B



C



D

Fig. VII-21.

Test of impedance matching via time-domain reflectometry for (a) the Molectron P-500 and (b) the same detector after modifications described in the text. Corresponding oscilloscope traces from the LASL 5-GHz oscilloscope of the CO₂ laser pulse response of: (c) the Molectron P-500 and (d) the modified detector. Sweep speed is 200 ps/division.

a large variety of high-quality Mylar pellicles from 1 to 48 cm in diameter. Initial studies of these pellicles using stock-grade 6- μm -thick Mylar show them to be flat to approximately $\lambda/20$ at 10.6 μm in transmission. Quality of reflection depends upon the flatness of the Mylar support frame. Using diamond-point or other precision machining techniques to produce the support-frame surface, one can easily obtain pellicles with high-quality reflecting surfaces.

The pellicle support rings are made of aluminum bar stock. After all machining and hole drilling is completed, the rings are thermally stress-relieved before machining the Mylar bedding surface. The Mylar is prestretched in a set of stretch rings to provide a surface that will ensure the formation of good optical images. Then the outer edges of the support ring are wet moderately with Eastman 910 glue, lightly pressed into the prestretched Mylar and

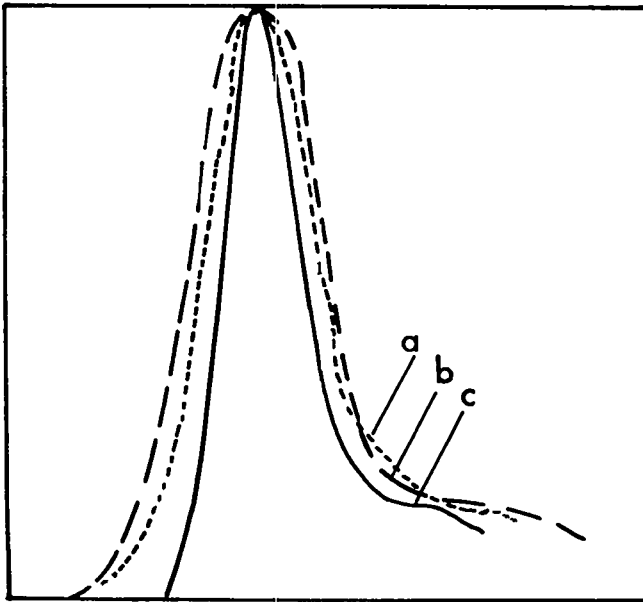


Fig. VII-22.

Normalized responses of the three oscilloscopes to a CO_2 pulse whose width is presumed to be 110 ps: (a) LASL-built 1776 oscilloscope; FWHM, 230 ps; 10 to 90% risetime, 150 ps. (b) Tektronix 7912 transient digitizer; FWHM, 255 ps; risetime, 170 ps. (c) LASL-built 5-GHz oscilloscope; FWHM, 150 ps; risetime, 100 ps. The Type 1776 oscilloscope is seen to more than double the true pulsewidth, while the 5-GHz device provides significantly less distortion.

left undisturbed until dry. Finally the excess Mylar is carefully removed from the pellicle frame by cutting it free with a sharp knife.

High-Voltage, Fast-Pulse Generation with Small Delay and Jitter (F. Wittman, N. Clabo, R. Carman)

General. Numerous parts of our laser program require electronics capabilities in the high-voltage pulse area, specifically when very small delays and jitters are desired. We have begun a program to systematically solve many of the problems involved.

Avalanche Transistor Circuits. Avalanche transistors have desirable delay and jitter characteristics. Single-stage switches typically

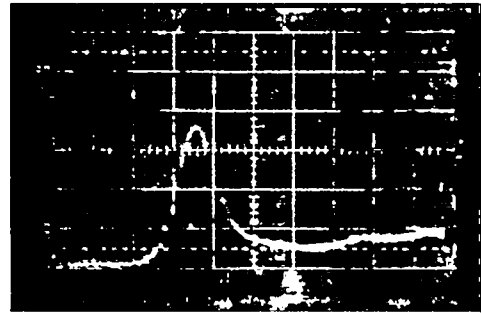


Fig. VII-23.

Actual trace photographs forming the basis for Fig. VII-22. The 7912 trace is stored in digitized form, and requires some operator skill for proper interpretation.

generate 250-V pulses with risetimes of 1 to 3 ns, whereas both delay and jitter are significantly less than 1 ns. Avalanche transistors can be cascaded with little change in delay, jitter, and risetime characteristics of the output pulses. Whereas single-stage switches are capable of driving a 50- Ω load, they function best when driving a higher load

impedance. In addition, we find that the minimum load impedance should be scaled up linearly with the number of stages in the avalanche string. Thus, pulses up to 1 kV have been generated by using a five-stage Motorola 2N5271 avalanche string, operating into a load impedance of $>200 \Omega$. Degradation of the risetime was observed as well as large-amplitude ringing for lower load impedances. No significant change was seen in the jitter characteristics, whereas the delay appeared to scale with the number of stages.

We attempted to modify some of these results by building the avalanche strings into a microwave, traveling-wave structure to minimize the effects of the external circuit parameters. This work is continuing, but we have not yet seen any significant change in the pulsed output characteristics.

Another aspect of avalanche transistor strings is the limited number of stages that can be assembled; thus, the ultimate output voltage, too, is limited. This limitation is caused by the buildup of noise and emitter-to-collector impedance fluctuations that spontaneously trigger the string. We attempted to pulse-charge the energy storage capacitors used in the avalanche string, but found this process impossible due to simultaneous triggering of the string. Marx-bank geometries do, however, appear feasible as long as the load impedance is high enough ($>40 \Omega$ times the total number of transistors). Finally, we experimented with grading the voltage down the avalanche string so that only the triggered transistor and one or two neighboring transistors were biased into the avalanche region; the rest were biased 10 to 30 V below avalanche conditions. Significantly higher voltage could then be sustained on the triggered transistor, greatly improving the trigger delay and jitter characteristics of the overall avalanche string. We did not attempt to increase the single-string pulsed-output voltage by using this voltage-grading technique because of the high load impedance required. Most of the identified applications do not have sufficiently high input impedances.

A serious drawback to avalanche transistors is that they are easily damaged. An example of this incompatibility is the use of avalanche-transistor strings for electrical triggering of spark gaps. Back pulses from the spark gap usually damage the string, whereas protective circuitry usually is too slow or otherwise modifies the overall circuit characteristics sufficiently to make other trigger-circuit alternatives

a better choice. We restricted the applications of avalanche-transistor strings thus far to triggering krytrons. Output circuit protection from back pulses from the krytrons was accomplished successfully by a series chain of V130L varistors. Larger current-capacity varistors were inferior because of the concomitant larger capacitance to ground, which shorts the forward pulse. The input circuit was easily protected with a 1-W, 10-V Zener diode.

Silicon-Controlled Rectifier (SCR) Circuits. Usually SCRs are thought of as very slow switches with poor risetime, delay, and jitter characteristics. However, we identified two cases in which electrically triggered SCR circuits led to very reliable pulsers. First, the Motorola 2N4443 SCR was used to produce pulses with 50-ns risetime. With 400 V applied per SCR, a pulse of >300 V was obtained. These SCRs are very rugged and reliable. Delays of ~ 10 to 20 ns were typical with a gate pulse of 15 to 20 V.

A much faster pulser can be built with Unitorde Corp.'s GA 301-type SCRs. They will switch with a risetime and delay of 3 to 5 ns and with a jitter of ~ 1 ns. Each SCR will take a 90- to 100-V bias and will deliver ~ 80 V in the pulse. We successfully stacked up to 10 SCRs in a string obtaining an output of ~ 800 V. However, these SCRs are not very rugged and are quite expensive.

Work at Bell Laboratories, and more recently at LLL and the University of Rochester, on optically gated SCRs indicated that much faster switches can be made by using the SCR structure. We have begun investigating the possibilities of building high-voltage pulsers with a risetime of <100 ps by using this technology. Apparently, many more materials can be used than just silicon. Further, we are considering doing more work on the production of electrical shocks in cables using nonlinear propagation effects associated with either the dielectric constant or the magnetic permeability to achieve similar risetimes.

Krytron Circuits. Considerable research effort was spent on the EG&G KN22B krytron and more recently on the KN6B krytron. A KN22B single unit will drive a 50- Ω load at up to the maximum anode voltage of 7 to 8 kV, but operating a cascade string increases the voltage output only if the load impedance is increased in such a manner that the pulse current does not exceed ~ 150 A. In the case of

the KN22B, we identified the cause of this limitation as current-pinching combined with the limited electron-generation capacity of the cathode. Single-stage pulsers were built that produced pulses with both risetime and jitter of <1 ns and with a delay of <25 ns. Short risetimes are obtained only when very-low-inductance capacitors of the ceramic type are used. No problems were encountered with several ceramic capacitors in parallel, but risetimes suffered when they were used in series.

A pulsed charging-mode of operation was tried by using KN22Bs, but difficulties were encountered in triggering the output krytron; most of the time the KN22B would fire spontaneously. After examining the krytron literature, we chose an unlikely candidate, KN6B. Under usual operating conditions, it had too slow a risetime with too much delay, but had a high-current capability of 3000 A. A single KN6B could be pulse-charged with 15 to 20 kV pulses and when triggered with ~ 1 -kV pulses, would have a risetime of ~ 2 ns. Output currents in excess of 1000 A were obtained. Interestingly, when an inductance was used to couple the pulse-charging circuit to the KN6B, a resonant-charging circuit was formed which, depending on the Q-factor of the circuit, led to a higher voltage on the KN6B than had been applied to the pulse-charging circuit. Capacitor coupling lengthened the period over which voltage was applied to the anode of the KN6B; thus, the circuit was less critical to the timing of the trigger to the KN6B, and less overvoltage could be employed successfully. Very significant overvoltages could be sustained by the KN6B for times of ~ 0.5 to $1 \mu\text{s}$, after which internal breakdown occurred. Delays for pulse-charged KN6B circuits appear to be <10 ns with jitters well under 1 ns. We will study pulse-charged cascade strings of KN6B krytrons to determine how high a voltage output can be obtained.

In Marx-bank technology spark gaps are usually employed as the switches. We successfully constructed a Marx-bank by using KN22B krytrons in cascade per bank. Two- and three-stage Marx banks were constructed. A maximum of 60 kV could be generated with either system as long as the keep-alive applied voltage did not follow instantaneously the applied anode voltage. The limitation was caused by internal breakdown in the krytron for anode-to-keep-alive potentials of ~ 30 kV. At 60 kV output, risetimes were ~ 1 ns into a load impedance of $\sim 500 \Omega$. We are now investigating transient voltage grading schemes that may allow us to

eliminate the present output voltage limitations on KN22B circuits. To date, 16 Marx-bank pulse generators have been built and successfully operated in connection with the six-tube low-pressure CO_2 oscillator pulse, low-pressure preamplifier program (see following discussion). These generators produce 50- to 60-kV biased with a measured risetime at the CO_2 tube of a few nanoseconds, despite the long leads and unoptimized external circuit parameters. This system is shown in Fig. VII-24.

A second application of our krytron technology was the construction of a variable-pulse-width square-wave generator with a nominal output of 10 kV. In Fig. VII-25 we show this circuit. Here two KN22s were used in cascade to produce the desired

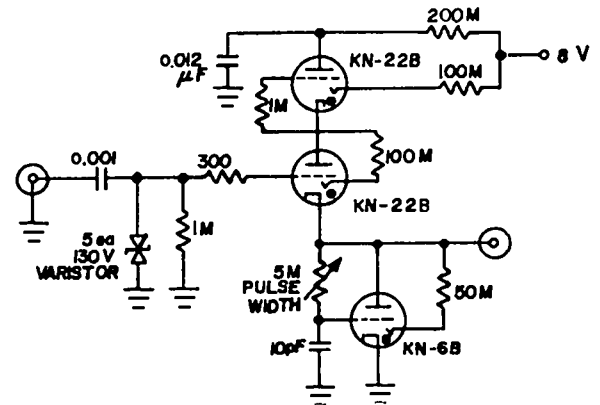


Fig. VII-24.
Square-wave pulser.

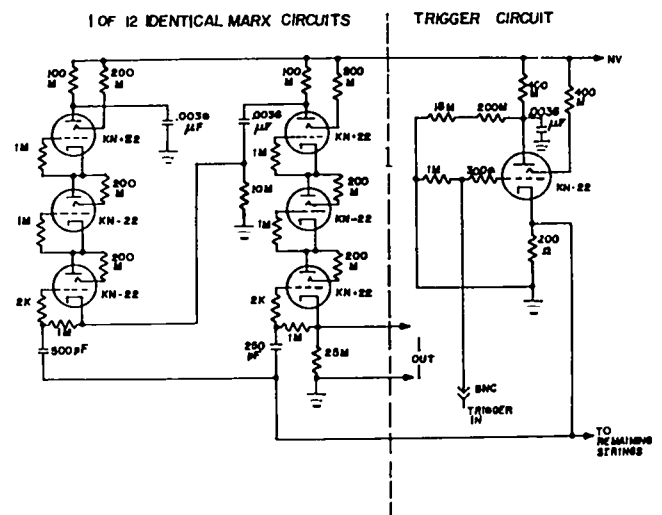


Fig. VII-25.
Variable pulsewidth square-wave generator.

fast risetime, whereas the pulse-charging and crowbar capability of the KN6B was used to generate the falltime characteristics.

In both circuits (Figs. VII-24 and -25), avalanche transistor strings producing nominally 1-kV pulses were used to trigger the krytrons.

COMPUTER TECHNOLOGY

Computer Management and Data Acquisition (R. C. Peck)

The PDP-11/70 computer operated with less than 1% down time while serving five time-sharing terminals. Seventeen time-sharing users used 54 550 min of connect time.

Data from experiments on the TBS were stored on 629 records from five types of CAMAC modules. The data files can be accessed by analytic programs and by programs that recall selected data sets for display. Software under development will provide for copying older data to magnetic tape for archival storage.

We have one microdensitometer interfaced with the NOVA 840 computer and with the PDP-11/70 computer through CAMAC. Densitometry is also provided for us by another LASL organization and sent to us stored on magnetic tape.

Computer System Design and Implementation (V. Cottles, D. Campbell)

The PDP-11/70-based data acquisition/reduction system for all our present and future laser systems evolved along guidelines established in the original specifications. This design allowed for extensive growth in capacity without any major system design changes. The usefulness of the system as designed was proved by a steady demand for access that exceeded projected growth.

Two aspects of the system were given highest attention: (1) the completion of all designs and testing of all prototypes for the various data-communications electronics to allow undiminished operating performance for remote sites up to 914 m (3000 ft) from the central computer site, and (2) the procurement and installation of greater disk and memory space to provide expanded throughput and to at-

tempt to meet newly determined demand levels for a target date (January 1979), at which time a new assessment can be made for future needs.

The installation and termination of all signal lines to the various sites was completed. Each site has the following capacity:

- Five 9600-baud terminals.
- One CAMAC serial highway port (or three ports if a single-loop unit is used on a port instead of the targeted dual-loop system).
- Three control lines for remote startup and shutdown of remote sites.

To test the system, one data-acquisition site (TBS) and two data-reduction sites were made operational. The experience gained at the sites provided information for their modification that will be incorporated in the installation of data-reduction terminals at three remote locations, and at a data-acquisition terminal to be installed in the Helios facility.

The electronic modules used for data transmission were tested over a period of six months and had a zero failure rate over that period while operating continuously 24 h per day. A failure did occur when lightning struck the power system, but all these prototype units were restored to proper operation within 4 h. An optical CAMAC serial highway prototype was also operational for this period. A final design was completed and is in production to allow the installation of CAMAC crates inside the screen rooms to prevent ground-loop problems. A similar optical line is being constructed to allow installation of terminals inside the screen rooms.

Disk space and memory are inadequate for current and future needs. Our current disk system consists of three RK05 units that have a total capacity of 7.5 Mbytes. A RP06 unit with a capacity of 176 Mbytes was procured and will be installed before January 1979. This will increase the available disk space by a factor of 20. Our memory size at the beginning of the period was 128 words. An additional 128 words were installed and made operational; thus, the memory of the system was doubled.

REFERENCES

1. R. L. Carman, R. T. Hawkins, and C. K. Rhodes, "The Interaction of Neutrons with Atomic Rydberg States," submitted to Phys. Rev. A.

2. T. F. Gallagher, R. M. Hill, S. A. Edelstein, Phys. Rev. A14, 744 (1976); T. W. Ducas, M. G. Littman, R. R. Freeman, and D. Kleppner, Phys. Rev. Lett. 35, 366 (1975).
3. E. M. Purcell, Astrophys. J. 116, 457 (1952).
4. S. R. Ryan, S. J. Czuchlewski, and M. V. McCusker, Phys. Rev. A16, 1892 (1977); J. I. Gersten, J. Chem. Phys. 51, 637 (1969); F. W. Byron, Jr. and J. I. Gersten, Phys. Rev. A3, 620 (1971).
5. C. A. Slocomb, W. H. Miller, and H. F. Schaefer III, J. Chem. Phys. 55, 926 (1971).
6. D. J. Kligler and C. K. Rhodes, Phys. Rev. Lett. 40, 309 (1978).
7. J. D. Jackson, *Classical Electrodynamics* (John Wiley and Sons, Inc., New York, 1962); L. Fonda and G. C. Ghirardi, *Symmetry Principles in Quantum Physics* (Marcel Dekker, Inc., New York, 1970).
8. H. A. Bethe, Ann. Phys. (Leipzig) 5, 325 (1930).
9. T. F. Gallagher, L. M. Humphrey, W. E. Cooke, R. M. Hill, and S. A. Edelstein, Phys. Rev. A16, 1098 (1977).
10. B. L. Henke, J. A. Smith, and D. T. Attwood, J. Appl. Phys. 48, 1852 (1977).
11. B. L. Henke, J. A. Smith, and D. T. Attwood, Appl. Phys. Lett. 29, 539 (1976).
12. R. H. Day, P. Lee, T. L. Elsberry, E. B. Saloman, and D. J. Nagel, Los Alamos Scientific Laboratory, unpublished data, 1978.
13. D. T. Attwood and L. W. Coleman, Lawrence Livermore Laboratory report UCRL-78422 (July 21, 1976).
14. P. Woiskoboinikow, W. J. Mulligan, H. C. Pradaude, and D. R. Cohn, Appl. Phys. Lett. 32, 527 (1978).
15. B. Yaakobi, T. C. Bristow, and A. Hauer, Opt. Commun. 14, 336 (1975).
16. A. J. Lieber, R. F. Benjamin, H. D. Sutphin, and G. H. McCall, Proc. 11th Congress of High Speed Photography, Imperial College, London (1974).
17. D. B. van Hulsteyn and R. F. Benjamin, Opt. Lett. 1, 76 (1977).
18. M. H. Key, R. G. Evans, D. J. Nichols, F. O'Neill, P. T. Rumsby, I. N. Ross, W. T. Tones, P. R. Williams, M. S. White, C. L. S. Lewis, J. G. Lunney, A. Moore, J. M. Ward, D. Brown, P. Carter, T. A. Hall, T. P. Hughes, P. Salter, E. Frabrikesi, A. Raven, J. Murdoch, J. Kilkenney, Rutherford Laboratory, Central Laser Facility report LD/78/01 (February 1978).
19. V. W. Slivinsky, G. R. Leipelt, and J. D. Eckels, Bull. Am. Phys. Soc. 22, 1112 (1977).
20. C. M. Dozier, D. J. Nagel, L. S. Birks, J. Phys. E. 10, 1183 (1977).
21. L. von Hamos, Ark. Mat. Astron. Fys. 31A, No. 25 (1945).
22. D. J. Nagel, Naval Research Laboratory, Washington, DC (private communication, 1978).
23. R. D. Bleach and D. J. Nagel, J. Appl. Phys. (to be published).
24. M. M. Mueller, "Geometrical Single-Aperture Imaging and Wide-Aperture Deconvolution," Los Alamos Scientific Laboratory internal report (June 1978).
25. E. Stark and F. Skoberne, "Laser Fusion Program at LASL, July 1—September 30, 1976," Los Alamos Scientific Laboratory report LA-6616-PR (May 1977).

VIII. APPLICATIONS OF LASER FUSION—FEASIBILITY AND SYSTEMS STUDIES

L. A. Booth and T. G. Frank

Our feasibility and systems studies are being performed to analyze the technical feasibility and economic aspects of various commercial and military applications of lasers and laser fusion. Commercial applications include electric power generation, fissile fuel production from fusion-fission hybrid reactors, and production of synthetic fuels such as hydrogen. Methods of increasing CO₂ laser efficiency by multipulse energy extraction are part of our laser systems studies. The general objectives of these studies are: the conceptualization and preliminary engineering assessment of laser fusion reactors and other energy production subsystems; the development of computer models of integrated plant systems for economic and technology tradeoff and comparison studies; and the identification of problems requiring long-term development efforts. Emphasis in military applications studies is placed on relatively near-term contributions to nuclear weapon technology.

LASER FUSION REACTOR AND GENERATING STATION STUDIES

New Plasma Model for Cavity Wall Protection with Magnetic Deflection (I. O. Bohachevsky and J. C. Goldstein)

General. In the magnetically protected ICF reactor cavity design,¹ shown in Fig. VIII-1, an axial magnetic field (of ~1 to 2 kG) deflects the charged particles generated by the fuel-pellet microexplosion away from the cylindrical wall into specially engineered conical energy sinks. However, the magnetic field does not protect the wall from x rays, and the highly energetic ions may erode the energy sinks unacceptably fast.² Therefore, R. Conn and collaborators³ suggested using, inside the cavity, a high-atomic-number buffer gas that would absorb the x rays and dissipate a significant amount of ion kinetic energy.

A gas atmosphere in the reactor cavity is admissible because both the implosion and the burn of ICF fuel pellets are independent of initial cavity condi-

tions; these are limited only by the requirements of laser-beam transmission, pellet trajectory consistency, and restoration of ambient conditions between pellet microexplosions for repetitive operation. To assess the feasibility of gaseous wall protection, it is necessary to investigate the conditions that develop inside gas-filled and magnetically protected ICF reactor cavities following fuel pellet microexplosions. These studies require a plasma model that includes and adequately represents all phenomena of interest. In this section we will describe such a model constructed for ICF reactor cavity studies.

In this report we will

- estimate conditions inside gas filled reactor cavities and determine representative values of characteristic parameters,
- indicate assumptions and approximations consistent and compatible with the relative magnitudes of these parameters,
- present the equations derived on the basis of these assumptions and approximations, and
- outline briefly the approach adopted to obtain solutions of these equations.

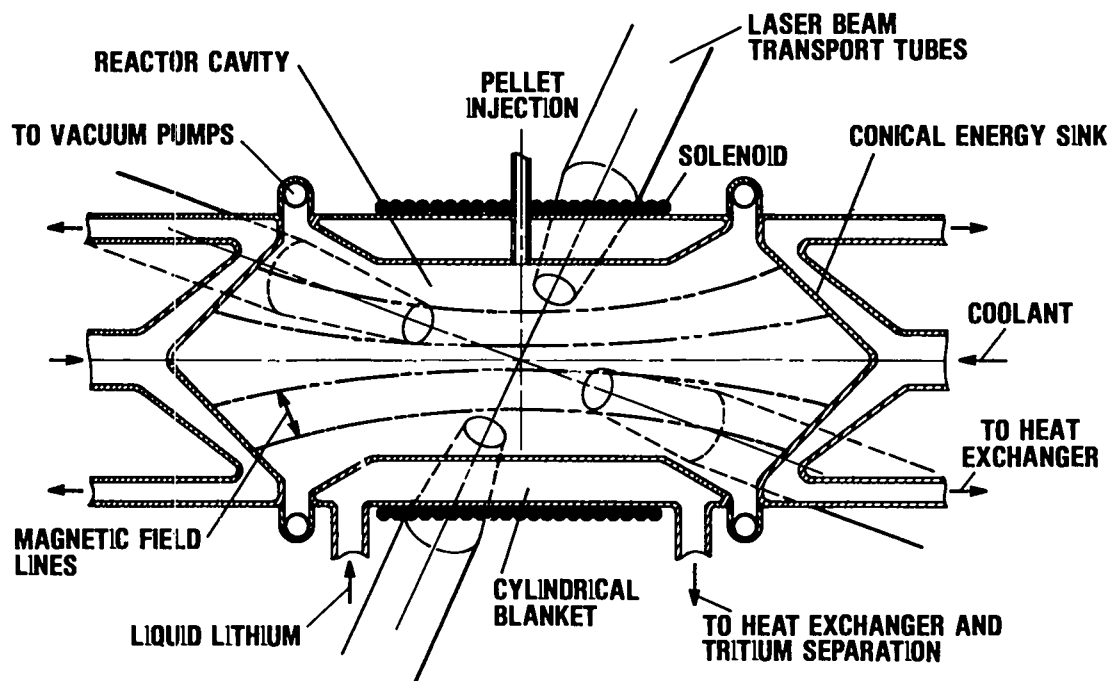


Fig. VIII-1.
Magnetically protected reactor cavity design.

Discussion

Ambient Cavity Conditions. Laser-beam transmission requirements impose an upper limit on buffer-gas density which, at present, is not known precisely,⁴ but which is expected to be in the neighborhood of 10^{15} or 10^{16} atoms/cm³. A representative volume of ICF reactor cavities (sphere with 5 m radius) is 3.75×10^9 cm³; the total number of atoms in such a cavity will be between 3.75×10^{25} and 3.75×10^{26} . Therefore, a nominal fuel-pellet microexplosion energy release of 375 MJ, of which a representative 1% fraction may be in x rays, will provide from 62.5 eV (at 10^{15} atoms/cm³) to 6.25 eV (at 10^{16} atoms/cm³) of radiation energy per atom. To be effective, the buffer gas must absorb a significant fraction of this energy and, consequently, will become ionized to a degree that will make it a perfectly conducting plasma.

The pressure in the buffer medium following total absorption of x rays may reach 10^4 Pa (0.1 atm). If, in addition to the absorption of x-ray energy, the buffer medium totally thermalizes the pellet debris ions containing ~20% of the thermonuclear energy yield, then the total cavity pressure (energy/cavity

volume) will rise to 2×10^6 Pa (2 atm). This value is 20 times the pressure generated by the x-ray energy deposition, as it should be because the pellet debris contains 20 times the x-ray energy.

At the above conditions, the cross sections, σ , for collisions between cavity medium particles are $\sim 10^{-16}$ cm²,^{5,6} consequently, the mean free path, λ , ($\lambda \approx 1/\pi n\sigma$) is between 3.0×10^{-1} and 0.3×10^{-1} cm. These estimates show that phenomena with characteristic lengths of 1 m or more can be modeled with a continuum description of the background medium.

The microexplosion-generated debris ions, however, behave differently. Calculations based on the Lindhard stopping theory show that, for example, at the neon density of 1.5×10^{16} atoms/cm³ (the upper limit of allowable densities) the mean debris-ion range is between 2 and 5 m.⁸ Ion ranges of that magnitude are comparable to the cavity radii considered in our ICF reactor designs and are much larger than the mean free paths of the background medium. Therefore, ion motion cannot be approximated within the framework of a continuum model, but must be determined from kinetic theory which,

in our model, is reduced to the determination of trajectories for a statistical sample (5000 to 25 000) of ions.

The Plasma Model. Consistent with the estimates presented above, our plasma model for the analysis of cavity phenomena consists of three parts: a continuum buffer medium, a collection of discrete high-energy ions, and an electromagnetic field. The single-component background medium is initially ionized by the flash of x rays emitted from the burning DT fuel pellet to a degree that makes it a perfectly conducting plasma. Therefore, its behavior is described by the Lundquist equations supplemented with an appropriate equation of state and a rate equation that determines changes in the degree of ionization.

The motion of fuel-pellet debris ions is obtained with statistical modeling (PIC) including a rate equation to determine the average ion charge. Sample ion trajectories are calculated by integrating the equation of motion for each simulation ion with the Lorentz force providing the acceleration. The model also includes phenomenological terms that describe momentum and energy transfer between the continuum medium and the discrete ions, but their form has not yet been determined.

Currently, the motions of the background fluid and of the ions are coupled only through the electromagnetic field described by Maxwell's equations in which the displacement current has been neglected. Ohm's law is replaced with postulates that the electric field is always and everywhere perpendicular to the magnetic field, that local charge neutrality prevails, and that the electrons have no mass, but drift in the direction perpendicular to electric and magnetic fields without time lag. Thus, the model constitutes a significant generalization and extension of considerations introduced by Dickman, Morse, and Nielson⁷ and developed further by Goldstein and coworkers.⁸

To be specific, we now present the differential equations and the supplementary relations corresponding to the above-described plasma model. For conciseness we employ vector representation and write the differential equations in conservation form to facilitate future discussion of finite-difference approximation. In our notation convention the operator acts on all factors that follow it.

For the background medium, the equations expressing conservation of mass, momentum, and energy are

$$\frac{\partial \rho}{\partial t} + \nabla \cdot (\rho \mathbf{u}) = 0, \quad (\text{VIII-1})$$

$$\frac{\partial}{\partial t} (\rho \mathbf{u}) + (\nabla \cdot \mathbf{u}) (\rho \mathbf{u}) + \nabla p + \frac{1}{c} \mathbf{B} \times (\mathbf{J} - \mathbf{J}_I) + \Gamma_B = 0, \quad (\text{VIII-2})$$

$$\begin{aligned} \frac{\partial}{\partial t} \left[\rho \left(\frac{1}{2} |\mathbf{u}|^2 + \epsilon \right) \right] + (\nabla \cdot \mathbf{u}) \left[\rho \left(\frac{1}{2} |\mathbf{u}|^2 + \epsilon \right) + p \right] \\ = \mathbf{E} \cdot (\mathbf{J} - \mathbf{J}_I) + S_B, \end{aligned} \quad (\text{VIII-3})$$

and the equation expressing the change in the ionization fraction, α , is

$$\frac{\partial \alpha}{\partial t} = F_1(\rho, T). \quad (\text{VIII-4})$$

In the above equations ρ is the mass density, \mathbf{u} the velocity vector, p the pressure, c the speed of light in vacuum, \mathbf{B} the magnetic-field vector, \mathbf{J} the total-current vector, \mathbf{J}_I the current carried by the debris ions, ϵ the internal energy, \mathbf{E} the electric-field vector, and T the temperature. The symbol ∇ denotes, as usual, the gradient operator and $|\mathbf{u}|$ the magnitude of the vector \mathbf{u} . The terms Γ_B and S_B , when determined, will represent collisional momentum and energy interchange between the background fluid and the debris ions.

The trajectories of the debris ions are determined^{7,8} by integrating the equations of motion,

$$m_i \frac{d\mathbf{v}_i}{dt} = q_i \left(\mathbf{E} - \frac{1}{c} \mathbf{B} \times \mathbf{v}_i \right) - \Gamma_I, \quad (\text{VIII-5})$$

where m_i , \mathbf{v}_i , and q_i are the mass, the velocity vector, and charge of the i^{th} ion and Γ_I is the collisional drag force exerted by the background medium on the ion. In practice Eq. (VIII-5) is integrated for simulation particles, which consist of many ions of a given element; a typical calculation may contain any number

between 5000 and 25 000 simulation particles. The charge of the simulation particle will change according to

$$\frac{dq_i}{dt} = F_2(\rho, T, m_i), \quad (\text{VIII-6})$$

where F_2 is the as-yet undetermined recombination rate for each ion material.

The electromagnetic field is governed by Maxwell's equations which, with the previously indicated approximations, reduce to

$$\frac{\partial \mathbf{B}}{\partial t} = -c \nabla \cdot \mathbf{E} \quad (\text{VIII-7})$$

$$\mathbf{J} = \frac{c}{4\pi} \nabla \cdot \mathbf{B}. \quad (\text{VIII-8})$$

Equations (VIII-1) through (-8) clearly do not form a closed system and therefore must be supplemented with auxiliary relations among different physical quantities. These are of two kinds: those relating the thermodynamic variables T , p , ϵ , and ρ (known as equation of state) and those relating the current density \mathbf{J} and the electric field \mathbf{E} (known as Ohm's Law).

The thermodynamic variables are related by

$$T = \frac{m(\gamma - 1)}{(N_A \rho + nm)K_B} \rho \epsilon \quad (\text{VIII-9})$$

$$p = \left(\frac{N_A \rho}{m} + n \right) K_B T, \quad (\text{VIII-10})$$

where m and Z are the atomic mass and atomic number of the background fluid, γ is the ratio of specific heats (assumed constant), N_A is Avogadro's number, K_B the Boltzmann constant, and n the electron density.

Consistent with the previously stated hypothesis about the behavior of the electrons (where e is the electronic charge), the expression for the current density \mathbf{J} is

$$\mathbf{J} = \mathbf{J}_I + \frac{N_A c}{m} Z \alpha \rho \mathbf{u} - nec \frac{\mathbf{E} \cdot \mathbf{B}}{|\mathbf{B}|^2}, \quad (\text{VIII-11})$$

where the debris-ion current density, \mathbf{J}_I , is given simply by

$$\mathbf{J}_I = \sum_{\text{VOLUME}}^{\text{UNIT}} q_i \mathbf{v}_i, \quad (\text{VIII-12})$$

and, from the assumption of charge neutrality, the electron density, n , is

$$n = \frac{1}{e} \sum_{\text{VOLUME}}^{\text{UNIT}} q_i + \frac{N_A \rho}{m} Z \alpha. \quad (\text{VIII-13})$$

The relation between current density and electric field (Ohm's Law) may be solved for the electric field \mathbf{E} ; using the postulated orthogonality of the electric and magnetic fields the resulting expression is

$$\mathbf{E} = \frac{\mathbf{B}}{nec} \cdot \left(\mathbf{J}_I + \frac{N_A c}{m} Z \alpha \rho \mathbf{u} - \mathbf{J} \right). \quad (\text{VIII-14})$$

Equations (VIII-1) through (-14) constitute a closed self-consistent system, which is our plasma model.

Modeling of ICF Reactor Cavity Phenomena.

The modeling of events and conditions inside ICF reactor cavities after a fuel-pellet microexplosion requires the solution of an initial value problem for the above presented set of equations inside a cylindrical symmetric region bounded by rigid electrically conducting walls. Therefore, the boundary conditions are: vanishing of the tangential component of the electric field and of the normal component of the mass velocity and continuity of the tangential component of the magnetic field. Because the events following a pellet microexplosion occur in times that are short in comparison to the characteristic time for the magnetic diffusivity in the wall material, it is appropriate to require that the magnetic field at the boundary does not change.

The plasma model described here does not contain viscosity and heat-conductivity effects; therefore, the above-stated boundary conditions are the only

requirements imposed by the physical considerations. However, to make the initial boundary value problem numerically well-posed, one must specify the boundary conditions for all primary variables, i.e., those determined from integrations of partial differential equations. To obtain these additional conditions we anticipate that the cavity phenomena will consist predominantly of wave reflections and postulate that the reflections will be nearly normal. Therefore, the reflection conditions, i.e., vanishing of the normal derivative at the boundary should be approximately valid for the remaining variables, i.e., pressure, density, and the tangential component of velocity.

Solutions describing the plasma behavior in reactor cavities will be obtained numerically. Toward this end, differential equations, Eqs. (VIII-1) through (-4) and Eq. (VIII-7), will be approximated with finite differences using the Lax-Friedrichs scheme introduced by Lax⁹ and employed effectively by Bohachevsky and his collaborators^{10,11,12} to calculate multidimensional time-dependent flows with shock waves.

After initialization, the variables will be advanced in discrete time steps in the following order:

1. the background fluid variables using finite-difference analogues of Eqs. (VIII-1) through (-4);
2. the pressure and temperature, using Relations (VIII-9) and (-10);
3. the current density, with Eq. (VIII-8);
4. the electric field, using Expression (VIII-14) with the above-determined value of current density;
5. the magnetic field B , with Eq. (VIII-7), using the above value of the electric field; and
6. the velocities, positions, and charges of the debris ions, using now-available values of electric and magnetic fields.

The capacity and speed of the CRAY-1 computer being used to calculate the solutions will allow future investigations of parametric dependencies. Availability of such results will greatly facilitate ICF reactor design studies.

Laser Fusion Pellet Injection Accuracies, Accelerations, and Deflections (J. J. Devaney, L. A. Booth)

The deuterium-tritium fuel for laser fusion reactors is encapsulated in pellets that are injected into a

reactor cavity where they are imploded by short-pulse laser beams that interact with pellet constituents. Assessments have been made for fuel pellets, by means of representative calculations, of the positional accuracy required, the accelerations that are permissible, and the perturbing effects on the pellet trajectory of residual gas motion.

A representative pellet was used in this study. The energy release per microexplosion is 300 MJ. The reactor chamber assumed is a 5-m-diam cylinder 10-m long with ports in the ends of the cylinder. Chamber gases considered include argon and lithium at particle densities ranging from vacuum to $10^{17}/\text{cm}^3$. The chamber temperature was assumed to be 773 K.

Based on the results of detailed analyses for our 100-kJ CO_2 laser, Antares, it is estimated that positional inaccuracies of up to 300 μm can be tolerated for 1-mm-diam targets while limiting beam energy losses to less than 4%. This permissible error must be apportioned among the pellet location error and the laser pointing errors.

Typical pellet structures can stand accelerations (or decelerations) of 6000 g's or greater. Calculations of accelerations due to pneumatic injection through a 100-cm-long pellet gun powered by hydrogen at 1-atm pressure indicate maximum accelerations well within the above limit. Pellet drag was estimated assuming pellet injection into either lithium or argon at a particle density of $10^{17}/\text{cm}^3$. The drag forces on the pellet proved to be negligible compared to those of acceleration.

The effects of residual gas motion in the cavity due to pellet microexplosions on successive pellet trajectories were evaluated both for the case of a pellet expanding into a vacuum and for a pellet expanding in a gas with a particle density of $10^{17}/\text{cm}^3$. For the case of a microexplosion in vacuum, the motion of the expanding pellet debris was calculated using detailed computer codes. The spherical expansion is converted by the cylindrical cavity walls into a bifurcated plane expansion. The slab theory developed by F. J. Dyson¹⁸ applies. The pellet debris that reflects off the cylindrical walls forms, by combining with oncoming gas, a combined flow similar to a Mach stem in blast theory and contributes to the down-axis flow. The spherical expansion was matched to plane flow on the axis of the cylindrical cavity by matching equal volumes and equal on-axis gas fronts, including frontal on-axis velocities. Gas

densities and velocities were then computed at the times of subsequent pellet injections corresponding to microexplosion repetition rates of 1 and 10/s. In each case the transverse drag forces on injected pellets are negligible.

For the case where a background gas is present in the chamber, a pellet microexplosion will produce a spherical blast wave that the cylindrical walls convert into two (roughly) plane waves that alternately reflect from the ends and from each other at the center repeatedly, being damped by pressure and matter loss at the ends. It was found that the fundamental acoustic mode dominates after the first end reflection. The method of analysis consisted of using the self-similar solutions of Sedov¹⁴ describing the expansion of a spherical blast wave that was then reflected off the cylinder to form, with the resulting Mach stems, a plane blast wave. The parameters of the plane blast wave were matched along the axis with the original spherical blast wave, as described above for the case of a microexplosion occurring in a vacuum. The plane blast wave was propagated to the ends of the cylinder and a detailed computer code was used to reflect the blast wave from the ends to form the fundamental acoustic mode of the chamber. The dynamics of the damped acoustic wave were followed until insertion of the next pellet. The background gas considered was argon at a particle density of $10^{17}/\text{cm}^3$. At microexplosion repetition rates of 1/s, the gas motion is damped sufficiently between microexplosions to permit slow pellet insertion (450 cm/s) and large differences (0.5 cm) in successive points of pellet location for laser illumination. For microexplosion repetition rates of 10/s, pellet injection at peak ringing pressure, and with a slow injection velocity (450 cm/s), pellet deflections of as much as 100 μm may occur, but correction of any of these parameters leads to at least an-order-of-magnitude decrease in the deflection.

The Lithium Boiler: a 1500 to 2000 K Fusion Reactor Breeding Blanket and Primary Heat Transport System Concept (J. H. Pendergrass)

General. Operation of fusion reactor blankets at temperatures higher than those at which "conventional" fusion or fission reactors deliver thermal energy may be attractive for several reasons:

- higher efficiencies for conversion of thermal energy to electric power, with associated reductions in thermal pollution and potential reductions in electric power generation costs, can be achieved;
- power cycles, e.g., thermionics, gas turbines, and magnetohydrodynamics, which cannot effectively couple with lower temperature heat sources, can be used efficiently for electric power production, especially as topping cycles;
- greater efficiencies for conversion of thermal energy to stored chemical energy of synthetic fuels, e.g., hydrogen, carbon monoxide, or methane, produced by thermochemical cycles or electrolysis can be attained;
- synthetic-fuel production processes requiring higher temperature heat sources, e.g., two-step thermochemical cycles, high-temperature electrolysis, or direct decomposition of carbon dioxide, become feasible; and
- fusion reactors can supply thermal energy for industrial processes, e.g., coal gasification, steel making, and ammonia production, which presently consume fossil fuels for lack of high-temperature nuclear heat sources.

"Conventional" fusion reactor concepts, including recent concepts investigated here and elsewhere for high-temperature thermal-energy generation for electrolytic and thermochemical hydrogen production by water splitting, employ either:

- relatively low-temperature (<1000 K) blankets containing pure liquid lithium, or liquid lithium-containing alloys (e.g., lithium-lead), or solid (e.g., lithium oxide), or liquid lithium-bearing compounds (e.g., "flibe," F_2LiBe) for both tritium breeding and conversion of neutron kinetic and capture energy, which constitute $\sim 80\%$ of total fusion reactor energy release, to heat, or
- relatively low-temperature lithium-containing blanket regions or modules (possibly also containing neutron multiplying materials such as lead or beryllium for tritium breeding) and solid, high-temperature blanket regions for conversion of neutron energy to heat (plus perhaps additional tritium breeding at a ratio less than one if lithium-bearing substances, e.g., lithium meta-aluminate are included).

A blanket concept, which involves conversion of neutron thermal energy in a refractory blanket, e.g.,

graphite, with no breeding capability and with energy transport by thermal radiation across a vacuum to process heat tubes, has also been proposed.¹⁸

Examples of laser fusion reactor concepts that fall into the first category include the LASL wetted-wall¹⁶ and magnetically protected-wall¹⁷ concepts, the LLL lithium-fall concept,¹⁸ and the University of Wisconsin SOLASE concept.¹⁹ Most magnetic-confinement fusion reactor concepts also fall into this category. Included in the second category are confinement-independent and magnetic-confinement-fusion process-heat blanket concepts developed recently at LASL²⁰ and at Brookhaven National Laboratory.²¹

In reactor concepts of the second type, a substantial fraction ($\geq 50\%$) of the neutron kinetic energy is deposited in the breeding regions or modules as relatively low-temperature heat. Recovery of the $\sim 20\%$ of the total thermal energy output of a fusion reactor resulting from energy deposition by x rays and thermonuclear reaction debris in cavity first walls as low-temperature heat means that considerably less than 50% of the total reactor thermal energy output will be delivered as high-temperature heat. This fact implies, insofar as thermochemical hydrogen production is concerned, that synthetic-fuel plants that produce hydrogen solely by such methods will be net electric power exporters if economically viable, low-temperature thermochemical cycles cannot be developed. The prospects for developing such cycles are not promising. Thus, synthetic-fuel plants that use "conventional" fusion reactor blankets must generate and use electricity for synthetic-fuel production, e.g., by electrolysis, if net electric power export is to be avoided.

For economic and/or technical reasons electric power cannot presently be substituted for fossil fuels in many applications. If substantial portions of present fossil-fuel usage, e.g., as transportable fuels for transportation, space heating, and process heat, are to be replaced by synthetic fuels produced with fusion reactors as thermal energy sources, the present energy consumption pattern in the United States (only $\sim 24\%$ used as electric power)²² suggests that electric power export from fusion-driven synthetic-fuel plants is not desirable.

There appear to be no lithium-containing materials that would give tritium breeding ratios of

at least 1.0 through neutron capture in such materials alone and yet remain solid at temperatures approaching 2000 K. Corrosion problems make molten lithium-containing salts for high-temperature breeding unpromising. Although breeding ratios significantly higher than 1.0 appear attainable in several "conventional" fusion reactor concepts, and although fusion reactors with high breeding ratios could support reactors with breeding ratios less than 1.0, shipment of massive amounts of tritium from one plant site to another may be prohibited by regulatory agencies. Therefore, the requirement that each plant site be self-sufficient in tritium production may be imposed both for safety reasons and as a ground rule for conceptual reactor design has been tentatively adopted. Furthermore, the cost penalty associated with maximizing tritium breeding ratios in supporting reactors may exceed the tritium fuel cycle costs resulting from requiring all commercial fusion reactors to operate with self-sufficient tritium fuel cycles, and more than one supporting reactor would be required for each supported reactor.

Thus, conventional fusion reactor process-heat blanket concepts involve tradeoffs between high tritium breeding ratios and conversion of most of fusion neutron-associated energy into high-temperature thermal energy. In contrast, the lithium-boiler fusion-reactor breeding blanket and primary-heat-transport system concept described below permits simultaneous achievement of tritium breeding ratios of 1.0 or greater and conversion of all but a small fraction of the neutron-associated energy into ~ 1500 to 2000 K heat. The concept appears applicable to magnetic-confinement as well as to inertial-confinement fusion.

The Lithium Boiler Concept. Two basic alternative lithium boiler concepts are illustrated schematically in Figs. VIII-2 and VIII-3. Many variations on these basic themes are possible.

In both basic alternatives, ~ 14 -MeV fusion-born neutrons, which are relatively highly penetrating, give up only a modest fraction of their kinetic energy in passing through cavity walls of moderate thicknesses, and only a small fraction of the neutrons is absorbed by nuclear interactions in first-wall structure. Most of the fusion neutron kinetic and capture energy is deposited in a liquid lithium blanket, which is maintained at its boiling point at

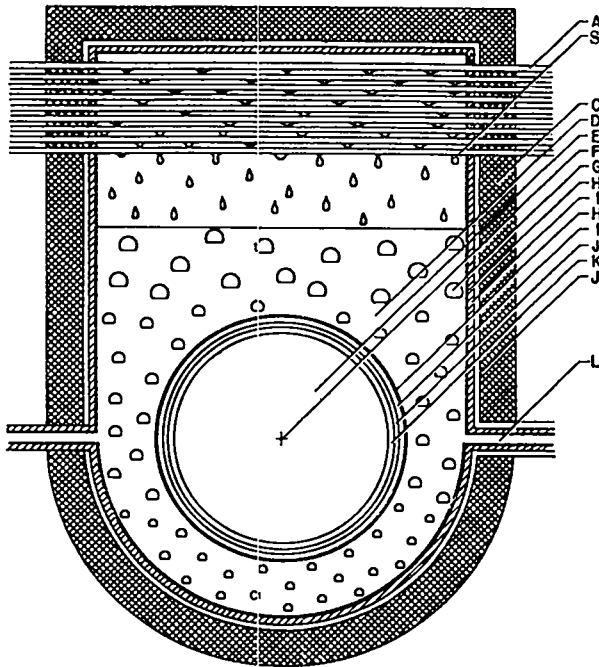


Fig. VIII-2.

Lithium-boiler pressure-vessel concept. A, process or power-cycle heat-exchanger tubes with tritium escape barrier and/or tritium recovery system; B, refluxing liquid lithium; C, shielding other reactor structure, and/or reactor subsystems; D, liquid lithium blanket at 1500 to 2000 K, 0.4 to 15 atm; E, reactor cavity; F, fusion energy source; G, lithium vapor bubble; H, liquid-lithium-resistant refractory-metal layer (e.g., a gettered molybdenum alloy such as TZM); I, structural wall (e.g., a ceramic at temperature, graphite at temperature, or a cooled-metal wall); J, thermal insulation (e.g., evacuated multiple metal foils, graphite cloth, or conventional high-temperature insulation); K, cavity first wall; L, duct to lithium purification and tritium recovery (if required) subsystem.

the operating pressure selected for the blanket, and which is sufficiently thick, ~ 1 m, to permit capture of all but a very small fraction of the fusion-born neutrons. The neutron-energy deposition in the blanket is highly nonuniform, but the high thermal conductivity of liquid lithium and vigorous boiling efficiently promote temperature uniformity within

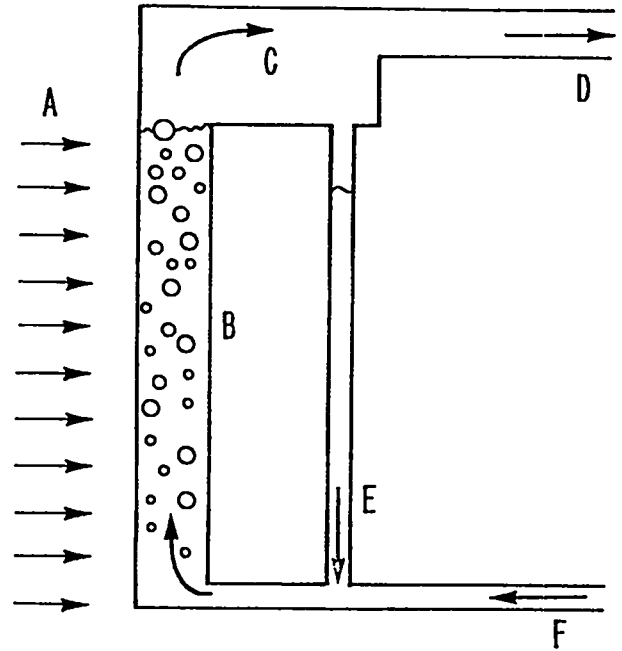


Fig. VIII-3.

Lithium-boiler pressure-tube blanket concept. A, fusion energy source; B, lithium two-phase mixture in pressure tubes; C, vapor-liquid disengagement region; D, saturated lithium vapor to process- or power-cycle heat-exchanger tubes; E, disengaged liquid lithium recycle; F, saturated or subcooled condensed liquid-lithium.

the blanket. The neutron-derived energy is rapidly converted into latent heat of vaporization of lithium, which means that the effective thermal capacity of the blanket is very large, and the boiling causes rapid mixing. Transport of lithium vapor to, and its condensation on, power-cycle or process-heat exchanger surfaces constitutes the primary heat-transport mechanism for the blanket. Condensed lithium can either be returned directly to the blanket in a saturated condition or further heat can be extracted by subcooling before recirculating the lithium to the blanket vessel. Subcooled liquid lithium could be used for cooling reactor structure if necessary or desirable.

Virtually all the first-wall protection schemes that do not call for thick molten lithium layers inside the cavity, but use, e.g., a thin lithium film, magnetic fields, replaceable sacrificial liners, and residual

cavity atmospheres, can be used. The energy carried by x rays and energetic fusion plasma ions (and pellet debris in the case of inertial confinement fusion), only ~20% of the total energy released in fusion reactions, apparently must be converted to relatively low-temperature thermal energy and removed from first-wall structure. Current estimates of recirculating electric power fractions required for fusion plant operation are ~20 to 30%, so that all the lower-temperature thermal energy derived from x-ray and ion energy deposition can be used for generation of recirculating power in fusion plants designed solely as process-heat sources.

Some advantages offered by the lithium boiler concept are summarized as follows:

- thermal energy is delivered at substantially higher temperatures, 1500 to 2000 K, than can be achieved by "conventional" fusion or fission reactor concepts, and thermal-energy delivery characteristics are well-matched to recirculating-power and process-heat-application requirements;
- breeding ratios greater than or equal to 1.0 are readily attained if only modest volume fractions of structural materials are interposed between the neutron source and the boiling lithium;¹⁶
- neutron energy losses to first walls of moderate thicknesses and other reactor structure can be limited to a small fraction of the total neutron-associated energy liberation;¹⁶
- blanket heat-transport mechanisms (boiling, vapor flow, and condensation) are efficient and require no mechanical pumping of hot fluids;
- thermal-energy delivery is essentially isothermal, being primarily in the form of latent heat of condensation ($\Delta H_v \sim 30$ kcal/g-at vs $C_p \sim 9$ cal/g-at K for the liquid) even with substantial subcooling of condensed lithium, and at maximum temperature so that many load-line restrictions are avoided;
- the reactor blanket and application can either be closely coupled, while still providing for isolation of process- or power-cycle streams from the neutron environment, or they can be separated by considerable distances and/or by intermediate coolant loops;
- lithium vapor pressures, which, together with hydrostatic heads ($\rho \sim 0.5$ g/cm³ for liquid lithium), determine blanket containment pres-

ures, are low, ranging from ~0.4 atm at 1500 K to ~15 atm at 2000 K;

- vapor bubbles and the free-lithium surface minimize static pressure rise and shock-wave overpressures due to rapid, nonuniform neutron-energy deposition in blanket lithium (a bubble void volume of ~1% at the outer wall seems sufficient to reduce stresses to negligible proportions);²⁸
- mechanical pumping losses resulting from pumping of electrically conductive liquid lithium across magnetic field lines, a serious consideration in magnetic-confinement fusion applications of liquid lithium as a tritium-breeding-blanket primary coolant material, are avoided;
- bred-tritium recovery methods, e.g., high-temperature distillation and tritium windows, not presently considered attractive by many investigators for lower temperature blanket concepts may become attractive, while all the lower temperature recovery methods can still be used;
- mechanical simplicity and lack of most geometric constraints;
- virtual independence of power-cycle or process-heat applications characteristics and of first-wall protection schemes characteristics, and
- boiling promotes blanket temperature uniformity, thereby minimizing the transport of materials of construction due to thermal gradients in the liquid lithium.

Additional advantages of the alternative pressure-tube concept illustrated in Fig. VIII-3 may include:

- elimination of leaks by tube-plugging and bypassing, or tube replacement, and
- lowered materials-strength requirements.

Disadvantages of the pressure tube concept relative to the concept illustrated in Fig. VIII-2 may include:

- increased neutron/structure interaction with attendant increased potential for activation, structural damage, and degradation of temperature level of a portion of the neutron-derived thermal energy, and
- greater complexity.

The most significant problems that must be addressed successfully to ensure the technological feasibility for the lithium boiler concept appear to be:

- identification of suitable materials of construction and development of appropriate component manufacturing and testing methods, and
- development of adequate engineered barriers to tritium escape through heat-transfer surfaces to the biosphere.

Materials that could contain lithium at temperatures approaching 2000 K at modest, i.e., up to ~15 atm pressures, do appear to exist. For example, TZM (~0.5% Ti, ~0.08% Zr, balance Mo) was not attacked detectably by lithium in 1000-h reflux experiments at ~1923 K.²⁴ Several ceramic materials, e.g., silicon nitride, silicon carbide, and sialon (silicon nitride and aluminum oxide), currently under development for commercial process-industry applications²⁵ and for construction of high-temperature gas-turbine blades,²⁶ possess strengths adequate for containment of lithium at such pressures and temperatures. Glass-ceramics²⁷ and graphites also possess adequate strengths under such conditions and may offer ease of manufacturing, as well as advantages such as low neutron activation and radiation-damage resistance. Because even refractory-metal alloys creep excessively at temperatures approaching 2000 K, ceramics coated with thin (a few mils) layers of molybdenum have been used for construction of heat pipes using lithium as a working fluid at such temperatures.²⁷ The heat pipe studies also addressed certain sealing problems successfully. Heat-exchanger design and materials of construction would depend in part on process-heat or power-cycle stream characteristics. A detailed conceptual mechanical design of a lithium boiler blanket compatible with the electrothermochemical cycles described elsewhere in this report will be developed in the near future.

Preliminary calculations indicate that tritium escape to the biosphere by permeation through primary heat-transfer surfaces into process-heat or power-cycle streams can be controlled by interposing vacuum spaces or spaces filled with a circulating fluid, e.g., low-pressure helium, between inner and outer heat-exchanger tubes. In the first instance heat transfer would be accomplished solely by thermal radiation across the vacuum space and tritium would be removed by pumping. Thermal-radiation heat fluxes (of the order of a few tenths of MW/m²) between surfaces at ~1800 to 2000 K and ~1500 to 1700 K are probably adequately high for most power-cycle and process-heat applications. In the se-

cond case, tritium would be converted to tritiated water, carried away by the circulating fluid, and trapped by adsorption. Radiation heat-transfer fluxes would be of similar magnitudes as for the vacuum barrier case, but a conductive mechanism would also operate to increase heat-transfer rates. Ceramics typically exhibit relatively low tritium permeabilities and, if used in constructing heat-transfer surfaces, could contribute significantly to minimization of tritium migration. Detailed design of engineered barriers to tritium escape under lithium boiler concept conditions will be attempted to adequately assess their technical feasibility.

Control of the locations within the blanket at which boiling occurs may be important. However, we foresee little difficulty in providing such control. Very efficient thermal insulation between the first wall and the blanket will be necessary unless a first-wall concept permitting operation of the first wall at high temperatures can be developed. Multiple refractory-metal foils or layers of graphite cloth appear to have the necessary characteristics.

Closure. The many benefits that could be derived from the lithium boiler concept suggest that a thorough investigation of its technical and economic feasibility is warranted.

Sensitivity of Electric Power Production Costs to Pellet Yield (I. O. Bohachevsky, T. G. Frank, and J. F. Hafer)

General. Systems configurations and economic studies of laser fusion electric generating stations are being carried out with the aid of the computer program TROFAN, developed at LASL.^{28,29} Specifically, this program is used (a) to make comparisons of alternative fusion reactor concepts, (b) to evaluate different subsystems configurations, and (c) to investigate power plant sensitivities to design-parameter changes. The figure of merit in parametric comparison studies is the calculated cost of producing electric power.

It is essential that systems analysis codes for advanced technologies be continually updated to reflect advances in relevant research programs, in economic data, and in natural priorities. A number of such changes have been made in TROFAN

recently including new scaling laws for reactor structural components,³⁰ an improved model of CO₂ lasers, and some updating of cost data. A major revision of the entire economic data base is scheduled for FY 79 following the completion of a contract with an outside firm to provide the necessary information. Until this is accomplished, we will remain reticent to predict absolute power production costs. However, we feel that relative power production costs reveal correct trends, and we will therefore continue to use such results to guide us in plant optimization studies.

Some recent results of parametric studies of the sensitivity of electric power production costs to fusion pellet yield are presented in this section together with plausible explanations.

Electric Power Production Cost Sensitivity. Meaningful studies of the effects of large variations in a single parameter for a laser fusion electric generating station are difficult to perform unless the design is modularized. Otherwise, significant changes in one component operating characteristic cannot be compensated by changes in another and consequently some quantity such as the total plant capacity will not remain constant as intended during the study. The reactor concept for which the best parametric description exists and which satisfies the above requirement for modularization in large electric generating stations is the wetted-wall reactor.

The results of some recent TROFAN calculations of the effects on power production costs of pellet yield are shown in Figs. VIII-4, -5, and -6. The generating stations analyzed have nominal net power outputs of 1000 MWe and are based on the wetted-wall reactor concept. (Each plant contains the minimum number of reactors required to produce at least 1000 MWe.)

It is generally agreed that economically competitive ICF electric generating stations will only be possible if a driver-pellet performance, expressed as the product of driver efficiency and pellet gain, of at least 10 can be achieved. This has led proponents of various driver concepts to advocate combinations of either high-driver efficiency and modest pellet gain or low-driver efficiency and high pellet gain. Figure VIII-4 gives the per cent change in power production cost as a function of laser efficiency when the product of laser efficiency and pellet gain is held

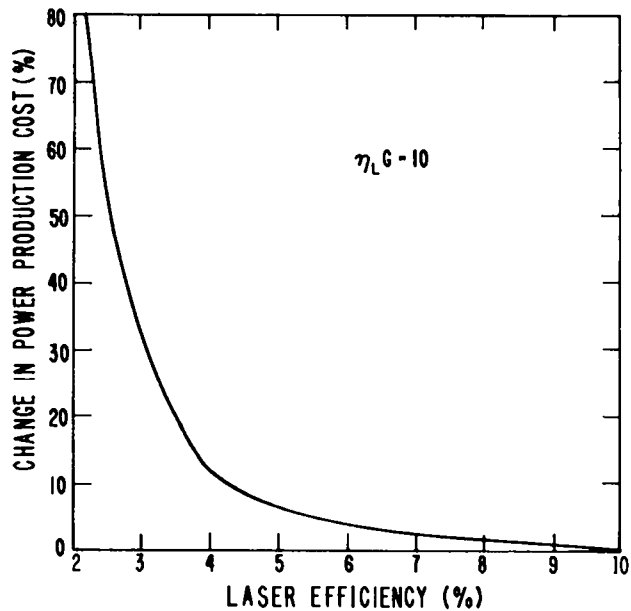


Fig. VIII-4.
Per cent change in power production cost vs laser efficiency (1000-MW electric generating station wetted wall reactor concept, $\eta_L G \approx 10$).

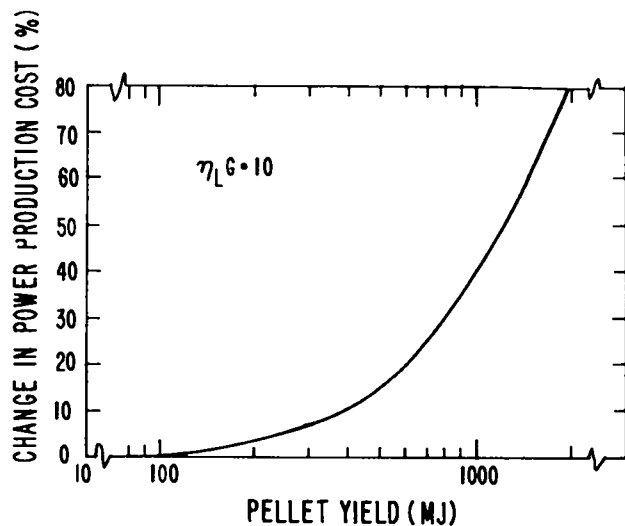


Fig. VIII-5.
Per cent change in power production cost vs pellet yield (1000-MW electric generating station wetted wall reactor concept, $\eta_L G \approx 10$).

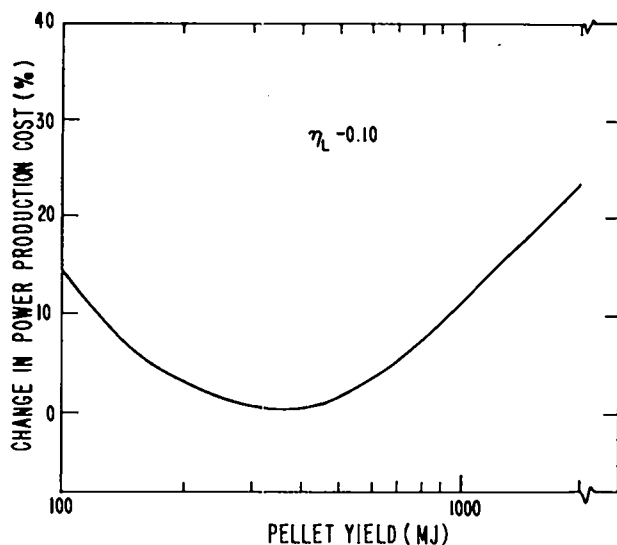


Fig. VIII-6.

Per cent change in power production cost vs pellet yield (1000-MW electric generating station wetted wall reactor concept, $\eta_L = 0.10$).

constant equal to 10. Laser efficiency considered ranges from 2 to 10 and pellet gain thus varies from 500 to 100. The relationship between laser energy incident on target and pellet gain used in these calculations is shown in Fig. VIII-7. This relationship together with the required pellet gain for a particular operating point determine the pellet yield that ranged from 1970 to 82 MJ. The results of Fig. VIII-4 are presented in Fig. VIII-5 as a function of pellet yield.

Figure VIII-6 shows the per cent change in power production cost as a function of pellet yield for 1000-MWe generating stations when the laser driver efficiency is held constant at 10%.

Scaling of Reactor Components. Changes in relative power costs for laser fusion generating stations do not always behave as would be predicted from simple economy-of-scale arguments. The reasons for unanticipated relative cost trends for certain ranges of pellet yield (see, e.g., Fig. VIII-6) are discussed below.

In the TROFAN model of the reactor vessel, cavity size is determined from the allowable wall-temperature increases, therefore, cavity radius is proportional to the square root of pellet yield.^{30,31}

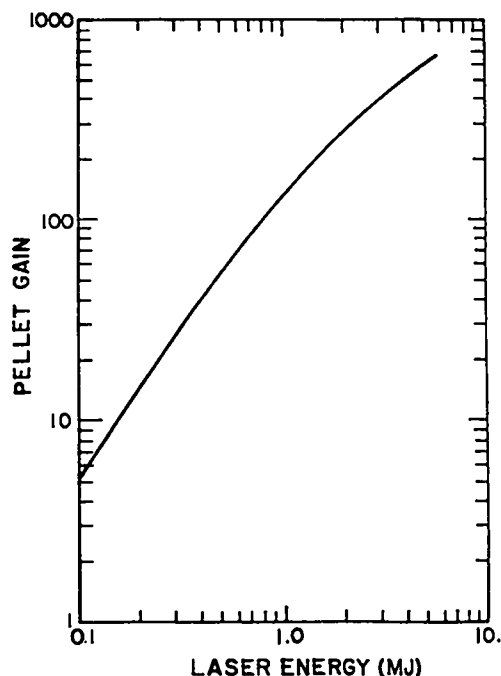


Fig. VIII-7.

Pellet gain as a function of incident laser energy.

Wall-thickness calculations based on the results of Ref. 30 show that, in the range of parameters of interest, thermal expansion of the blanket is the dominant load. For pellet yields below 5000 MJ, the failure mode of wetted-wall reactor structures, based on the fatigue stress limit, is buckling of the innermost structural shell. For impulsively applied loads, the results of Ref. 30 show that the wall thickness required to bear the load is proportional to the square root of the yield and is independent of radius.

The reactor-vessel cost algorithm in TROFAN is based on the premise that structural-vessel cost is proportional to the mass of material used in its construction. Vessel capital cost, therefore, is proportional to the volume of structural material, i.e., the product of the square of the radius and wall thicknesses. The scaling rules for cavity radius and wall thickness, derived above, indicate that the cost of the reactor vessel is proportional to the three-halves power of pellet yield, and thus the cost of the vessel per unit yield increases as the square root of pellet yield. Consequently, there is no economy of scale in reactor-vessel construction even when

fabrication and erection costs are disregarded (these costs usually increase faster than the size of the containment vessel).

Discussion. Laser fusion power production costs are dominated by the costs of capital. As illustrated by the scaling laws discussed above wetted-wall reactor vessel costs per unit of pellet yield (or unit of power production) increases with pellet yield. This trend is opposed by power plant components that decrease in cost per unit of power production, e.g., laser power amplifiers and energy collection and conversion systems. Capital costs are also affected by component operating characteristics, in particular, efficiencies. For example, as laser efficiency is decreased, the energy storage capacity of the pulse-forming networks associated with the laser systems and the capacity of the lasing-medium cooling system must be increased.

Increased capital costs associated with decreasing laser efficiency plus increases in costs of reactors with increases in pellet yield are largely responsible for the behavior of the relative power production costs exhibited in Figs. VIII-4 and -5 for which the product of laser efficiency and pellet gain is constant. The results shown in Fig. VIII-6 are explained by the fact that for pellet yields less than ~400 MJ, changes in capital costs are dominated by subsystems for which there is an economy of scale; whereas, for pellet yields greater than 400 MJ, changes in capital costs are dominated by increases in reactor vessel costs.

FUSION-FISSION HYBRID REACTOR STUDIES (W. R. Reupke and T. G. Frank)

Introduction

Our study of fusion-fission hybrid reactor concepts for the production of ^{238}U from ^{232}Th was resumed. In previous studies, we emphasized high performance systems that included a ^{238}U - ^{239}Pu neutron multiplier region between the fusion neutron source and the ^{232}Th breeding blanket.³² This concept would produce large amounts of fissile fuel for conventional power reactors but would also produce large amounts of thermal power. Because of proliferation concerns, such a reactor might have to be government controlled, and it may be desirable to

minimize the power production per unit of fuel produced in such a facility. For this reason, we have initiated a study of concepts that may satisfy this objective.

For the current effort, assistance is being obtained from a LASL engineering design group, for structural and thermal-hydraulic analyses. The results of neutronics and energy deposition calculations are provided to the engineering design group and, through iteration, point designs will be identified.

Neutronics Studies

As was the case for previous studies, our initial investigations are based on the wetted-wall laser fusion reactor concept in spherical geometry in which 100-MJ fusion pellet microexplosions occur at the rate of 1/s. The blankets being evaluated include thorium metal rods in stainless steel cladding cooled by liquid lithium. We require that the tritium breeding ratio exceed unity (i.e., ~1.1) to ensure tritium self-sufficiency for the fuel cycle. The use of neutron multipliers such as beryllium or lead to improve the nuclear performance of the system is being investigated.

Preliminary neutronics scoping studies have been completed with the identification of several point designs that satisfy the requirement on tritium breeding ratio. A general description of the systems for which calculations have been done is given in Table VIII-I. The neutronic characteristics of some designs that satisfy the tritium breeding ratio requirement are summarized in Table VIII-II. This table is self-explanatory except for the column headed "breeding figure of merit," which is defined as the ratio of potential power production from bred ^{238}U to the power produced by the hybrid system.

For a minimum pitch-to-diameter ratio of the thorium rods (13-mm in diameter with 0.2-mm-thick cladding) of 1.05, the volume fraction of thorium in the breeding region is 0.69 with the rest consisting of stainless steel cladding and lithium coolant. Only beryllium neutron multipliers have been investigated at this time. All structural components are assumed made of stainless steel. For systems with relatively thin beryllium neutron multiplier regions, i.e., 4 cm thick, the lithium-coolant volume fraction in the blanket must be quite large to satisfy the tritium breeding requirement. Either the

TABLE VIII-I
FUSION-FISSION HYBRID NEUTRONICS MODEL

<u>Region</u>	<u>Composition and/or Function</u>	<u>Thickness (cm)</u>
1	Reactor cavity	200.(radius)
2	Lithium wetted wall	1.1
3	Neutron multiplier plus structure (if present)	variable
4	Lithium plenum	variable
5	Structural wall	2.0
6	Thorium breeding region	50.
7	Structural wall	2.0
8	Lithium plenum	8.0
9	Outer containment	4.0

TABLE VIII-II
SUMMARY OF BLANKET NEUTRONICS CALCULATIONS

<u>Case</u>	<u>B. Neutron Multiplier Thickness (cm)</u>	<u>Variable Li Plenum Thickness (cm)</u>	<u>Th Volume Fraction in Breeding Region (%)</u>	<u>²³⁵U Production per Fusion Neutron (atom)</u>	<u>Thermal Power Level (MW)</u>	<u>Breeding Figure of Merit</u>
1	04	02	12	0.30	125	2.5
2	11	02	69	0.78	199	4.1
3	04	20	69	0.71	159	4.6
4	---	29	69	0.67	153	4.5

Note: Tritium breeding ratio = 1.1 for all cases.

volume fraction of lithium coolant in the breeding region can be increased at the expense of the thorium content, or the thickness of the lithium region between the neutron multiplier and the breeding region can be increased beyond its nominal value of 2 cm. The first and third cases in Table VIII-II illustrate these alternatives. A thinner blanket that satisfies the tritium breeding requirement results from increasing the beryllium thickness to 11 cm, Case 2. Finally, the beryllium may be eliminated and the lithium plenum thickness increased to 29 cm to provide adequate tritium breeding.

Mechanical Design

Various polygon configurations have been considered for possible use as the basis of a modular blanket design with a triangular fuel element lattice. Included in this evaluation are configurations defined by an icosohedron, a truncated icosohedron, and a truncated octahedron. The truncated octahedron was selected as the most appropriate configuration for use in preliminary design and analysis. This concept is illustrated in Figs. VIII-8 and VIII-9 which consist of side and top views of the reactor and

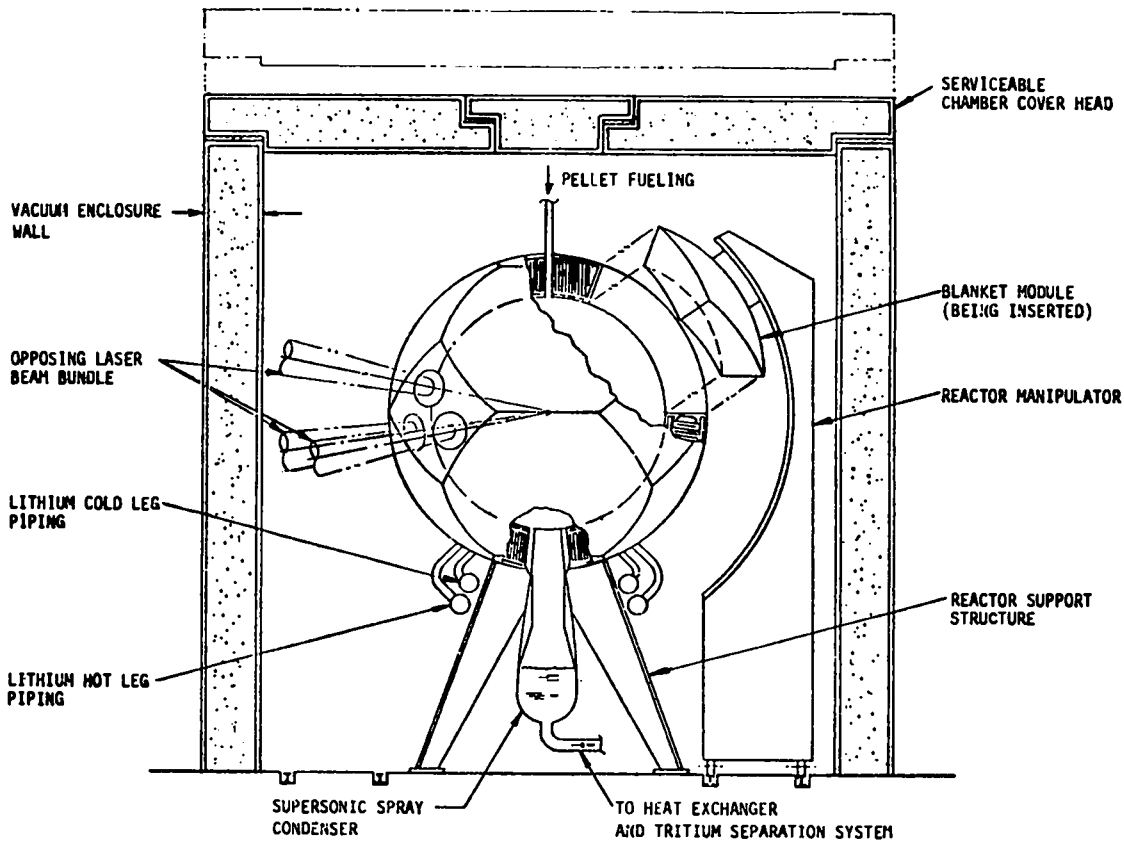


Fig. VIII-8.
Side view of reactor and shielded chamber.

shielded chamber, respectively. The blanket includes eight hexagonal and two square modules, a fueling port at the top, an exhaust port at the bottom, and two equatorial ports for laser beam transport tubes. A remotely operated module manipulator and the reactor support structure are also indicated. Preliminary module designs include sections of the fusion chamber wall and individual coolant systems. The modules with hexagonal cross sections contain 583 thorium rods each and the square modules 145 thorium rods each.

A detailed design of the blanket structure will result from the following efforts in progress.

- Review and evaluation of prospective structural materials. Major considerations include structural and thermal properties, lithium com-

patibility, fabricability, and cost. Materials being considered include zirconium, stainless steel, molybdenum, and niobium as well as their alloys.

- Nuclear evaluation of blanket composition. Neutronics analyses of preliminary designs are being performed to determine energy deposition profiles and breeding performance.
- Thermal-hydraulic performance of blanket modules. Heat transfer, fluid flow, and stress analyses are being performed for cavity wall and blanket configurations using calculated energy deposition data.
- Operation, remote maintenance, safety, system integration and cost will be addressed as detailed blanket designs are established.

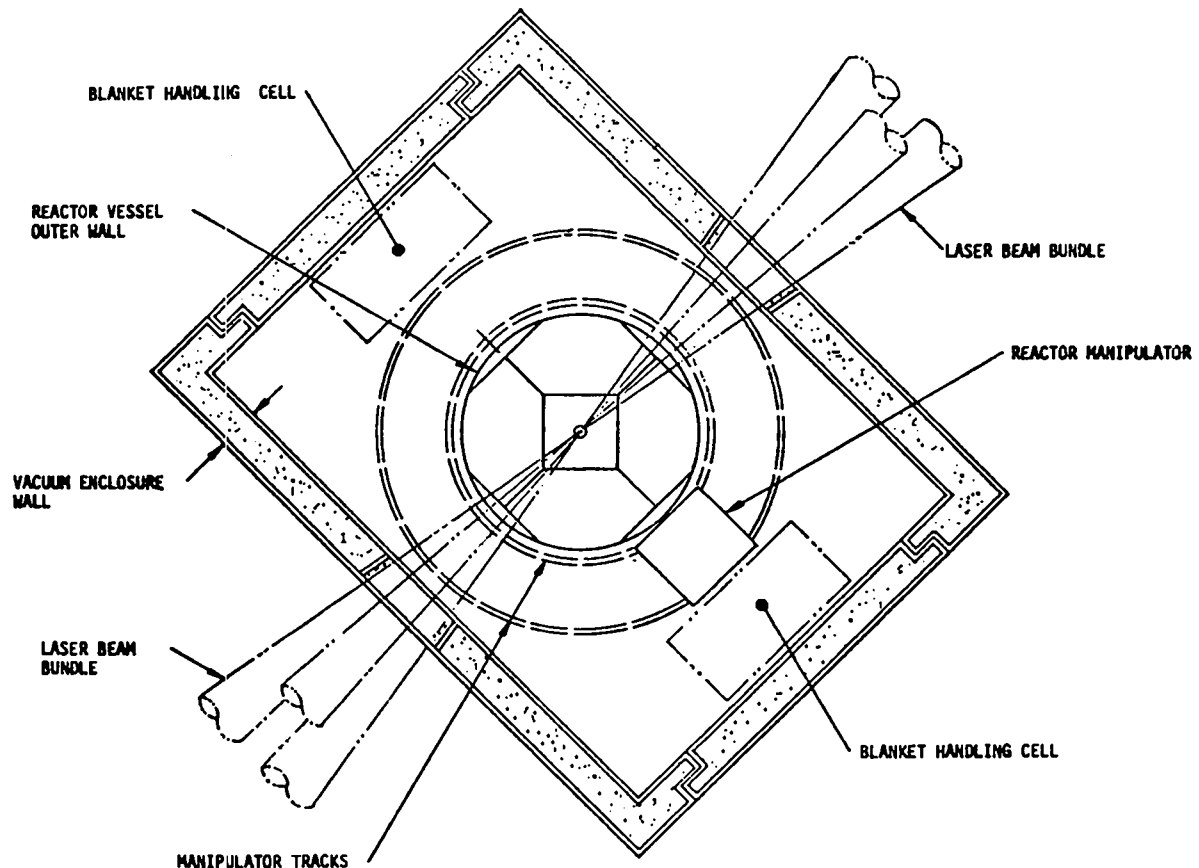


Fig. VIII-9.
Top view of reactor and shielded chamber.

REFERENCES

1. T. Frank, D. Freiwald, T. Merson, and J. Devaney, "A Laser Fusion Reactor Concept Utilizing Magnetic Fields for Cavity Wall Protection," Proc. ANS 1st Topical Meeting on Tech. of Controlled Nuclear Fusion, San Diego, California (1974), V. I, p. 83.
2. I. O. Bohachevsky and J. F. Hafer, "Sputtering Erosion of Fusion Reactor Cavity Walls," Los Alamos Scientific Laboratory report LA-6633-MS (December 1976).
3. R. W. Conn, "SOLACE, A Conceptual Laser Fusion Reactor Design," University of Wisconsin report UWFD-220 (December 1977).
4. I. O. Bohachevsky, J. F. Hafer, J. J. Devaney, and J. H. Pendergrass, "Inertial Confinement Fusion Reactor Cavity Phenomena," Proc. ANS 3rd Topical Meeting on Tech. of Controlled Nuclear Fusion, Santa Fe, New Mexico (1978).
5. J. L. Delcroix, *Introduction to the Theory of Ionized Gases* (Interscience Publishers, New York, New York, 1960), p. 21.
6. S. Chapman and T. G. Cowling, *The Mathematical Theory of Nonuniform Gases* (Cambridge University Press, 1952), p. 220, 252.
7. D. O. Dickman, R. L. Morse, and C. W. Nielson, "Numerical Simulation of Axisymmetric, Collisionless, Finite-Plasma," Phys. Fluids 12, 1708-1716 (1969).

8. J. C. Goldstein, I. O. Bohachevsky, and D. O. Dickman, "Ion Motion in Laser Fusion Reactor Studies," *Bull. Am. Phys. Soc. Paper 9P7, Series 11*, 21, 1185 (1976).
9. P. D. Lax, "Weak Solutions of Nonlinear Hyperbolic Equations and their Numerical Computation," *Comm. Pure and Appl. Math.* VII, 159-193 (1954).
10. I. O. Bohachevsky and E. L. Rubin, "A Direct Method for Computation of Nonequilibrium Flows with Detached Shock Waves," *AIAA Journ.* 4, 600-607 (1966).
11. I. O. Bohachevsky and R. E. Mates, "A Direct Method for Calculation of the Flow About an Axisymmetric Blunt Body at an Angle of Attack," *AIAA Journ.* 4, 776-782 (1966).
12. I. O. Bohachevsky and R. N. Kostoff, "Supersonic Flow Over Convex and Concave Shapes with Radiation and Ablation Effects," *AIAA Journ.* 8, 1024-1031 (1972).
13. F. J. Dyson, "Free Expansion of a Gas, III," *GAMD-566* (October 1958).
14. L. J. Sedov, *Similarity and Dimensional Methods in Mechanics*, M. Holt and M. Friedman, editors and translators (Academic Press, New York, 1959).
15. F. Skoberne, "Laser Fusion Program at LASL, July 1 - December 31, 1975," Los Alamos Scientific Laboratory report LA-6245-PR (July 1976), p. 107.
16. L. A. Booth, "Central Station Power Generation by Laser-Driven Fusion," Los Alamos Scientific Laboratory report LA-4858-MS, V. I (February 1972).
17. T. Frank, D. Freiwald, T. Merson, and J. Devaney, "A Laser Fusion Reactor Concept Utilizing Magnetic Fields for Cavity Wall Protection," *Proc. 1st Topical Meeting on the Tech. of Controlled Nuclear Fusion*, CONF-740402-P1, V. I (1974).
18. J. A. Maniscalco, J. A. Blink, J. Hovingh, W. R. Meier, M. J. Monsler, and P. E. Walker, "A Laser Fusion Power Plant Based on a Fluid Wall Reactor Concept," *Proc. 3rd ANS Topical Meeting on the Tech. of Controlled Nuclear Fusion* (to be published).
19. R. W. Conn, "SOLASE, A Conceptual Laser Fusion Reactor Design," University of Wisconsin report UWFD-220 (December 1977).
20. L. A. Booth, M. G. Bowman, G. E. Cort, K. E. Cox, D. J. Dudziak, R. A. Krakowski, J. H. Pendergrass, and A. S. Tai, "Production of Electrothermochemical Hydrogen Using a Fusion Source of High-Temperature Process Heat," *Proc. 3rd ANS Topical Meeting on the Tech. of Controlled Nuclear Fusion* (to be published).
21. J. A. Fillo, Ed., "Fusion Reactors—High-Temperature Electrolysis (HTE)," Brookhaven National Laboratory report HCP/T0016 (January 1978).
22. L. A. Booth, compiler, "Fusion Energy Applied to Synthetic Fuel Production," US Department of Energy report CONF-770593 (October 1977).
23. L. Dresner, "Mechanical Stress in the Pressure Vessel of a Lithium-Filled, Exploding Pellet, Thermonuclear Reactor," Oak Ridge National Laboratory report ORNL-TM-4050 (1973).
24. J. A. DeMastry, "Corrosion Studies of Tungsten, Molybdenum, and Rhenium in Lithium," *Nucl. Appl.* 3, 127 (1967).
25. J. H. Mannon, "Hot Future for Ceramics," *Chem. Eng.* 84(26), 75 (1977).
26. B. A. Smith, "Ceramic Parts Tested in T76 Engine," *Aviation Week and Space Tech.* 109(4), 43 (1978).
27. W. A. Ranken, "Ceramic Heat Pipe Heat Exchangers," Los Alamos Scientific Laboratory report LA-6514-MS (October 1976).
28. F. T. Finch, E. A. Kern, and J. M. Williams, "Laser Fusion Power Plant Systems Analysis,"

- 1st Top. Meeting on Tech. of Controlled Nuclear Fusion, San Diego, California (ANS) (1974).
29. E. A. Kern, T. G. Frank, and L. A. Booth, "Systems Analysis of Laser Fusion Power Plants," ANS Winter Meeting, San Francisco, California (1975).
 30. I. O. Bohachevsky, "Scaling of Reactor Cavity Wall Loads and Stresses," Los Alamos Scientific Laboratory report LA-7014-MS (November 1977).
 31. T. G. Frank, I. O. Bohachevsky, L. A. Booth, and J. H. Pendergrass, "Heat Transfer Problems Associated with Laser Fusion," 16th Nat'l. Heat Transfer Conf., St. Louis, Missouri (1976).
 32. E. Stark and F. Skoberne, "Laser Fusion Program at LASL, January 1-June 30, 1976," Los Alamos Scientific Laboratory report LA-6510-PR (November 1976).

IX. RESOURCES, FACILITIES, AND OPERATIONAL SAFETY

The design and construction of HEGLF Facilities continued. Safety policies and procedures continued to be applied successfully to minimize the hazards of operating high-energy lasers.

MANPOWER DISTRIBUTION

The distribution of employees assigned to the various categories of the Department of Energy-supported Laser Fusion Research Program is shown in the table.

APPROXIMATE STAFFING LEVEL OF LASER PROGRAM June 30, 1978

<u>Tasks</u>	<u>Direct Employees</u>
CO ₂ Laser Development	102
CO ₂ Laser Experiments	100
Pellet Design	25
Pellet Fabrication	30
Diagnostics Development	30
Systems and Advanced Technology	21
TOTAL	308

FACILITIES

High-Energy Gas Laser Facility (HEGLF)

Construction Package I, including the laser building, the mechanical building and a warehouse is 23% complete, with a scheduled completion date of July 1979.

Construction Package II, including the target building, the power-transmission system, and miscellaneous other construction is 21% complete, with a scheduled completion date of July 1979.

In the interest of continuity, we have presented details in HEGLF Design and Construction in Section II.

New Laboratories

The contract for the High-Voltage and Optical-Evaluation Laboratories was awarded in January 1978; construction is 56% complete, with a scheduled completion date of October 1978.

OPERATIONAL SAFETY

General

Historically, the Laser Fusion Research Program activities have never caused biological damage to any employee from laser radiation. This record continued during this period.

Employees of the Laser Research and Technology Division, since its formation in 1972, have worked a total of 2.4 million man-hours and have experienced 9 lost-time injuries, resulting in a total of 27 days lost time. The severity rate of only 11 days lost time per 1 000 000 man-hours is well below minimum (110) reported for any industry by the National Safety Council (1975 figures).

Laser Protective Eyewear

The need to increase the power of visible (He:Ne and Kr) alignment lasers for Helios in accommodating the neutron diagnostics resulted in the use of protective eyewear of colored filter glass for reducing exposure to retinal tissue to acceptable levels in viewing the beam.

X. PATENTS, PRESENTATIONS, AND PUBLICATIONS

APPLICATION FILED IN US PATENT OFFICE

S. N. 908 031, "Enhancement of CO₂ Pulse Contrast Ratios Via Transient Response of Low-Pressure Resonant Absorbers," Barry J. Feldman, Robert A. Fisher, Edward J. McLellan, filed May 22, 1978.

PRESENTATIONS

The following presentations were made at the 3rd ANS Topical Meeting on Technology of Cont. Nuclear Fusion, Santa Fe, New Mexico (May 5, 1978).

J. Pendergrass, "Theoretical Analysis of Liquid-Metal-Filled Heat Pipes Used for Tritium Concentration from Fusion Reactor Breeding Blankets"; "Computer Programs for Capital Cost Estimation, Lifetime Economic Performance Simulation, and Computation of Cost Indexes for Laser Fusion and Other Advanced Technology Facilities"; "Mixing Rules and Effects of the Presence of Other Hydrogen Isotopes and Isotopic Swamping on Tritium Recovery and Loss to Biosphere from Fusion Reactors."

E. E. Stark, Jr., "Lasers and Power Systems for Inertial Confinement Fusion Reactors"; "CO₂ Laser Fusion."

I. O. Bohachevsky, L. A. Booth, J. F. Hafer, and J. H. Pendergrass, "The Effects of Pellet Yield on Production Cost in Laser Fusion Electric Generating Stations."

I. O. Bohachevsky, J. J. Devaney, J. F. Hafer, and J. H. Pendergrass, "Inertial Confinement Fusion Reactor Cavity Phenomena."

T. G. Frank, "A Thorium-Uranium Cycle ICF Hybrid Concept."

The following presentations were made at the Topical Meeting on Inertial Confinement Fusion, San Diego, California (February 1978).

J. J. Devaney, L. A. Booth, J. H. Pendergrass, and T. G. Frank, "Environmental Effects and Potential Hazards of Laser Fusion Generating Stations."

L. A. Booth, "Applications of Inertial Confinement Fusion."

P. N. Wolfe and C. E. Knapp, "Energy Extraction and Pulse Shaping in Antares."

T. F. Stratton, F. P. Durham, J. Jansen, W. T. Leland, W. H. Reichelt, and V. L. Zeigner, "The LASL 100-kJ CO₂ Laser for ICF Research: Antares."

K. Riepe, "High-Voltage Engineering in the Eight-Beam System."

W. H. Reichelt, J. L. Munroe, K. C. Jones, A. C. Saxman, and J. E. Sollid, "Antares Optical Design and Analysis."

J. Jansen, K. C. Jones, K. B. Riepe, G. Ross, G. Allen, and R. Lindstrand, "Antares Power Amplifier Module Design."

J. T. Ganley, W. T. Leland, D. Swanson, and G. York, "Prototype Antares Power Amplifier Module."

J. R. Miller, R. D. Day, E. H. Farnum, W. G. Hansen, H. E. Tucker, and W. A. Teasdale, "Laser Fusion Target Positioning."

R. L. Whitman, R. P. Kruger, R. H. Day, and D. M. Stupin, "Two-Dimensional Computer Modeling and Analysis of Thin-Wall Microspheres."

D. M. Stupin, R. H. Day, R. L. Whitman, R. P. Kruger, "Microradiography of Laser Fusion Targets with Monochromatic X-Rays."

E. H. Farnum and H. R. Maltrud, "A Minimum Release, High-Pressure DT Fill System for Laser Fusion Targets."

B. Cranfill, E. H. Farnum, A. T. Lowe, and J. R. Miller, "Fabrication of Complex Cryogenic Targets."

R. F. Benjamin, P. D. Goldstone, and J. P. Carpenter, "Recent Advances in High-Resolution Alignment Techniques at 10.6 μ m."

R. L. Carman, "Plans for Picosecond Interferometry of Plasmas."

The following presentations were made at various institutions.

A. R. Larson and C. D. Cantrell, "Homogeneous Nucleation Master Equation," APS Meeting, Washington, D.C. (April 1978).

D. O. Dickman, "Laser Fusion Cavity Geometry using Computer Simulation," Joint Institute of Laboratory Astrophysics, University of Colorado (March 1978).

D. O. Dickman, "The Making of a Movie Target for Antares," Annual Conf. of Ind. Photographers of the Southwest, (May 1978).

C. R. Phipps, Jr., "Observation of Absorption and Wavefront Distortion Due to Plasma Formation in Ge at 10.6 μ m," Stanford University Quantum Electronics Seminar, Palo Alto, California (February 7, 1978).

C. W. Cranfill, "The Need for Improved Atomic Physics in Laser Fusion Codes," H-Division Seminar at Lawrence Livermore Laboratory, Livermore, California (March 30, 1978).

S. J. Gitomer, "Laser Fusion," Seminar Department of Electrical Engineering, Texas Tech Univ., Lubbock, Texas (February 1978).

S. J. Gitomer and H. Brysk, "Space Charge Effects in Laser Plasma Particle Diagnostics," Topical Conference on High-Temperature Plasma Diagnostics, Santa Fe, New Mexico (May 1978) and

at the 1978 IEEE International Conference on Plasma Science, Monterey, California (May 1978).

S. J. Gitomer, E. J. Linnebur, and G. H. McCall, "Modeling Emission Spectra from CO₂ Laser Produced Plasmas," 1978 International Conference on Plasma Science, Monterey, California (May 15-17, 1978).

M. S. Stroschio and D. B. Henderson, "Two-Dimensional Resolution of CO₂ Profile Modification," Eighth Anomalous Absorption Meeting, Tucson, Arizona (April 19, 1978).

M. A. Stroschio, D. W. Forslund, S. J. Gitomer, D. B. Henderson, J. M. Kindel, K. Lee, and E. Lindman, "Field Gradient Force as a Dominant Effect in High-Intensity Laser-Plasma Interactions," Tenth International Quantum Electronics Seminar, Atlanta, Georgia (May 29-June 1, 1978).

W. P. Gula, "Target Design to Achieve 20 X Liquid Density with a CO₂ Laser," 1978 IEEE International Conf. on Plasma Science, Monterey, California (May 15-17, 1978).

R. J. Mason, "Double-Diffusion Hot-Electron Transport in Laser Produced Plasmas," 1978 IEEE Conf. on Plasma Science, Monterey, California (May 15-17); Colloquium, Naval Research Laboratory, Washington, D.C. (June 20, 1978); and Colloquium, Laboratory for Laser Energetics, Rochester, New York (June 22, 1978).

M. E. Thuot, "Fiber Optics and Microprocessors: A Control System Solution for the Laser Fusion Environment," NEPCON/WEST, Anaheim, California (February 28-March 2, 1978).

W. T. Leland, "Design Engineering of Large High-Pressure Gas Laser Amplifiers," SPIE Technical Symposium East 1978, Washington, D.C. (March 28-31, 1978).

M. E. Thuot, "Fusion Optics and Microprocessors: A Control-System Solution for the Laser-Fusion Environment," NEPCON 1978 East Conf., New York, New York (May 9-11, 1978).

R. Williamson, "Batch Cleaning and Drying of Optics Using a Spin Dryer," OSA Optical Fabrication Workshop, Rochester, New York (May 11, 1978).

G. York, "Sodium Vapor Heat Pipe Laser Cell," 3rd International Heat Pipe Conference, Palo Alto, California (May 22-24, 1978).

W. H. Reichelt, "The Optical Train and Optical Fabrication Processes for the Antares Laser System, Lawrence Livermore Laboratory, Livermore, California (June 14, 1978).

K. Bickford and K. Reipe, "Development of a 400-kA, 6-C, Compact Marx Switch," Thirteenth Pulse Power Modulator Symposium, Buffalo, New York (June 20-22, 1978).

V. M. Cottles, L. G. White, and A. H. Williams, "The Absorption of 1-ns CO₂ Laser Pulses by Plane Finite Targets," 8th Annual Conf. on Anomalous Absorption of Electromagnetic Waves, Tucson, Arizona (March 19-21, 1978).

G. T. Schappert, S. Singer, J. Ladish, and M. Montgomery, "Comparison of Theory and Experiment on the Performance of the Los Alamos Scientific Laboratory Eight-Beam 10 kJ CO₂ Laser," Sixth Conf. on Chem. and Molecular Lasers, Tenth International Quantum Electronics Conf., Atlanta Georgia (May 29-June 1, 1978).

W. S. Hall, J. Sollid, et al., "Interferogram Reduction and Interpretation as Applied to the Optical Analysis of the 10 kJ LASL Laser Fusion System," American Society for Testing and Materials Mini-Symposium—Reduction and Interpretation of Interferograms, Ft. Lauderdale, Florida (January 11-12, 1978).

PUBLICATIONS

E. R. Grilly, "Development of Cryogenic Targets for Laser Fusion," in *Advances in Cryogenic Engineering*, K. D. Tinnerhaus, ed. (Plenum Press, New York, London, 1978), Chap. 23, p. 676.

A. Lieber, H. D. Sutphin, R. C. Hyer, J. S. McGurn, K. Winn, "Sub-Picosecond Proximity—Focused Visible Streak Camera Evaluation and Application," Proc. SPIE Conf., San Diego, CA (August 25-26, 1977).

S. J. Czuchlewski, A. V. Nowak, E. Foley, J. F. Figueira, "Broadband Gas Isolator for High-Power Carbon Dioxide Lasers," Opt. Lett. 2, 39-41 (1978).

R. C. Malone, R. L. Morse, "Resonant Absorption in Plasma Density Profiles Produced by Laser Heating," Phys. Fluids 21, 143-44 (1978).

T. F. Stratton, W. H. Reichelt, "Optical Design and Components for a 100 kJ Carbon Dioxide Laser," Optics in Adverse Environments Seminar, San Diego, California, Proc. S.P.I.E., E. Bernal, Ed., 128-30 (1978).

M. D. Bausman, I. Liberman, J. P. Manning, S. Singer, "Alignment System for Large High-Power Pulsed Carbon Dioxide Laser Fusion Systems," Clever Optics, Innovative Applications of Optics Seminar, San Diego, California, Proc. S.P.I.E., N. Balasubramanian, Ed., 23-31 (1977).

C. J. Elliott, "Assessment of Dynamical Parasitics in the EBS," Los Alamos Scientific Laboratory report LA-7166-MS (1978).

B. G. Strait, M. E. Thuot, J. P. Hong, "Distributed Microcomputer Control System for a High-Energy Gas-Laser Facility," Micro 77 Computer Conf. Record, 99-104 (April, 1977).

K. B. Riepe and M. Kircher, "Design of the Energy Storage System for the High Energy Gas Laser," 7th Symp. Engineering Problems of Fusion Research, Knoxville, Tennessee, M. S. Lubell, Ed., Proc. IEEE 2, 1053-55 (1977).

H. Jansen and V. L. Zeigner, "Design of the Power Amplifier for the HEGLF at LASL," 7th Symp. Engineering Problems of Fusion Research, Knoxville Tennessee, Proc. IEEE 1, M. S. Lubell, Ed., 489-493 (1977).

- M. D. Montgomery, R. Carlson, D. E. Casperson, S. J. Czuchlewski, R. F. Haglund, J. S. Ladish, A. V. Nowak, and S. Singer, "Stabilization of High-Gain Multipass Power Amplifiers Using Saturable Absorbers. Experience on the Los Alamos Scientific Laboratory Eight-Beam System," *Appl. Phys. Lett.* **32**, 324-6 (1978).
- J. M. Kindel and M. A. Stroschio, "Double-Shell Target Designs for the Los Alamos Scientific Laboratory Eight-Beam Laser System," Los Alamos Scientific Laboratory report LA-7167-MS (March 1978).
- J. R. Miller and J. E. Sollid, "Interferometric Measurement of Cryogenic Laser Fusion Target Uniformity," *Appl. Opt.* **17**, 852-3 (1978).
- B. J. Feldman, R. A. Fisher, C. R. Pollock, S. W. Simons, and R. G. Tercovich, "Sequence-Band Lasing in a High-Pressure Carbon Dioxide Discharge," *Laser and Electro-optical Systems, 1978 OSA/IEEE Conf.*, San Diego, California, Digest of Technical Papers, No. WEEL, 48-9 (1978).
- B. S. Cranfill, "Preparation of Ultrathin Polyethylene Foils by Film Casting," *Rev. Sci. Instrum.* **49**, 264-5 (1978).
- T. S. Fahlen, "Discharge Pumped Excimer Lasers," *OSA/IEEE Conference on Laser and Electro-optical Systems, San Diego, California, Digest of Technical Papers, OSA* (1978).
- S. J. Gitomer and H. Brysk, "Space-Charge Effects on Particle Diagnostics of Laser-Produced Plasmas," *Appl. Phys. Lett.* **32**, 616-8 (1978).
- V. K. Viswanathan, W. S. Hall, I. Liberman, and G. Lawrence, "Interferogram Reduction and Interpretation as Applied to the Optical Analysis of the 10-kJ LASL Laser Fusion Systems," in *Optical Interferograms, Reduction and Interpretation*, A. Guenther and D. Liebenberg, eds. (ASTM Publication STP-666, Philadelphia, 1978), pp. 98-106.
- M. E. Thuot, "Fiber Optics and Microprocessors—A Control-System Solution for the Laser-Fusion Environment," *Proc. Tech. Program Nat. Electronic Packaging and Production Conf.*, Anaheim, California (February 28, 1978).
- D. V. Giovanielli and C. W. Cranfill, "Simple Model for Exploding Pusher Targets," Los Alamos Scientific Laboratory report LA-7218-MS (May 1978).
- R. K. Ahrenkiel, P. B. Weiss, D. W. Watkins, S. K. Gulati, and W. W. Grannemann, "Faraday Effect in Mercury (1-X) Cadmium (X) Telluride at Carbon Dioxide Laser Wavelengths," *J. Appl. Phys.* **49**, 2265-7 (1978).
- S. J. Czuchlewski, A. V. Nowak, and E. Foley, "Efficient Gas Isolator for Carbon Dioxide 10-Micrometer P-Branch," *Proc. Electro-Optics/Laser 77 Conference and Exposition, Anaheim, California*, 303-11 (1977).
- A. Lieber, "Modern Ultrafast Streak Camera Development and Application Review," *Proc. Electro-Optics/Laser 77 Conference and Exposition, Anaheim, California*, 336-9 (1977).
- R. F. Benjamin and L. White, "Measurement of Alignment Accuracy for Laser Fusion Experiments," *Appl. Opt.* **17**, 1160 (1978).
- J. R. Miller, "New Method for Producing Cryogenic Laser Fusion Targets," *Advances in Cryogenic Engineering* **23**, 669-75 (1978).
- W. T. Leland, J. T. Ganley, M. Kircher, and G. York, "Large-Aperture Discharges in E-Beam Sustained Carbon Dioxide Amplifiers," *Proc. 7th Symp. on Engineering Problems of Fusion Research, Knoxville, Tennessee* (1977).
- F. Skoberne and E. E. Stark (compilers), "Laser Fusion Program at Los Alamos Scientific Laboratory, January 1-June 30, 1977," Los Alamos Scientific Laboratory report LA-6982-PR (April 1978).
- W. T. Leland, G. York, J. T. Ganley, D. A. Swanson, G. Loda, E. J. Yavornik, K. B. Riepe, R. Lindstrand, and J. C. Comply, "Antares Prototype Power Amplifier—Final Report," Los Alamos Scientific Laboratory report LA-7186 (July 1978).
- G. S. Fraley, K. Lee, and M. A. Stroschio, "Hybrid Method for the Numerical Solution of the Electron Transport Equation—The Reduced Source Method," Los Alamos Scientific Laboratory report LA-7410-MS (August 1978).

The following were presented at the Topical Meeting on Inertial Confinement Fusion, 1978, San Diego, CA, Digest of Technical Papers OSA (1977).

R. W. Springer, "Controlling Surface Finished in Vacuum Deposited Coating for Laser Fusion."

W. J. McCreary and D. S. Catlett, "Application of Chemical Vapor Deposition to the Fabrication of Laser Fusion Targets."

A. Mayer and E. S. Catlett, "Plating Laser Fusion Targets."

R. L. Whitman, R. Kruger, R. H. Day, and D. M. Stupin, "Two-Dimensional Computer Modeling and Analysis of Thin-Wall Microspheres."

E. H. Farnum and H. R. Maltrud, "Minimum Release, High Pressure DT Fill System for Laser Fusion Targets."

W. H. Reichelt, J. Munroe, K. C. Jones, A. C. Saxman, and J. E. Sollid, "Antares Optical Design and Analysis."

A. H. Williams, "Calorimeter for Laser Beams and Plasma Diagnostics."

L. A. Booth, "Applications of Inertial Confinement Fusion."

L. A. Booth and I. O. Bohachevsky, "Requirements for Commercialization of Inertial Confinement Fusion."

L. A. Booth and J. H. Pendergrass, "Synthetic Fuel Production From ICF Sources."

E. E. Stark, Jr. and H. Jansen, "Carbon Dioxide Laser Systems Studies."

M. D. Montgomery, R. Carlson, D. E. Casperson, S. J. Czuchlewski, J. F. Figueira, R. F. Haglund, E. Jolly, J. S. Ladish, A. V. Nowak, J. G. Sutton, M. D. Thomason, and E. L. Zimmermann, "Stabilization of High Gain Multipass Power Amplifiers Using Saturable Absorbers. Experience on the Los Alamos Scientific Laboratory Eight-Beam System."

J. H. Pendergrass, "Tritium Processing Systems for Inertial Confinement Fusion Facilities."

B. S. Cranfill, E. H. Farnum, A. T. Lowe, and J. R. Miller, "Fabrication of Complex Cryogenic Targets."

J. P. Manning, Q. G. Klingler, C. J. Stump, and I. Liberman, "Carbon Dioxide Laser Fusion Target Alignment."

J. C. Brown, F. J. Feldman, R. A. Fisher, S. W. Simons, and R. G. Tercovich, "1800 Torr Large Aperture Double Discharge Carbon Dioxide Laser Amplifier."

A. W. Ehler and J. P. Carpenter, "Vacuum UV Imaging of a Laser Produced Plasma."

A. V. Nowak, S. J. Czuchlewski, E. Foley, and J. F. Figueira, "Development of Broadband Gas Isolator Mixes for High Power Carbon Dioxide Lasers."

I. O. Bohachevsky and T. G. Frank, "Containment Vessel Structural Design Considerations."

A. T. Lowe and R. J. Fries, "Plasma Polymerized Films as Laser Fusion Targets."

D. Kohler and P. B. Weiss, "Use of Pyroelectric Vidicons for Measurements on Carbon Dioxide Laser Systems."

E. J. McLellan and J. F. Figueira, "Variable Pulse Width Generation for Carbon Dioxide Lasers in the 100-ps to 1-ns Range."

C. R. Phipps, Jr., and S. J. Thomas, "Characterization of P-Type Germanium for 10 Micrometer Region Passive Isolation and Pulse Shaping."

V. K. Viswanathan, "Optical Analysis and Predictions for the LASL Eight Beam Laser Fusion System."

R. D. Day and C. E. Cummings, "LASL Eight Beam Laser Target Insertion System."

J. J. Devaney, L. A. Booth, J. H. Pendergrass, and T. G. Frank, "Environmental Effects and Potential

Hazards of Laser Fusion Electric Generating Stations."

E. E. Stark, W. T. Leland, and H. C. Volkin, "Nanosecond Pulse Amplification in Carbon Dioxide at Efficiencies Exceeding 20 Percent."

P. N. Wolfe, B. J. Feldman, J. F. Hafer, C. E. Knapp, and H. C. Volkin, "Energy Extraction and Pulse Shaping in Antares."

J. T. Ganley, W. T. Leland, D. A. Swanson, and G. York, "Prototype Antares Power Amplifier Module."

T. F. Stratton, F. P. Durham, H. Jansen, W. T. Leland, W. H. Reichelt, and V. L. Zeigner, "LASL 100-kJ Carbon Dioxide Laser for ICF Research Antares."

I. O. Bohachevsky, L. A. Booth, T. G. Frank, J. F. Hafer, and J. H. Pendergrass, "General ICF Reactor Design Considerations."

W. L. Bongianni, S. Butler, and J. R. Miller, "Batch Processing Techniques for Microballoon Fusion Targets."

Printed in the United States of America. Available from
 National Technical Information Service
 U.S. Department of Commerce
 5285 Port Royal Road
 Springfield, VA 22161

Microfiche \$3.00

001-025	4.00	126-150	7.25	251-275	10.75	376-400	13.00	501-525	15.25
026-050	4.50	151-175	8.00	276-300	11.00	401-425	13.25	526-550	15.50
051-075	5.25	176-200	9.00	301-325	11.75	426-450	14.00	551-575	16.25
076-100	6.00	201-225	9.25	326-350	12.00	451-475	14.50	576-600	16.50
101-125	6.50	226-250	9.50	351-375	12.50	476-500	15.00	601-625	

Note: Add \$2.50 for each additional 100-page increment from 601 pages up.